IMPACT OF INTERFACIAL CHEMISTRY ON CORROSION, SENSING, AND CATALYTIC PROPERTIES OF MATERIALS

Thesis by

John Matthew Evans

In Partial Fulfillment of the Requirements for

the degree of

Doctor of Philosophy

CALIFORNIA INSTITUTE OF TECHNOLOGY

Pasadena, California

2024

(Defended May 17, 2024)

ORCID: 0000-0002-8721-5316

ACKNOWLEDGEMENTS

There are frankly too many people to thank for their role in making this all possible. First, I would like to acknowledge the work of coworkers and collaborators that participated in the work contained in this document. Sean Byrne, Kyra Lee, Ellen Yan, Zach Ifkovits, Jackie Dowling, Madeline Meier, Mo Morla, Pai Buabthong, and Alex Ye at Caltech, as well as Kris Koskela at University of Southern California, Changsub Kim at NASA Jet Propulsion Laboratory, and Kamsy Anderson and Martin Edwards at the University of Arkansas. While this is not an exhaustive list, all of these people contributed significantly to the work in this thesis, and I thank all of them for their work, guidance, and support. I would like to highlight the team at the University of Arkansas who graciously hosted me for a month to do collaborative work. Of course, I also need to acknowledge my advisor Nate Lewis who allowed me the freedom to work on projects I found interesting, allowed me to dedicate a significant portion of time to the Caltech and Pasadena community, and helped me grow into an independent scientist. Bruce Brunschwig taught me so much about how to be a careful scientist and take care of instruments—specifically a Kratos Axis Ultra—and his approach of hands-on learning was critical to my work and career. Bruce also is an excellent source of wisdom and was a great advisor and boss. Kimberly Papadantonakis was also critical in keeping my head on straight, and I am very glad to have continued to have her on my side. Azhar Carim has been a steady presence in the group since I joined, and the work he does to keep our group afloat cannot be understated, though everyone in the group knows we would actually be nowhere without Barbara Miralles. I have also had

the privilege of having a great relationship with my committee. Geoff Blake and Kimberly See have been there for me to discuss my career and scientific topics but have also been looking out for me behind the scenes and I thank both for the pleasure of having them on my committee. Special thanks are in order for Harry Gray, my committee chair and—I am thankful to say—my friend. Harry, I don't know what else I can say besides thank you for everything. Thank you as well to unofficial committee members Scott Cushing and Karthish Manthiram for their advice, support, and friendship over the years. Thank you to Alison Ross, who is the bedrock of the Caltech chemistry department. I would also like to thank Aaron Taggart, Shannon McCullough, and Jim Cahoon from the University of North Carolina at Chapel Hill for their mentorship while I was an undergraduate student and beyond.

Beyond the lab, Kitty Cahalan and Mitch Aiken have been steadfast supporters of me personally and have enabled my passion for outreach. Thank you to Madison Elementary for welcoming us to teach their students all these years. Michael Mazza deserves the credit for getting me involved in this program, and he—as well as Madeline Meier, Haley Bauser, Zach Ifkovits, Christian Goodnow, and Elizabeth Littlefield—have been a fantastic group of friends with whom I have had many adventures. Speaking of friends, Jose Sintas, Yaman Peksenar, Andrew Traywick, and Griffin Barnes have been a fabulous crew. I would like to specially acknowledge Jose for his unwavering support and Yaman for his infectious excitement. It is important to have a solid group of friends to make it through the ups and downs of graduate school and I couldn't be more grateful for mine. My graduate school cohort included Michelle Qian, Laura Quinn, Danika Nimlos, Sadie Dutton, Brian

Lee, Kim Pham, and Sarah Simon whose friendship has meant more to me than they'll ever know. Beyond just my cohort, Sean Byrne, Zak McFarland, Wendy Zhang, Vince Nguyen, Skyler Ware, Sam Engle, and Anna Overholts have been wonderful, close friends. I am grateful to have had the opportunity to attend several conferences, partially for the ability to become part of the wider scientific community, but mostly because it allowed me to meet the incomparable Allie Zito. Allie has truly supported me through everything ever since and I can never really thank her enough for what she has done for me.

Finally, I would like to thank Mikayla and Jackson Welker who may as well be my siblings at this point as well as Shannon Evans, who is actually my sibling. I treasure you all. Thank you to Jack and Margaret McDermott, as well as Joyce Murphy. All of whom would have been overjoyed to read this document. I miss you all, and I know Jack would have had lots of questions. And, of course, this document is a testament to John and Mary Evans who sacrificed and worked carefully and tirelessly to raise me to have a curious mind and an open heart. Thank you, Mom and Dad. For everything.

ABSTRACT

Interfaces are critical for the development of new technologies spanning applications from energy to sensing. Here, electrochemical and spectroscopic investigations of interfacial chemistry reveal how the sensitivity of chemical vapor sensors can be tuned, how stoichiometry and electrolysis affect the chemical state of a Mn-based oxygen evolution catalyst, and how the presence of barrier protection layers affects the stability of photoanodes in alkaline solution. Additionally, an in-depth discussion of x-ray photoelectron spectroscopy gives advice and insight into this surface-sensitive technique and several practical examples are discussed.

PUBLISHED CONTENT AND CONTRIBUTIONS

- P. Buabthong, J.M. Evans, K.Z. Rinaldi, K.M. Kennedy, H.J. Fu, Z.P. Ifkovits, T.J. Kuo, B.S. Brunschwig, N.S. Lewis. "GaAs Microisland Anodes Protected by Amorphous TiO2 Films Mitigate Corrosion Spreading During Water Oxidation in Alkaline Electrolytes" *ACS Energy Letters* 2021, 6 (10), 3709-3714 https://doi.org/10.1021/acsenergylett.1c01174
    - J.M.E. participated in experiments and manuscript editing.
- J.M. Evans, K.S. Lee, E.X. Yan, A.C. Thompson, M.B. Morla, M.C. Meier, Z.P. Ifkovits, A.I. Carim, N.S. Lewis "Demonstration of a Sensitive and Stable Chemical Gas Sensor Based on Covalently Functionalized MoS_2" *ACS Materials Letters* 2022, 4 (8), 1475-1480 https://doi.org/10.1021/acsmaterialslett.2c00372
    - J.M.E. Analyzed data and wrote manuscript.
- K.M. Koskela, C. Mora Perez, D.B. Eremin, J.M. Evans, M.J. Strumolo, N.S. Lewis, O.V. Prezhdo, R.L. Brutchey. "Polymorphic Control of Solution-Processed Cu_2SnS_3 Films with Thiol–Amine Ink Formulation" *Chemistry of Materials* 2022, 34 (19), 8654-8663 https://doi.org/10.1021/acs.chemmater.2c01612
    - J.M.E. performed XPS experiments and assisted in data analysis.
- Z.P. Ifkovits, J.M. Evans, P.A. Kempler, M.B. Morla, K.H. Pham, J.A. Dowling, A.I. Carim, N.S. Lewis. "Powdered $Mn_ySb_{1-y}O_x$ Catalysts for Cerium-Mediated Oxygen Evolution in Acidic Environments" *ACS Energy Letters* 2022, 7, (12), 4258-4264 https://doi.org/10.1021/acsenergylett.2c01754
    - J.M.E. performed XPS experiments, performed data analysis, assisted in conception of project and interpretation of electrochemical data, and assisted in manuscript writing.
- C. Kim, C. Bell, J.M. Evans, J. Greenfield, E. Batson, K.K. Berggren, N.S. Lewis, D.P. Cunnane "Wafer-Scale MgB_2 Superconducting Devices" ArXiv preprint 2023 https://doi.org/10.48550/arXiv.2305.15190
    - J.M.E. performed XPS experiments, performed data analysis, assisted in manuscript editing
- J.A. Dowling, Z.P. Ifkovits, A.I. Carim, J.M. Evans, M.C. Swint, A.Z. Ye, M.H. Richter, A.X. Li, N.S. Lewis. "Catalysis of the Oxygen-Evolution Reaction in 1.0 M Sulfuric Acid by Manganese Antimonate Films Synthesized via Chemical Vapor Deposition" *ACS Applied Energy Materials* 2024 https://doi.org/10.1021/acsaem.4c00135

- J.M.E. performed XPS experiments and data analysis, assisted in conception of project, and assisted in manuscript writing and editing.

TABLE OF CONTENTS

Chapter 1

Demonstration of a Sensitive and Stable Chemical Gas Sensor Based on Covalently Functionalized MoS_2

1.1—Introduction and background

Artificial olfactory systems, or electronic noses, are capable of detecting and distinguishing volatile organic vapors, and consequently have potential applications in air quality management, disease diagnosis, and detection of chemical weapons.[1–12] In one implementation of an electronic nose, an array of cross-reactive, chemically sensitive resistive sensors can perform vapor detection by mimicking the functionality of biological olfactory systems.[7,9,13–19] When an analyte such as an organic vapor is introduced to the sensor array, the analyte interacts with the sensing material, either through permeation, adsorption or other mechanism, producing a change in the dc electrical resistance of the sensor film.[1,2,6] Artificial olfactory chemiresistive sensor arrays have been developed using a variety of materials such as intrinsically conducting or non-conducting polymers loaded with conducting material (e.g., carbon black or graphene), as well as individually functionalized metal nanoparticles.[1–12,17,20–27]

Two-dimensional (2-D) materials such as graphene and transition metal dichalcogenides have also been considered for chemical sensing applications.[3,16,17] MoS_2 has been used for a variety of electronic applications such as sensors, photovoltaics, and batteries, as well as for

gas sensing.[28–39] Experimental and computational analyses have indicated that MoS_2-based sensors have excellent sensitivity, providing detection of a variety of analytes at concentrations lower than 1 part per million, due to favorable electronic interactions coupled with a high surface-area-to-volume ratio.[3,30,37–39]

MoS_2 commonly exists in several phases with different properties, including the 2H, 3R, and 1T phases, where the number denotes the number of layers in the unit cell and the letter denotes the symmetry (H = hexagonal, R = rhombohedral, T = tetragonal).[40] Chemical exfoliation of the thermodynamically stable, semiconducting 2H phase yields the metastable, semimetallic 1T′ phase (a distortion of 1T).[35,41–45]

The 1T′ phase is more reactive than the 2H phase and has been used to covalently functionalize the MoS_2 surface.[35,40,41,43,46,47] Covalent surface functionalization of MoS_2 with organic groups enables tailoring of the electronic and optical properties of the material and increases its stability in a variety of ambients.[40,41,48–51] Specifically, the ability of a bound moiety to donate or withdraw electron density is a major factor in affecting the catalytic performance of MoS_2.[50,51] Moreover, when analytes interact with the bare 2H MoS_2 surface, changes in carrier concentration and band structure result in a change in the electrical conductivity of the material.[37,39,52] A similar effect is proposed to occur here with 1T′ MoS_2.

Herein, chemiresistive sensors based on bare 2H MoS_2, chemically exfoliated 1T′ MoS_2, and functionalized MoS_2 were prepared and characterized for the detection of volatile organic compounds having a range of polarities. This approach combines the excellent

sensitivity observed for MoS_2 as a sensing material with chemical tailoring of the surface. Thus, the effect of bound moieties on gas-sensing ability and selectivity will be determined with the goal of producing even more sensitive devices than those based on MoS_2 alone and expanding the library of materials for chemical vapor sensing. Further, the dependence of the sensitivity on the polarity of both the substrate and analyte is unknown and would provide useful information in the design of future devices.

1.2—Sensitivity of functionalized MoS_2 chemiresistive sensors to organic vapor analytes

Sensors based on bare MoS_2 in either the 2H or 1T′ phase were exposed to a variety of polar VOCs (Figure 1.2.4). These sensors provided a measure of the intrinsic sensitivity of MoS_2 and served as control samples for comparison to the behavior of functionalized MoS_2 surfaces. A schematic and scanning electron micrograph of an electrode, molecular structures of functional groups, as well as the experimental methods, are available in the Supporting Information (Figure 1.2.1–1.2.3). Sensors were exposed to repeated pulses of a specific analyte concentration. The partial pressures of the analyte were then increased stepwise monotonically from P/P^0 = 0.1% to 0.5%, exposing a sensor to several analyte pulses at each test condition. Background N_2 gas was always flowed between analyte pulses to re-establish the baseline resistance. The dimensionless sensitivity value S_R was calculated by generating a linear least-squares fit to the differential resistance value as a function of analyte partial pressure fraction (Equation 1.S.1, Figure 1.2.4a). The slope of this line is the dimensionless quantity S_R, where a large value indicates large changes in resistance per increase in concentration, generally leading to lower detection limits and

better concentration resolution. Tabulated data of S_R values and standard error as well as plots of R_{max}/R_b vs. P/P^0 used for calculation are provided (Tables 1.2.1–1.2.2, Figures 1.S.5–1.S.11).

2H MoS_2 exhibited a 20–30% lower S_R value for all analytes compared to the 1T′ phase, however, S_R values were on the same order of magnitude for both the 2H and 1T′ phases. This difference in sensitivity is in accord with expectations based on increases in the surface energy of the metastable 1T′ state enhancing interactions with the analyte molecules of concern.[42,45,53]

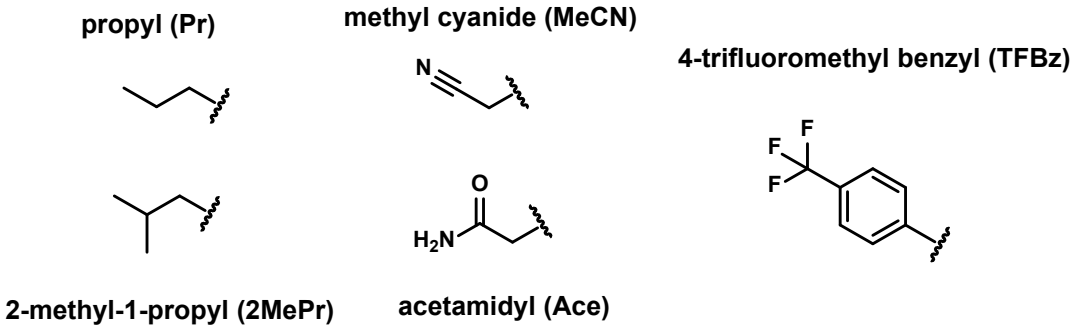

Figure 1.2.1. Molecular structures of functional groups

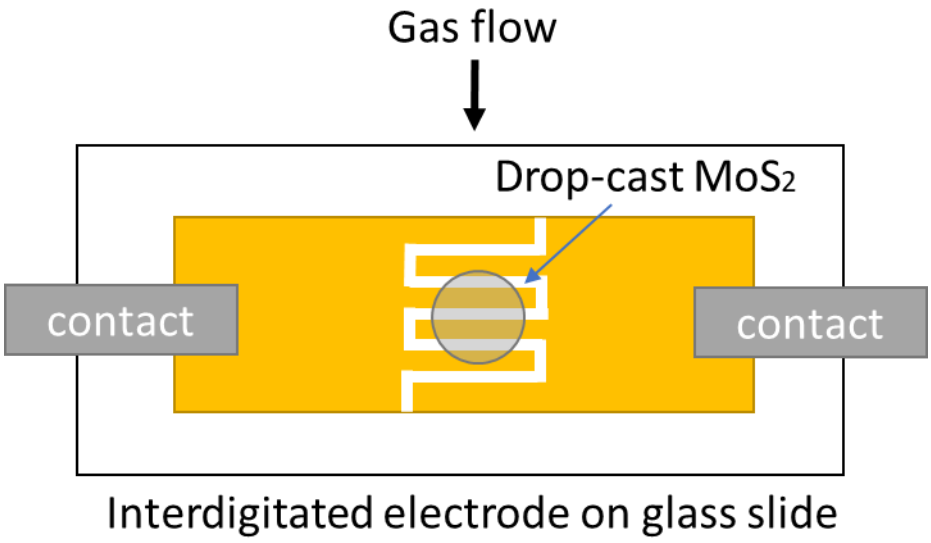

Figure 1.2.2. Diagram of interdigitated Au electrode with drop-cast MoS_2 sensing material. Contacts are made to either side of the electrode and the resistance across the contacts is measured.

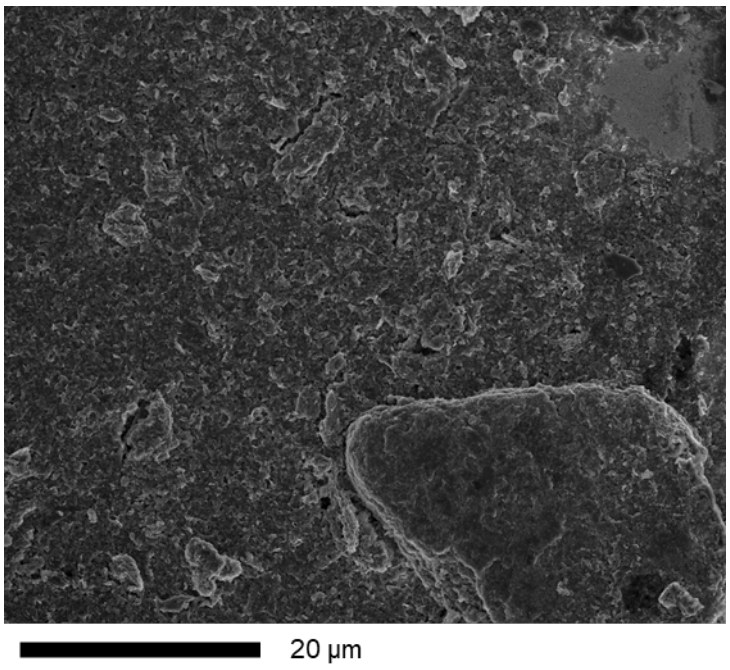

Figure 1.2.3. Scanning electron microscopy (SEM) of MoS_2 drop cast on Au interdigitated electrode.

The S_R values for ethyl acetate on either the 1T′ or 2H phases of MoS_2 were an order of magnitude higher than those exhibited by carbon black composites or Au nanoparticles (Figure 1.2.4c).[1,6,24] The values being referenced are unitless S_R values, which are independent of concentration, assuming linearity over the tested regime of analyte partial pressures. This increased sensitivity cannot be attributed to higher surface area in the MoS_2, as carbon black and chemically exfoliated MoS_2 have similar Brunauer–Emmett–Teller (BET) surface areas (~100–200 m^2 g^{-1}).[54,55] When analyte molecules adsorb onto the surface of an MoS_2 sheet, the electron density and therefore the carrier concentration of the film changes, resulting in a change in the measured dc resistance.[37,52] The observed enhancement in sensitivity is thus hypothesized to be due to the difference in carrier density between MoS_2 flakes and bulk material such as carbon black (carrier concentrations ~10^{18} cm^{-3} and 10^{21} cm^{-3}, respectively).[56,57]

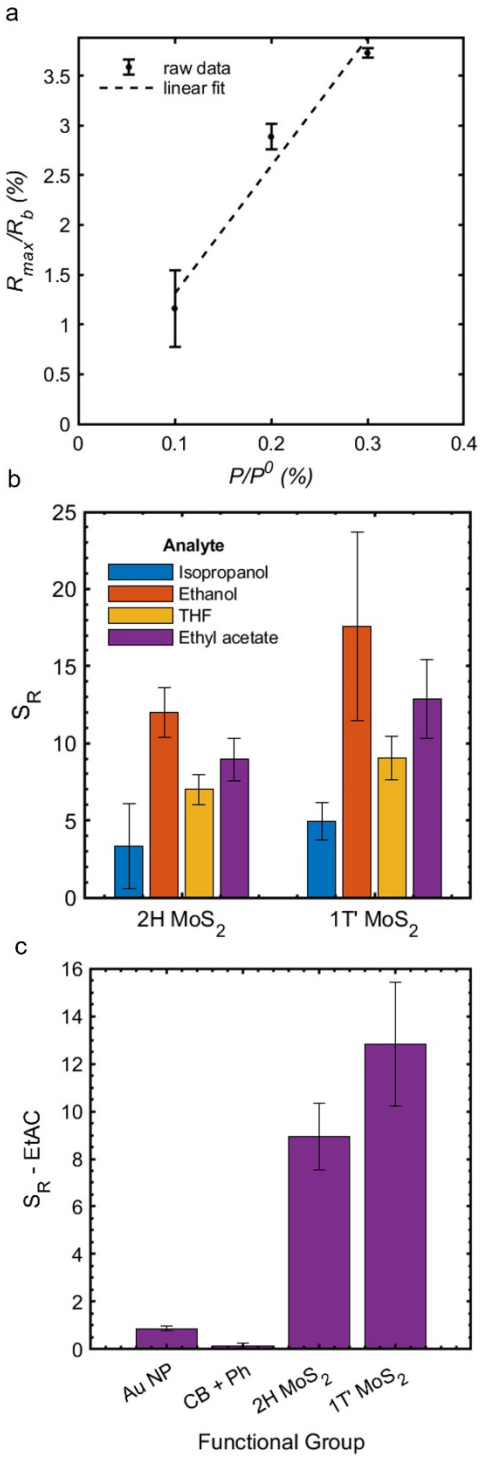
a
raw data
linear fit
R_{max}/R_b (%)
P/P^0 (%)
b
Analyte
Isopropanol
Ethanol
THF
Ethyl acetate
S_R
2H MoS_2
1T' MoS_2
c
S_R - EtAC
Au NP
CB + Ph
2H MoS_2
1T' MoS_2
Functional Group

Figure 1.2.4. (a) R_{max}/R_b vs. P/P^0 plot used for calculation of S_R for 1T′ MoS_2 exposed to ethyl acetate. Each R_{max}/R_b point is the average of four sensors and error bars represent standard deviation. Linear least-squares fit line (slope = S_R) is a dashed line. (b) Calculated sensitivities of 2H and 1T′ MoS_2 to polar VOC analytes over a range of concentrations ($0.1\% \leq P/P^0 \leq 0.3\%$), where P is the partial pressure and P^0 is the vapor pressure of the analyte at room temperature) at a flow rate of 3000 mL min^{-1} N_2, These data establish a baseline for the sensitivity of non-functionalized MoS_2 surfaces. Each value is the average of four sensors per sensor type. (c) Sensitivities toward ethyl acetate of various chemiresistive vapor sensors based on gold nanoparticles (Au NP), carbon black with phenanthroline (CB + Ph), bare 2H, and bare 1T′ MoS_2, respectively. Au NP and CB + Ph values sourced from literature.[1,23] Error bars represent calculated standard error in slope of R_{max}/R_b vs. P/P^0 plot used for calculation of S_R. Error bars on literature data sourced from original publications.

Table 1.2.1. Sensitivities (S_R) and Calculated Error of Bare MoS_2 for Polar Analytes

Phase	***isopropanol***	***ethanol***	***ethyl acetate***	***THF***
2H	3.3±2.8	12.0±1.6	8.9±1.4	7.0±1.0
1T′	4.9±1.2	17.6±6.1	12.8±2.6	9.0±1.4

Table 1.2.2. Sensitivity (S_R) of Functionalized MoS_2 for Analytes Studied

Functional group	***isopropanol***	***ethanol***	***ethyl acetate***	***THF***	***toluene***	***heptane***	***chloroform***
2MPr	2.8±0.2	4.8±0.3	3.4±0.2	4.0±0.4	3.5±0.1	2.4±0.2	3.0±0.1

Pr	2.3±0.1	3.5±0.2	4.0±0.2	4.0±0.4	1.5±0.1	1.3±0.5	1.7±0.1
Ace	3.3±0.3	5.8±0.1	3.3±0.2	3.7±0.4	4.3±0.3	3.1±0.1	1.1±0.3
MeCN	2.0±0.2	7.0±0.4	3.2±0.3	3.1±.05	2.6±0.1	2.0±0.2	0.9±0.3
TFBz	9.0±0.6	10±0.4	24±2.1	21±1.8	14±1.7	15±3.1	9.1±0.3

Modification of the carrier concentration by covalent functionalization is thus expected to alter substantially the sensing properties of MoS_2. To probe the effect of surface modification on sensitivity and selectivity, covalent functionalization of MoS_2 was performed using methyl cyanide (MeCN), acetamidyl (Ace), propyl (Pr), 2-methyl propyl (2MePr), or trifluoromethyl benzyl (TFBz) groups. The functionalized MoS_2 nanosheets were then used to fabricate sensors that were exposed to the same analytes as the bare MoS_2 controls in addition to exposure to selected nonpolar analytes (chloroform, heptane, and toluene). TFBz-functionalized MoS_2 displayed remarkable sensitivity to a range of analytes, however, S_R values for the other functionalized MoS_2 sensors were lower than those of the bare MoS_2 controls (Figure 1.2.4–1.2.5).

Initially, it was hypothesized that matching the polarity of the surface moieties and analytes would result in increased sensitivity. If polarity matching were the primary trait that controlled the sensitivity of the functionalized MoS_2 sensors, functionalization with MeCN or Ace should result in an increase in sensitivity for polar analytes and functionalization

with TFBz, 2MePr, or Pr should result in an increase in sensitivity for nonpolar analytes. However, the functionalized sensors all exhibited similar sensitivity toward polar and nonpolar VOCs (Figure 1.2.4–1.2.5). Thus, it was hypothesized that electronic effects dominated the response. If carrier concentration controlled the sensitivity of functionalized sensors, surface polarity would not affect sensitivity and instead the sensitivity would depend on the electron withdrawing or donating nature of the functional group.

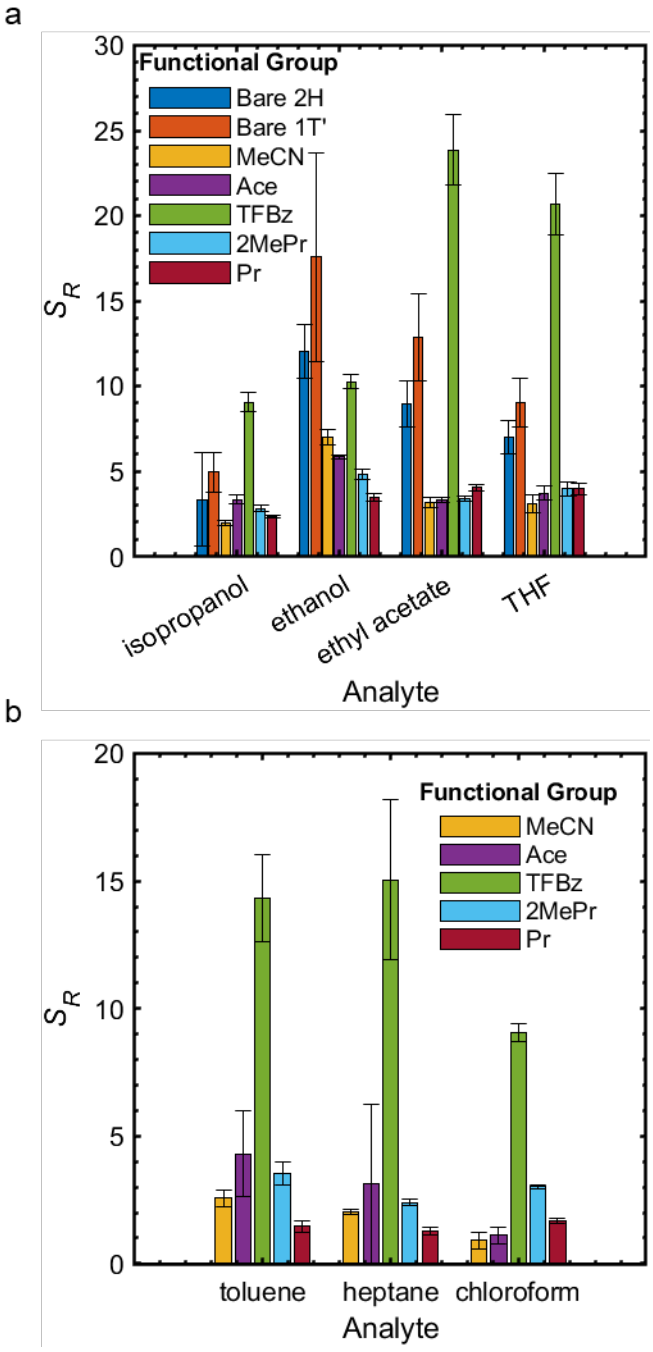

Figure 1.2.5. Sensitivity of covalently functionalized MoS_2 films to (a) polar and (b) nonpolar VOCs. All sensors were exposed to analytes at a range of concentrations ($0.1\% \leq P/P^0 \leq 0.5\%$) under a flow rate of 3000 mL min^{-1} of N_2. Each value is the average of four

sensors per sensor type. Error bars represent calculated standard error in slope of R_{max}/R_b vs. P/P^0 plot used for calculation of S_R.

1.3—Chemical origin of sensitivity in functionalized MoS_2 chemiresistive sensors

Goniometry measurements were performed to determine the affinity of the various bare and functionalized MoS_2 surfaces by measuring the contact angle between the surfaces and water. TFBz, MeCN, and Ace-functionalized surfaces exhibited higher water contact angles than bare MoS_2 or than MoS_2 functionalized with Pr or 2MePr moieties (Figure 1.3.1). The sensor response data are thus consistent with the hypothesis that sensor response to polar analytes is controlled primarily by electronic effects, wherein an adsorbed polar molecule substantially changes the local electron density and consequently changes the conductivity of the sensor film. The analyte, then, may cause a larger or smaller percent change in the dc resistance depending on whether the functionalized moiety increased or decreased local electron density.

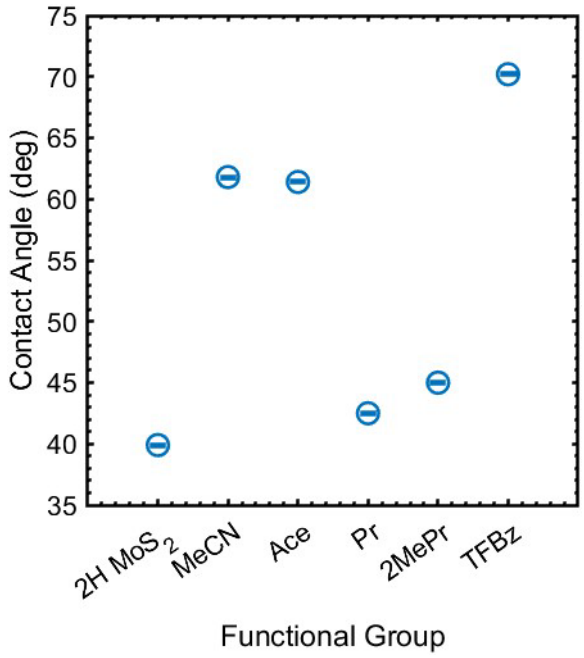

Figure 1.3.1. Water contact angle as a function of surface functionalization for MoS_2 drop cast on Si. Each data point is the average of three measurements on a sample. Error bars quantifying standard error of three measurements are included, but on the order of ±0.1 degree and thus appear as lines.

TFBz exhibited a large S_R for most analytes (Figure 1.2.5), specifically showing a twofold increase upon exposure to isopropanol, THF, and ethyl acetate as compared to the 1T′ control sample (Figure 1.2.5). In contrast, the S_R value upon exposure to ethanol decreased by 40% relative to the behavior of the bare 1T′ sensor. The observations are consistent with expectations for primary control of the sensor response by electronic inductive effects, wherein the TFBz moiety removes electron density through σ interactions to the bound sulfur, reducing the carrier density of the MoS_2. This lower overall carrier density should then produce an increased relative differential resistance change in response to electron

withdrawal from analytes, in accord with the primary factor dominating the response of MoS_2 to various VOCs.[37,52]

The Hammett parameters of arenes bound to MoS_2 have been correlated with the catalytic activity of such surfaces (Figure 1.3.2).[50] The Hammett parameter of a functional group roughly quantifies its ability to withdraw or donate electrons by measuring how the addition of the functional group of interest to a benzoic acid affects the ionization constant of the resulting acid.[58] Hammett parameters sourced from literature were thus used as a proxy for the electron-withdrawing abilities of each functional group.[58] An approximately linear relationship between the Hammett parameter and S_R was observed for exposure of various functionalized MoS_2 surfaces to ethanol, but the other analytes displayed a roughly flat relationship until a "turn on" was observed for the highly electron-withdrawing TFBz moiety. A similar "turn on" relationship has been observed for functionalized MoS_2 surfaces used for hydrogen evolution, except that the behavior occurs in the opposite direction as the sensor sensitivity, with turn on observed with more donating functional groups.[50] The observed behavior is consistent with expectations for enhancement of hydrogen production by an increased electron density whereas the vapor sensing response is enhanced by decreases in electron density.[39,50,52]

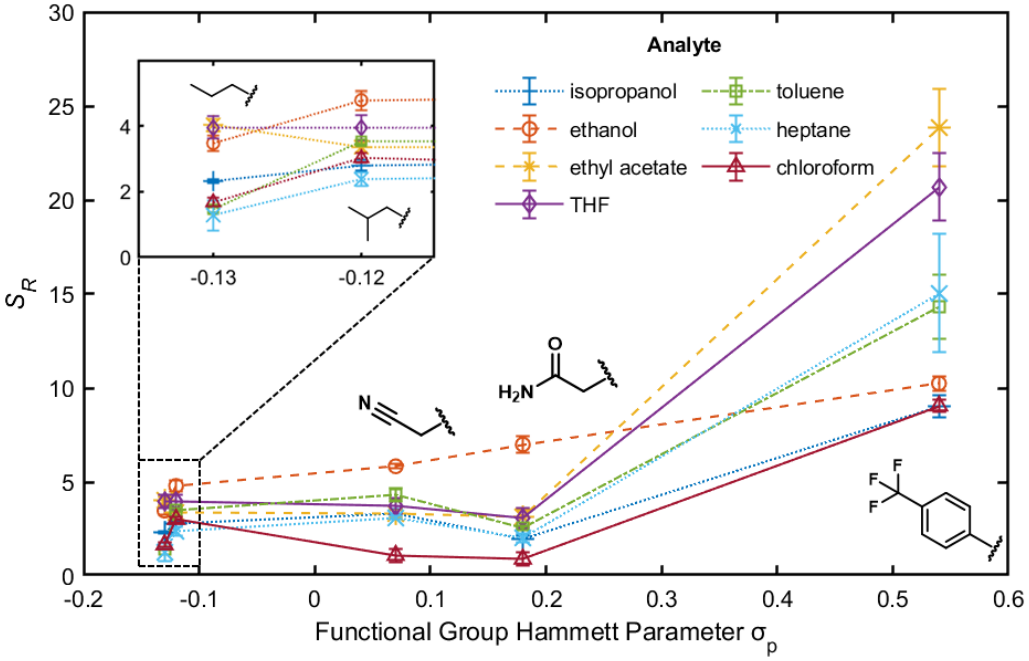

Figure 1.3.2. Average S_R values of covalently functionalized MoS_2 films to polar and nonpolar VOCs plotted vs. Hammett parameter of functional group. All sensors were exposed to analytes at a range of concentrations ($0.1\% \leq P/P^0 \leq 0.5\%$) under a flow rate of 3000 mL min^{-1} of N_2. Each value is the average of four sensors per functional group. Error bars represent calculated standard error in slope of R_{max}/R_b vs. P/P^0 plot used for calculation of S_R. for functionalized MoS_2 exposed to a range of analyte vapors plotted against Hammett parameters for functional groups.[58] Tabulated Hammett parameters for each functional group are provided in Table S4.

The relationship between the surface coverage of the functional group and the vapor sensor response was studied by varying the concentration of iodopropane in the MoS_2 functionalization step in addition to adding cobaltocene ($CoCp_2$) to further activate the electrophilic addition reaction (Figure 1.3.3).[40]

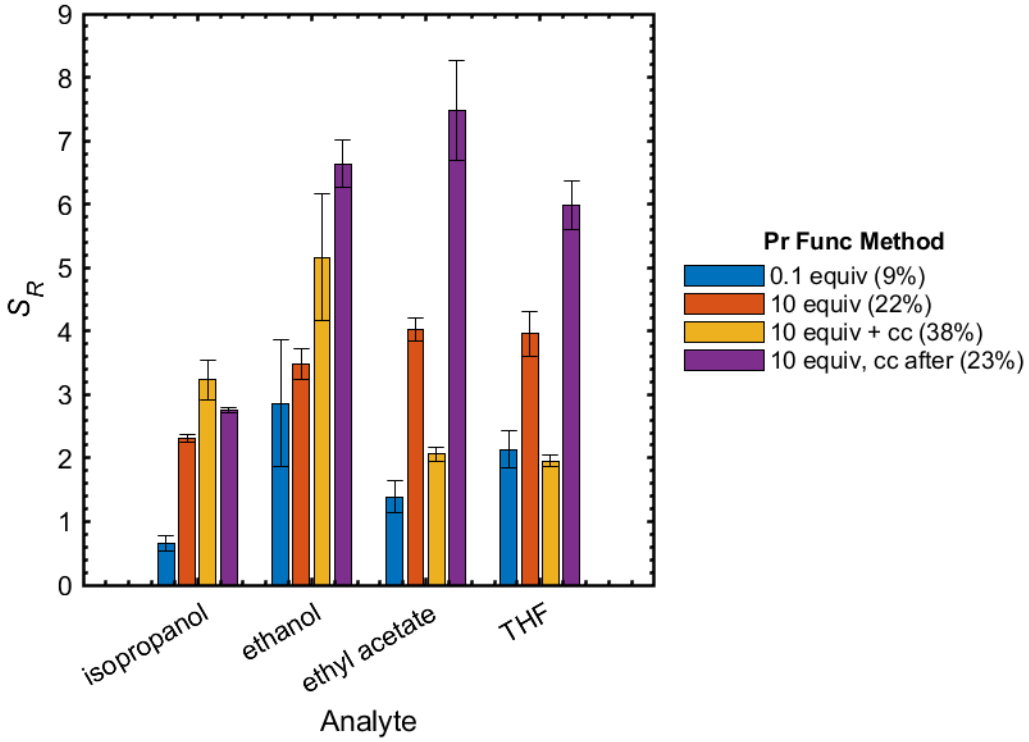

Figure 1.3.3. Sensitivity of Pr-functionalized MoS_2 to a variety of different analytes. All sensors were exposed to analytes at a range of concentrations ($0.1\% \leq P/P^0 \leq 0.5\%$) under a flow rate of 3000 mL min^{-1} of N_2. Each value is the average of four sensors per sensor type. Pr functionalization percent was carried out by varying the equivalents of alkyl halides present in the functionalization step and through the addition of cobaltocene (cc) as a reducing agent. Error bars represent calculated standard error in slope of R_{max}/R_b vs. P/P^0 plot used for calculation of S_R.

For exposure to polar analytes, S_R increased from 9% to 22% as the surface coverage increased. However, samples with 38% fractional surface coverage of functional groups did not exhibit an increase in S_R upon exposure to all VOCs. Co oxide species, likely CoO or $Co(OH)_2$ as evidenced by large satellite features, were observed after reductant-activated functionalization via analysis of the Co 3d x-ray photoelectron spectroscopy (XPS) region.[59] These species may also contribute to the sensitivity of the resulting sensors

(Figure 1.3.4). Consistently, samples treated with $CoCp_2$ after functionalization, at which point $CoCp_2$ would not be expected to affect surface coverage, displayed an increase in S_R despite having a near identical coverage of Pr to a standard functionalization (23% vs. 22%). Co oxides may withdraw electron density from the MoS_2 in a similar fashion to that proposed for the various functional groups.

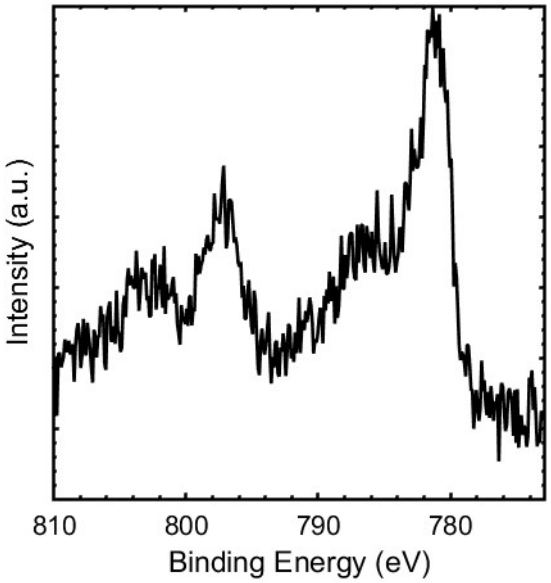

Figure 1.3.4. Co 2p XP spectrum for reductant-activated Pr-functionalized MoS_2. Presence of large satellite features at binding energies of ~787 and ~803 eV indicate CoO or CoOH rather than Co_3O_4.

1.4—Stability of functionalized MoS_2 chemiresistive sensors

To understand the stability and reusability of the sensing material, two functionalized MoS_2 sensors were tested with 50 cycles of 0.5% P/P^0 ethyl acetate immediately after sensor fabrication and then another 50 cycles after 72 h in ambient conditions (Figure 1.4.1). Each cycle consisted of a 1 s pulse of ethyl acetate at P/P^0 = 0.5% with a rest period of 3 s under N_2 to allow recovery of the baseline resistance (Figure 1.4.2). The Pr-functionalized MoS_2

sensor did not display a substantial change in the initial test to ethyl acetate over 50 cycles in the maximum relative differential resistance response (R_{max}/R_b), with R_{max}/R_b consistent at 4.9 ± 0.2%. After 72 h, the R_{max}/R_b of the Pr-functionalized sensor showed an initial response of $R_{max,initial}/R_b$ = 4.2% which decreased to a steady-state value of R_{max}/R_b = 3.3 ± 0.2%. The response of TFBz-functionalized MoS_2 sensors was less stable than that of the Pr-functionalized MoS_2 sensors. Nevertheless, despite a decrease from the initial R_{max}/R_b of 27.8%, a relatively large response of 26.0 ± 0.5% was maintained over 50 cycles. After aging for 72 h, the TFBz sensor displayed a lower R_{max}/R_b of 19.1 ± 0.5% and a similar decrease in initial signal ($R_{max,initial}/R_b$ = 21.7%). Both functionalized sensors showed a similar decrease in average R_{max}/R_b of approximately 30% after 72 hours at rest in ambient conditions.

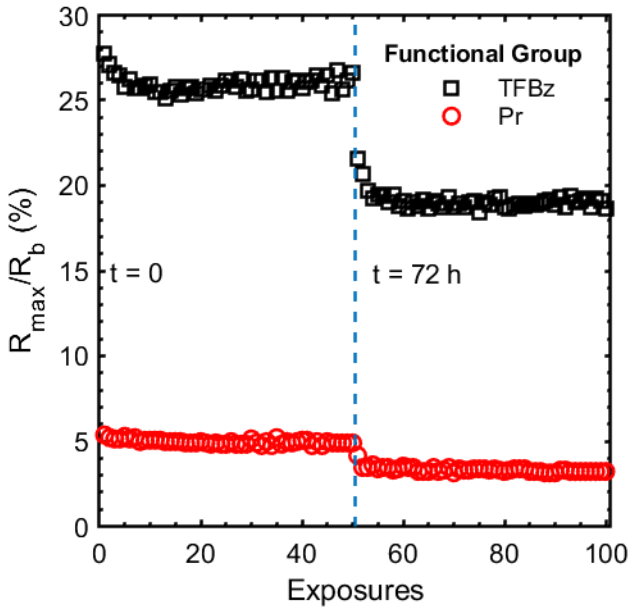

Figure 1.4.1. 50 repeated exposures of 1T′ MoS_2 functionalized with trifluoromethyl benzene and propane to 0.5% P/P^0 ethyl acetate in nitrogen immediately after sensor

fabrication and after 50 repeated exposures after exposure for 72 h to ambient conditions, respectively.

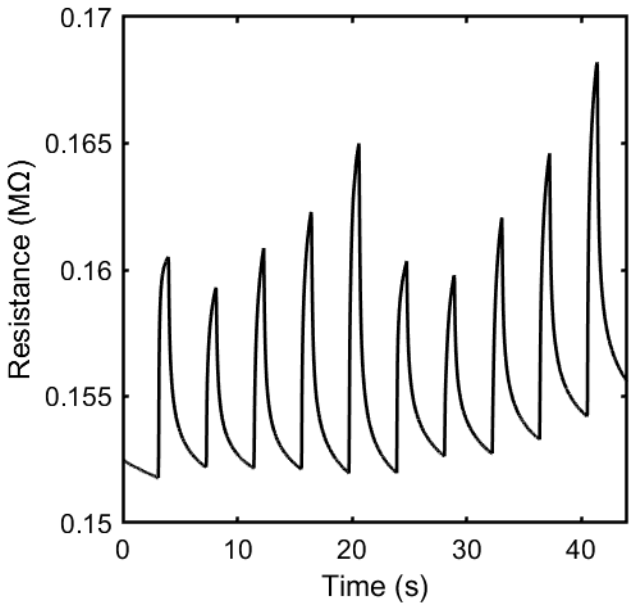

Figure 1.4.2. Resistance vs. time measurements for 10 repeated exposures of TFBz-functionalized MoS_2 to P/P^0 = 0.5% ethyl acetate. Analyte was pulsed for 1 second, then 3 seconds of background N_2 was flowed to recover baseline resistance of sensor. Flow rate was 3000 mL min^{-1}.

Bare MoS_2 sensors exhibited relatively high sensitivities for a variety of polar analytes relative to the behavior of analogous sensors based on metal nanoparticles or carbon black/polymer composites. Functionalized MoS_2 sensors exhibit marked differences in sensitivity attributable to the change in carrier concentration in the films due to electron withdrawal or donation from covalently bound moieties. Functionalization of MoS_2 with TFBz yielded higher sensitivities to most VOCs relative to the behavior of bare MoS_2

sensors. This work demonstrates the potential of functionalized MoS_2 to produce highly sensitive, stable devices.

1.E—Experimental methods

Materials

All solvents including n-butyllithium (1.6 M in hexanes) were from VWR and Sigma-Aldrich, all of which was used as needed without need for further purification. Molybdenum disulfide powder (99%), iodopropane, 2-methyl-1-iodopropane, iodoacetonitrile, iodoacetamide, and trifluoromethyl benzyl bromide were obtained from Sigma-Aldrich. All chemicals listed were stored in Argon in a glove box (<1 ppm O2). Nanopure water (resistivity > 18.2 MΩ·cm) was obtained from Nanopure E-Pure system.

Synthesis of chemically exfoliated 1T MoS_2

400 mg of MoS_2 (99%) was heated at 98 ºC with 4 mL of n-butyllithium for 46 h in a sealed glass tube. Afterward the MoS_2 was filtered and washed with 20 mL of anhydrous hexanes. The MoS_2 was sonicated in 180 mL nanopure water for 1 h (Bandelin, Sonorex Digital 10P, DK 255 P, 640 W), then centrifuged at 2000 rpm for 5 min to remove unexfoliated material. The supernatant was collected, washed repeatedly with H_2O and then washed with anhydrous dimethylformamide (DMF) until clear. The final product was resuspended in 2:1 water/isopropanol or DMF, at a concentration of 2 mg/mL. Samples were characterized by XPS.

X-ray photoelectron spectroscopy

XPS data were collected using a Kratos Axis Ultra spectrometer. Samples were excited with a monochromatic Al Kα x-ray source (1486.6 eV) at 150 W at pressures < 1×10^{-9} Torr. The analyzer pass energy was set to 10 eV and all spectra were calibrated to adventitious C at 284.8 eV. Data were analyzed using CasaXPS software. Spectra were fit according to a method described previously.[40]

Scanning Electron Microscopy

Scanning electron microscopy (SEM) was performed with a FEI Nova NanoSEM 450 at an accelerating voltage of 5.00 kV with a working distance of 5 mm and an in-lens secondary electron detector.

Functionalization of IT'-MoS2

The chemically exfoliated MoS_2 was functionalized in DMF where the alkyl halides were added tenfold and stirred for 42 h, completely covered in Al foil. The reaction was than centrifuged and washed at 6000 rpm for 30 min. The precipitate was collected, resuspended and rewashed 3x. The final product was washed with isopropanol, methanol, and nanopure water. The final product was characterized by XPS and the solvent was removed in vacuum, obtaining the final dry powder.[40]

For reductant-activated functionalization, MoS_2 was suspended in DMF (10 mL) and the alkyl halide was added (10 eq.). Cobaltocene was then added in an Ar-purged glovebox. The solution was covered with aluminum foil and stirred for 66 h, then purified by centrifugation at 6500 rpm (5820 rcf (×g)) in 10 min rounds, resuspending the precipitate by sonication in between rounds. The product was washed with DMF until the cobaltocene

color was not visible (typically 3–4 rounds ×12 mL), then with isopropanol (2 ×12 mL), and methanol (2 ×12 mL).

Sensor fabrication

Gold interdigitated electrodes and contacts were prepared on glass slides. Glass slides were cleaned with acetone and isopropanol, and then baked at 170 ºC to remove any residual solvent. Microposit S1813 photoresist (MicroChem) was spun onto the cleaned slide at 500 rpm for 30 s and then 4000 rpm for 60 s. The coated slides were exposed to a 425 nm lamp for 10 s underneath a mask in a contact mask aligner (Suss MicroTech MA6/BA6). The pattern was developed in MF-319 developer (MicroChem) for 90 s. Contacts were formed by sequentially evaporating 5 nm Ti and then 90 nm Au onto the masked slides. Lift off was completed by sonicating slides at 60 ºC in Remover PG (MicroChem) for 45 min.

MoS_2 samples were redispersed for electrode placement. Electrode construction was conducted using 1.3–1.5 mg of respective material immersed in 2.6 - 3.0 mL of the respective solvent to bring the nanomaterial concentration to 0.5 g/L. The dispersed samples were sonicated for 20 min before being drop casted onto gold interdigitated electrodes. Sensors were placed in the gas-tight vapor testing chamber and baseline resistance was measured.

Vapor testing

Sensors were tested using a custom setup that has been described previously.[1,6,24,27,40] N_2 (g) was used as a carrier gas at a flow rate of 3000 mL/min. Organic vapors were generated by sparging N_2 through 45 cm tall bubblers filled with the appropriate solvents. The analyte

concentration was controlled by adjusting the volumetric mixing ratio of the saturated analyte stream to the background N_2 stream. The flow rates of the background and analyte gases were regulated using mass flow controllers. Each run started with a 700 s background collection. Each analyte exposure consisted of 300 s of pure background gas, 80 s of diluted analyte, and then 300 s of background gas to purge the system. The sensors were loaded into a rectangular, 16-slot chamber connected by Teflon tubing to the gas delivery system. For each sensor type, 4 identical sensors would be loaded. The resistance of each of the sensors in the array was measured by a Keysight technologies 34970A data acquisition/switch unit with Keysight 34903A 20 Channel Actuator. The measurement electronics were interfaced with a computer via a GPIB connection and were controlled with LabVIEW software.

Data processing

All data processing was conducted through custom-routines in MATLAB, where the sensor response was expressed as $\Delta R_{max}/R_b$, where ΔR_{max} is the baseline-corrected maximum resistance change of the sensor, and where R_b is the baseline resistance under inert N_2. A spline was best fit and the values of $\Delta R_{max}/R_b$ were determined by subtracting the values of the spline over the deduced exposure time with its observed resistance during the length of exposure. The sensitivity (S_R) of the sensors (a dimensionless quantity) was quantified as the slope of the linear least-squares fit of $\Delta R_{max}/R_b$ vs. the P/P^0 where P is the partial pressure of the analyte in the gas stream and P^0 is the vapor pressure of the analyte.

Equation 1.S.1

$$S_R = \frac{\sum_{i=1}^{n}(p_i - \bar{p})(\Delta R_i - \Delta\bar{R})}{\sum_{i=1}^{n}(p_i - \bar{p})^2}$$

Where $\bar{p}$ is the mean of exposure partial pressures relative to the vapor pressure (P/P^0), $\Delta\bar{R}$ is the mean of the $\Delta R_{max}/R_b$ values, p_i is the value of P/P^0 on the i^{th} exposure and ΔR_i is the $\Delta R_{max}/R_b$ value at the respective p_i value.

1.S—Supplemental figures

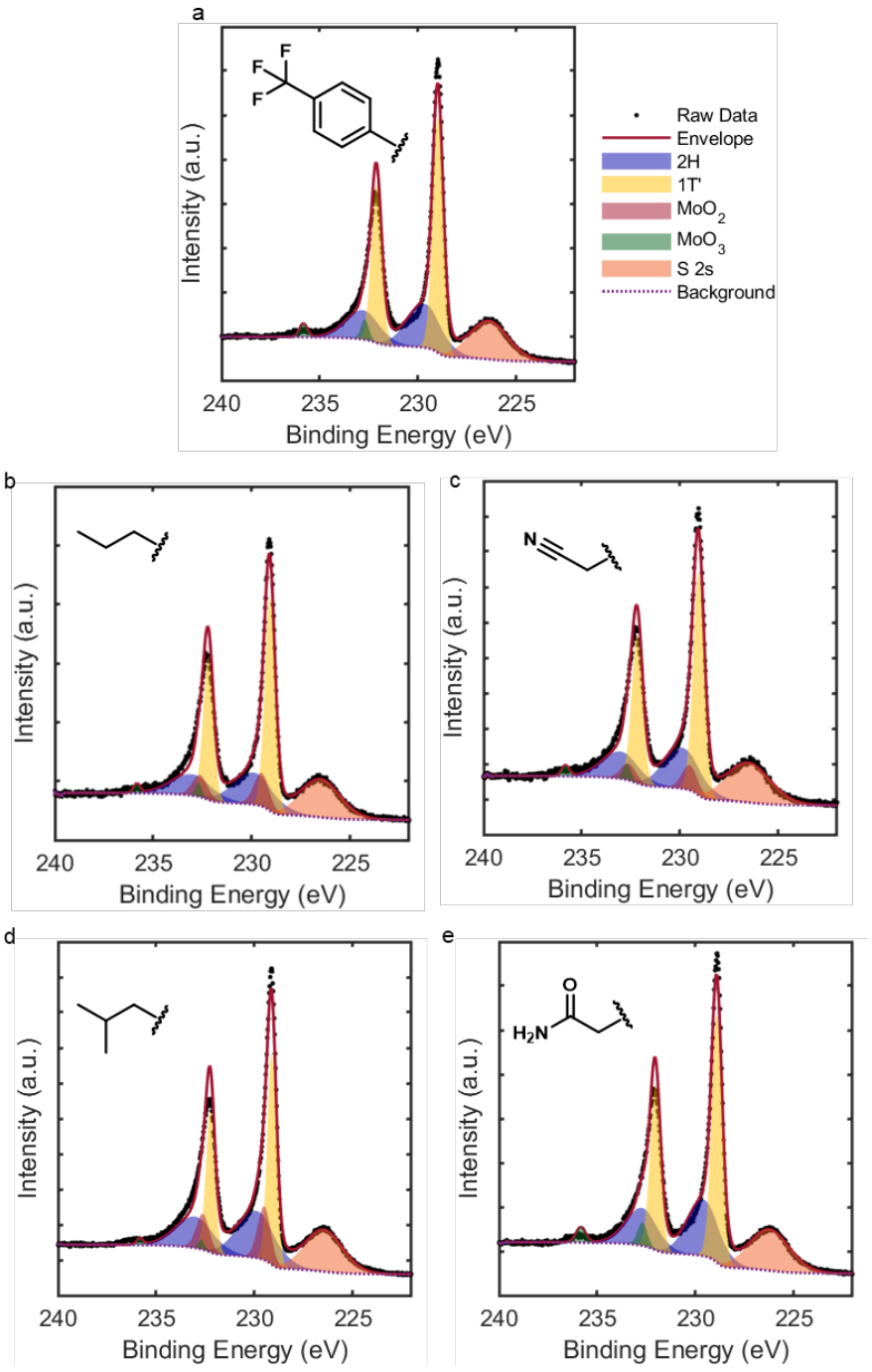

Figure 1.S.1. Mo 3d XP spectra for functionalized MoS_2.

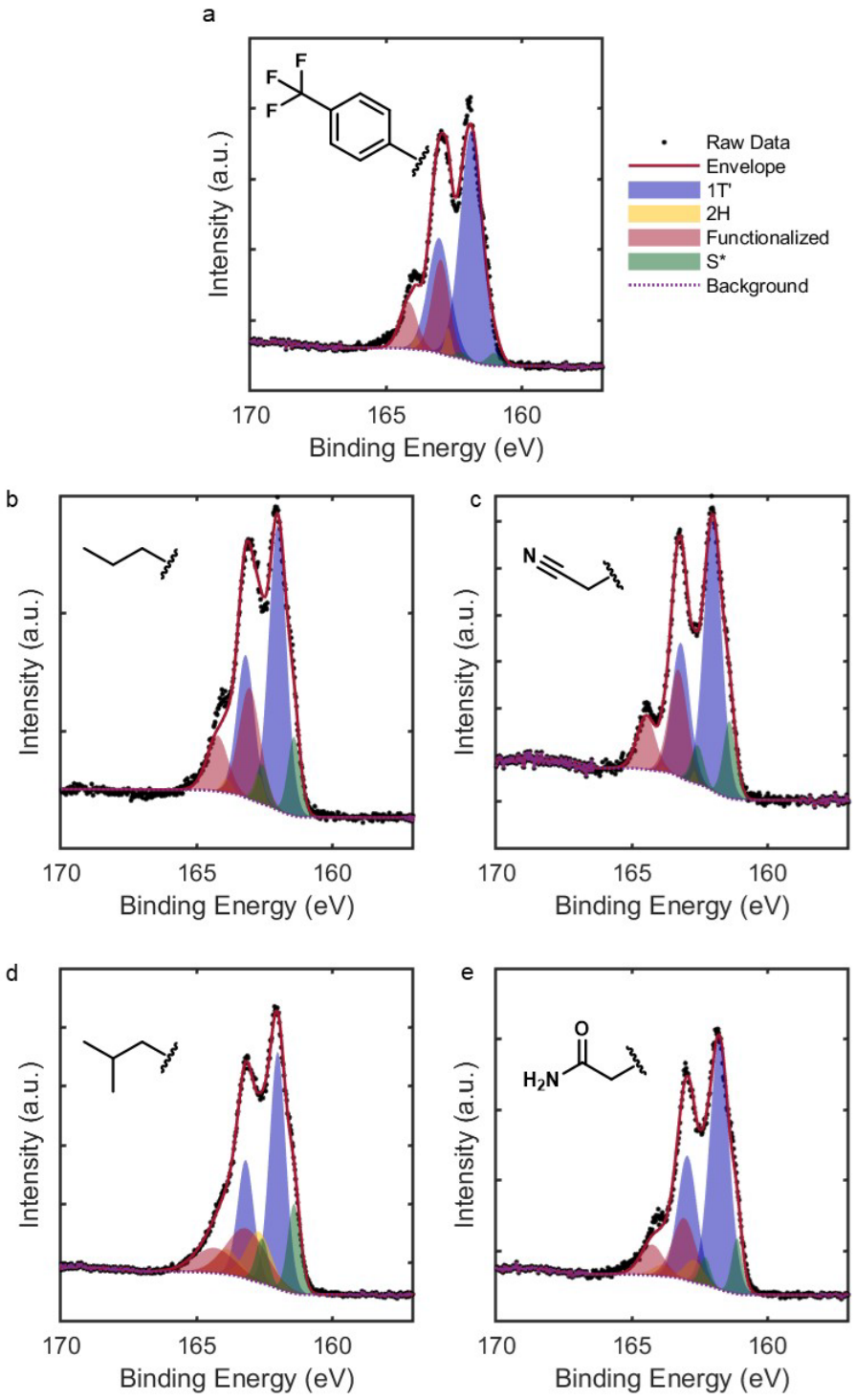

Figure 1.S.2. S 2p XP spectra for functionalized MoS_2. Fitting accomplished as in previous work on functionalized MoS_2.[40] Slightly oxidized S species indicate S-C bonds forming.

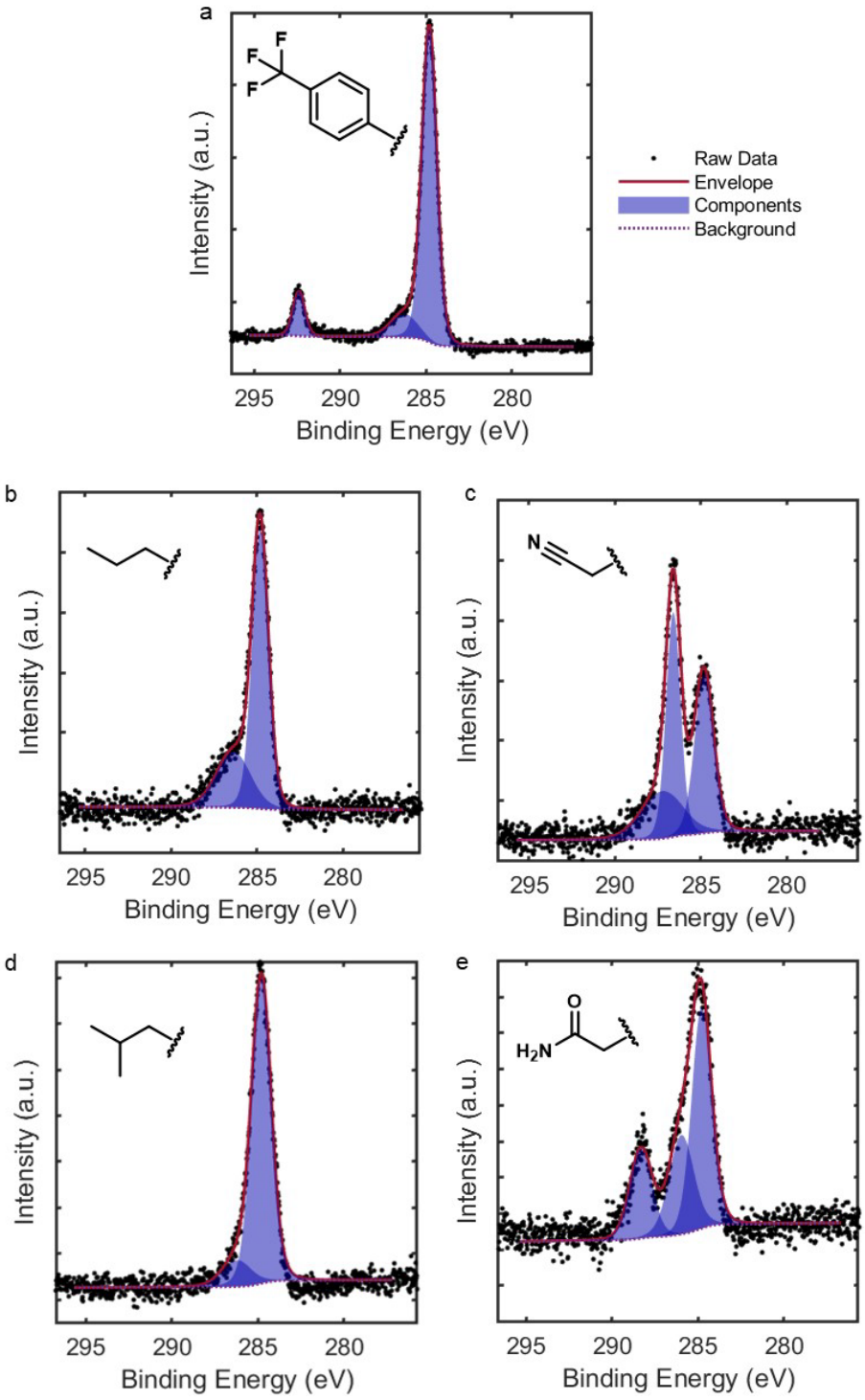

Figure 1.S.3. C 1s XP spectra for functionalized MoS_2.

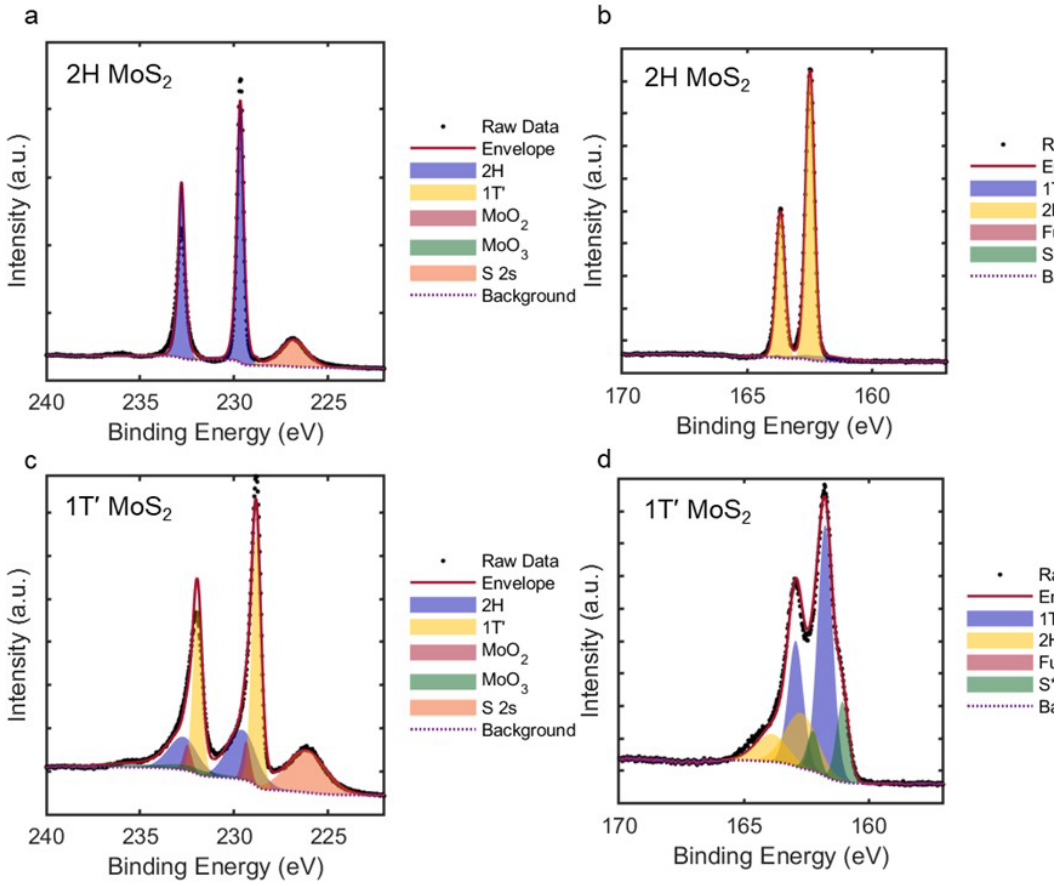

Figure 1.S.4. (a) Mo 3d and (b) S 2p XP spectra for 2H MoS_2 and (c) Mo 3d and (d) S 2p XP spectra for chemically exfoliated MoS_2 used for functionalization.

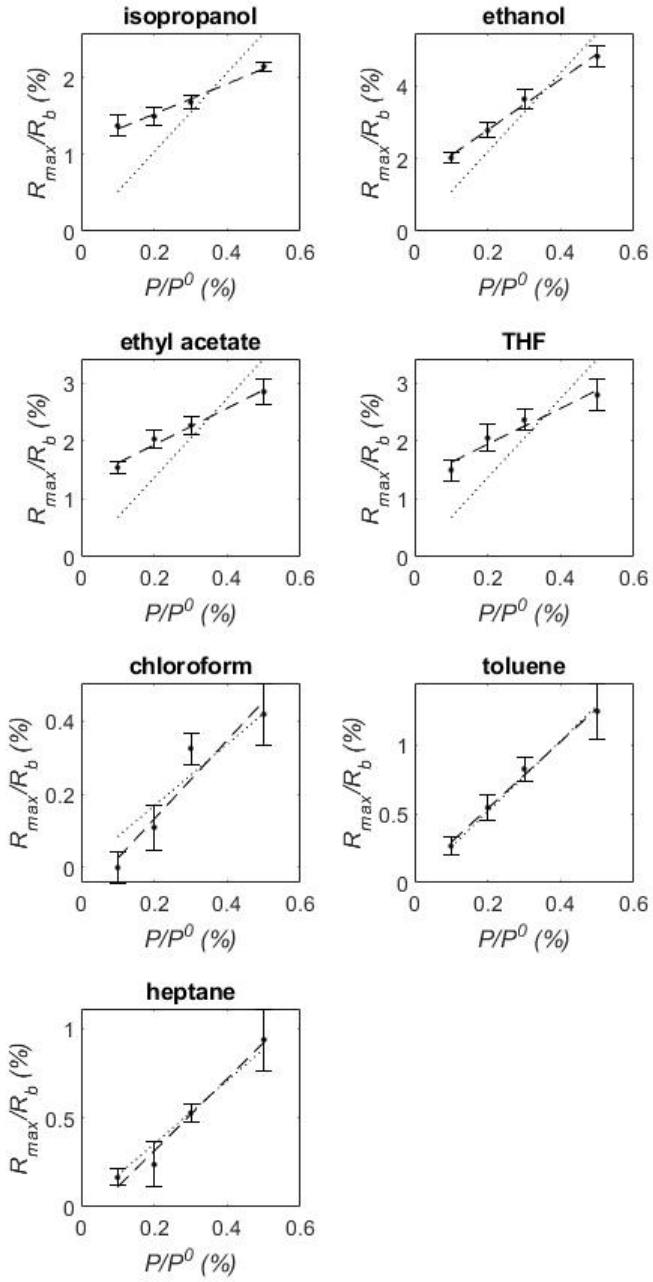

Figure 1.S.5. R_{max}/R_b vs. P^0/P data for MeCN-functionalized MoS_2. Points are raw data, dashed line is a linear fit with unrestricted intercept, and dotted line is a linear fit with the

intercept set at the origin. Each R_{max}/R_b value is the average of four sensors with error bars representing the standard deviation. All sensors were exposed to analytes at a range of concentrations ($0.1\% \leq P/P^0 \leq 0.5\%$) under a flow rate of 3000 mL min^{-1} of N_2.

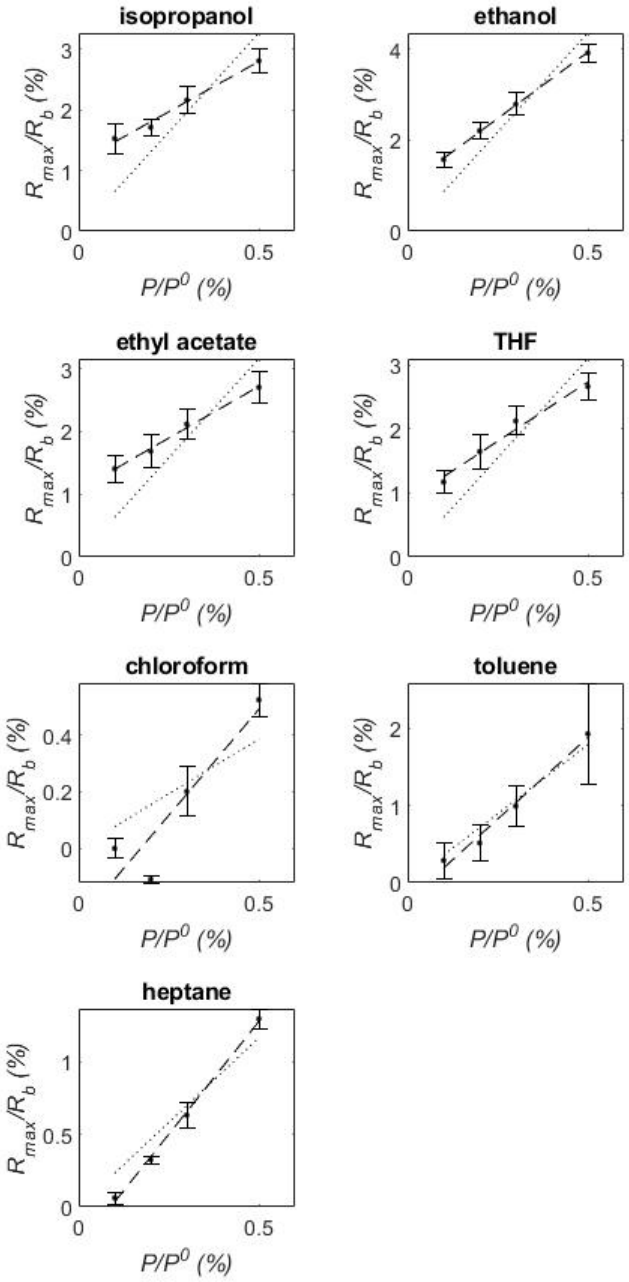

Figure 1.S.6. R_{max}/R_b vs. P^0/P data for Ace-functionalized MoS_2. Points are raw data, dashed line is a linear fit with unrestricted intercept, and dotted line is a linear fit with the

intercept set at the origin. Each R_{max}/R_b value is the average of four sensors with error bars representing the standard deviation. All sensors were exposed to analytes at a range of concentrations ($0.1\% \leq P/P^0 \leq 0.5\%$) under a flow rate of 3000 mL min^{-1} of N_2.

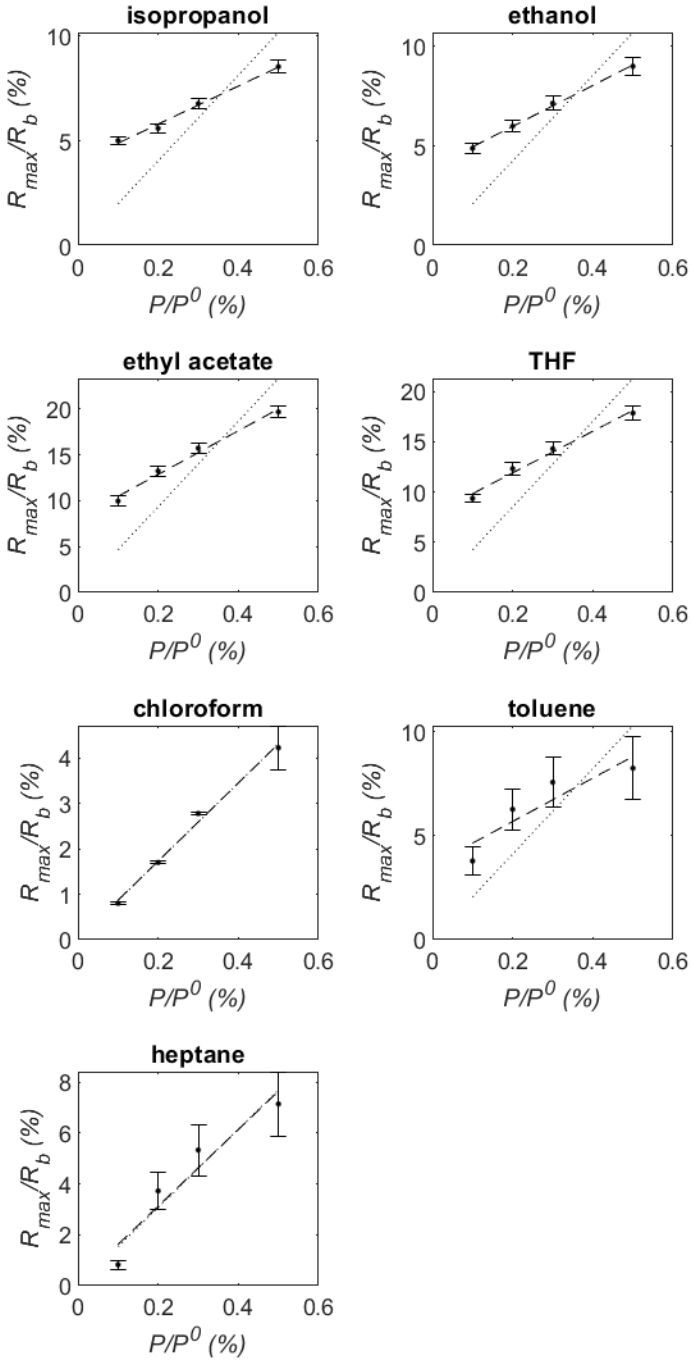

Figure 1.S.7. R_{max}/R_b vs. P^0/P data for TFBz-functionalized MoS_2. Points are raw data, dashed line is a linear fit with unrestricted intercept, and dotted line is a linear fit with the intercept set at the origin. Each R_{max}/R_b value is the average of four sensors with error bars representing the standard deviation. All sensors were exposed to analytes at a range of concentrations ($0.1\% \leq P/P^0 \leq 0.5\%$) under a flow rate of 3000 mL min^{-1} of N_2.

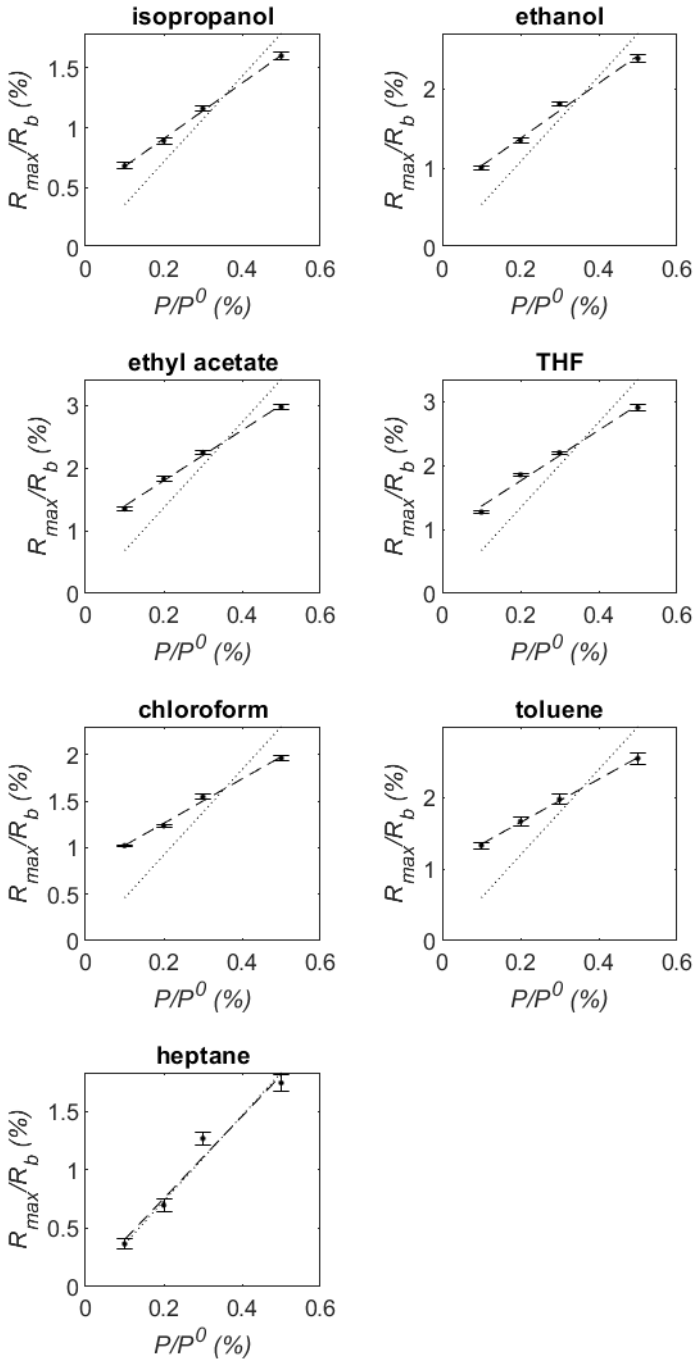

Figure 1.S.8. R_{max}/R_b vs. P^0/P data for Pr-functionalized MoS_2. Points are raw data, dashed line is a linear fit with unrestricted intercept, and dotted line is a linear fit with the intercept set at the origin. Each R_{max}/R_b value is the average of four sensors with error bars representing the standard deviation. All sensors were exposed to analytes at a range of concentrations ($0.1\% \leq P/P^0 \leq 0.5\%$) under a flow rate of 3000 mL min^{-1} of N_2.

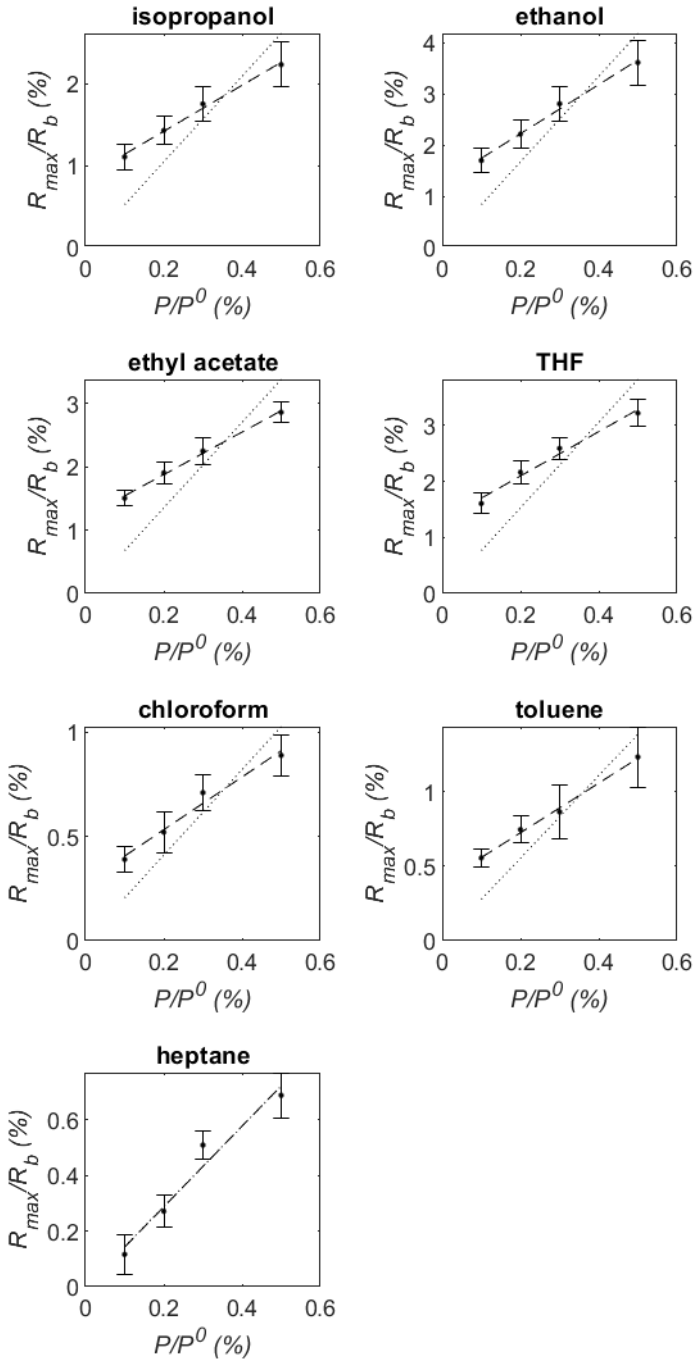

Figure 1.S.9. R_{max}/R_b vs. P^0/P data for 2MePr-functionalized MoS_2. Points are raw data, dashed line is a linear fit with unrestricted intercept, and dotted line is a linear fit with the intercept set at the origin. Each R_{max}/R_b value is the average of four sensors with error bars representing the standard deviation. All sensors were exposed to analytes at a range of concentrations ($0.1\% \leq P/P^0 \leq 0.5\%$) under a flow rate of 3000 mL min^{-1} of N_2.

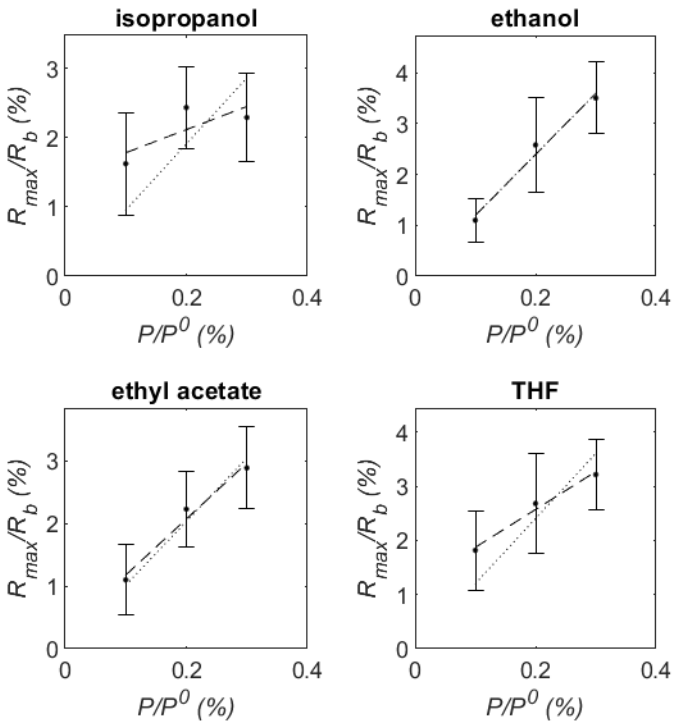

Figure 1.S.10. R_{max}/R_b vs. P^0/P data for 2H MoS_2. Points are raw data, dashed line is a linear fit with unrestricted intercept, and dotted line is a linear fit with the intercept set at the origin. Each R_{max}/R_b value is the average of four sensors with error bars representing the standard deviation. All sensors were exposed to analytes at a range of concentrations ($0.1\% \leq P/P^0 \leq 0.3\%$) under a flow rate of 3000 mL min^{-1} of N_2.

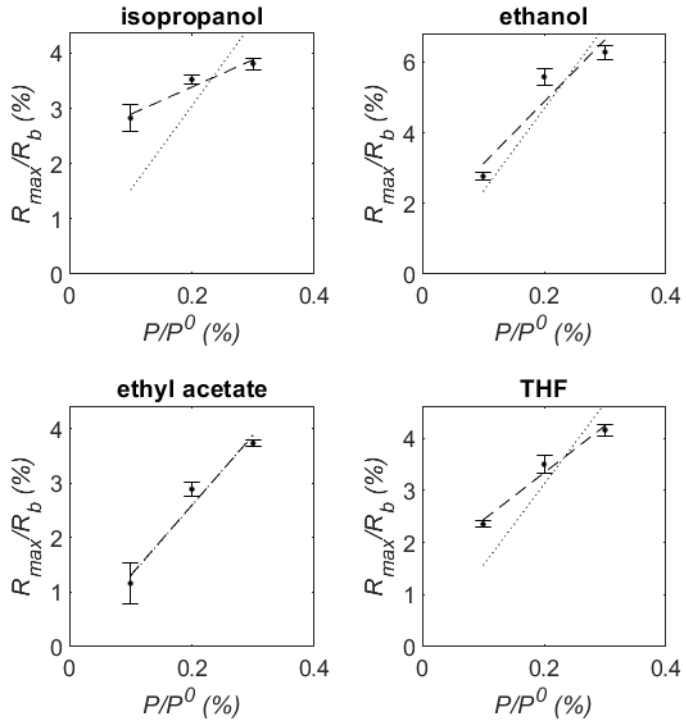

Figure 1.S.11. R_{max}/R_b vs. P^0/P data for 1T′ MoS_2. Points are raw data, dashed line is a linear fit with unrestricted intercept, and dotted line is a linear fit with the intercept set at the origin. Each R_{max}/R_b value is the average of four sensors with error bars representing the standard deviation. All sensors were exposed to analytes at a range of concentrations ($0.1\% \leq P/P^0 \leq 0.3\%$) under a flow rate of 3000 mL min^{-1} of N_2.

References

(1) García-Berríos, E.; Theriot, J. C.; Woodka, M. D.; Lewis, N. S. Detection of Ammonia, 2,4,6-Trinitrotoluene, and Common Organic Vapors Using Thin-Film Carbon Black-Metalloporphyrin Composite Chemiresistors. *Sensors and Actuators B: Chemical* **2013**, *188*, 761–767. https://doi.org/10.1016/j.snb.2013.07.006.

(2) García-Berríos, E.; Gao, T.; Walker, D.; Brunschwig, B. S.; Lewis, N. S. Composites of Carboxylate-Capped TiO2 Nanoparticles and Carbon Black as

Chemiresistive Vapor Sensors. *Sensors and Actuators B: Chemical* **2011**, *158* (1), 17–22. https://doi.org/10.1016/j.snb.2011.04.022.

(3) Pham, T.; Li, G.; Bekyarova, E.; Itkis, M. E.; Mulchandani, A. MoS_2 -Based Optoelectronic Gas Sensor with Sub-Parts-per-Billion Limit of NO_2 Gas Detection. *ACS Nano* **2019**, *13* (3), 3196–3205. https://doi.org/10.1021/acsnano.8b08778.

(4) Wohltjen, H.; Snow, A. W. Colloidal Metal−Insulator−Metal Ensemble Chemiresistor Sensor. *Anal. Chem.* **1998**, *70* (14), 2856–2859. https://doi.org/10.1021/ac9713464.

(5) Han, L.; Shi, X.; Wu, W.; Kirk, F. L.; Luo, J.; Wang, L.; Mott, D.; Cousineau, L.; Lim, S. I.-I.; Lu, S.; Zhong, C.-J. Nanoparticle-Structured Sensing Array Materials and Pattern Recognition for VOC Detection. *Sensors and Actuators B: Chemical* **2005**, *106* (1), 431–441. https://doi.org/10.1016/j.snb.2004.09.003.

(6) Maldonado, S.; García-Berríos, E.; Woodka, M. D.; Brunschwig, B. S.; Lewis, N. S. Detection of Organic Vapors and NH3(g) Using Thin-Film Carbon Black–Metallophthalocyanine Composite Chemiresistors. *Sensors and Actuators B: Chemical* **2008**, *134* (2), 521–531. https://doi.org/10.1016/j.snb.2008.05.047.

(7) Woodka, M. D.; Brunschwig, B. S.; Lewis, N. S. Use of Spatiotemporal Response Information from Sorption-Based Sensor Arrays to Identify and Quantify the Composition of Analyte Mixtures. *Langmuir* **2007**, *23* (26), 13232–13241. https://doi.org/10.1021/la7026708.

(8) Guo, L.; Yang, Z.; Dou, X. Artificial Olfactory System for Trace Identification of Explosive Vapors Realized by Optoelectronic Schottky Sensing. *Adv. Mater.* **2017**, *29* (5), 1604528. https://doi.org/10.1002/adma.201604528.

(9) Gardner, J. W.; Bartlett, P. N.; Dodd, G. H.; Shurmer, H. V. The Design of an Artificial Olfactory System. In *Chemosensory Information Processing*; Schild, D., Ed.; Springer Berlin Heidelberg: Berlin, Heidelberg, 1990; pp. 131–173. https://doi.org/10.1007/978-3-642-75127-1_10.

(10) Seiyama, T.; Kato, A.; Fujiishi, K.; Nagatani, M. A New Detector for Gaseous Components Using Semiconductive Thin Films. *Anal. Chem.* **1962**, *34* (11), 1502–1503. https://doi.org/10.1021/ac60191a001.

(11) Severin, E. J.; Doleman, B. J.; Lewis, N. S. An Investigation of the Concentration Dependence and Response to Analyte Mixtures of Carbon Black/Insulating Organic Polymer Composite Vapor Detectors. *Anal. Chem.* **2000**, *72* (4), 658–668. https://doi.org/10.1021/ac9910278.

(12) Severin, E. J.; Lewis, N. S. Relationships among Resonant Frequency Changes on a Coated Quartz Crystal Microbalance, Thickness Changes, and Resistance Responses of Polymer−Carbon Black Composite Chemiresistors. *Anal. Chem.* **2000**, *72* (9), 2008–2015. https://doi.org/10.1021/ac991026f.

(13) Wilson, A.; Baietto, M. Applications and Advances in Electronic-Nose Technologies. *Sensors* **2009**, *9* (7), 5099–5148. https://doi.org/10.3390/s90705099.

(14) Kim, C.; Raja, I. S.; Lee, J.-M.; Lee, J. H.; Kang, M. S.; Lee, S. H.; Oh, J.-W.; Han, D.-W. Recent Trends in Exhaled Breath Diagnosis Using an Artificial Olfactory System. *Biosensors* **2021**, *11* (9), 337. https://doi.org/10.3390/bios11090337.

(15) Gardner, J. W.; Hines, E. L.; Wilkinson, M. Application of Artificial Neural Networks to an Electronic Olfactory System. *Meas. Sci. Technol.* **1990**, *1* (5), 446–451. https://doi.org/10.1088/0957-0233/1/5/012.

(16) *Hybrid Materials: Synthesis, Characterization, and Applications*; Kickelbick, G., Ed.; Wiley—VCH: Weinheim, 2007.

(17) Bouvet, M. Hybrid and 2D Nanomaterials. In *Advanced Nanomaterials for Inexpensive Gas Microsensors*; Elsevier, 2020; pp. 85–102. https://doi.org/10.1016/B978-0-12-814827-3.00005-0.

(18) Doleman, B. J.; Severin, E. J.; Lewis, N. S. Trends in Odor Intensity for Human and Electronic Noses: Relative Roles of Odorant Vapor Pressure vs. Molecularly Specific Odorant Binding. *Proceedings of the National Academy of Sciences* **1998**, *95* (10), 5442–5447. https://doi.org/10.1073/pnas.95.10.5442.

(19) Lewis, N. S. Comparisons between Mammalian and Artificial Olfaction Based on Arrays of Carbon Black−Polymer Composite Vapor Detectors. *Acc. Chem. Res.* **2004**, *37* (9), 663–672. https://doi.org/10.1021/ar030120m.

(20) Wang, L.; Kariuki, N.; Schadt, M.; Mott, D.; Luo, J.; Zhong, C.-J.; Shi, X.; Zhang, C.; Hao, W.; Lu, S.; Kim, N.; Wang, J.-Q. Sensing Arrays Constructed

from Nanoparticle Thin Films and Interdigitated Microelectrodes. *Sensors* **2006**, *6* (6), 667–679. https://doi.org/10.3390/s6060667.

(21) Grate, J. W. A Sorptive Behavior of Monolayer-Protected Gold Nanoparticle Films Containing Alkanethiols and Alkanedithiols. *Anal. Chem.* **2003**, *75* (23), 6759–6759. https://doi.org/10.1021/ac030280b.

(22) Grate, J. W.; Nelson, D. A.; Skaggs, R. Sorptive Behavior of Monolayer-Protected Gold Nanoparticle Films: Implications for Chemical Vapor Sensing. *Anal. Chem.* **2003**, *75* (8), 1868–1879. https://doi.org/10.1021/ac0206364.

(23) García-Berríos, E.; Gao, T.; Woodka, M. D.; Maldonado, S.; Brunschwig, B. S.; Ellsworth, M. W.; Lewis, N. S. Response versus Chain Length of Alkanethiol-Capped Au Nanoparticle Chemiresistive Chemical Vapor Sensors. *J. Phys. Chem. C* **2010**, *114* (50), 21914–21920. https://doi.org/10.1021/jp101331g.

(24) García-Berríos, E.; Gao, T.; Theriot, J. C.; Woodka, M. D.; Brunschwig, B. S.; Lewis, N. S. Response and Discrimination Performance of Arrays of Organothiol-Capped Au Nanoparticle Chemiresistive Vapor Sensors. *J. Phys. Chem. C* **2011**, *115* (14), 6208–6217. https://doi.org/10.1021/jp110793h.

(25) Guthrie, B. Machine Olfaction. In *Springer Handbook of Odor*; Buettner, A., Ed.; Springer International Publishing: Cham, 2017; pp. 55–56. https://doi.org/10.1007/978-3-319-26932-0_21.

(26) Gao, T.; Woodka, M. D.; Brunschwig, B. S.; Lewis, N. S. Chemiresistors for Array-Based Vapor Sensing Using Composites of Carbon Black with Low

Volatility Organic Molecules. *Chem. Mater.* **2006**, *18* (22), 5193–5202. https://doi.org/10.1021/cm060905x.

(27) Thompson, A. C.; Lee, K. S.; Lewis, N. S. Strain-Based Chemiresistive Polymer-Coated Graphene Vapor Sensors. *ACS Omega* **2022**, *7* (12), 10765–10774. https://doi.org/10.1021/acsomega.2c00543.

(28) Wang, Q. H.; Kalantar-Zadeh, K.; Kis, A.; Coleman, J. N.; Strano, M. S. Electronics and Optoelectronics of Two-Dimensional Transition Metal Dichalcogenides. *Nature Nanotech* **2012**, *7* (11), 699–712. https://doi.org/10.1038/nnano.2012.193.

(29) Radisavljevic, B.; Radenovic, A.; Brivio, J.; Giacometti, V.; Kis, A. Single-Layer MoS2 Transistors. *Nature Nanotech* **2011**, *6* (3), 147–150. https://doi.org/10.1038/nnano.2010.279.

(30) Hau, H. H.; Duong, T. T. H.; Man, N. K.; Thi Viet Nga, T.; Thi Xuan, C.; Thi Thanh Le, D.; Van Toan, N.; Hung, C. M.; Van Duy, N.; Van Hieu, N.; Hoa, N. D. Enhanced NO2 Gas-Sensing Performance at Room Temperature Using Exfoliated MoS2 Nanosheets. *Sensors and Actuators A: Physical* **2021**, *332*, 113137. https://doi.org/10.1016/j.sna.2021.113137.

(31) Han, Y.; Ma, Y.; Liu, Y.; Xu, S.; Chen, X.; Zeng, M.; Hu, N.; Su, Y.; Zhou, Z.; Yang, Z. Construction of MoS2/SnO2 Heterostructures for Sensitive NO2 Detection at Room Temperature. *Applied Surface Science* **2019**, *493*, 613–619. https://doi.org/10.1016/j.apsusc.2019.07.052.

(32) Yadav, V.; Roy, S.; Singh, P.; Khan, Z.; Jaiswal, A. 2D MoS_2 -Based Nanomaterials for Therapeutic, Bioimaging, and Biosensing Applications. *Small* **2019**, *15* (1), 1803706. https://doi.org/10.1002/smll.201803706.

(33) Tong, Y.; Liu, Y.; Zhao, Y.; Thong, J.; Chan, D. S. H.; Zhu, C. Selectivity of MoS 2 Gas Sensors Based on a Time Constant Spectrum Method. *Sensors and Actuators A: Physical* **2017**, *255*, 28–33. https://doi.org/10.1016/j.sna.2016.12.024.

(34) Donarelli, M.; Prezioso, S.; Perrozzi, F.; Bisti, F.; Nardone, M.; Giancaterini, L.; Cantalini, C.; Ottaviano, L. Response to NO2 and Other Gases of Resistive Chemically Exfoliated MoS2-Based Gas Sensors. *Sensors and Actuators B: Chemical* **2015**, *207*, 602–613. https://doi.org/10.1016/j.snb.2014.10.099.

(35) Fan, X.-L.; Yang, Y.; Xiao, P.; Lau, W.-M. Site-Specific Catalytic Activity in Exfoliated MoS_2 Single-Layer Polytypes for Hydrogen Evolution: Basal Plane and Edges. *J. Mater. Chem. A* **2014**, *2* (48), 20545–20551. https://doi.org/10.1039/C4TA05257A.

(36) Wu, S.; Zeng, Z.; He, Q.; Wang, Z.; Wang, S. J.; Du, Y.; Yin, Z.; Sun, X.; Chen, W.; Zhang, H. Electrochemically Reduced Single-Layer MoS2 Nanosheets: Characterization, Properties, and Sensing Applications. *Small* **2012**, *8* (14), 2264–2270. https://doi.org/10.1002/smll.201200044.

(37) Perkins, F. K.; Friedman, A. L.; Cobas, E.; Campbell, P. M.; Jernigan, G. G.; Jonker, B. T. Chemical Vapor Sensing with Monolayer MoS_2. *Nano Lett.* **2013**, *13* (2), 668–673. https://doi.org/10.1021/nl3043079.

(38) Bazylewski, P.; Van Middelkoop, S.; Divigalpitiya, R.; Fanchini, G. Solid-State Chemiresistors from Two-Dimensional MoS_2 Nanosheets Functionalized with L -Cysteine for In-Line Sensing of Part-Per-Billion Cd^{2+} Ions in Drinking Water. *ACS Omega* **2020**, *5* (1), 643–649. https://doi.org/10.1021/acsomega.9b03246.

(39) Liu, B.; Chen, L.; Liu, G.; Abbas, A. N.; Fathi, M.; Zhou, C. High-Performance Chemical Sensing Using Schottky-Contacted Chemical Vapor Deposition Grown Monolayer MoS_2 Transistors. *ACS Nano* **2014**, *8* (5), 5304–5314. https://doi.org/10.1021/nn5015215.

(40) Yan, E. X.; Cabán-Acevedo, M.; Papadantonakis, K. M.; Brunschwig, B. S.; Lewis, N. S. Reductant-Activated, High-Coverage, Covalent Functionalization of 1T′-MoS_2. *ACS Materials Lett.* **2020**, *2* (2), 133–139. https://doi.org/10.1021/acsmaterialslett.9b00241.

(41) Knirsch, K. C.; Berner, N. C.; Nerl, H. C.; Cucinotta, C. S.; Gholamvand, Z.; McEvoy, N.; Wang, Z.; Abramovic, I.; Vecera, P.; Halik, M.; Sanvito, S.; Duesberg, G. S.; Nicolosi, V.; Hauke, F.; Hirsch, A.; Coleman, J. N.; Backes, C. Basal-Plane Functionalization of Chemically Exfoliated Molybdenum Disulfide by Diazonium Salts. *ACS Nano* **2015**, *9* (6), 6018–6030. https://doi.org/10.1021/acsnano.5b00965.

(42) Pal, B.; Singh, A.; G., S.; Mahale, P.; Kumar, A.; Thirupathaiah, S.; Sezen, H.; Amati, M.; Gregoratti, L.; Waghmare, U. V.; Sarma, D. D. Chemically

Exfoliated Mo S 2 Layers: Spectroscopic Evidence for the Semiconducting Nature of the Dominant Trigonal Metastable Phase. *Phys. Rev. B* **2017**, *96* (19), 195426. https://doi.org/10.1103/PhysRevB.96.195426.

(43) Voiry, D.; Goswami, A.; Kappera, R.; Silva, C. de C. C. e; Kaplan, D.; Fujita, T.; Chen, M.; Asefa, T.; Chhowalla, M. Covalent Functionalization of Monolayered Transition Metal Dichalcogenides by Phase Engineering. *Nature Chem* **2015**, *7* (1), 45–49. https://doi.org/10.1038/nchem.2108.

(44) Toh, R. J.; Sofer, Z.; Luxa, J.; Sedmidubský, D.; Pumera, M. 3R Phase of MoS_2 and WS_2 Outperforms the Corresponding 2H Phase for Hydrogen Evolution. *Chem. Commun.* **2017**, *53* (21), 3054–3057. https://doi.org/10.1039/C6CC09952A.

(45) Qin, X. R.; Yang, D.; Frindt, R. F.; Irwin, J. C. Real-Space Imaging of Single-Layer MoS 2 by Scanning Tunneling Microscopy. *Phys. Rev. B* **1991**, *44* (7), 3490–3493. https://doi.org/10.1103/PhysRevB.44.3490.

(46) Manjunatha, S.; Rajesh, S.; Vishnoi, P.; Rao, C. N. R. Reaction with Organic Halides as a General Method for the Covalent Functionalization of Nanosheets of 2D Chalcogenides and Related Materials. *J. Mater. Res.* **2017**, *32* (15), 2984–2992. https://doi.org/10.1557/jmr.2017.224.

(47) Vishnoi, P.; Sampath, A.; Waghmare, U. V.; Rao, C. N. R. Covalent Functionalization of Nanosheets of MoS_2 and $MoSe_2$ by Substituted Benzenes and Other Organic Molecules. *Chem. Eur. J.* **2017**, *23* (4), 886–895. https://doi.org/10.1002/chem.201604176.

(48) Presolski, S.; Pumera, M. Covalent Functionalization of MoS2. *Materials Today* **2016**, *19* (3), 140–145. https://doi.org/10.1016/j.mattod.2015.08.019.

(49) Stergiou, A.; Tagmatarchis, N. Molecular Functionalization of Two-Dimensional MoS $_2$ Nanosheets. *Chem. Eur. J.* **2018**, *24* (69), 18246–18257. https://doi.org/10.1002/chem.201803066.

(50) Benson, E. E.; Zhang, H.; Schuman, S. A.; Nanayakkara, S. U.; Bronstein, N. D.; Ferrere, S.; Blackburn, J. L.; Miller, E. M. Balancing the Hydrogen Evolution Reaction, Surface Energetics, and Stability of Metallic MoS $_2$ Nanosheets via Covalent Functionalization. *J. Am. Chem. Soc.* **2018**, *140* (1), 441–450. https://doi.org/10.1021/jacs.7b11242.

(51) García-Dalí, S.; Paredes, J. I.; Villar-Rodil, S.; Martínez-Jódar, A.; Martínez-Alonso, A.; Tascón, J. M. D. Molecular Functionalization of 2H-Phase MoS $_2$ Nanosheets via an Electrolytic Route for Enhanced Catalytic Performance. *ACS Appl. Mater. Interfaces* **2021**, *13* (28), 33157–33171. https://doi.org/10.1021/acsami.1c08850.

(52) Babar, V.; Vovusha, H.; Schwingenschlögl, U. Density Functional Theory Analysis of Gas Adsorption on Monolayer and Few Layer Transition Metal Dichalcogenides: Implications for Sensing. *ACS Appl. Nano Mater.* **2019**, *2* (9), 6076–6080. https://doi.org/10.1021/acsanm.9b01642.

(53) Heising, J.; Kanatzidis, M. G. Exfoliated and Restacked MoS_2 and WS_2 : Ionic or Neutral Species? Encapsulation and Ordering of Hard Electropositive Cations. *J. Am. Chem. Soc.* **1999**, *121* (50), 11720–11732. https://doi.org/10.1021/ja991644d.

(54) Zhang, Y.; Xu, L.; Walker, W. R.; Tittle, C. M.; Backhouse, C. J.; Pope, M. A. Langmuir Films and Uniform, Large Area, Transparent Coatings of Chemically Exfoliated MoS_2 Single Layers. *J. Mater. Chem. C* **2017**, *5* (43), 11275–11287. https://doi.org/10.1039/C7TC02637D.

(55) Cho, W.; Lee, S.-H.; Ju, W.-S.; Baek, Y.; Lee, J. K. Conversion of Natural Gas to Hydrogen and Carbon Black by Plasma and Application of Plasma Carbon Black. *Catalysis Today* **2004**, *98* (4), 633–638. https://doi.org/10.1016/j.cattod.2004.09.051.

(56) Bera, B.; Chakraborty, A.; Kar, T.; Leuaa, P.; Neergat, M. Density of States, Carrier Concentration, and Flat Band Potential Derived from Electrochemical Impedance Measurements of N-Doped Carbon and Their Influence on Electrocatalysis of Oxygen Reduction Reaction. *J. Phys. Chem. C* **2017**, *121* (38), 20850–20856. https://doi.org/10.1021/acs.jpcc.7b06735.

(57) Dagan, R.; Vaknin, Y.; Henning, A.; Shang, J. Y.; Lauhon, L. J.; Rosenwaks, Y. Two-Dimensional Charge Carrier Distribution in MoS_2 Monolayer and Multilayers. *Appl. Phys. Lett.* **2019**, *114* (10), 101602. https://doi.org/10.1063/1.5078711.

(58) Hansch, Corwin.; Leo, A.; Taft, R. W. A Survey of Hammett Substituent Constants and Resonance and Field Parameters. *Chem. Rev.* **1991**, *91* (2), 165–195. https://doi.org/10.1021/cr00002a004.

(59) *Handbook of X-Ray Photoelectron Spectroscopy: A Reference Book of Standard Spectra for Identification and Interpretation of XPS Data*, Update.; Moulder, J. F., Chastain, J., Eds.; Perkin-Elmer Corporation: Eden Prairie, Minn, 1992.

C h a p t e r 2

Applications of X-Ray Photoelectron Spectroscopy

2.1—Introduction and background

X-ray photoelectron spectroscopy (XPS) is a method for characterizing the elemental composition and chemical state of a surface.[1–3] X-ray photons incident to a surface will, with some probability, be absorbed by electrons bound to atoms at the surface.[2,3] If the energy of the incident photon is larger than the energy binding the electron to the atom, the electron is ejected, with a kinetic energy given by the difference between the photon energy and binding energy (Eq. 2.1.1).[2,3]

Equation 2.1.1

$$KE_{electron} = h\nu_{photon} - BE_{electron} - \phi$$

Where *KE* is the kinetic energy of the electron, *h* is Planck's constant, *v* is the frequency of the photon, and *BE* is the binding energy of the electron. The ϕ term is constant which is relates to instrument contact potential and instrument work function which is corrected for during calibration, and can therefore be neglected in most collected data. The kinetic energy of the ejected electron is measured with a hemispherical electron energy analyzer combined with an electron multiplier tube.[2] Knowing the energy of the incident photon (1486.6 eV in the case of the typical Al Kα line, 1253.6 for Mg Kα, and 2984.3 for Ag Lα), the BE of the electron can then be calculated. Each element will have a characteristic XP

spectrum where peaks in the spectrum correspond to specific orbitals of the element.[2] However, a variety of factors can affect the observed BE of an electron, including scattering, charging, and chemical state change.[1–4]

Scattering limits the analysis depth of XPS, as ejected electrons may scatter off neighboring atoms, losing some kinetic energy.[3] If all the kinetic energy is lost or the electron changes direction significantly, the electron is not detected and is instead recaptured by the substance or otherwise not captured by the detector. The inelastic mean-free path (IMFP) of the electron is a measurement of the average distance an electron travels in a solid before substantially losing energy and can be roughly estimated by a "universal curve" (Figure 2.1.1).[5,6] A decrease in mean-free path—not IMFP, as that quantity is specific to solids—as pressure increases is the reason that nearly all XPS experiments are conducted at ultra-high vacuum (UHV) conditions. Fewer gas molecules in between the sample and the detector leads to a lower probability of scattering, and therefore a longer IMFP.[7] Additionally, XPS can only be expected to detect electrons at a depth of approximately 3×IMFP into a sample due to the exponential decay of electrons leaving the sample.[5,6] As a result, despite the penetration depth of X-rays typically being on the order of μm, XPS can only detect electrons approximately 10 nm deep in a sample.[5,6] Because of this small distance of detection, XPS characterizes only the surface and shallow subsurface of a material. Another consequence of scattering is the presence of background signal in an XP spectrum.[8] Electrons which were ejected from a given orbital may scatter yet still be detected by the analyzer. Such electrons have lost some amount of kinetic energy,

appearing to have a higher BE. This background signal will present as a continuum of detected electrons at a higher BE than a primary photoelectron peak.[8]

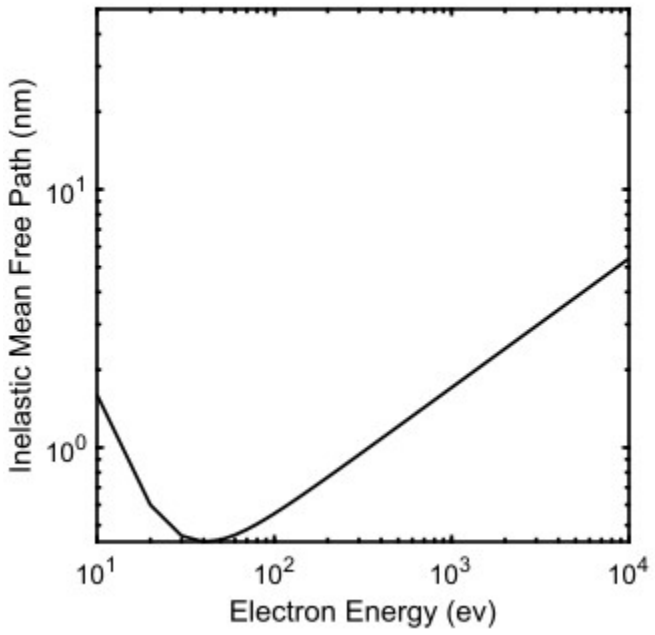

Figure 2.1.1. Approximate IMFP for electrons in materials plotted as a function of electron kinetic energy calculated using the "universal" IMFP curve.[5] Electrons in XPS typically have a kinetic energy between 100 and 1000 eV.

Charging occurs when a sample is poorly electrically connected to the XPS instrument.[1,3,9–12] A sample which loses electrons to the photoelectric effect will naturally acquire a positive electrostatic charge, but a sample in good electric contact with the instrument will replenish any lost electrons, staying in a charge-neutral state. However, insulating samples or those with poor contact to the instrument will keep the positive charge, causing electrons to bind more strongly to the sample as they need to overcome the typical BE as well as the generated electric field to be ejected.[9,10,12,13] Charging is evidenced by photoelectron peaks

which are at a higher BE than expected, and possibly increasing in BE with time.

This can be compensated by an electron flood gun that directs a steady flow of electrons at the charged surface.[3,9,12] The flood gun can cause artifacts in the spectrum as well, so practically, it is preferred to use metallic or semiconducting materials in XPS.[3,9–12]

Chemical state can also affect the observed BE of an electron. When atoms are bound together, the electron density of either participant in the bond changes and the formal oxidation state of the atom may change, resulting in a change in the screening of nuclear charge and therefore the BE of electrons in the atoms.[1,2,4] For example, the BE of a C 1s electron in a C-C bond is approximately 285 eV but is approximately 290 eV in a C-F bond due to the polarization of the bond.[4,11] Chemical state changes can also result in changes in peak shape or other spectral features and will be discussed in depth in this chapter.

A typical photoelectron peak of a pure substance observed in XPS contains 1–2 peaks, depending on the orbital investigated. XPS probes the energy required to eject an electron and produce a final state which is one electron poorer than the neutral state. As a result, if there are multiple possible final states with differing energies of formation, more than one peak may occur.[14–17] The most common example of this is spin-orbit splitting in p, d, and f-orbitals. Electrons relevant to XPS can be described by quantum numbers nl_j where n is the principal quantum number determined by the electronic shell, l is the angular momentum quantum number determined by the orbital (s = 0, p = 1, d = 2, etc.), and j is the total angular momentum quantum number where:

Equation 2.1.2

$$j = l + s$$

and s is the spin of the system, here limited to $+\frac{1}{2}$ and $-\frac{1}{2}$.[3] Note that for any orbital other than s-orbitals, two possible j values exist. The two j values have differing energies and probabilities, where the larger j value always appears at a lower BE and is larger in intensity than the smaller j peak, corresponding to a known ratio depending on the orbital (e.g., p-orbital is 2:1, d-orbital is 3:2).[2,3] These spin-orbit split peaks are spaced a characteristic energy apart. Practically, the element identity is reported, and l quantum number is reported as s, p, d, etc. for ease of communication. For example, a peak corresponding to excitation of an electron residing in the s orbital in the first electron shell of C will be reported as C 1s. To specify a peak in a doublet, the j value is included so an electron originating from the second electron shell in the p-orbital with a final angular momentum state of $j = \frac{1}{2}$ would be denoted Si $2p_{1/2}$.

In this chapter, XPS is applied for chemical analysis in a variety of systems. Specific techniques and considerations for different elements are noted, and the information gained from each analysis is discussed.

2.2—Survey spectra for identification of elemental composition and impurities

A full-spectrum scan can identify which elements are present at the surface.[2,13] A specific XPS study performed by the author is used here as an example.[18] In this case, a scalable, solution-processing method was used to create semiconducting Cu_2SnS_3 films which are of interest as Earth-abundant replacements for CdTe sensors.[18] Samples used in this study were not synthesized by the author of this thesis, nor was any characterization performed

other than XPS. For detailed experimental methods information, readers are referred to the published work.[18] XPS was employed here to confirm the identity of elements at the surface, identify any impurities, and determine the chemical state of each element in the film (Figure 2.2.1). Note that in typical XPS convention, the x-axis direction is reversed to descending order.[2,3] The spectrum shows evidence of Cu, Sn, and S as expected as well as a small amount of N left over from the thiol–amine ink used to synthesize the films.[18]

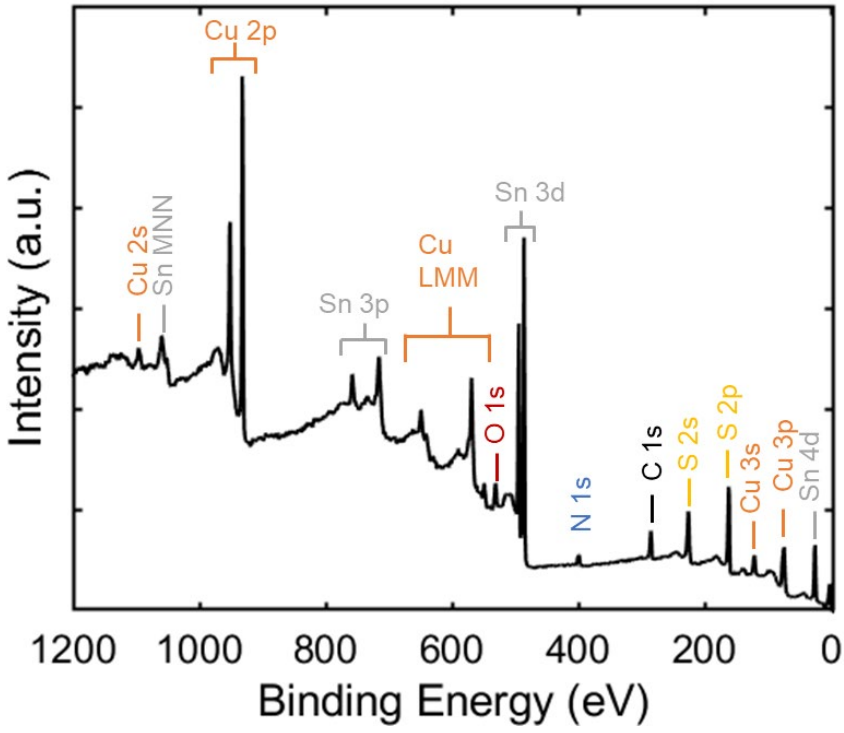

Figure 2.2.1. Survey spectrum of Cu_2SnS_3 from literature source. Several elements are present in the spectrum, distinguishable by BE. Reproduced from reference.[18]

Another application of survey spectra is quantitative XPS. Quantification regions can be defined using Casa XPS software, which is the program used throughout this thesis for analysis of XP spectra. These regions will have a user-defined background, a Shirley background, for example, and a defined "relative sensitivity factor" (RSF) which accounts for the variation of x-ray cross section among elements.[2,3,19] The area above the background in each region is integrated, and divided by the RSF to give a normalized signal which is then compared to the total signal of all regions of interest to give a relative atomic abundance for each element of interest.[19] Selection of background is thus quite important and interested readers are referred to an overview of this topic.[8] Importantly, XPS cannot provide an absolute abundance of elements in most circumstances, and the signal of each element may only be compared for elements with identical conditions (i.e., the same experimental run with same instrumental parameters) as small variations between experiments can lead to large differences in absolute signal obtained.[19]

2.3—High-resolution XP Spectra for chemical state analysis

High-resolution XP spectra are a common type of XP spectrum in the scientific literature because analysis of these spectra allows for characterization of the chemical state of the element probed. Differences in coordination, oxidation state, and bond polarization can all have an impact on the observed BE for a photoelectron peak.[3,4,20] For example, S is a common element in XPS analysis which may have multiple chemical states present on a surface at the same time.[21–23] Sulfides and oxidized sulfur species are particularly common and frequently overlap in energy to a degree.[20–22] Careful modeling and fitting of peaks

enables these species to be deconvoluted and the relative abundance of each species quantified. Here, S 2p signal for Cu_2SnS_3 is used as an example.[18] It is again noted that the author of this thesis participated only in XPS data collection and analysis for this work.

Over-fitting of peaks is a common error in XPS analysis wherein peaks are fit to a spectrum until a minimal amount of residual occurs between the raw data and fit model without consideration of physical properties.[24,25] To accurately fit a series of overlapping peaks, as few assumptions as possible should be made, and preferably backed up with other observations.[24] For example, in the case of Cu_2SnS_3 the S 2p spectrum could not be accurately fit with just one set of S 2p doublets. A large residual error remains as the signal is not adequately represented. By adding a second set of doublets, the signal is better modeled, but to ensure that erroneous fitting has not occurred, the position and full width at half maximum (FWHM) should be considered. In this case, a surface oxide was suspected due to air exposure so a second set of doublets should be at a higher BE than the sulfide peaks due to the more electronegative O causing less electron density on the S atoms.[2,20,22] Additionally, these peaks are expected to have a larger FWHM because surface oxides tend to be more disordered in their stoichiometry, resulting in wider peaks as multiple similar states overlap in BE.[2,3,22,26]

Once this second set of peaks was fit, they best fit the data at a higher BE and with a wider FWHM, in line with expectations for a surface oxide. To support assignment of these additional peaks as a surface oxide, O must be detected at the surface. Analysis of the

survey scan confirmed the presence of O, leading to the conclusion that there is likely one set of metal sulfide peaks with a set of surface oxide peaks in the S 2p spectrum (Figure 2.2.1). In this case, the remaining signal is minimal, and to fit another set of peaks would require a chemical explanation that would be difficult to support with the collected data. Thus, the fit of this spectrum is considered acceptable as the residual has been minimized while requiring as few peaks as possible that all have chemical explanations supported by data.

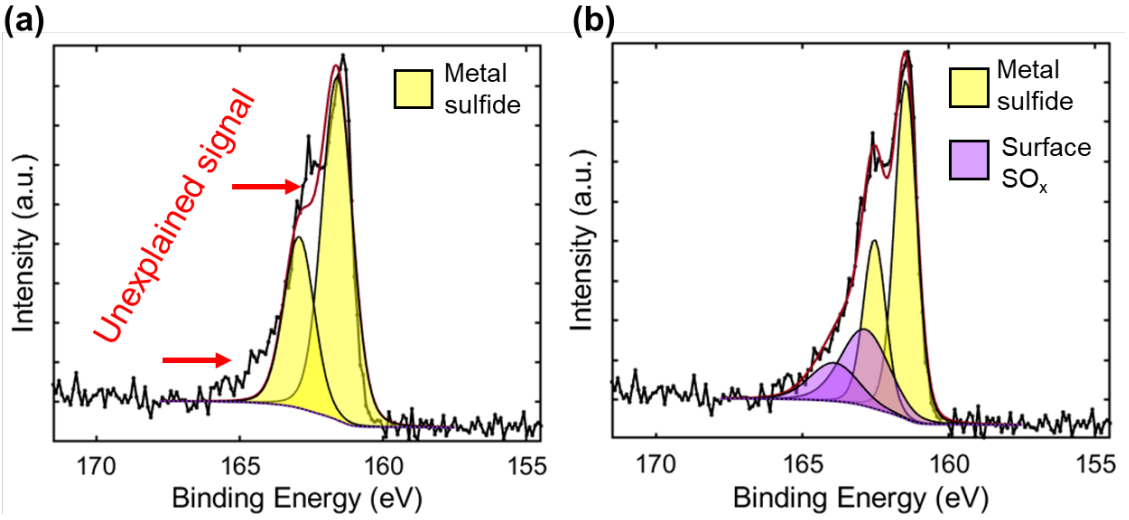

Figure 2.3.1. High-resolution S 2p spectrum for Cu_2SnS_3 reproduced from reference.[18] Spectrum fit to (a) one and (b) two sets of peaks are fit to the data to demonstrate process of generating an acceptable fit.

This general procedure should be followed for all XP spectra, where each set of peaks has a chemical origin that can be supported by data. All assumptions made should be stated explicitly to aid future readers in analyzing data, either by using those assumptions in their own data or reanalyzing data with new assumptions. XP spectra are rarely conclusive independently, especially for complex materials systems, and the goal of analyzing XPS

data is generally not to perfectly fit the data and "discover" new chemical states, but rather to develop a reasonable model that is informative about the surface being studied. Caution should be used when referencing published work to ensure that erroneous assumptions and fitting procedures in past work do not influence future work. Additionally, the spectral behavior of each element studied should be known to prevent incorrect assignment of spectral features such as doublets, multiplet splitting, and shake-up peaks.

Auger electrons can also be used for chemical analysis. Here, another study performed by the author on Cu oxide films is used as an example. Samples used in this study were not synthesized by the author of this thesis, nor was any characterization performed other than XPS. Cu is a common element encountered in XPS analysis that presents a unique set of factors useful for chemical state identification. Most notably, a Cu (II) species such as CuO will exhibit large satellite features in the Cu 2p spectrum.[26,27] These peaks, known as "shake-up" structures, are caused by an additional excitation occurring with photoionization, resulting in photoexcited electrons losing a quantized amount of energy and appearing at a higher BE (Figure 2.3.2).[28] In the case of Cu, the excitation is a ligand to metal charge transfer resulting in an additional 3d electron in the final state.[28] This does not occur in Cu (I) or metallic Cu, thus the presence of shake-up structures is qualitatively indicative of Cu (II) at the surface.[27,28] To distinguish between Cu (I)—especially Cu_2O—and Cu metal, the Cu 2p spectrum alone is insufficient, as there is minimal difference in the Cu $2p_{3/2}$ BE between these two species.[2,27,28] Instead, the Cu 2p spectrum must be combined with the Cu LMM Auger spectrum to accurately identify surface species.[27,28]

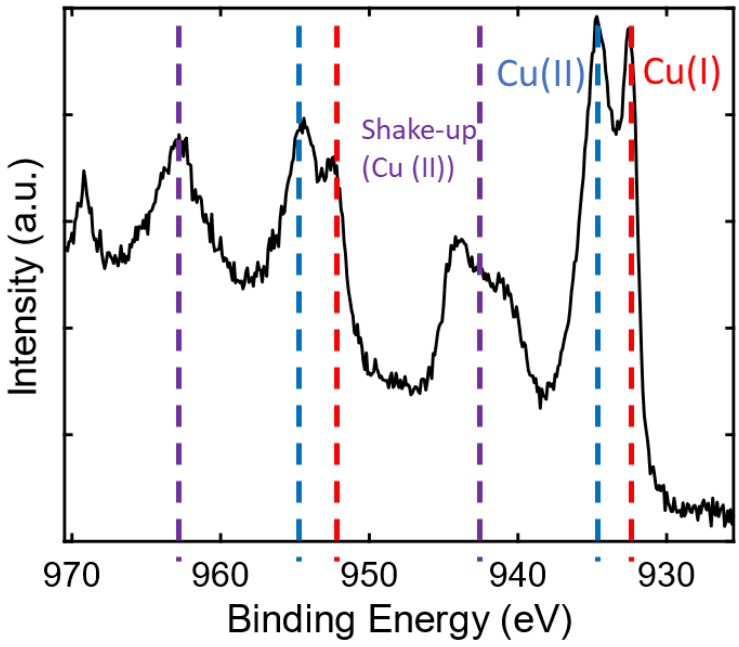

Figure 2.3.2. High-resolution Cu 2p spectrum for Cu_2O film electrodeposited in dark conditions. Two Cu species are evident, with a low-BE Cu (I) or Cu metal set of peaks and a higher BE CuO set of peaks including a set of shake-up peaks associated with intra-atomic transitions in Cu (II) species.

Auger electrons are emitted via a different process to normal XPS photoexcitation.[3,29,30] In XPS, photoexcitation produces a charged excited state with a hole in a core level in the atom, which can relax via a variety of pathways.[3,30] To produce an Auger electron, a valence electron recombines with the hole in the core level, releasing the difference in energy between the valence orbital and core orbital.[3,29,30] If this energy is released radiatively, this is referred to as fluorescence and is the basis of x-ray fluorescence spectroscopy.[31] However, the recombining electron may instead transfer the energy of the transition to a neighboring valence electron, ejecting it with an energy equal to the difference between valence and core orbital energies minus the binding energy of the

valence electron, which is typically small.[3,29,30] Thus, electrons may be detected with apparent BE that is invariant with incident x-ray photon energy and instead have KE that is invariant with photon energy.[2,3,30] The KE of the electron is dependent on the energy difference between core and valence orbitals and is therefore quite sensitive to differences in bonding environment. This sensitivity is the basis for differentiating Cu (I) and Cu metal, as the Cu (I) species (i.e., Cu_2O) will have a more polar bond, and therefore different valence electron energy as compared to Cu metal.[28,29]

The Auger spectrum can be used to measure the splitting of valence orbitals if it is known which peaks correspond to which orbital transitions (Figure 2.3.3).[29] The Auger electrons are referred to with X-ray spectroscopy notation where K is the first shell (e.g., 1s), L is the second shell (e.g., 2s, 2p) M is the third, and so on.[29,30] The Auger electron will be referred to with three letters, wherein the first letter indicates the shell that has been ionized, the second indicates the shell of the electron which relaxed to fill the core hole, and the third indicates the shell of the electron that was ejected. So, a Cu LMM peak is caused by an electron in the second shell being ionized, resulting in an electron in the third shell relaxing and ejecting an electron also in the third shell. Due to the complexity of Auger transitions, it is common shorthand to omit the specific orbitals causing the transition and use only the letters, but if the orbitals are known, they can be indicated with subscripts. The subscript denotes the identity of orbitals with different quantum numbers in order of increasing energy. For example, L_1 indicates the lowest energy orbital in the second shell, which is the 2s, while L_2 indicates the second lowest which is $2p_{1/2}$. If multiple orbitals contribute to the

same peak, two subscripts separated by a comma are used. It is important to note that the Auger spectrum here does not refer to Auger electron spectroscopy, which causes similar electronic transitions—hence the name—but utilizes electrons as the excitation source rather than X-rays and typically utilizes the derivative of the signal on the y-axis.[3,30]

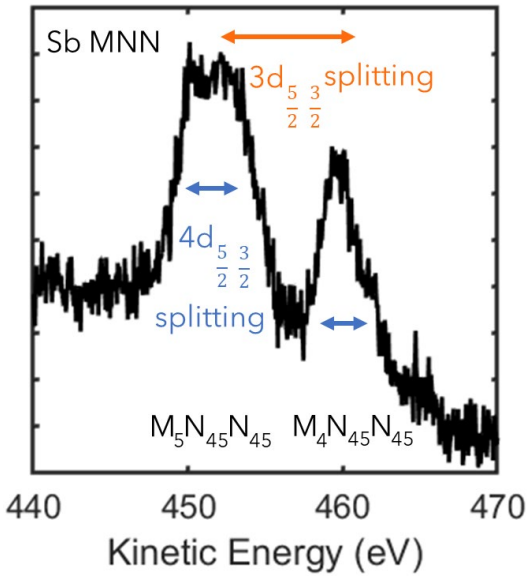

Figure 2.3.3. Auger spectrum of Sb MNN transition as an example of how Auger spectra can be interpreted, specifically the $M_4N_{4,5}N_{4,5}$ and $M_5N_{4,5}N_{4,5}$ excitations with peak assignments.[32] There are two major features which are related to the Sb 3d orbital splitting and two peaks within each of these features which are identical in splitting due to originating from the same Sb 4d orbital splitting.

Analysis of the XP spectra and Auger spectra of a Cu-based inorganic phototropic growth structure provides a case study for this analysis. The aqueous deposition solution for these films included I^-, Cu^{2+}, and sodium azide and the final oxidation state and chemical composition was unknown. Key questions for this analysis were what the chemical identity of surface species was, how films deposited under illumination differ chemically from

those grown without illumination, and whether I or N was included in the lattice of the resulting structure.

To address these questions, XP spectra of Cu 2p, Cu LMM, O 1s, C 1s, I 3d, and N 1s were collected for dark-grown and light-grown samples as a function of etch depth. In the case of dark-grown samples, the Cu 2p spectrum before etching showed evidence of at least two Cu species, likely CuO, as evidenced by a BE of ~934 eV and the presence of shake-up features, and a Cu^0 or Cu^+ species at ~932.5 eV (Figure 2.3.4).[28] Analysis of the Cu LMM spectrum indicated a KE of ~917 eV which, combined with the observed Cu $2p_{3/2}$ BE of 932.5 eV, is characteristic of a Cu_2O species. No signal from CuO is present in the Cu LMM spectrum (expected at a KE of ~918 eV) hypothesized to be caused by the increased KE of the ejected Cu LMM electrons relative to the Cu 2p electrons causing an increase in detection depth and a thin film of mostly CuO covering a Cu_2O bulk.[28] This hypothesis is corroborated by peak fitting of the O 1s spectrum. One larger peak at a BE of ~531 eV is visible, with a shoulder at a lower BE of ~530 eV. This data is consistent with a hypothesis that there are two oxide species on the surface, with the dominant species exhibiting a more electron-poor O than the less dominant oxide. Combined with the Cu spectrum, this data corroborates the earlier hypothesis that both CuO and Cu_2O are present at the surface, with CuO as the dominant stoichiometry.

Upon etching the dark-grown sample via Ar^+ ion sputtering, a significant change in surface chemistry is observed. The signal in the Cu 2p spectrum assigned to CuO disappears, and the Cu LMM signal associated with Cu_2O increases in intensity (Figure

2.3.4). Similarly, the O 1s spectrum displays a reversal of the prior observation, where the lower BE peak assigned to Cu_2O is more apparent and the peak assigned to CuO is now a shoulder. The lower FWHM for the Cu_2O O 1s peak compared to the CuO peak also corroborates the peak assignment. Of interest in this case is the effect of etching on I 3d signal. The nanostructures generated in the light have been shown to require I^- in solution, and it has been hypothesized that some I incorporates into the lattice during deposition. Before etching, the I 3d spectrum shows little to no evidence of I at the surface, but after etching, a distinct I $3d_{5/2}$ peak is visible at 619.7 eV. The peaks at 630 and 640 eV are part of the Cu Auger spectrum. The observed I $3d_{5/2}$ signal is difficult to definitively assign due to low signal, but the peak appears to lie between previously reported values for CuI (619.0 eV) and elemental I_2 (620.2 eV).[20] Thus, the I species observed is likely more electron rich than neutral I_2, but more electron poor than pure CuI. This observation, combined with the increased signal after etching leads to the hypothesis that I is indeed incorporated into the CuO_x lattice, but is a minor impurity with a Cu:I ratio of 99.3:.07 and it is bound nearly exclusively to Cu atoms bound to O rather than I, resulting in a more polar Cu-I bond that decreases e^- density on the I. The generation of target nanostructure similarly requires the presence of azides in solution, but XPS analysis before and after etching indicates that N is not incorporated into the lattice and is not detected at the surface.

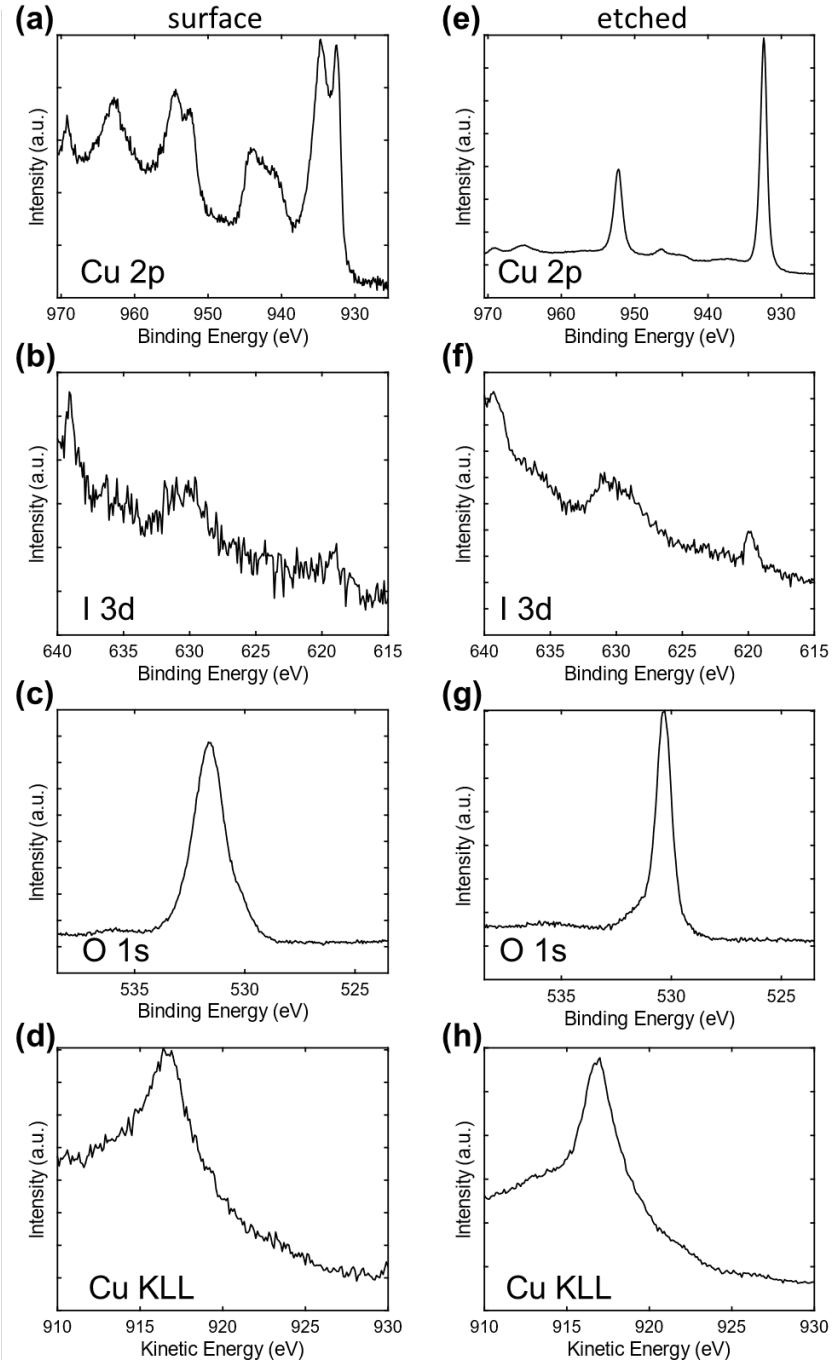

Figure 2.3.4. (a,e) Cu 2p, (b,f) I 3d, and (c,g) O 1s XP spectra and (d,f) Cu LMM Auger spectrum for Cu_2O films electrodeposited in dark conditions (a,b,c,d) before and (d,e,f,g) after etching with Ar^+ etching. C 1s spectra were also collected for calibration but are not

shown here. N 1s was also collected, but no signal was observed so these spectra were also omitted here.

With the character of the dark deposition now understood, nanostructured samples grown under illumination were then analyzed via XPS in the same manner as described previously (Figure 2.3.5). Similar conclusions were reached regarding the identity of the Cu species, with Cu_2O and CuO as the primary stoichiometries present. In the case of the nanostructured samples, even without etching, the Cu 2p spectrum indicates a preference for Cu_2O at the surface. CuO is still observed, but at a consistently lower abundance than observed in dark-growth films. The O 1s spectrum of light-grown samples also displays a more prominent Cu_2O peak when compared to dark-grown films. However, the peak at ~532 eV is still quite large, which is hypothesized to be caused by overlapping signals from surface hydroxide moieties. The deposition process for light-grown nanostructured films thus likely favors the formation of Cu_2O over CuO. More I 3d signal is apparent at in the illuminated samples than the dark-grown samples, and the signal increases after etching just as in the dark-grown case. Peak positions lead to similar conclusions of a Cu-I bond modified in strength by surrounding Cu-O bonds. The relative increase in Cu:I ratio is hypothesized to be due to a thinner CuO overlayer in the illuminated samples which does not allow for I substitution. However, in both cases the I 3d spectra support the hypothesis that I is incorporated into the lattice in small quantities and likely destabilized the lattice somewhat, leading to a more polycrystalline structure in the light-grown samples that is conducive to the formation of phototropic nanostructures. N is not observed in the lattice of

the illuminated samples, indicating its effect on nanostructure growth is likely a solution-phase process.

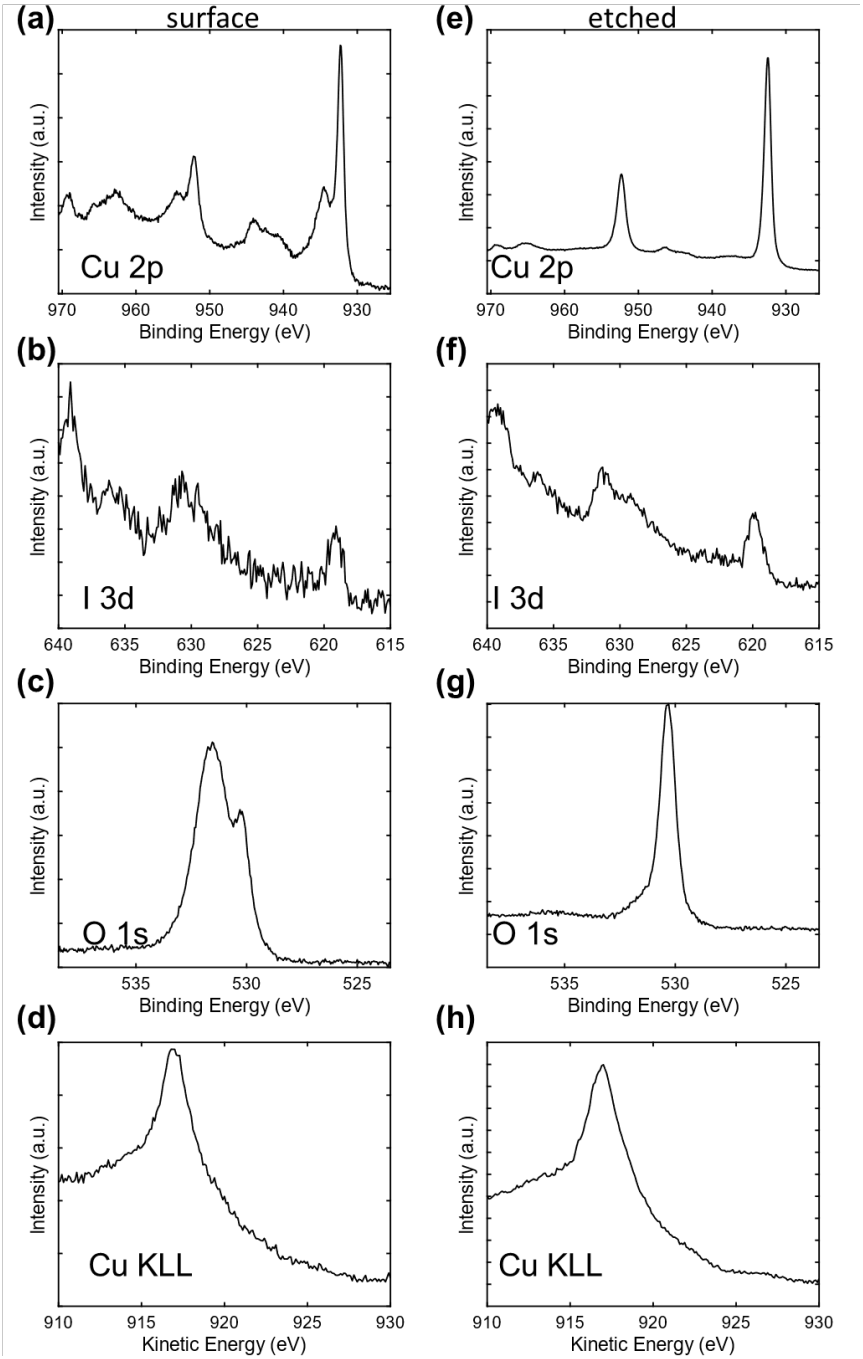

Figure 2.3.5. . (a,e) Cu 2p, (b,f) I 3d, and (c,g) O 1s XP spectra and (d,f) Cu LMM Auger spectrum for Cu_2O films electrodeposited in illuminated conditions (a,b,c,d) before and (d,e,f,g) after etching with Ar^+ sputtering. C 1s spectra were also collected for calibration but are not shown here. N 1s was also collected, but no signal was observed so these spectra were also omitted here.

In summary, analysis of the XP spectra of CuO_x films deposited in dark conditions and under illumination has provided significant insight into the surface chemistry of resulting films and origin of observed nanostructures under illumination. Films are primarily Cu_2O in the bulk, with a CuO layer on top that is more apparent in dark-grown films than light-grown films, likely due to a thicker layer (Figure 2.3.6). These films incorporate I into the lattice as a minor impurity which is hypothesized to cause a lattice destabilization that results in a more polycrystalline film than one grown without I. The higher polycrystallinity then leads to a light-directed film growth as opposed to crystalline film.

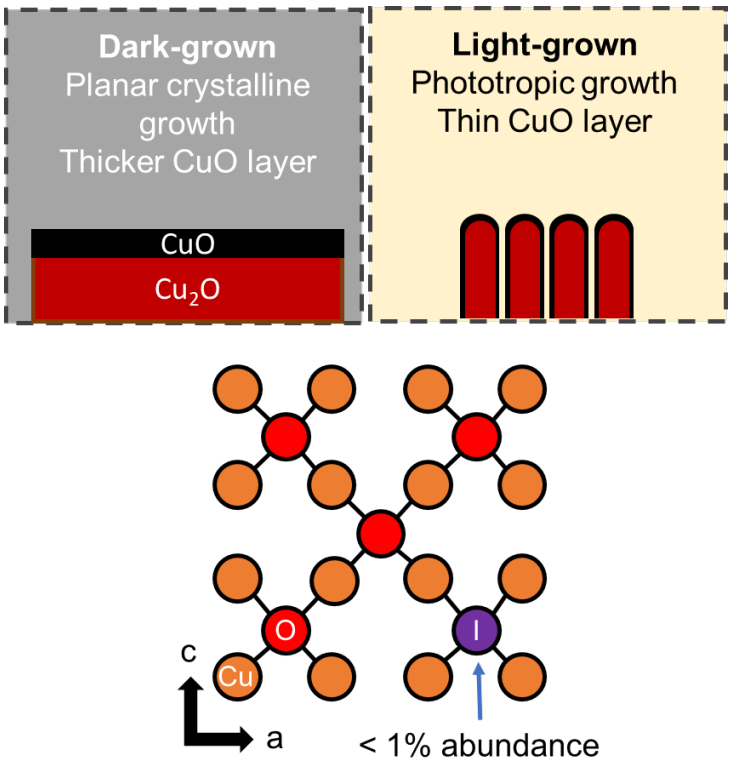

Figure 2.3.6. Schematic of Cu_2O film character as measured via XPS. In the dark, electrodeposited films exhibit higher CuO signal than in illuminated conditions, hypothesized to be due to a thicker layer of CuO. In both cases, a CuO surface layer is observed with a Cu_2O bulk. Depth-profiled XPS indicates I is incorporated into the lattice as a minor impurity, at less than 1% atomic abundance.

Another example of standard XPS combined with Auger spectrum analysis and depth profiling illustrates the analytical power of XPS as a technique. An analysis performed by the author is used as an example here.[33] As in prior sections, the samples herein were not synthesized by the author of this thesis. MgB_2 has attracted attention for its superconducting properties at relatively high temperatures.[34–37] However, difficulties with Mg vapor pressure limit applications. The addition of a B overlayer can preserve the superconducting properties while protecting the underlying MgB_2 from Mg evaporation.[33]

Unknown, however, is how the addition of the B cap affected the stoichiometry of the MgB_2, especially after an annealing step. Several phases are thermodynamically probable in the conditions used.[38] It was also of interest to determine whether Si_3N_4 substrates could be used as opposed to the traditional Al_2O_3 (sapphire) substrates due to device advantages and whether the annealing step caused any diffusion of species across the interface.[33] For this analysis, Mg KLL Auger spectra were used for Mg characterization because Mg 2p spectra are relatively insensitive to chemical environment.[39] Additionally, B 1s, O 1s and either Si 2p and N 1s or Al 2p were collected along with C 1s as a reference. To access the chemistry of the MgB_2 layer, it was necessary to etch through approximately 50 nm of B. To characterize the interfaces, depth profile XPS was performed. In this technique, XP spectra are collected at regular intervals after short etch cycles to give depth resolution.

Depth profiling of the B cap indicated an etch rate of approximately 1.6 nm/min while the MgB_2 layer had an etch rate of approximately 3.0 nm/min. Examining the stoichiometry as a function of etch time, the content of each layer can be examined (Figure 2.3.7). At the initial surface for both Si_3N_4 and sapphire substrates, a native B_2O_3 layer is present, while a small amount of Mg is detected. This is likely due to the relatively high KE of the Mg Auger electrons, as Auger detection depth is typically deeper than normal photoelectron peaks.[30,39] As the B cap is etched, the O signal disappears, and the remaining signal is almost exclusively from B, as expected. At the interface, the B signal decreases, and the Mg signal increases, though it is not a sharp takeoff due to the depth sensitivity of the XPS.

Little difference is observed between the annealed and unannealed samples at the B/MgB_2 interface, indicating that the annealing step does not result in a diffuse interface. In the MgB_2 region, stoichiometry is roughly constant until the MgB_2/substrate interface though it is more consistent in the unannealed sample. At the MgB_2/Si_3N_4 interface, the B signal decreases rapidly, and the Mg signal decreases more gradually, though both are still detected inside the Si_3N_4 layer. This continues into the underlying Si substrate, indicating the MgB_2/Si_3N_4 interface is diffuse and a substantial fraction of the Si_3N_4 is contaminated with Mg and B. Additionally, a small amount of O is detected at the interface but not in the MgB_2 or Si_3N_4 layer. At the MgB_2/sapphire interface, the Mg and B signal drop to near zero while O and Al signals spike. There is some overlap of the MgB_2 and sapphire signals, and more in the annealed sample, but in both cases the Mg and B do not appear to diffuse as deeply into the substrate, indicative of a sharper interface.

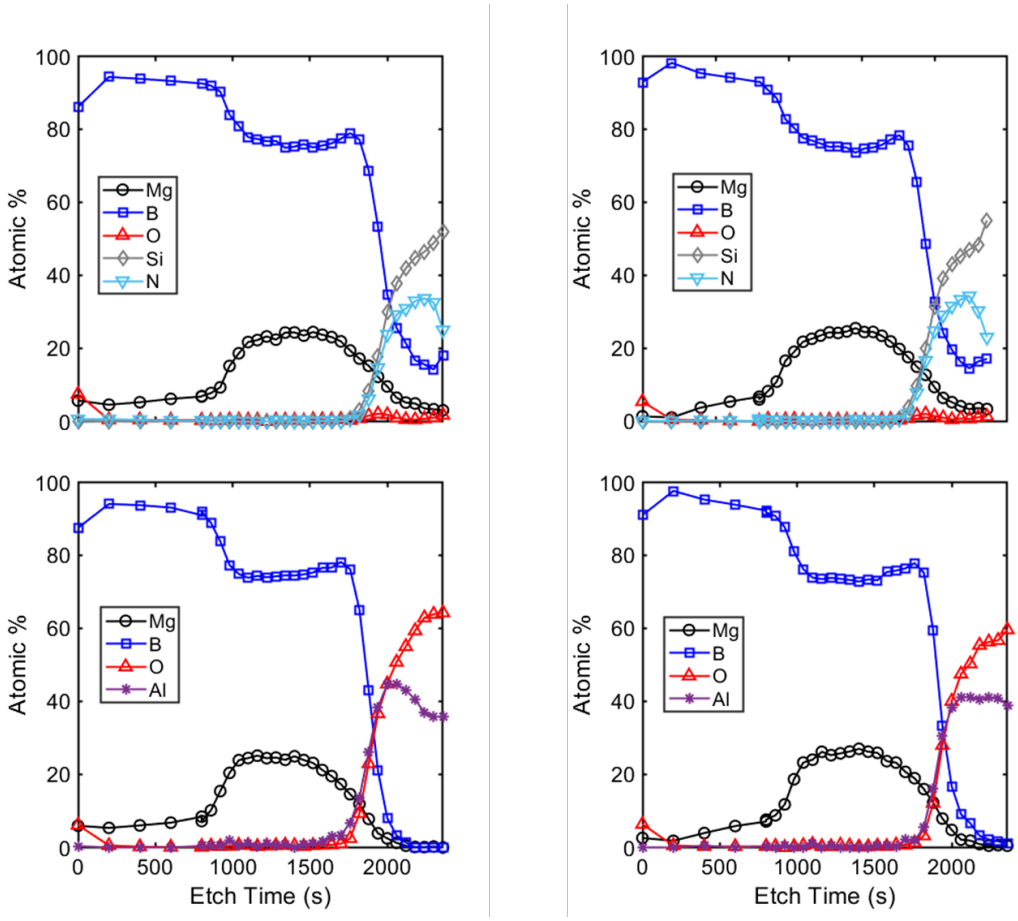

Figure 2.3.7. Depth-profiled XPS for B-capped MgB_2 on Si_3N_4 and sapphire substrates with and without annealing. Atomic % is quantified as (abundance of atom/abundance of all atoms quantified)*100.

The advantage of depth-profiled XPS as opposed to other depth-sensitive measurements is the ability to perform detailed chemical analysis at each step of the etch to identify whether chemical changes accompany observed changes in stoichiometry and whether interfacial species occur. For the unannealed Si_3N_4 sample, representative spectra for each major region are displayed in Figure 2.3.8. In the B cap layer, only B 1s and Mg KLL signal is detected. The B 1s is a single, well-defined peak which is well fit by an assignment of

elemental B. The Mg KLL signal contains three peaks. Due to the nature of Auger signal, wherein electrons are ejected due to intra-atomic transitions rather than a fixed-energy x-ray beam, the origin of each peak is difficult to assign without computation. Instead, changes in the number and intensity of the Mg KLL peaks relative to each other will be used to draw conclusions about the chemical changes in Mg because changes in chemical environment will result in rather large changes to the Mg KLL signal. In the MgB_2 layer, the B, O, Si, and N signals remain relatively unchanged, but the Mg KLL spectrum contains an additional peak.

The lack of change in the B 1s spectrum with stoichiometry is likely due to the relatively low polarizability of the B atom, and it is known to be somewhat insensitive to chemical environment. The addition of a lower BE (higher KE) peak in the Mg KLL spectrum is likely due to a unique state present in the MgB_2 material. For clarity, all the peaks in the Mg KLL spectrum in this region likely originate from MgB_2, but this new state is not present in the Mg signal observed in the B cap. The higher KE means that the difference between the core state and the valence orbital where these electrons originated is larger than that for the states previously observed. Since the Mg 2p peak is relatively insensitive, this state is likely from a relatively high-energy valence state only present in the MgB_2.[39]

At the interface, some interesting chemistry is observed in multiple spectra. In this region, Si and N are detected, as is a small amount of O at a relatively high BE not expected for most metal oxides but more similar to SiO_2. Additionally, a new peak is observed in both the B 1s and Mg KLL spectra. The high BE of this new state in both cases, plus the

presence of oxygen points towards an interfacial oxide state. Interestingly, two peaks are observed in the Si 2p spectrum. The higher BE state is well modeled as Si_3N_4, but the lower BE state does not fit an assignment of Si metal nor SiO_2. The N 1s spectrum does not indicate any additional states or oxides of N. This extra state is observed in four different spectra and appears and disappears simultaneously in all cases, pointing towards shared chemistry. Thus, it can be concluded that at the MgB_2/Si_3N_4 interface, a suboxide is formed composed of Mg, B, Si, and O but not N. Once the interface is etched away, a minimal amount of Mg and B is detected, with only Si_3N_4 and metallic Si detected in the Si 2p and N 1s spectra. It is noted as well that the Si KLL spectrum overlaps with B 1s so a portion of the signal observed in B 1s may originate from Si instead.[2]

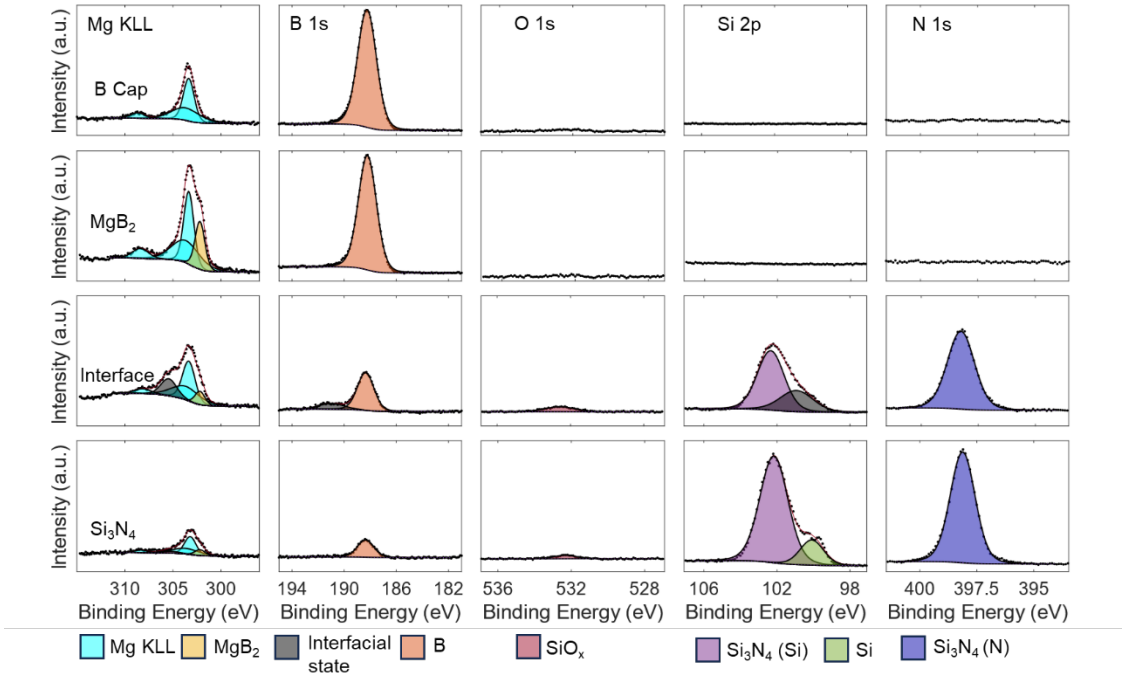

Figure 2.3.8. Representative XP spectra (columns) of Mg KLL, B 1s, O 1s, Si 2p and N 1s in each layer of un-annealed MgB_2 on Si_3N_4 stacked as denoted by row labels. Mg KLL

transitions are not assigned here due to uncertainty in the composition and intensity of transitions in the observed chemistry. In the B cap layer, Mg KLL displayed 3 peaks, but likely originating from a Mg boride as no other elements were detected in this region. In the MgB_2 layer, an additional peak is found at a lower BE (higher KE, in Auger convention) which is likely from MgB_2. At the MgB_2/Si_3N_4 interface, an additional Mg KLL peak is observed at ~306 eV BE along with a B 1s peak at ~191 eV and a Si 2p peak at ~101 eV as an O impurity is detected. Each of these observations is consistent with an oxide impurity, likely consisting of Mg, B, and Si, but not N. Once the interface is etched through, a small amount of Mg, B, and O is still detected, but the primary signals are Si_3N_4 and underlying Si.

In the annealed Si_3N_4 substrate, similar conclusions may be drawn (Figure 2.3.9). In the B cap, a well-defined B 1s peak is observed, as well as three peaks in the Mg KLL that are of similar relative intensity to that of the unannealed sample, though of a lower intensity relative to the B signal. In the MgB_2 region, the new peak reappears, supporting the assignment as a unique MgB_2 state. At the interface, the oxygen and new peaks in Mg, B, and Si reappear at identical BEs as well, supporting the hypothesis that an interfacial oxide is the cause of these new peaks. No substantial difference is seen between the chemistry of the annealed and unannealed Si_3N_4 samples beyond the interfacial region.

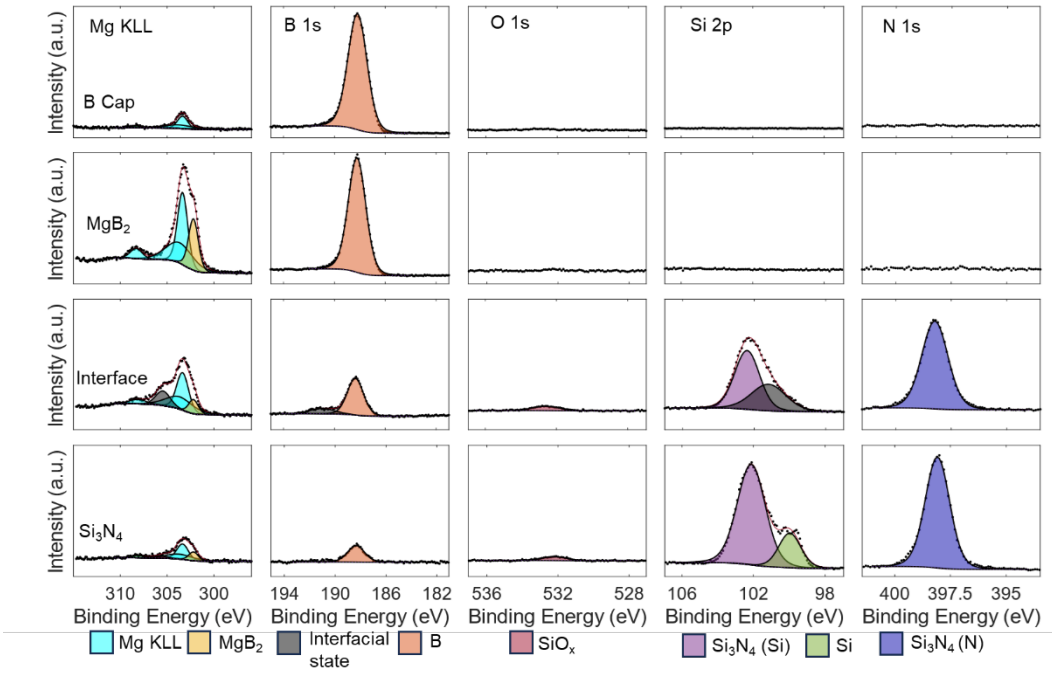

Figure 2.3.9. Representative XP spectra (columns) of Mg KLL, B 1s, O 1s, Si 2p and N 1s in each layer of annealed MgB_2 on Si_3N_4 stacked as denoted by row labels. Mg KLL transitions are not assigned here due to uncertainty in the composition and intensity of transitions in the observed chemistry. In the B cap layer, Mg KLL displayed 3 peaks, but likely originating from a Mg boride as no other elements were detected in this region. In the MgB_2 layer, an additional peak is found at a lower BE (higher KE, in Auger convention) which is likely from MgB_2. This peak is identical to the one found in Figure 2.3.8. At the MgB_2/ Si_3N_4 interface, an additional Mg KLL peak is observed at ~306 eV BE along with a B 1s peak at ~191 eV and a Si 2p peak at ~101 eV as an O impurity is detected. Each of these observations is consistent with an oxide impurity, likely consisting of Mg, B, and Si, but not N. Once the interface is etched through, a small amount of Mg, B, and O is still detected, but the primary signals are Si_3N_4 and underlying Si.

For the sapphire substrates, a similar analysis was performed (Figure 2.3.10). Identically to the Si_3N_4 samples, three Mg KLL peaks are observed as well as a single B 1s peak in the B cap region. The same additional Mg KLL peak occurs in the MgB_2 region of this sample, further supporting the assignment of that peak. At the interface, the high-BE peak observed in the Si_3N_4 samples does not appear. Instead, a low-BE peak is observed in the Al 2p

spectrum and the high-BE peak present in the original B cap spectrum increases in relative intensity. This high-BE (low KE) peak in the Mg KLL spectrum has been associated with Mg oxides in previous studies, thus, it is concluded that an interfacial state also occurs in the sapphire samples, but the data indicates a Mg-Al oxide with no contributions from B. Past the interface, virtually no Mg or B is detected. The O 1s and Al 2p spectra do show a shift in the primary peaks, but this is due to uncompensated charging of the sapphire.

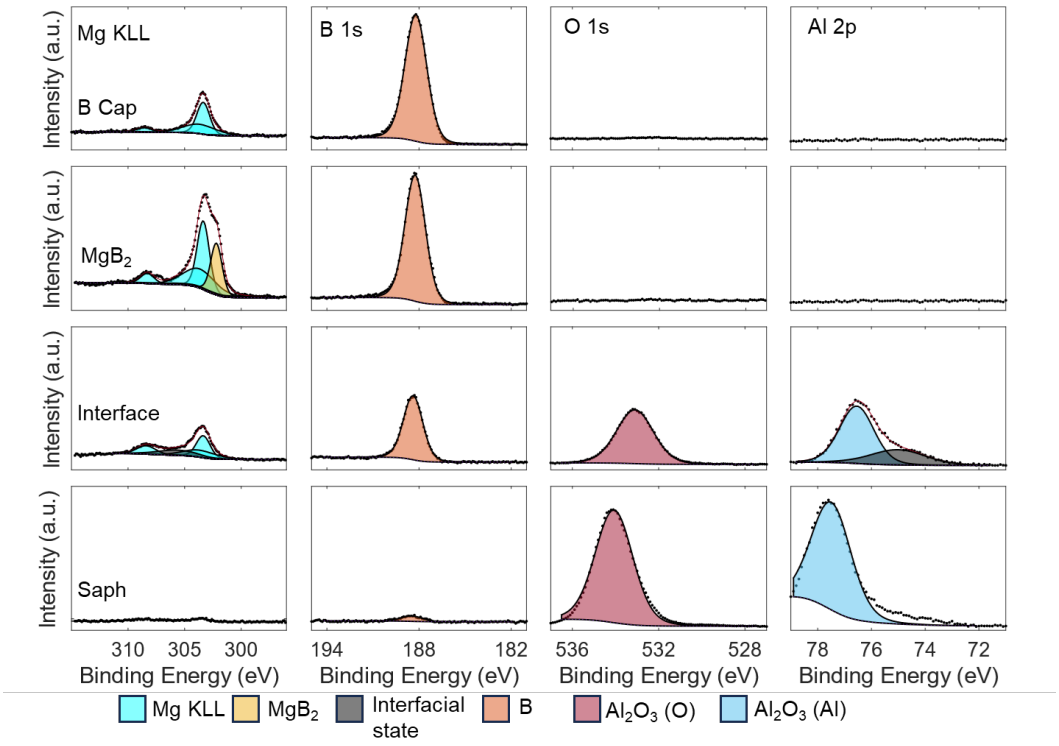

Figure 2.3.10. Representative XP spectra (columns) of Mg KLL, B 1s, O 1s, and Al 2p in each layer of un-annealed MgB_2 on sapphire stacked as denoted by row labels. Mg KLL transitions are not assigned due to uncertainty in the composition and intensity of transitions in the observed chemistry. In the B cap layer, Mg KLL displayed 3 peaks, but likely originating from a Mg boride as no other elements were detected in this region. In the MgB_2 layer, an additional peak is found at a lower BE (higher KE, in Auger

convention) which is likely from MgB_2. This peak is identical to the one found in Figures 2.3.8–9. At the MgB_2/Si_3N_4 interface, an additional Mg KLL peak is observed at ~306 eV BE and the peak at 308 eV is intensified, indicative of a Mg oxide. No corresponding peak is observed in the B spectra so the interfacial species is likely primarily composed of Mg, Al and O. Once the interface is etched through, a virtually no Mg and B is detected and the primary signal is of Al_2O_3 which, due to differential charging of the sapphire substrate and MgB_2 overlayer, has an uncompensated shift due to charging so BE of these peaks is not diagnostic of chemical states.

In the annealed sapphire sample, similar chemistry is observed through the interfacial layer (Figure 2.3.11). Less Mg is observed in the B cap layer, and the same MgB_2 signals are observed in the corresponding regions. At the interface, the same enlarging of the Mg KLL high-BE peak is observed along with the low-BE peak in the Al 2p spectrum, again pointing to a Mg-Al oxide as an interfacial species. At the interface and past it, the Mg and B signals are more intense, as the interface is more diffuse due to the annealing step. Charging of Al and O is again observed, though a lower BE peak is observed in the O 1s spectrum. Because of the charging, it is difficult to properly assign this peak, but it is hypothesized that it is either an Al suboxide or a less charged layer of sapphire.

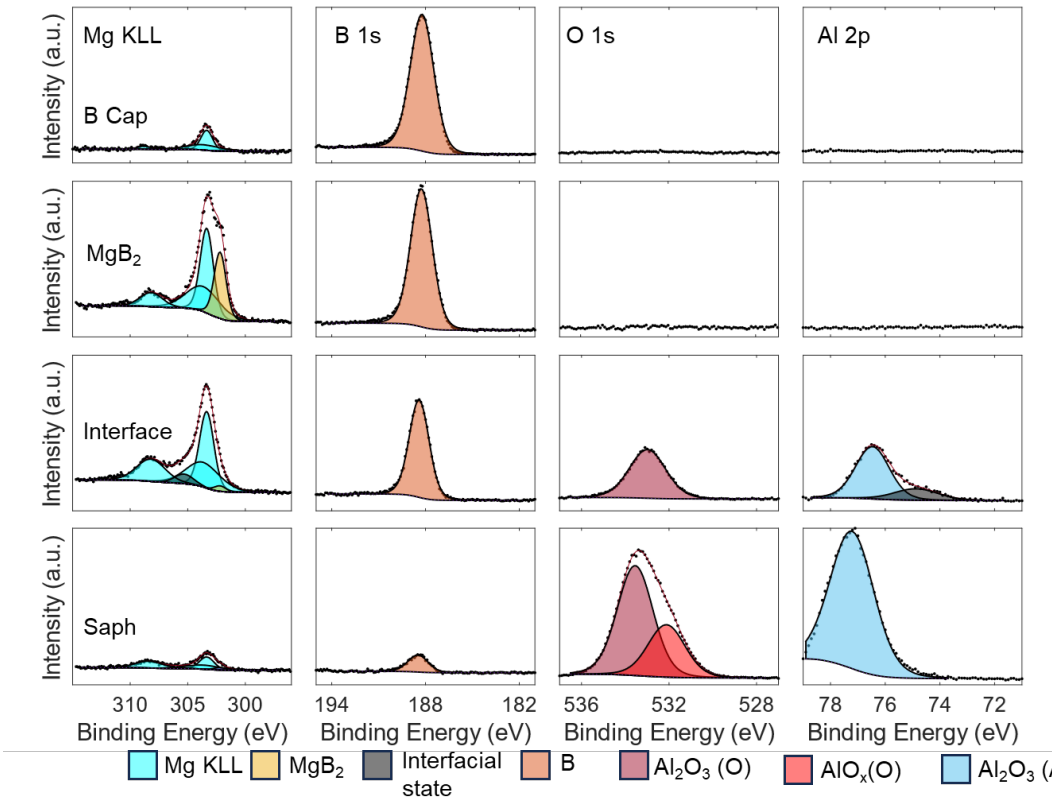

Figure 2.3.11. Representative XP spectra (columns) of Mg KLL, B 1s, O 1s, and Al 2p in each layer of annealed MgB_2 on sapphire stacked as denoted by row labels. Mg KLL transitions are not assigned due to uncertainty in the composition and intensity of transitions in the observed chemistry. In the B cap layer, Mg KLL displayed 3 peaks, but likely originating from a Mg boride as no other elements were detected in this region. In the MgB2 layer, an additional peak is found at a lower BE (higher KE, in Auger convention) which is likely from MgB_2. This peak is identical to the one found in Figures 2.3.8-10. At the MgB_2/Si_3N_4 interface, an additional Mg KLL peak is observed at ~306 eV BE and the peak at 308 eV is intensified, indicative of a Mg oxide. No corresponding peak is observed in the B spectra so the interfacial species is likely primarily composed of Mg, Al and O. Once the interface is etched through, a small amount of Mg and B is still detected, but the primary signal is of sapphire, Al_2O_3 which, due to differential charging of the sapphire substrate and MgB_2 overlayer, has an uncompensated shift due to charging so BE of these peaks is not diagnostic of chemical states. Thus, the additional peak observed in O 1s may be due to the differential charging and not from an additional chemical state.

Detailed XPS analysis of the MgB_2 devices has revealed that the MgB_2/B interface is relatively sharp and not affected much by annealing, while the substrate/MgB_2 interface

exhibits noticeable diffusion of Mg and B after annealing. Additionally, interfacial oxide states have been observed in both cases, though the chemistry of these oxides varies, with a Mg-B-Si oxide in the Si_3N_4 samples and a Mg-Al oxide in the sapphire samples (Figure 2.3.12). Comparison between multiple spectra supports the assignment of these interfacial oxides and the identity of a unique Mg KLL peak originating from MgB_2. This work has enabled comparison of the quality of different interfaces in the MgB_2 device architectures studied and identified multiple spectral handles which will be of use for future studies on these superconducting devices.

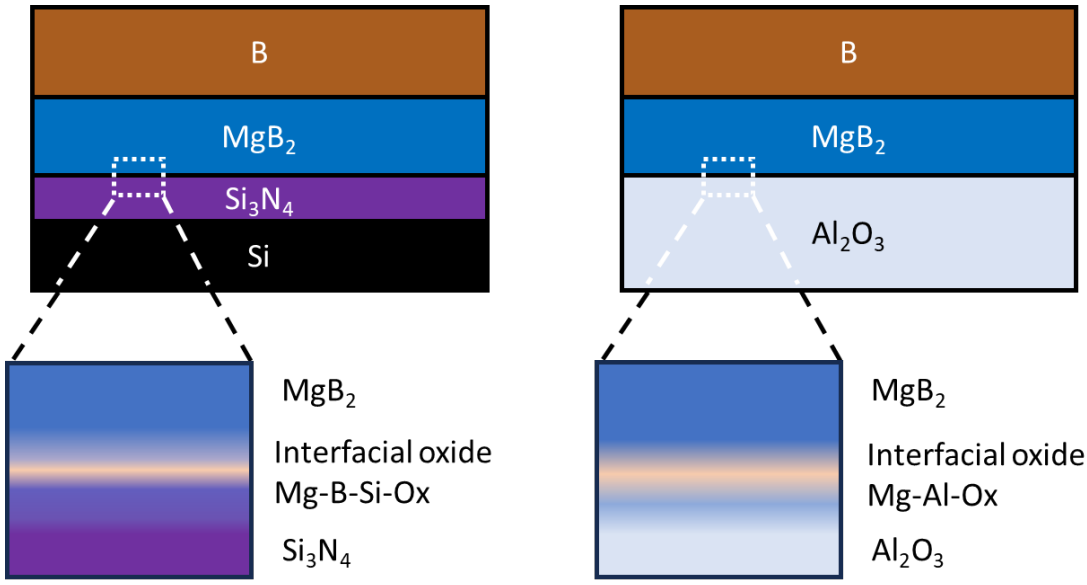

Figure 2.3.12. Schematic of B-capped MgB_2 films on Si_3N_4 and sapphire substrates. Both substrates have an interfacial oxide at the MgB_2/substrate interface, but the identity of the oxide is different for the different substrates. Additionally, some MgB_2 is observed to diffuse into the substrate, with more diffusion observed in the annealed samples.

References

(1) Baer, D. R.; Artyushkova, K.; Richard Brundle, C.; Castle, J. E.; Engelhard, M. H.; Gaskell, K. J.; Grant, J. T.; Haasch, R. T.; Linford, M. R.; Powell, C. J.; Shard, A. G.; Sherwood, P. M. A.; Smentkowski, V. S. Practical Guides for X-Ray Photoelectron Spectroscopy: First Steps in Planning, Conducting, and Reporting XPS Measurements. *Journal of Vacuum Science & Technology A* **2019**, *37* (3), 031401. https://doi.org/10.1116/1.5065501.

(2) Briggs, D. Handbook of X-Ray Photoelectron Spectroscopy C. D. Wanger, W. M. Riggs, L. E. Davis, J. F. Moulder and G.E. Muilenberg Perkin-Elmer Corp., Physical Electronics Division, Eden Prairie, Minnesota, USA, 1979. 190 Pp. $195. *Surf. Interface Anal.* **1981**, *3* (4), v–v. https://doi.org/10.1002/sia.740030412.

(3) Castle, J. E. Practical Surface Analysis by Auger and X-Ray Photoelectron Spectroscopy. D. Briggs and M. P. Seah (Editors). John Wiley and Sons Ltd, Chichester, 1983, 533 Pp., £44.50. *Surface and Interface Analysis* **1984**, *6* (6), 302–302. https://doi.org/10.1002/sia.740060611.

(4) Gengenbach, T. R.; Major, G. H.; Linford, M. R.; Easton, C. D. Practical Guides for X-Ray Photoelectron Spectroscopy (XPS): Interpreting the Carbon 1s Spectrum. *Journal of Vacuum Science & Technology A* **2021**, *39* (1), 013204. https://doi.org/10.1116/6.0000682.

(5) Seah, M. P.; Dench, W. A. Quantitative Electron Spectroscopy of Surfaces: A Standard Data Base for Electron Inelastic Mean Free Paths in Solids.

Surface and Interface Analysis **1979**, *1* (1), 2–11. https://doi.org/10.1002/sia.740010103.

(6) Powell, C. J. Practical Guide for Inelastic Mean Free Paths, Effective Attenuation Lengths, Mean Escape Depths, and Information Depths in X-Ray Photoelectron Spectroscopy Information. *NIST* **2020**, *38* (2).

(7) Axnanda, S.; Crumlin, E. J.; Mao, B.; Rani, S.; Chang, R.; Karlsson, P. G.; Edwards, M. O. M.; Lundqvist, M.; Moberg, R.; Ross, P.; Hussain, Z.; Liu, Z. Using "Tender" X-Ray Ambient Pressure X-Ray Photoelectron Spectroscopy as A Direct Probe of Solid-Liquid Interface. *Sci Rep* **2015**, *5* (1), 9788. https://doi.org/10.1038/srep09788.

(8) Engelhard, M. H.; Baer, D. R.; Herrera-Gomez, A.; Sherwood, P. M. A. Introductory Guide to Backgrounds in XPS Spectra and Their Impact on Determining Peak Intensities. *Journal of Vacuum Science & Technology A* **2020**, *38* (6), 063203. https://doi.org/10.1116/6.0000359.

(9) Cros, A. Charging Effects in X-Ray Photoelectron Spectroscopy. *Journal of Electron Spectroscopy and Related Phenomena* **1992**, *59* (1), 1–14. https://doi.org/10.1016/0368-2048(92)85008-U.

(10) Lizarbe, A. J.; Major, G. H.; Fernandez, V.; Fairley, N.; Linford, M. R. Insight Note: X-Ray Photoelectron Spectroscopy (XPS) Peak Fitting of the Al 2p Peak from Electrically Isolated Aluminum Foil with an Oxide Layer. *Surface and Interface Analysis* **2023**, *55* (9), 651–657. https://doi.org/10.1002/sia.7238.

(11) Biesinger, M. C. Accessing the Robustness of Adventitious Carbon for Charge Referencing (Correction) Purposes in XPS Analysis: Insights from a Multi-User Facility Data Review. *Applied Surface Science* **2022**, *597*, 153681. https://doi.org/10.1016/j.apsusc.2022.153681.

(12) Baer, D. R.; Artyushkova, K.; Cohen, H.; Easton, C. D.; Engelhard, M.; Gengenbach, T. R.; Greczynski, G.; Mack, P.; Morgan, D. J.; Roberts, A. XPS Guide: Charge Neutralization and Binding Energy Referencing for Insulating Samples. *Journal of Vacuum Science & Technology A* **2020**, *38* (3), 031204. https://doi.org/10.1116/6.0000057.

(13) Easton, C. D.; Kinnear, C.; McArthur, S. L.; Gengenbach, T. R. Practical Guides for X-Ray Photoelectron Spectroscopy: Analysis of Polymers. *Journal of Vacuum Science & Technology A* **2020**, *38* (2), 023207. https://doi.org/10.1116/1.5140587.

(14) Gupta, R. P.; Sen, S. K. Calculation of Multiplet Structure of Core p - Vacancy Levels. *Phys. Rev. B* **1974**, *10* (1), 71–77. https://doi.org/10.1103/PhysRevB.10.71.

(15) Gupta, R. P.; Sen, S. K. Calculation of Multiplet Structure of Core p - Vacancy Levels. II. *Phys. Rev. B* **1975**, *12* (1), 15–19. https://doi.org/10.1103/PhysRevB.12.15.

(16) Hermsmeier, B. D.; Fadley, C. S.; Sinkovic, B.; Krause, M. O.; Jimenez-Mier, J.; Gerard, P.; Carlson, T. A.; Manson, S. T.; Bhattacharya, S. K. Energy

Dependence of the Outer Core-Level Multiplet Structures in Atomic Mn and Mn-Containing Compounds. *Phys. Rev. B* **1993**, *48* (17), 12425–12437. https://doi.org/10.1103/PhysRevB.48.12425.

(17) Nelson, A. J.; Reynolds, J. G.; Roos, J. W. Core-Level Satellites and Outer Core-Level Multiplet Splitting in Mn Model Compounds. *Journal of Vacuum Science & Technology A: Vacuum, Surfaces, and Films* **2000**, *18* (4), 1072–1076. https://doi.org/10.1116/1.582302.

(18) Koskela, K. M.; Mora Perez, C.; Eremin, D. B.; Evans, J. M.; Strumolo, M. J.; Lewis, N. S.; Prezhdo, O. V.; Brutchey, R. L. Polymorphic Control of Solution-Processed Cu2SnS3 Films with Thiol–Amine Ink Formulation. *Chem. Mater.* **2022**, *34* (19), 8654–8663. https://doi.org/10.1021/acs.chemmater.2c01612.

(19) Shard, A. G. Practical Guides for X-Ray Photoelectron Spectroscopy: Quantitative XPS. *Journal of Vacuum Science & Technology A* **2020**, *38* (4), 041201. https://doi.org/10.1116/1.5141395.

(20) Powell, C. X-Ray Photoelectron Spectroscopy Database XPS, Version 4.1, NIST Standard Reference Database 20, 1989. https://doi.org/10.18434/T4T88K.

(21) Fantauzzi, M.; Elsener, B.; Atzei, D.; Rigoldi, A.; Rossi, A. Exploiting XPS for the Identification of Sulfides and Polysulfides. *RSC Adv.* **2015**, *5* (93), 75953–75963. https://doi.org/10.1039/C5RA14915K.

(22) Smart, R. St. C.; Skinner, W. M.; Gerson, A. R. XPS of Sulphide Mineral Surfaces: Metal-Deficient, Polysulphides, Defects and Elemental Sulphur. *Surface*

and Interface Analysis **1999**, *28* (1), 101–105. https://doi.org/10.1002/(SICI)1096-9918(199908)28:1<101::AID-SIA627>3.0.CO;2-0.

(23) Pratt, A. R.; Muir, I. J.; Nesbitt, H. W. X-Ray Photoelectron and Auger Electron Spectroscopic Studies of Pyrrhotite and Mechanism of Air Oxidation. *Geochimica et Cosmochimica Acta* **1994**, *58* (2), 827–841. https://doi.org/10.1016/0016-7037(94)90508-8.

(24) Major, G. H.; Avval, T. G.; Moeini, B.; Pinto, G.; Shah, D.; Jain, V.; Carver, V.; Skinner, W.; Gengenbach, T. R.; Easton, C. D.; Herrera-Gomez, A.; Nunney, T. S.; Baer, D. R.; Linford, M. R. Assessment of the Frequency and Nature of Erroneous X-Ray Photoelectron Spectroscopy Analyses in the Scientific Literature. *Journal of Vacuum Science & Technology A* **2020**, *38* (6), 061204. https://doi.org/10.1116/6.0000685.

(25) Baer, D. R.; Gilmore, I. S. Responding to the Growing Issue of Research Reproducibility. *Journal of Vacuum Science & Technology A* **2018**, *36* (6), 068502. https://doi.org/10.1116/1.5049141.

(26) Biesinger, M. C.; Payne, B. P.; Grosvenor, A. P.; Lau, L. W. M.; Gerson, A. R.; Smart, R. St. C. Resolving Surface Chemical States in XPS Analysis of First Row Transition Metals, Oxides and Hydroxides: Cr, Mn, Fe, Co and Ni. *Applied Surface Science* **2011**, *257* (7), 2717–2730. https://doi.org/10.1016/j.apsusc.2010.10.051.

(27) Biesinger, M. C.; Lau, L. W. M.; Gerson, A. R.; Smart, R. St. C. Resolving Surface Chemical States in XPS Analysis of First Row Transition Metals, Oxides and Hydroxides: Sc, Ti, V, Cu and Zn. *Applied Surface Science* **2010**, *257* (3), 887–898. https://doi.org/10.1016/j.apsusc.2010.07.086.

(28) Biesinger, M. C. Advanced Analysis of Copper X-Ray Photoelectron Spectra. *Surface and Interface Analysis* **2017**, *49* (13), 1325–1334. https://doi.org/10.1002/sia.6239.

(29) Moretti, G. Auger Parameter and Wagner Plot in the Characterization of Chemical States by X-Ray Photoelectron Spectroscopy: A Review. *Journal of Electron Spectroscopy and Related Phenomena* **1998**, *95* (2), 95–144. https://doi.org/10.1016/S0368-2048(98)00249-7.

(30) Matthew, J. Surface Analysis by Auger and X-Ray Photoelectron Spectroscopy. D. Briggs and J. T. Grant (Eds.). IM Publications, Chichester, UK and SurfaceSpectra, Manchester, UK, 2003. 900 Pp., ISBN 1-901019-04-7, 900 Pp. *Surface and Interface Analysis* **2004**, *36* (13), 1647–1647. https://doi.org/10.1002/sia.2005.

(31) Karathanasis, A. D.; Hajek, B. F. Elemental Analysis by X-Ray Fluorescence Spectroscopy. In *Methods of Soil Analysis*; John Wiley & Sons, Ltd, 1996; pp. 161–223. https://doi.org/10.2136/sssabookser5.3.c7.

(32) Garbassi, F. XPS and AES Study of Antimony Oxides. *Surf. Interface Anal.* **1980**, *2* (5), 165–169. https://doi.org/10.1002/sia.740020502.

(33) Kim, C.; Bell, C.; Evans, J.; Greenfield, J.; Batson, E.; Berggren, K.; Lewis, N.; Cunnane, D. Wafer-Scale MgB2 Superconducting Devices. arXiv December 21, 2023. https://doi.org/10.48550/arXiv.2305.15190.

(34) Kang, W. N.; Kim, H.-J.; Choi, E.-M.; Jung, C. U.; Lee, S.-I. MgB2 Superconducting Thin Films with a Transition Temperature of 39 Kelvin. *Science* **2001**, *292* (5521), 1521–1523. https://doi.org/10.1126/science.1060822.

(35) Liu, Z.-K.; Schlom, D. G.; Li, Q.; Xi, X. X. Thermodynamics of the Mg–B System: Implications for the Deposition of MgB2 Thin Films. *Applied Physics Letters* **2001**, *78* (23), 3678–3680. https://doi.org/10.1063/1.1376145.

(36) Naito, M.; Ueda, K. MgB2 Thin Films for Superconducting Electronics. *Supercond. Sci. Technol.* **2004**, *17* (7), R1. https://doi.org/10.1088/0953-2048/17/7/R01.

(37) Shimakage, H.; Miki, S.; Tsujimoto, K.; Wang, Z.; Ishida, T.; Tonouchi, M. Characteristics of As-Grown MgB/Sub 2/ Thin Films Made by Sputtering. *IEEE Transactions on Applied Superconductivity* **2005**, *15* (2), 3269–3272. https://doi.org/10.1109/TASC.2005.848849.

(38) Balducci, G.; Brutti, S.; Ciccioli, A.; Gigli, G.; Manfrinetti, P.; Palenzona, A.; Butman, M. F.; Kudin, L. Thermodynamics of the Intermediate Phases in the Mg–B System. *Journal of Physics and Chemistry of Solids* **2005**, *66* (2), 292–297. https://doi.org/10.1016/j.jpcs.2004.06.063.

(39) Bouvier, Y. Use of an Auger Parameter for Characterizing the Mg Chemical State in Different Materials. *Surface and Coatings Technology* **2004**, *180–181*, 169–173. https://doi.org/10.1016/j.surfcoat.2003.10.062.

Chapter 3

Spectroscopic Investigation of the Stability of Manganese Antimonate Oxygen Evolution Catalysts

3.1—Analysis of $Mn_ySb_{1-y}O_x$ surface chemistry for decoupled water splitting

Electrochemical cells typically have two half reactions that occur simultaneously but are separated in space.[1] The cathode performs a reduction reaction while the anode performs an oxidation which must produce as many electrons as the cathode consumes.[1] Thus, the maximum current—and therefore reaction rate—in an electrochemical system is limited by the slowest reaction.[1] This is why counter electrodes are often much larger in surface area than the working electrode; the increased surface area ensures that the reaction rate is always limited by the working electrode.

This property is critical to consider when developing fuel-forming electrolyzers. The fuel (e.g., H_2 (g)) is usually generated at the cathode while the anode tries to balance the flow of electrons.[2–6] The oxygen evolution reaction (OER) is a common anodic half reaction in aqueous electrolyzers but suffers from slow kinetics.[7–9] Additionally, the catalysts with the lowest overpotential for OER are precious metal oxides such as IrO_x and RuO_x which are among the rarest elements in the Earth's crust and are unstable in acidic conditions.[5,7–9] These challenges have driven interest in the development of stable, Earth-abundant alternative catalysts for OER, specifically in acidic conditions.[5,8–11] One such

catalyst family is the $Mn_ySb_{1-y}O_x$ system.[12–15] This catalyst combines an active OER catalyst with poor stability in acid, MnO_x, with a poor catalyst with excellent stability in acid, SbO_x, to produce a material with intermediate properties.[12–15] Of interest is how this material achieves this blend of properties and how the surface chemistry changes as a result of electrolysis.[14,15] To this end, XPS of the $Mn_ySb_{1-y}O_x$ catalyst family was carried out for a variety of electrochemical systems and synthetic methods.

One application of $Mn_ySb_{1-y}O_x$ is use in a decoupled electrolysis system.[14] Unlike a traditional electrochemical cell which requires both the oxidation and reduction reactions to occur simultaneously, but spatially separated, decoupled electrolysis allows each half reaction to be separated temporally.[16] Electrons are "stored" in a redox mediator which is consumed during one of the reaction processes. The mediator is then regenerated by the opposite reaction process, which can occur in a separate reaction chamber and at a later time.[16] In this way, large increases in efficiency can be achieved as the anodic and cathodic reaction rates are no longer dependent on one another.[16] Powdered $Mn_ySb_{1-y}O_x$ was investigated for use in this decoupled system using a $Ce^{3+/4+}$ redox mediator for stable, Earth-abundant, decoupled OER in acidic conditions.[14] A key aspect of this study was the effect of catalyst stoichiometry on reaction rate and turnover frequency. By increasing Mn content, an increase in reaction rate and turnover number was generally observed, though above a Mn:Sb ratio of 6:4, the reaction rate and turnover frequency decrease (Figure 3.1.1).[14] This decline in activity and stability replicates a similar observation for planar $Mn_ySb_{1-y}O_x$ catalysts and points towards a change in the surface chemistry.[12,14] XPS was

therefore used to examine how the surface chemistry changes with stoichiometry to assist in drawing conclusions about the mechanism of stabilization.

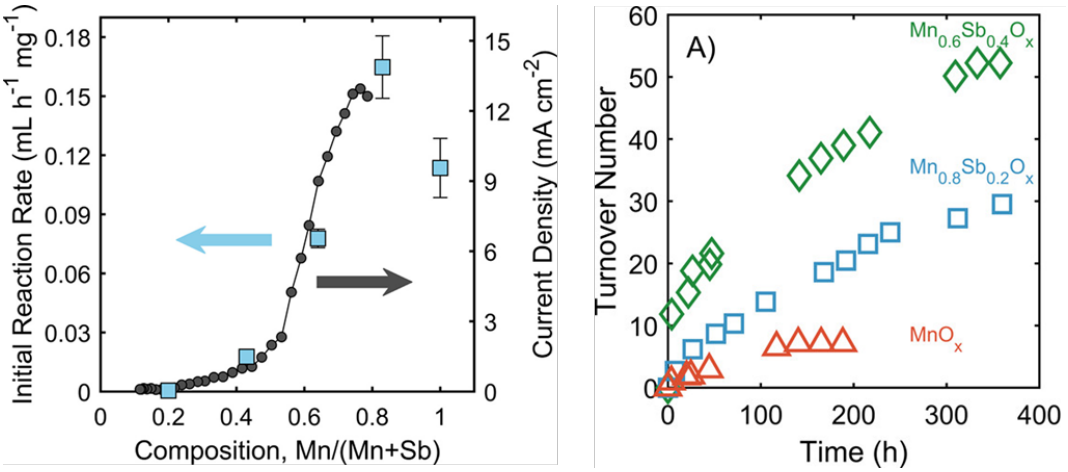

Figure 3.1.1. (a) Reaction rate and faradaic current density as a function of Mn:Sb ratio in acidic (1.0 M H_2SO_4) conditions. It can be seen that catalytic activity generally increases with increasing Mn content until pure MnO_x is used. (b) Turnover number for $Mn_ySb_{1-y}O_x$ with various stoichiometries as a function of time, where it can be seen that the Mn:Sb ratio of 6:4 has the highest turnover number and thus the highest stability. Figures reproduced with permission from reference.[14]

Analysis of the $Mn_ySb_{1-y}O_x$ XP spectrum is complicated by a variety of factors. Mn has a variety of stable oxidation states including Mn (II), Mn (III), and Mn (IV) which can coexist in the same sample.[17,18] Additionally, the Mn 2p peaks exhibit significant multiplet splitting, wherein a number of similar final spin states are possible after photoionization depending on the configuration of d-orbital electrons and core electrons.[17–20] This multiplet splitting causes the peaks to broaden, and little to no observed change in Mn 2p peak BE with oxidation state.[17,18,21] Instead, the Mn 2p peaks change shape with oxidation state (and a shake-up peak appears for Mn (II)), but with multiple possible states and overlapping peaks, this becomes challenging to rigorously fit.[17,18] To address this, peak models from

high-quality, pure oxide standards are used, where three "packets" of peaks are simultaneously fit to the same data.[17] While this method allows an estimation of average oxidation state and oxidation state composition, it runs the risk of over-fitting the spectrum and producing erroneous or unreliable results. For more rigorously assigning oxidation state, two other spectra should be taken for Mn: the Mn 3p and Mn 3s spectra.[17,18,21–24] The Mn 3p spectrum is generally straightforward to analyze, where the BE of the peak maximum correlates linearly with oxidation state in pure oxides.[17,18,21,23] Unlike most s-orbitals, the Mn 3s spectrum will contain a doublet, but this is caused by multiplet splitting rather than spin-orbit coupling.[17,18,22–24] Two spin states are possible after Mn 3s photoionization: ^{7}S and ^{5}S.[22–24] This causes two distinct peaks depending on which final state occurs. The splitting of these peaks has been shown to be roughly linearly dependent on oxidation state in pure Mn oxides (Figure 3.1.2).[22–25] By combining three spectra for the same element, more reliable conclusions can be drawn regarding the oxidation state of Mn in $Mn_ySb_{1-y}O_x$ (Figure 3.1.2).[17,18,21,22]

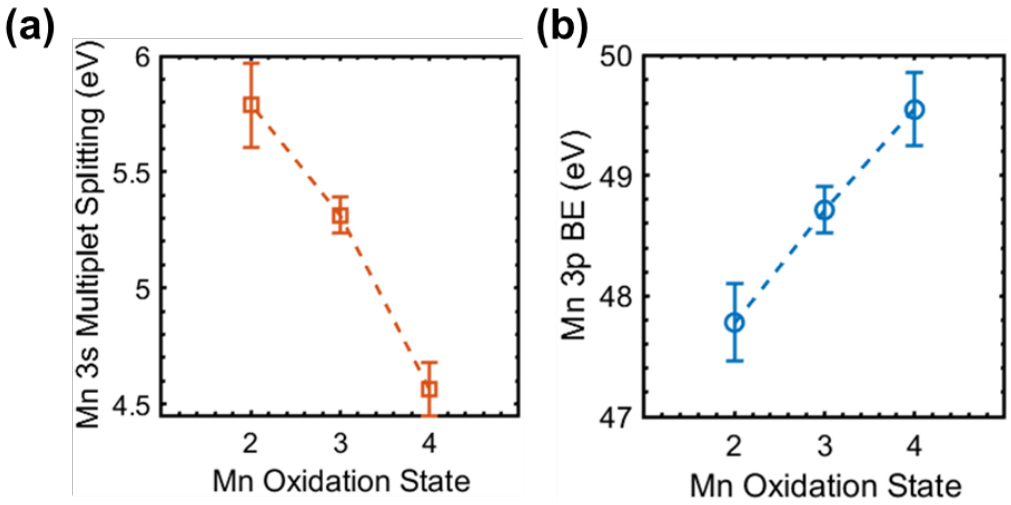

Figure 3.1.2. Relationship between (a) Mn 3s ^{7}S-^{5}S multiplet splitting and (b) Mn 3p BE and Mn oxidation state in pure Mn oxides. Error bars represent standard deviation in measurements sourced from literature.[17,18,21,22,25–27]

Sb also presents a challenge for XPS due to overlapping of the Sb $3d_{5/2}$ peak and O 1s.[28,29] Because of this, BE of the Sb $3d_{5/2}$ peak will not be a reliable indicator of Sb chemistry nor relative atomic abundance. Similarly to Mn, Sb has two common oxidation states which can also coexist on the same sample: Sb (III) and Sb (V) with a less common Sb (IV) oxidation state reported as well.[25,29] To accurately fit the Sb 3d spectrum, the physics of spin-orbit splitting can be leveraged. The peak splitting of Sb $3d_{5/2}$ and $3d_{3/2}$ is invariant with oxidation state and the relative ratio of peak area will always be 3:2.[28,30,31] Therefore, the Sb $3d_{3/2}$ peak, which does not overlap with O 1s, can be fit and then the resulting $3d_{5/2}$ peaks can be calculated. Any remaining signal at a BE of ~530 eV can then be assumed to be from O 1s.

By fitting the spectra of Mn and Sb as described above, the oxidation state and relative abundance of oxidation states for both elements as a function of catalyst stoichiometry can be estimated. Examination of the Mn 2p spectra showed that Mn (III) was the dominant oxidation state predicted by the peak model in all cases, but at lower Mn concentrations, Mn (II) became more abundant, evidenced most obviously by the presence of a shake-up peak (Figure 3.1.3). This observation is consistent with prior observations of multiple Mn oxidation states existing in a single catalyst.[32–34] In the case of Mn:Sb of 4:6, a significant quantity of Mn (IV) is predicted by the peak model due to reproducibly higher BE signal that is not present in the other spectra.

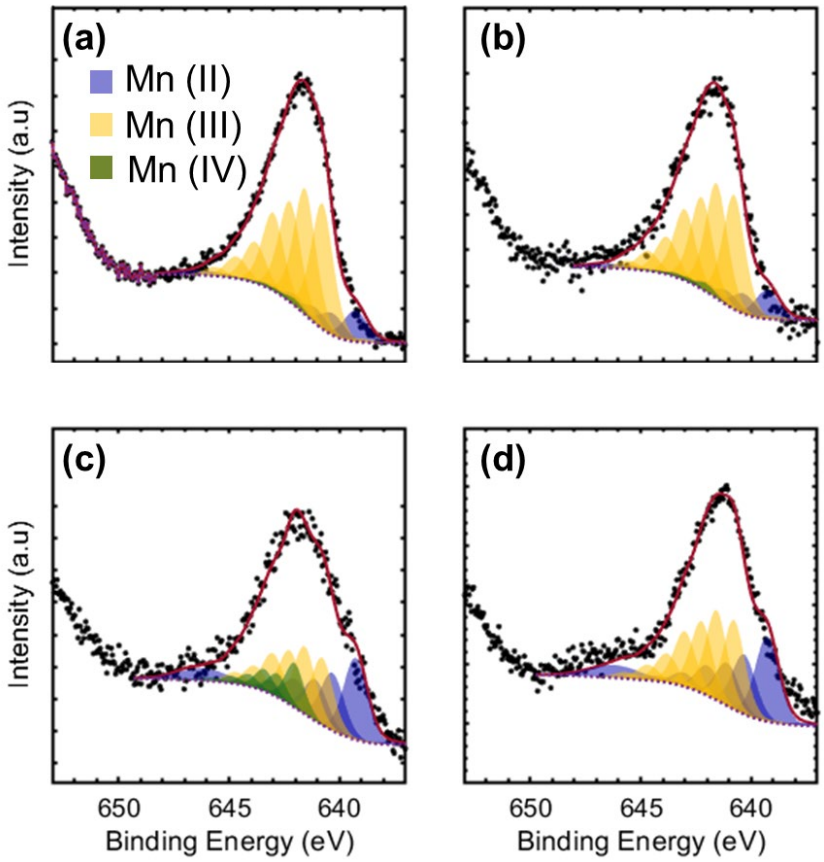

Figure 3.1.3. Mn $2p_{3/2}$ for powdered $Mn_ySb_{1-y}O_x$ where (a) y = 0.8, (b) y = 0.6, (c) y = 0.4, and (d) y = 0.2. Peaks are fit using pure oxide standard models. Raw data is black dots and fit envelope is a solid red line.

By quantifying the fraction of each oxidation state that contributes to the overall signal, an average oxidation state can be calculated, summarized in Table 3.1.1. As the Mn content in the catalyst increases, it can be seen that the average oxidation state generally increases as well, until stabilizing at a value of 2.9 above a 6:4 Mn:Sb fraction. It is also generally true that in the case of the material studied, the fraction of the signal predicted to originate from

Mn (IV) is low, except in the case of 4:6 Mn:Sb. Mn (II) is the largest secondary state of Mn observed in all cases.

Table 3.1.1. Quantification of Relative Abundance of Mn Oxidation States in $Mn_ySb_{1-y}O_x$ via Mn 2p XP Spectra as a Function of Stoichiometry

Mn Content	*Mn 2 %*	*Mn 3%*	*Mn 4%*	*Effective Ox State*
0.2	44%	56%	0%	2.56
0.4	42%	42%	16%	2.73
0.6	17%	80%	3%	2.86
0.8	17%	81%	2%	2.86

To verify the methodology of fitting peak models derived from pure oxides and calculating an average oxidation state, UV-Vis spectroscopy measurements were done on powder samples and, using a Kubelka–Munk transform, the average oxidation state was predicted based on pure oxide standards (Figure 3.1.4). While the surface oxidation state may not be expected to be identical to the bulk state measured by UV-Vis, if radically different oxidation states or trends were observed the methodology for fitting the data could be called into question. The results indicate a nearly identical trend of Mn oxidation state increasing and then stabilizing as Mn concentration increases in both XPS and UV-Vis measurements. While the values calculated are not identical, both measurements agree on a maximum oxidation state of approximately three and a minimum oxidation state of

approximately 2.6. This agreement in trend and rough agreement in magnitude supports the conclusion from XPS that Mn oxidation state increases with Mn concentration.

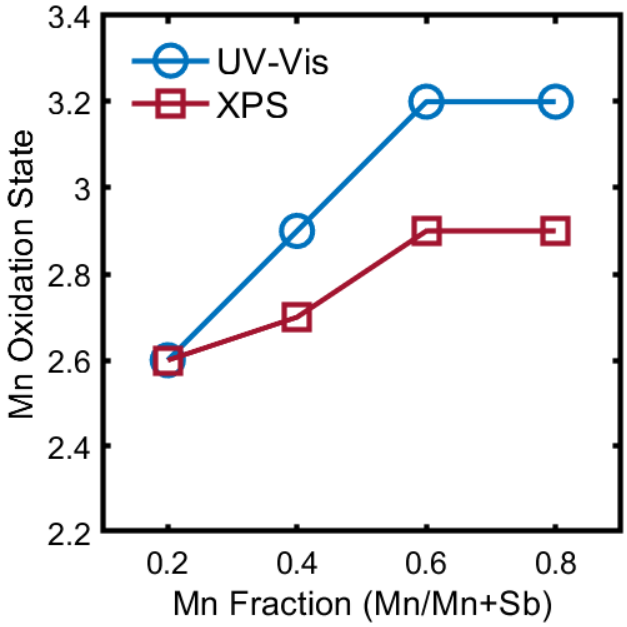

Figure 3.1.4. Average Mn oxidation state in $Mn_ySb_{1-y}O_x$ as a function of stoichiometry as quantified by Mn 2p XP spectra fitting and Kubelka–Munk transform in UV-Vis spectroscopy.

As discussed previously, while the agreement between Mn 2p XPS and bulk UV-Vis measurements does support the validity of the model fitting approach, additional information can be gained by collecting the Mn 3p and Mn 3s spectra. The results of these experiments are summarized in Figure 3.1.5. The same trend of increasing oxidation state followed by stabilization is found in both Mn 3p and Mn 3s, though the 3s trend does not flatten completely. The reproducibility of the trend across spectroscopic techniques and orbitals of interest further supports the conclusion that increasing Mn content increases the

observed Mn oxidation state until approximately a ratio of 6:4 Mn:Sb, at which point the oxidation state stabilizes. However, looking at the magnitude of the predicted oxidation state by these spectra, the Mn 3p BE indicates a minimum oxidation state of 2.0 and maximum of 2.7 while the Mn 3s multiplet splitting indicates a range of 1.6 to 2.4. The magnitude of these oxidation states is substantially different both from each other and the Mn 2p and UV/Vis data. This is hypothesized to be caused by limitations in comparing a binary oxide to a pure Mn oxide coupled with the relative energetic positions of the 3p and 3s orbitals. The identity of the atom bound to Mn has been shown to have an impact on the Mn 3s multiplet splitting and as a shallower orbital relative to Mn 2p, the 3p and 3s orbitals are hypothesized to be more sensitive to bonding environment than the deeper 2p orbital. Thus, it is hypothesized that the presence of Sb in the lattice modulates the strength of the bonds formed by Mn such that more electron density is preserved on Mn atoms in the $Mn_ySb_{1-y}O_x$ system, resulting in erroneously low modeled oxidation states. This hypothesis would allow, however, the trend of increasing oxidation state to be conserved, but the absolute magnitude calculated is lower than its true value. By combining these observations, it can be concluded that increasing Mn content in $Mn_ySb_{1-y}O_x$ causes an increase in Mn oxidation state from a value of roughly 2.6 to approximately 3.0, where Mn (III) is the dominant oxidation state at the surface and Mn (II) is the secondary state present. This correlates with the observations that catalyst activity increases as Mn content increases up to a Mn:Sb ratio of 8:2, where Mn (III) is reported to be the most active state

for OER. However, once Mn content gets too high, the ability of Sb to stabilize the material decreases, causing a lower turnover number.

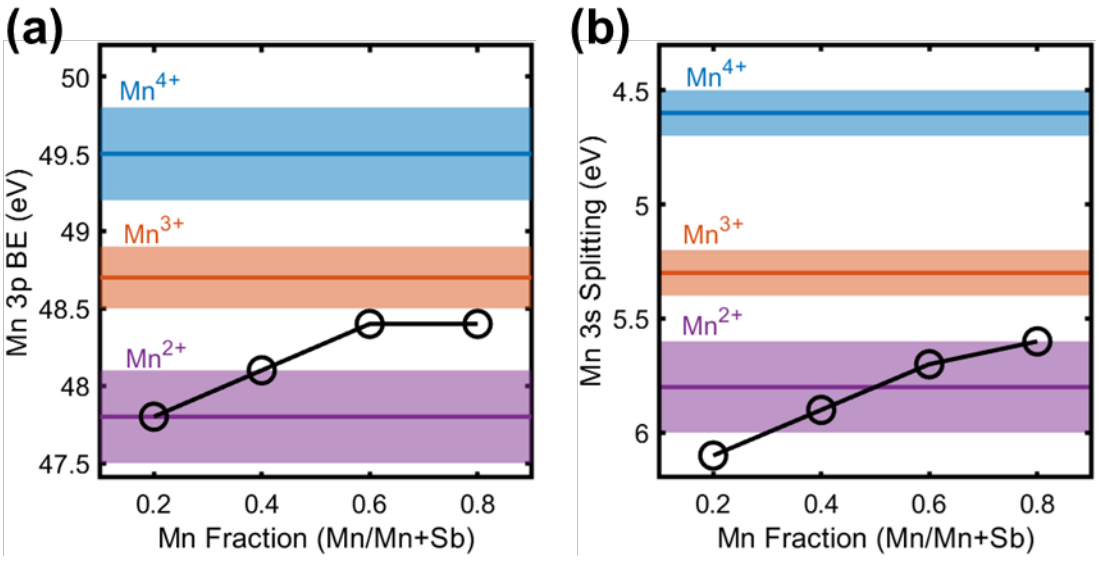

Figure 3.1.5. Mn oxidation state in $Mn_ySb_{1-y}O_x$ as a function of stoichiometry as quantified by (a) Mn 3p BE and (b) Mn 3s multiplet splitting.

The change in Sb oxidation state was assessed via analysis of the Sb 3d spectrum (Figure 3.1.6). As mentioned previously, the Sb $3d_{5/2}$ and O 1s peaks overlap with one another at ~530 eV. These can be deconvoluted by fitting of the Sb $3d_{3/2}$ peak, which does not overlap. In the collected spectra, it was noticed that the Sb $3d_{3/2}$ peak had a noticeable shoulder in several cases, pointing to the presence of two oxide species simultaneously. To account for this possibility, two sets of Sb 3d doublets were applied to the spectrum in all cases, where the BE was restricted to previously reported ranges for Sb (III) and Sb (V) but peak area and FWHM was allowed to vary. A large portion of the signal at ~529–535 eV

was found to be from O 1s, where the largest component was at ~533 eV and a smaller O 1s peak was fit at ~530 eV. A peak at approximately 530 eV is common for many metal oxides, while a higher BE peak is likely due to a hydroxide moiety on the surface. This hypothesis may explain why the higher BE peak was larger in area, because the surface area of a powder is large relative to the volume and therefore if a hydroxide forms at the surface, the relative quantity of hydroxide in the XP spectrum would be expected to be larger.

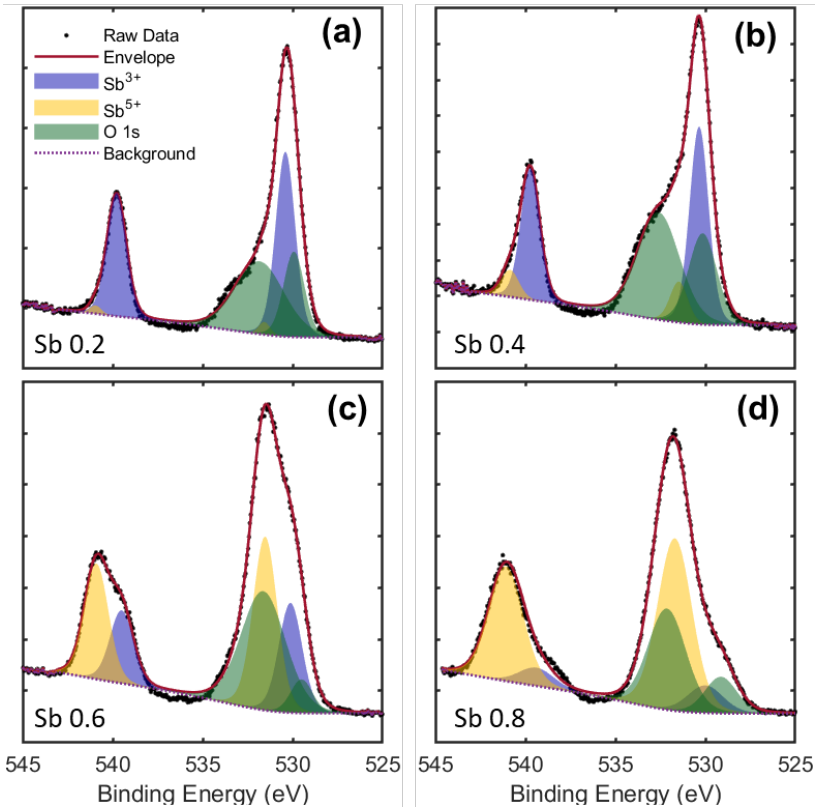

Figure 3.1.6. Sb 3d XP spectra in $Mn_ySb_{1-y}O_x$ where (a) y = 0.8, (b) y = 0.6, (c) y = 0.4, and (d) y = 0.2.

Quantifying the concentration of Sb (III) and Sb (V) and plotting as a function of Mn concentration, the oxidation state of Sb correlates negatively with Mn concentration (Figure 3.1.7). At a Mn:Sb ratio of 2:8, the spectrum is well fit by a model with primarily Sb (V) character, though a shoulder corresponding to Sb (III) is still observed. As Mn concentration is increased, the fraction of the Sb signal corresponding to Sb (V) decreases almost linearly, replaced by Sb (III). Stability in the $Mn_ySb_{1-y}O_x$ system has previously been attributed to the presence of Sb (V), so the decrease in stability observed in this system as Mn content increases beyond a Mn:Sb ratio of 6:4 is hypothesized to be related to the presence of Sb (III) instead of Sb (V).

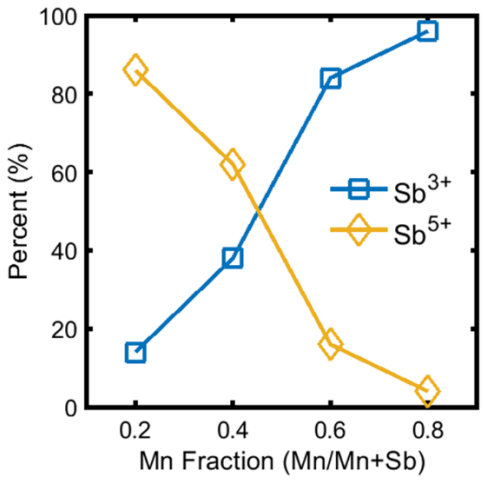

Figure 3.1.7. Quantification of Sb (III) and Sb (V) relative abundance as a function of MnSb oxide stoichiometry. At high Mn content, Sb (III) is the dominant oxidation state while at low Mn concentration Sb (V) is the dominant state.

By analyzing the surface chemistry of a powdered $Mn_ySb_{1-y}O_x$ catalyst and comparing to catalytic activity, conclusions can be drawn about the relationship between catalytic properties and surface oxidation state. The concentration of Mn (III) increases as

Mn content increases, eventually causing a plateau of the average oxidation state at approximately 3.0. As Mn (III) has been previously reported to be the most active and stable of the Mn oxidation states towards OER, the increases in catalytic activity and stability up to a Mn:Sb ratio of 6:4 can be attributed to Mn (III). At higher Mn concentrations, the Mn oxidation state remains the same while turnover number (i.e., stability) decreases. This is hypothesized to be caused by Sb chemistry, where the Sb (V) state previously shown to stabilize OER catalysts almost disappears, replaced by Sb (III) which may be less stabilizing. Additionally, observations of the Mn 3p and 3s spectra indicate an increase in electron density on the Mn atoms, likely caused by a less polar Mn-O bond in the $Mn_ySb_{1-y}O_x$ system compared to a pure Mn oxide, which may be the mechanism by which Sb causes an increase in catalyst turnover number.

5.1.E—Experimental methods for Section 3.1

Readers are referred to Ifkovits et al. for detailed materials and experimental methods information for this section.[14]

3.2. Assessing the impact of electrolysis on $Mn_ySb_{1-y}O_x$ deposited via atomic-layer deposition

A similar XPS analysis was conducted for a $Mn_ySb_{1-y}O_x$ catalyst family deposited via atomic-layer deposition (ALD).[15] This process is scalable and can provide single-atomic-layer precision in catalyst thickness.[15] Of interest in this case was whether the ALD process generated the same material chemistry as other synthetic methods (e.g., powder

calcinization and sputtering) and how the surface chemistry changes as a result of electrolysis.[15] Analysis of Mn and Sb XP spectra was carried out as outlined in Chapter 3.1.

Analysis of the Mn 2p spectrum for $Mn_ySb_{1-y}O_x$ before electrolysis indicates a similar chemical state to previously synthesized $Mn_ySb_{1-y}O_x$ systems (Figure 3.2.1).[12–14] The ALD films had an approximate Mn:Sb ratio of 6:4, previously shown to be the most stable stoichiometric ratio.[12,14] From prior work, an average oxidation state of slightly below 3.0 is expected, where Mn (III) is the dominant oxidation state and Mn (II) is present in small amounts.[12–14] The resulting Mn 2p spectra were well fit by a peak model which was primarily Mn (III) and as expected, Mn (II) is the second-most abundant oxidation state predicted by the model, with no Mn (IV) detected. The average oxidation state predicted by the Mn 2p peak model was 2.9. To corroborate this evidence, Mn 3p spectra were also collected. Mn 3s spectra were collected as well, but low signal and interference from electrode materials made analysis unreliable. From the Mn 3p BE, an oxidation state of 2.8 was calculated, similar to that calculated from the Mn 2p data. Additionally, the Mn 3p data predicting a lower oxidation state than the Mn 2p data is consistent with observations for the $Mn_ySb_{1-y}O_x$ powders, supporting the hypothesis that the surface chemistry is consistent across synthetic methods. The Sb 3d spectrum before electrolysis is consistent with an assignment of Sb (III) as the primary oxidation state and an average oxidation state of 3.2. This is consistent with observations in the $Mn_ySb_{1-y}O_x$ powders where a Mn:Sb ratio of 6:4 produced a majority Sb (III) surface (Figure 3.1.7). Additionally, the O 1s spectrum

contains two components, one at a lower BE of approximately ~530 eV and another at ~533 eV (Figure 3.2.1). These are consistent with prior observations in the $Mn_ySb_{1-y}O_x$ powder system where the low-BE peak is attributed to a metal oxide and the higher BE peak is assigned as a hydroxide moiety on the surface. The hydroxide component is smaller than the oxide component in this spectrum, consistent with expectations of a lower surface-area-to-volume ratio for a thin film compared to a powder.

After the catalyst performed OER for 168 h, the surface chemistry was re-examined to determine how electrolysis affects the catalyst. Significant changes were observed for both Mn and Sb (Figure 3.2.1–3.2.2). In the Mn 2p spectrum, Mn (III) remains the largest component, but Mn (IV) is the second largest component after electrolysis, with 23% of the observed Mn signal attributable to Mn (IV) (Figure 3.2.2). The average oxidation state increases as a result, calculated to be 3.2 compared to the pre-electrolysis value of 2.9. The Mn 3p spectrum supports this conclusion, as the BE increases from 48.5 eV to 49.0, corresponding to oxidation states of 2.8 and 3.4, respectively. It has been observed that quasi-reversible redox wave appears in $Mn_ySb_{1-y}O_x$ over time at a potential negative of OER. This, in addition to observations reported in literature, leads to the hypothesis that Mn (IV) is generated at OER potentials and may contribute to the mechanism of OER in $Mn_ySb_{1-y}O_x$ materials. Thus, the presence of Mn (IV) after electrolysis may be due to imperfect catalytic cycles or a competing Mn (III)/(IV) redox reaction occurring at the surface during OER.

The Sb 3d spectrum also exhibits an oxidation, wherein the Sb (III) signal disappears completely and all Sb signal is attributable to Sb (V). Sb is expected to be electrochemically innocent in electrolysis, as Sb_2O_5 is a very poor OER catalyst. This oxidation cannot be explained by stoichiometry changes, as the Mn:Sb ratio changes only from 6:4 to 5:5 and prior observations indicate that a significant concentration of Sb (III) would still be present at that stoichiometry. It is hypothesized that Sb (III) is a metastable state in $Mn_ySb_{1-y}O_x$ and that applying an oxidative potential in an acidic, aqueous system leads to irreversible conversion of metastable Sb (III) to stable Sb (V). The O 1s spectrum also exhibits a change. The peak assigned to surface hydroxide increases in relative abundance compared to the surface oxide peak. This is hypothesized to be caused by the acidic, aqueous solution causing significant protonation of the surface during OER. Combined, these XP spectra support the conclusion that electrolysis causes irreversible oxidation of the $Mn_ySb_{1-y}O_x$ surface, both in Mn and Sb.

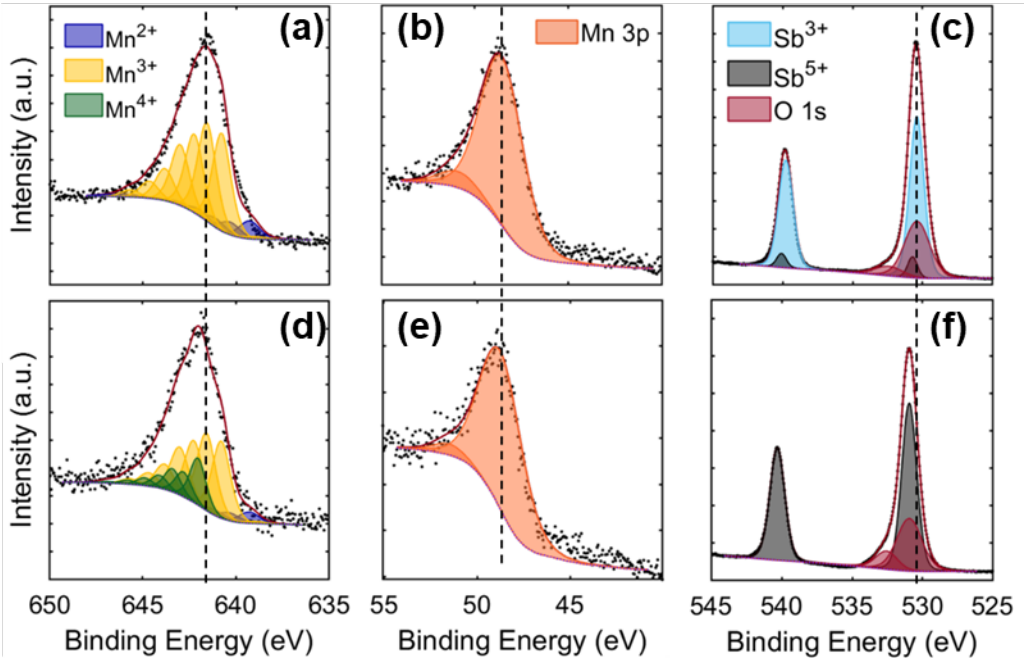

Figure 3.2.1. (a,d) Mn 2p, (b,e) Mn 3p, and (c,f) Sb 3d XP spectra for $Mn_ySb_{1-y}O_x$ synthesized via ALD where (a,b,c) are measurements before OER experiments and (d,e,f) are measurements after OER experiments.

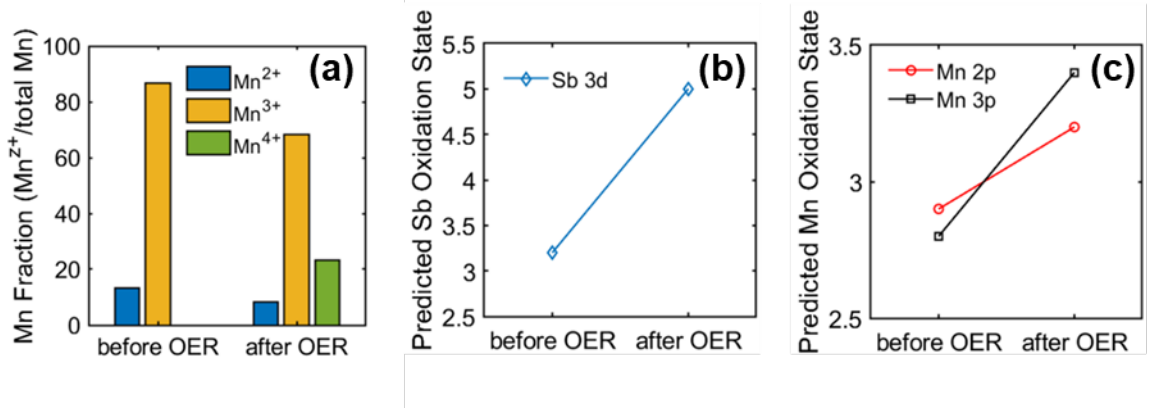

Figure 3.2.2. Quantification of (a) Mn oxidation state abundance as quantified by Mn 2p XP spectra fits, (b) Sb oxidation state as quantified by Sb 3d XP spectra fits, and (c) average Mn oxidation state as quantified by fits of Mn 2p and Mn 3p XP spectra all for ALD-deposited $Mn_ySb_{1-y}O_x$ films before and after OER experiments.

The impact of Sb on the Mn-O bond has been previously speculated on in Section 3.1 and in prior literature.[12,13,35] In other metal antimonates, Sb has been computationally and experimentally shown to cause a shortening of the metal-oxygen bond, while causing a lengthening of the Sb-O bond, relative to pure oxides.[36,37] To probe whether this effect is present in $Mn_ySb_{1-y}O_x$, the Sb MNN spectrum was collected. By constructing a Wagner plot and comparing to literature sources for pure oxides, the Sb MNN signal in $Mn_ySb_{1-y}O_x$ is shown to have a higher KE than would be expected for a pure oxide of similar oxidation state (Figure 3.2.3).[25,29] This indicates a destabilization in the valence Sb orbitals, as the corresponding Sb 3d core orbitals changes by less than 1 eV while the MNN KE is ~3 eV higher than would be expected for a pure Sb (V) oxide. This observation, combined with the previously noted anomalously low oxidation state predictions by Mn 3p and 3s supports the hypothesis that the presence of Sb in the lattice causes a destabilized Sb-O bond and a stabilized Mn-O bond, leading to more electron density on Mn and a destabilized Sb valence orbital relative to pure oxides. This effect is hypothesized to be the mechanism by which $Mn_ySb_{1-y}O_x$ exhibits a combination of activity and stability and the primary reason that Mn turnover number increases in this system relative to Mn oxides.

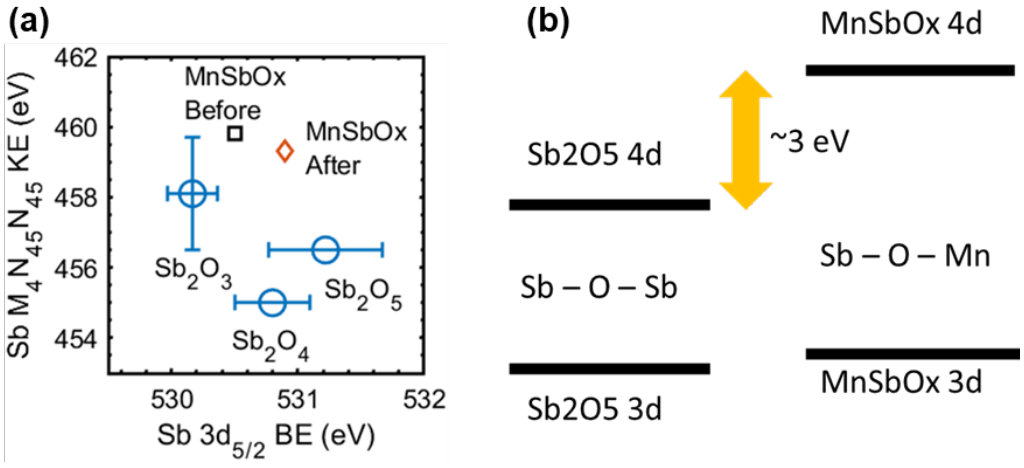

Figure 3.2.3. (a) Wagner plot of Sb oxides and $Mn_ySb_{1-y}O_x$ for identification of bonding character in Sb. Error bars represent standard deviation in measurements sourced from literature.[25,29,38]

5.2.E—Experimental methods for Section 3.2

Readers are referred to Dowling et al. for detailed materials and experimental methods information.[15]

3.3. Determining surface chemistry during active OER for $Mn_ySb_{1-y}O_x$ via ambient-pressure XPS

Traditional electrochemical fuel-forming processes involve a cathodic half reaction that produces the fuel (e.g., H_2(g) for H_2O electrolysis) and an anodic half reaction that produces a byproduct, most commonly O_2(g) in the case of aqueous systems.[2,7,39,40] The OER typically has slower kinetics than the hydrogen-evolution reaction (HER), so accelerating the OER is a significant challenge associated with electrochemical hydrogen production and/or CO_2 reduction.[7,8,10,11] Commercial proton-exchange membrane (PEM) electrolysis systems utilize IrO_x electrocatalysts that can drive the OER effectively at

current densities of 1–3 A cm^{-2} with modest (0.3–0.5 V) overpotentials and slow rates of catalyst dissolution.[11,41–43] However, Ir is a trace element in the crust of the Earth and is a secondary metal, so the supply of Ir may not be sufficient to support a global energy transition.[41,43]

Mn oxides can be used to drive the OER at overpotentials of 0.6–0.8 V at current densities of 10 mA -1000 mA cm^{-2} in aqueous acidic or alkaline conditions.[12,33,39,44,45] The oxidation state of Mn is a key factor in determining the activity and stability of the catalytic material, with Mn (III) having a low OER overpotential as well as a relatively slow corrosion rate in acidic aqueous solutions relative to other earth-abundant metal OER electrocatalysts.[33,39,44,46,47] Alloying additional elements with Mn to generate binary oxides can tune the resulting activity and stability of the electrocatalyst by manipulating the bond strengths within the catalyst material as well as between the catalyst surface and reactants and products.[12,14,46,48] In acidic conditions, the rest state for the $Mn_{1-y}Sb_yO_x$ OER catalyst at all Mn concentrations has an oxidation state of Mn(III).[12–14] As described previously in sections 3.1 and 3.2, Sb has been used to stabilize multiple metal centers, with experimental and theoretical data suggesting that Sb increases the hybridization between the metal d orbitals and the O 2p orbitals in the $Mn_{1-y}Sb_yO_x$ family of materials.[36,49]

In this work, XPS analysis was utilized to identify the surface state of $Mn_{1-y}Sb_yO_x$ under a variety of conditions to reveal the impact of variables such as surface wetting, electrolyte, and applied potential on the surface chemistry of this electrocatalyst. To obtain a sufficient electron mean-free path for signal detection, XPS typically utilizes UHV (< 10^{-8} Torr)

conditions. In contrast, ambient-pressure XPS (AP-XPS) enables direct investigation of the surface composition at near-ambient pressure (~16 Torr, the vapor pressure of water) by using a higher energy excitation source (4 keV vs. 1.4 keV) and a differential pumping system. In situ AP-XPS involves spectroscopic analysis through a thin (~30 nm) electrolyte meniscus, enabling direct observation of an electroactive surface while performing an electrochemical transformation.[50–52] A schematic of the AP-XPS experimental setup is available as Figure 3.3.1. Direct measurement of the surface composition of the catalyst while the OER is occurring can reveal differences between the reactive surface chemistry of the electrocatalyst during the OER and the rest state and can facilitate evaluating the proposed reaction mechanisms and stabilization hypothesis of this set of electrocatalytic materials.

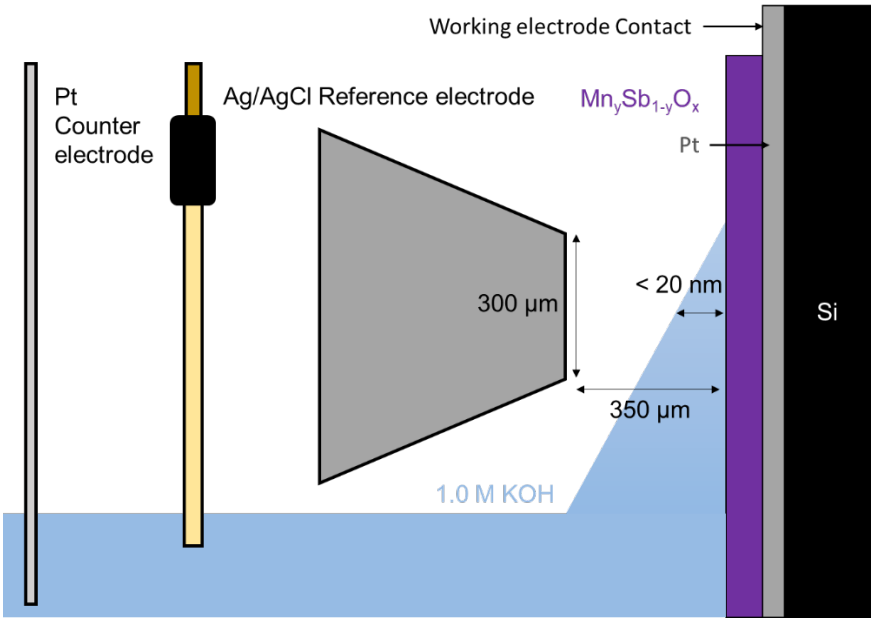

Figure 3.3.1. Schematic of AP-XPS experimental setup including a $Mn_ySb_{1-y}O_x$ sample on a Si support, electrolyte wicking, and a schematic of the sample cone.

To validate assumptions and compare observations to known literature trends, our XPS peak models and analysis methods were first performed on UHV XPS data from a thermally oxidized Mn standard as well as for $Mn_ySb_{1-y}O_x$ materials with three stoichiometries, y = 1.0, y = 0.7, and y = 0.4, as determined by energy dispersive X-ray spectroscopy (Figure 3.3.2).

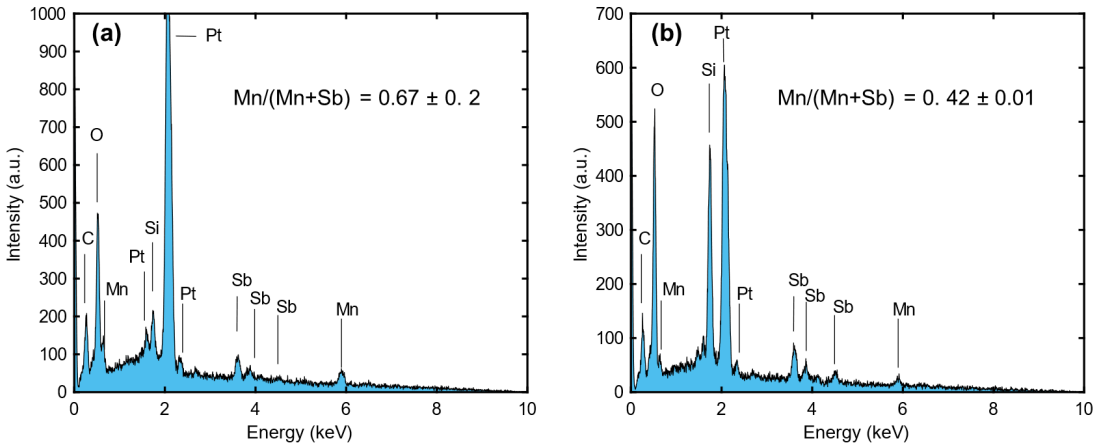

Figure 3.3.2. Energy dispersive X-ray spectroscopy (EDX) data for (a) $Mn_7Sb_3O_{18}$ and (b) $Mn_4Sb_6O_{21}$

Analysis of the O 1s XPS peak of the thermally oxidized y = 1.0 standard indicated a nearly pure phase of Mn_2O_3, with XPS emissions in agreement with literature values and fits for Mn (III) (Figure 3.3.3).[17,18,21,27] The O 1s spectrum of the Mn_2O_3 standard revealed two O species, assigned as Mn oxide (MnO_x) and Mn hydroxide ($Mn(OH)_x$) (Figure 3.3.3). These signals were used to assign the O 1s emissions observed for $Mn_{1-y}Sb_yO_x$.

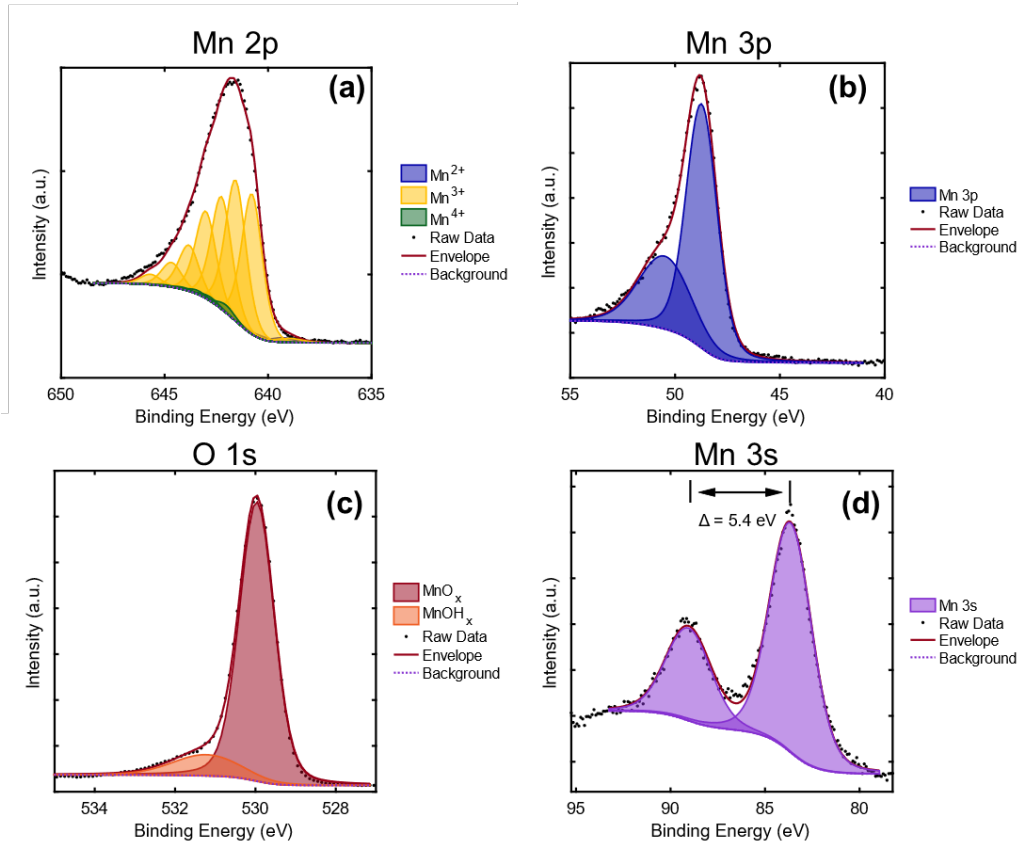

Figure 3.3.3. XP spectra of a pure Mn_2O_3 standard. Each Mn signal (a), (b), and (d) indicates a Mn (III) dominated surface. (c) O 1s signal contains both an oxide and hydroxide component, the BE of which was used to constrain fits of manganese antimonate O 1s spectra.

UHV XPS data for $Mn_{1-y}Sb_yO_x$ verified that increases in the Sb stoichiometry led to an increase in the amount of Mn (II) in the $Mn_{1-y}Sb_yO_x$ species, as well as an increase in Mn (IV), with a concomitant decrease in Mn (III).[12,14] The UHV XPS data for the Mn 2p and 3p emissions of the material with y = 0.3 were well fit by an assignment of Mn(III) (Figure 3.3.4) as the predominant oxidation state, but the Mn 3s splitting was larger than expected for Mn_2O_3. This splitting increased further for y = 0.6 and is consistent with a shortened Mn-O bond causing a shift in the energy of the ^5S and ^7S states.[12,36] At high Sb

concentrations, all three types of spectra indicated a decrease in the average Mn oxidation state from ~ 3+ to ~ 2.7+. The Mn 2p spectrum indicated that the change in average Mn oxidation state correlated with the increase in the fractional Mn (II) stoichiometry (Figure 3.3.4e) in the $Mn_{1-y}Sb_yO_x$ materials. The effect was more pronounced in the Mn 3s spectrum than in the Mn 3p emissions and is consistent with hypotheses based on the impact of Sb on the length of the Mn-O bond. In accord with prior observations, the Sb 3d spectrum indicated that Sb^{5+} was the dominant oxidation Sb state for all $Mn_{1-y}Sb_yO_x$ compositions (Figure 3.3.4c).[12–14] Based on the MnO_x standard, the O 1s spectrum was fit with an oxide denoted as $Mn_{1-y}Sb_yO_x$ and with a hydroxide, denoted as $Mn_{1-y}Sb_y(OH)_x$ (Figure 3.3.4d).

Combined with EDX and X-ray diffraction (XRD) data, the chemical formulae for the synthesized materials were assigned as Mn_2O_3, $Mn_7Sb_3O_{18}$, and $Mn_4Sb_6O_{21}$, assuming formal oxidation states for Mn, Sb, and O of 3+, 5+, and 2-, respectively. The UHV XPS data thus established a baseline for these materials for use in analysis of subsequent AP-XPS experiments, and the peak model used in this work successfully reproduced oxidation state trends that have been reported for related materials systems.[12–14]

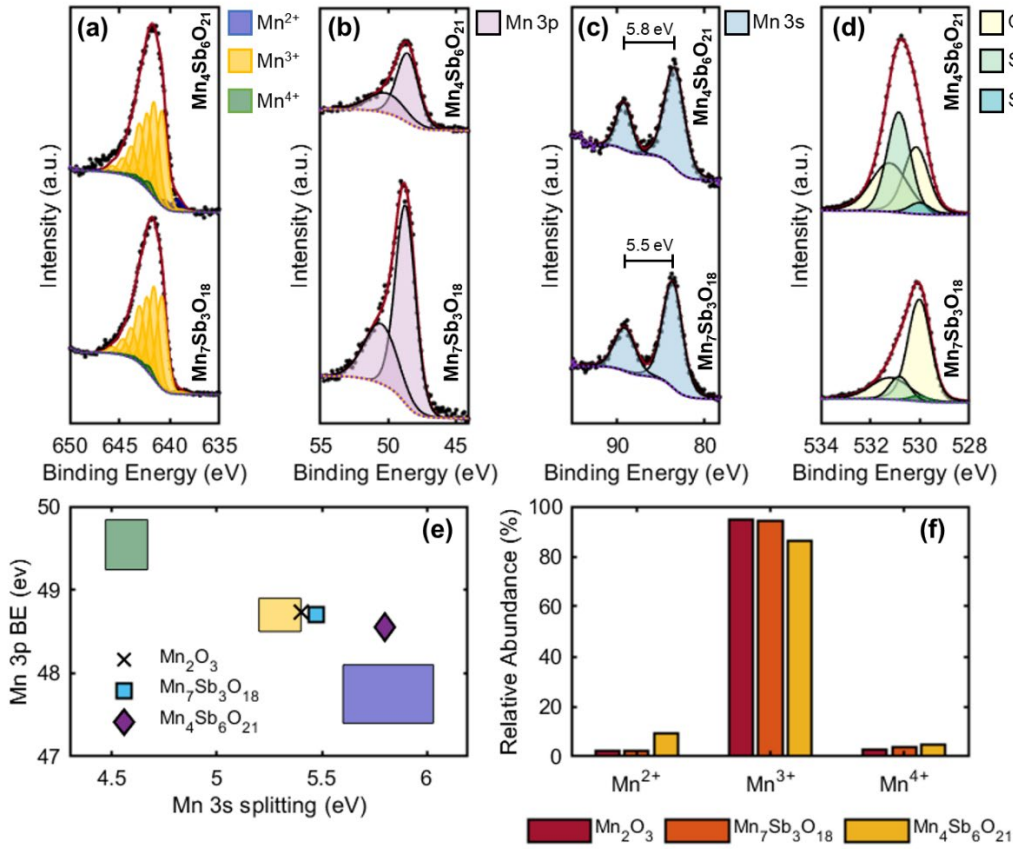

Figure 3.3.4. (a) Mn 2p XP spectra in UHV for $Mn_7Sb_3O_{18}$ and $Mn_4Sb_6O_{21}$ fit with peak models of Mn_2O, Mn_2O_3, and MnO_2 standards derived from the literature.[18] (b) Mn 3p XP spectra in UHV for $Mn_7Sb_3O_{18}$ and $Mn_4Sb_6O_{21}$. (c) Mn 3s XP spectra in UHV for $Mn_7Sb_3O_{18}$ and $Mn_4Sb_6O_{21}$. (d) O 1s and Sb 3d XP spectra in UHV for $Mn_7Sb_3O_{18}$ and $Mn_4Sb_6O_{21}$. (e) Mn oxidation state assigned to a MnO_x standard, $Mn_7Sb_3O_{18}$, and $Mn_4Sb_6O_{21}$, respectively, using the Mn 3p binding energy (BE) as well as using the Mn 3s multiplet splitting. Shaded regions indicate the standard deviation of literature reports for Mn(II), Mn(III), and Mn(IV).[17,18,21–24,26,27] (f) Abundance of each Mn oxidation state (Mn(X)/Mn_{Total} where Mn_{total} = [Mn(II) + Mn(III) + Mn(IV)]) for the Mn_2O_3 standard, $Mn_7Sb_3O_{18}$, and $Mn_4Sb_6O_{21}$ from the fit in panel (a)

For ambient-pressure XPS analysis, water vapor was introduced into the analysis chamber and spectra were collected as a function of pressure. Minimal changes in the average Mn or Sb oxidation state were observed as a function of pressure for either $Mn_7Sb_3O_{18}$ or

$Mn_4Sb_6O_{21}$ (Figure 3.3.5a, b). The O 1s spectrum indicated a change in the amount of surface hydroxide (Figure 3.3.5c). When liquid water was observed on the surface, the degree of protonation increased for $Mn_7Sb_3O_{18}$, but decreased for $Mn_4Sb_6O_{21}$ (Figure 3.3.5c).

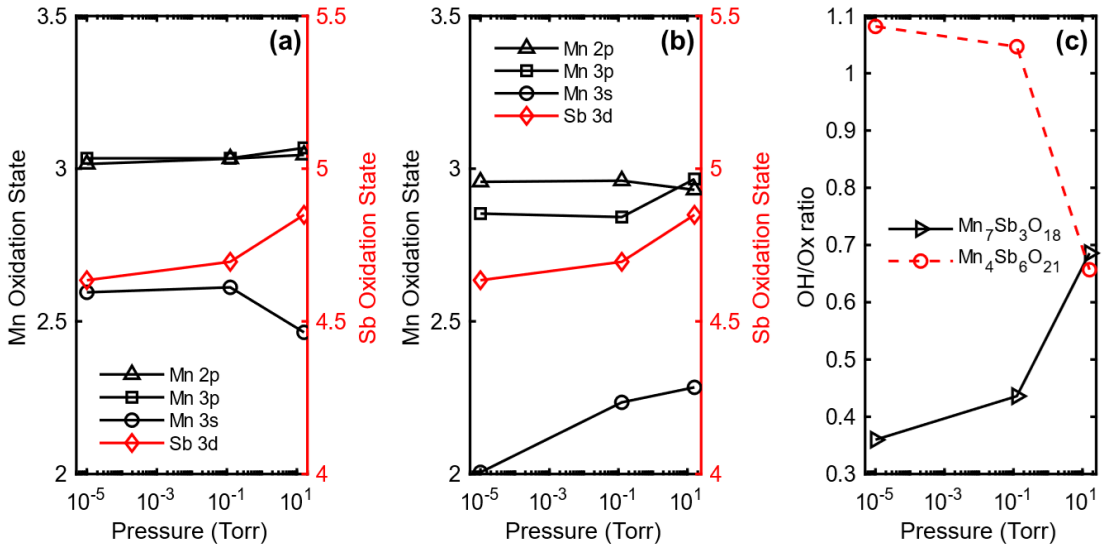

Figure 3.3.5. (a) Averaged oxidation state as a function of water vapor pressure for Mn and Sb in the rest state of $Mn_7Sb_3O_{18}$ as predicted by the Mn 2p, 3p and 3s emissions as well as by the Sb 3d emissions observed in ambient-pressure XP spectra. (b) Averaged oxidation state as a function of water vapor pressure for Mn and Sb in the rest state of $Mn_4Sb_6O_{21}$ as predicted by the Mn 2p, 3p and 3s emissions as well as by the Sb 3d emissions in ambient-pressure XP spectroscopy. (c) Plot of the metal hydroxide/oxide ratio as a function of water vapor pressure.

In situ measurements were performed as described previously to generate a thin stable (~20 nm) meniscus that enabled simultaneous electrode polarization and collection of emitted photoelectrons from the electrocatalyst on the electrode surface.[51–54] Effective meniscus establishment and persistence is readily obtained in alkaline solution, and only alkaline

solutions were permitted in the available XPS analysis chamber, so the in situ analysis was performed using 1.0 M KOH (aq). In situ XPS analysis of $Mn_7Sb_3O_{18}$ in 1.0 M KOH (aq) indicated an increased protonation at the surface relative to the behavior observed in ambient-pressure XPS measurements (Figure 3.3.5). This increase in protonation is consistent with observations of polarization of the Mn-O bond. The degree of protonation, and the Mn oxidation state as calculated by the Mn 2p spectra, showed a linear correlation between the oxidation state and the $Mn(OH)_x/MnO_x$ ratio (Figure 3.3.6). Sb 3d and Mn 3s XPS signals were not detected when an electrolyte meniscus formed.

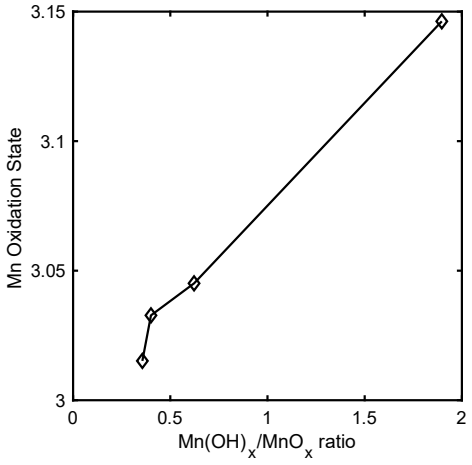

Figure 3.3.6. Relationship between predicted formal oxidation state and the hydroxide/oxide ratio at the surface at open circuit as determined by peak fit model of O 1s.

Mn-based electrocatalysts oxidize from Mn (III) to Mn (IV) under OER conditions, thus Mn (IV) is expected to be the dominant oxidation state of the surface at potentials approaching the OER, approximately 1.7 V vs. RHE in ex situ conditions (Figure 3.3.7).[55] However, at all potentials, Mn(III) was the dominant oxidation state on the electrocatalyst surface detected in the Mn 2p and 3p in situ XP spectra (Figure 3.3.8a, b). The Mn 2p

spectrum indicated that some Mn (IV) was generated at potentials approaching the OER, with ~15% of the Mn 2p signal attributable to Mn (IV) (Figure 3.3.8c). Similarly, analysis of the Mn 3p signal showed only slight shifts in BE and was not consistent with a full surface transformation to Mn (IV) (Figure 3.3.8b).

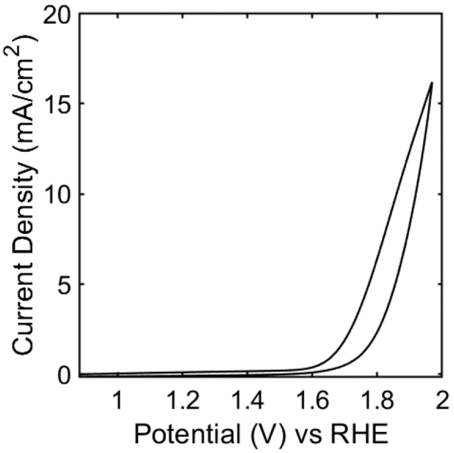

Figure 3.3.7. Cyclic voltammogram of a $Mn_7Sb_3O_{18}$ electrode in 1.0 M KOH (aq). Current takeoff above 1.6 V vs. RHE indicates OER initiation.

A nearly identical positive, linear trend of oxidation state with applied potential was observed for both Mn regions in the in situ XPS data for $Mn_7Sb_3O_{18}$ (Figure 3.3.8d). Thus, Mn (III) was the dominant oxidation state for $Mn_7Sb_3O_{18}$ even while the OER occurred, but some oxidation of the surface was apparent, with the Mn 2p spectrum providing evidence for the formation of Mn (IV) at potentials > 1.2 V vs. RHE. This behavior is consistent with the hypothesis that Mn (III) alone is not the most active form of the catalyst and that Mn (IV) contributes to the catalytic activity. The in situ XPS observations are also consistent with prior indications that Mn compounds partition into multiple oxidation states at different potentials.[32]

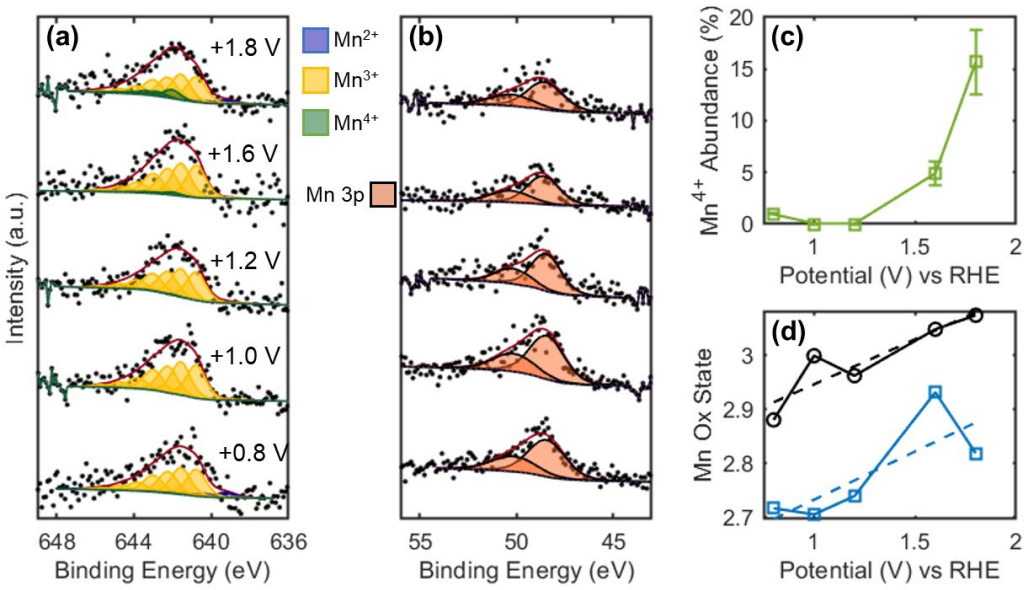

Figure 3.3.8. (a) Normalized Mn 2p XP spectra for $Mn_7Sb_3O_{18}$ as a function of the applied potential as fit with peak models for Mn_2O, Mn_2O_3, and MnO_2 standards.[18] (b) Normalized Mn 3p XP spectra for $Mn_7Sb_3O_{18}$ as a function of applied potential. (c) Mn(IV) abundance (Mn(IV)/Mn_{Total} where Mn_{total} = [Mn(II) + Mn(III) + Mn(IV)]) as a function of the applied potential as fit in panel (a), with error bars calculated by Monte Carlo analysis of the peak packet fits. (d) Oxidation state of Mn as calculated by Mn 2p peak fitting and Mn 3p BE fits in panels (a) and (b).

In summary, the surface chemistry of a stable, Mn-based OER catalyst was investigated using ex situ and in situ XPS techniques. The dominant Mn oxidation state in all conditions was Mn (III), whereas the dominant oxidation state observed for Sb was Sb^{5+}. As the Mn content of the catalyst decreased, Mn (II) formed, leading to a decrease in the observed oxidation state. Differences in the Mn content led to different Mn surface compositions, with $Mn_4Sb_6O_{21}$ exhibiting a higher $Mn(OH)_x$ concentration ex situ than $Mn_7Sb_3O_{18}$. When water was introduced, $Mn_7Sb_3O_{18}$ protonated more readily than $Mn_4Sb_6O_{21}$, suggesting a correlation between the susceptibility of the antimonate surface to protonation and the

catalytic activity towards the OER. Under in situ conditions, the two observable Mn XP signals indicated a surface dominated by Mn^3, even though a positive trend in observed oxidation state was observed. The positive trend is hypothesized to be due to fractional oxidation of the surface as indicated by a 15% abundance of Mn (IV) in the Mn 2p peak model at 1.8 V vs. RHE. Thus, in alkaline conditions, the surface partitioned into a combination of Mn (III) and Mn (IV) as the active state of the antimonate catalyst, consistent with prior observations that MnO_2 is a relatively inactive catalyst.[34,45,56] Thus, for Mn-based OER catalysts, future research could beneficially focus on compositions that stabilize Mn (III) at the surface of the electrocatalyst. These observations also suggest that the surface chemistry of Mn-based catalysts may be quite different from their bulk chemistry. Future work could be directed towards determining whether similar surface chemistry to that reported herein is observed for this catalyst in neutral and acidic conditions.

5.3.E.—Experimental methods for Section 3.3

Materials Synthesis

Electrodes were prepared via reactive sputtering with an AJA International RF sputtering system at a base pressure of $1x10^{-7}$ Torr and a deposition pressure of 5 mTorr. A Ti adhesion layer was sputtered onto a Si substrate (Addison Engineering p-Si [100]) with an RF power of 130 W and 20 min, following by sputtering a conductive top Pt contact at 100 W for 30 min. The Mn and Sb were then co-sputtered for 10 min in O_2 at either 83 and 30 W, respectively, for high Mn content, or at 45 and 40 W, respectively, for low Mn content.

Electrodes were then annealed for 3 h in air at 700 ºC to form the final crystal structure. This procedure resulted in films with ~350 nm thickness. The Mn standard was prepared using a nominally identical procedure, except that the Sb was omitted during film deposition and the deposition time was increased to 20 min to maintain an ~350 nm thickness. Loctite EA 9460 epoxy was coated on the back and sides of electrodes used for AP-XPS analysis to prevent interference from the Si substrate.

Materials Characterization

XRD data were collected using a Bruker D2 Phaser with a Cu source at 30 kV and 10 mA. Data were analyzed using DiffracEva software. Electrochemical data were collected with a Biologic VMP-3 potentiostat. SEM and energy dispersive X-ray spectroscopy (EDX) were performed with an FEI Nova SEM with a 5 mm working distance and 10 kV accelerating voltage with a base pressure of $1x10^{-6}$ Torr.

X-ray Spectroscopy

XPS and AP-XPS measurements were performed at Lawrence Berkeley National Laboratory's Advanced Light Source at station 9.3.1. A "tender" X-ray source with an energy of 4 keV was used for photoexcitation. For vapor isotherm experiments, water was introduced into the vacuum chamber through a needle valve. For electrochemical experiments, a beaker containing 1.0 M KOH(aq) solution was added to the vacuum chamber and the pressure was maintained at approximately 16 Torr using the vapor pressure of the electrolyte as well as a second beaker of deionized water that was present in the vacuum chamber. A Pt wire counter electrode and leakless Ag/AgCl reference electrode

as well as the $MnSbO_x$ working electrode were connected to a custom sample holder that could be dipped into solution and pulled out to generate a meniscus.[53]

The oxidation state of Mn is typically assessed by analysis of the Mn 2p photoelectron peak, but the Mn 3p and Mn 3s signals also contain chemical information. The Mn 2p peak has two spin-orbit split components, Mn $2p_{3/2}$ and $2p_{1/2}$, and each of those components is further convoluted by multiplet splitting, leading to a wide peak that does not shift much in binding energy (BE) with oxidation state but changes shape and can include features such as a high-BE satellite peak for Mn (II).[17–20,26,27] The Mn 3p peak shifts approximately linearly with oxidation state whereas the Mn 3s is multiplet split into two components, due to the two possible spin states (^5S and ^7S) after photoionization, the spacing of which is also associated with oxidation state and in pure oxides also varies approximately linearly, though other factors may affect the splitting.[18,21,23,24,26,27] Disproportionation reactions can occur in Mn, leading to multiple coexisting Mn oxidation states, necessitating an initial assumption that multiple states may be present simultaneously.[32,34,39,45,56] Analysis of all three signatures enables more robust oxidation state assignment and identification of deviations from trends expected for pure oxides. In addition to Mn, the chemistry of Sb and O can be analyzed via XPS. Sb 3d and O 1s spectra overlap with one another, with both the O 1s and Sb $3d_{5/2}$ peaks appearing at a BE of ~530 eV. This confounding signal can be deconvoluted by fitting of the Sb $3d_{3/2}$ peak, which does not overlap with the signals at of ~530 eV.

For in situ measurements, a limited range of overpotentials was used to effect oxygen evolution while preventing bubble formation that would destabilize the meniscus. Electrochemical measurement on $Mn_7Sb_3O_{18}$ indicated that 1.8 V vs. RHE was the OER onset potential, thus 1.8 V vs. RHE was the highest potential applied in these experiments (Figure S5). To verify potential control of the system, K 2p spectra were collected at the potentials studied, alongside the Mn and O 1s spectra. If potential control were achieved, chemical species in solution, such as K^+ ions, should shift linearly with the potential applied to the system, whereas species bound to the electrode should not shift in BE, due to the common electrical ground with the instrument.[51,53,54] A simplified energy diagram is presented as Figure S8. As the electrode potential was varied, a linear trend was observed for K $2p_{3/2}$ BE, with a slope of 0.9, indicating that potential control was established in the system. Measurements of surface chemistry were therefore performed at the desired potentials (Figure S9).

XPS data were analyzed using Casa XPS software. A Shirley background was used for all spectra. All peaks were referenced to adventitious C at 285 eV, however, in the AP-XPS experiments the C 1s peak shifts in BE due to dissolved C, so a constant offset of 3.85 eV was applied, aligning with the initial correction and resulting in aligned valence-band takeoffs. The Mn $2p_{3/2}$ peak was fit to standards previously reported to estimate the oxidation state and the contribution of various oxidation states to the XPS peaks. Mn 3p and Mn 3s spectra were also compared to literature references to estimate the Mn oxidation state. The $Sb_{3/2}$ peak was fit by first fitting the $Sb_{5/2}$ peak and constraining the peak splitting

(ΔSb 3d = 9.38 eV), peak width (equivalent for the same chemical state), and area ratio ($3d_{5/2}$:$3d_{3/2}$ = 3:2) and assuming that the remaining signal was due to O 1s. The O 1s spectra were then fit by comparison with a Mn_2O_3 standard, which did not have any overlap with the Sb emissions.

Electrochemistry

Electrochemical characterization outside of the vacuum chamber was performed with a BioLogic VMP3 potentiostat. Cyclic voltammetry was performed with a sweep rate of 50 mV s^{-1}, a Hg/HgO reference electrode (CHI 152, CH Instruments), a flame-cleaned Pt mesh counter electrode, and a $MnSbO_x$ working electrode that had been prepared identically to samples that were analyzed by AP-XPS. No iR compensation was performed, to most closely match the conditions under which AP-XPS data were collected.

Electrochemical measurements during AP-XPS were performed with a BioLogic SP200 potentiostat using a leakless Ag/AgCl reference electrode (Edaq ET072-1), a Pt wire counter electrode, and a $Mn_7Sb_3O_{18}$ working electrode that was prepared as described above.

References

(1) Bard, A. J.; Faulkner, L. R. *Electrochemical Methods: Fundamentals and Applications*, 2nd ed.; Wiley: New York, 2001.

(2) Bard, A. J.; Fox, M. A. Artificial Photosynthesis: Solar Splitting of Water to Hydrogen and Oxygen. *Acc. Chem. Res.* **1995**, *28* (3), 141–145. https://doi.org/10.1021/ar00051a007.

(3) You, B.; Sun, Y. Innovative Strategies for Electrocatalytic Water Splitting. *Acc. Chem. Res.* **2018**, *51* (7), 1571–1580. https://doi.org/10.1021/acs.accounts.8b00002.

(4) Anantharaj, S.; Ede, S. R.; Sakthikumar, K.; Karthick, K.; Mishra, S.; Kundu, S. Recent Trends and Perspectives in Electrochemical Water Splitting with an Emphasis on Sulfide, Selenide, and Phosphide Catalysts of Fe, Co, and Ni: A Review. *ACS Catal.* **2016**, *6* (12), 8069–8097. https://doi.org/10.1021/acscatal.6b02479.

(5) McCrory, C. C. L.; Jung, S.; Ferrer, I. M.; Chatman, S. M.; Peters, J. C.; Jaramillo, T. F. Benchmarking Hydrogen Evolving Reaction and Oxygen Evolving Reaction Electrocatalysts for Solar Water Splitting Devices. *J. Am. Chem. Soc.* **2015**, *137* (13), 4347–4357. https://doi.org/10.1021/ja510442p.

(6) Carmo, M.; Fritz, D. L.; Mergel, J.; Stolten, D. A Comprehensive Review on PEM Water Electrolysis. *International Journal of Hydrogen Energy* **2013**, *38* (12), 4901–4934. https://doi.org/10.1016/j.ijhydene.2013.01.151.

(7) Liang, Q.; Brocks, G.; Bieberle-Hütter, A. Oxygen Evolution Reaction (OER) Mechanism under Alkaline and Acidic Conditions. *J. Phys. Energy* **2021**, *3* (2), 026001. https://doi.org/10.1088/2515-7655/abdc85.

(8) Xie, X.; Du, L.; Yan, L.; Park, S.; Qiu, Y.; Sokolowski, J.; Wang, W.; Shao, Y. Oxygen Evolution Reaction in Alkaline Environment: Material Challenges and Solutions. *Advanced Functional Materials* **2022**, *32* (21), 2110036. https://doi.org/10.1002/adfm.202110036.

(9) Fabbri, E.; Schmidt, T. J. Oxygen Evolution Reaction—The Enigma in Water Electrolysis. *ACS Catal.* **2018**, *8* (10), 9765–9774. https://doi.org/10.1021/acscatal.8b02712.

(10) Fabbri, E.; Habereder, A.; Waltar, K.; Kötz, R.; Schmidt, T. J. Developments and Perspectives of Oxide-Based Catalysts for the Oxygen Evolution Reaction. *Catal. Sci. Technol.* **2014**, *4* (11), 3800–3821. https://doi.org/10.1039/C4CY00669K.

(11) Oener, S. Z.; Bergmann, A.; Cuenya, B. R. Designing Active Oxides for a Durable Oxygen Evolution Reaction. *Nat. Synth* **2023**. https://doi.org/10.1038/s44160-023-00376-6.

(12) Zhou, L.; Shinde, A.; Montoya, J. H.; Singh, A.; Gul, S.; Yano, J.; Ye, Y.; Crumlin, E. J.; Richter, M. H.; Cooper, J. K.; Stein, H. S.; Haber, J. A.; Persson, K. A.; Gregoire, J. M. Rutile Alloys in the Mn–Sb–O System Stabilize Mn^{3+} To Enable Oxygen Evolution in Strong Acid. *ACS Catal.* **2018**, *8* (12), 10938–10948. https://doi.org/10.1021/acscatal.8b02689.

(13) Moreno-Hernandez, I. A.; MacFarland, C. A.; Read, C. G.; Papadantonakis, K. M.; Brunschwig, B. S.; Lewis, N. S. Crystalline Nickel

Manganese Antimonate as a Stable Water-Oxidation Catalyst in Aqueous 1.0 M H2SO4. *Energy Environ. Sci.* **2017**, *10* (10), 2103–2108. https://doi.org/10.1039/C7EE01486D.

(14) Ifkovits, Z. P.; Evans, J. M.; Kempler, P. A.; Morla, M. B.; Pham, K. H.; Dowling, J. A.; Carim, A. I.; Lewis, N. S. Powdered MnySb1–yOx Catalysts for Cerium-Mediated Oxygen Evolution in Acidic Environments. *ACS Energy Lett.* **2022**, *7* (12), 4258–4264. https://doi.org/10.1021/acsenergylett.2c01754.

(15) Dowling, J. A.; Ifkovits, Z. P.; Carim, A. I.; Evans, J. M.; Swint, M. C.; Ye, A. Z.; Richter, M. H.; Li, A. X.; Lewis, N. S. Catalysis of the Oxygen-Evolution Reaction in 1.0 M Sulfuric Acid by Manganese Antimonate Films Synthesized via Chemical Vapor Deposition. *ACS Appl. Energy Mater.* **2024**. https://doi.org/10.1021/acsaem.4c00135.

(16) Ifkovits, Z. P.; Evans, J. M.; Meier, M. C.; Papadantonakis, K. M.; Lewis, N. S. Decoupled Electrochemical Water-Splitting Systems: A Review and Perspective. *Energy Environ. Sci.* **2021**, *14* (9), 4740–4759. https://doi.org/10.1039/D1EE01226F.

(17) Biesinger, M. C.; Payne, B. P.; Grosvenor, A. P.; Lau, L. W. M.; Gerson, A. R.; Smart, R. St. C. Resolving Surface Chemical States in XPS Analysis of First Row Transition Metals, Oxides and Hydroxides: Cr, Mn, Fe, Co and Ni. *Applied Surface Science* **2011**, *257* (7), 2717–2730. https://doi.org/10.1016/j.apsusc.2010.10.051.

(18) Ilton, E. S.; Post, J. E.; Heaney, P. J.; Ling, F. T.; Kerisit, S. N. XPS Determination of Mn Oxidation States in Mn (Hydr)Oxides. *Applied Surface Science* **2016**, *366*, 475–485. https://doi.org/10.1016/j.apsusc.2015.12.159.

(19) Gupta, R. P.; Sen, S. K. Calculation of Multiplet Structure of Core p - Vacancy Levels. *Phys. Rev. B* **1974**, *10* (1), 71–77. https://doi.org/10.1103/PhysRevB.10.71.

(20) Gupta, R. P.; Sen, S. K. Calculation of Multiplet Structure of Core p - Vacancy Levels. II. *Phys. Rev. B* **1975**, *12* (1), 15–19. https://doi.org/10.1103/PhysRevB.12.15.

(21) Cerrato, J. M.; Hochella, M. F.; Knocke, W. R.; Dietrich, A. M.; Cromer, T. F. Use of XPS to Identify the Oxidation State of Mn in Solid Surfaces of Filtration Media Oxide Samples from Drinking Water Treatment Plants. *Environ. Sci. Technol.* **2010**, *44* (15), 5881–5886. https://doi.org/10.1021/es100547q.

(22) Fujiwara, M.; Matsushita, T.; Ikeda, S. Evaluation of Mn3s X-Ray Photoelectron Spectroscopy for Characterization of Manganese Complexes. *Journal of Electron Spectroscopy and Related Phenomena* **1995**, *74* (3), 201–206. https://doi.org/10.1016/0368-2048(94)02375-1.

(23) Nelson, A. J.; Reynolds, J. G.; Roos, J. W. Core-Level Satellites and Outer Core-Level Multiplet Splitting in Mn Model Compounds. *Journal of Vacuum Science & Technology A: Vacuum, Surfaces, and Films* **2000**, *18* (4), 1072–1076. https://doi.org/10.1116/1.582302.

(24) Hermsmeier, B. D.; Fadley, C. S.; Sinkovic, B.; Krause, M. O.; Jimenez-Mier, J.; Gerard, P.; Carlson, T. A.; Manson, S. T.; Bhattacharya, S. K. Energy Dependence of the Outer Core-Level Multiplet Structures in Atomic Mn and Mn-Containing Compounds. *Phys. Rev. B* **1993**, *48* (17), 12425–12437. https://doi.org/10.1103/PhysRevB.48.12425.

(25) Powell, C. X-Ray Photoelectron Spectroscopy Database XPS, Version 4.1, NIST Standard Reference Database 20, 1989. https://doi.org/10.18434/T4T88K.

(26) Militello, M. C.; Gaarenstroom, S. W. Manganese Dioxide (MnO2) by XPS. *Surface Science Spectra* **2001**, *8* (3), 200–206. https://doi.org/10.1116/11.20020401.

(27) Stranick, M. A. Mn_2O_3 by XPS. *Surface Science Spectra* **1999**, *6* (1), 39–46. https://doi.org/10.1116/1.1247889.

(28) Briggs, D. Handbook of X-Ray Photoelectron Spectroscopy C. D. Wanger, W. M. Riggs, L. E. Davis, J. F. Moulder and G. E. Muilenberg Perkin-Elmer Corp., Physical Electronics Division, Eden Prairie, Minnesota, USA, 1979. 190 Pp. $195. *Surf. Interface Anal.* **1981**, *3* (4), v–v. https://doi.org/10.1002/sia.740030412.

(29) Garbassi, F. XPS and AES Study of Antimony Oxides. *Surf. Interface Anal.* **1980**, *2* (5), 165–169. https://doi.org/10.1002/sia.740020502.

(30) Matthew, J. Surface Analysis by Auger and X-Ray Photoelectron Spectroscopy. D. Briggs and J. T. Grant (Eds.). IM Publications, Chichester, UK

and SurfaceSpectra, Manchester, UK, 2003. 900 Pp., ISBN 1-901019-04-7, 900 Pp. *Surface and Interface Analysis* **2004**, *36* (13), 1647–1647. https://doi.org/10.1002/sia.2005.

(31) Castle, J. E. Practical Surface Analysis by Auger and X-Ray Photoelectron Spectroscopy. D. Briggs and M. P. Seah (Editors). John Wiley and Sons Ltd, Chichester, 1983, 533 Pp., £44.50. *Surface and Interface Analysis* **1984**, *6* (6), 302–302. https://doi.org/10.1002/sia.740060611.

(32) Huynh, M.; Bediako, D. K.; Nocera, D. G. A Functionally Stable Manganese Oxide Oxygen Evolution Catalyst in Acid. *J. Am. Chem. Soc.* **2014**, *136* (16), 6002–6010. https://doi.org/10.1021/ja413147e.

(33) Tsunekawa, S.; Yamamoto, F.; Wang, K.-H.; Nagasaka, M.; Yuzawa, H.; Takakusagi, S.; Kondoh, H.; Asakura, K.; Kawai, T.; Yoshida, M. Operando Observations of a Manganese Oxide Electrocatalyst for Water Oxidation Using Hard/Tender/Soft X-Ray Absorption Spectroscopy. *J. Phys. Chem. C* **2020**, *124* (43), 23611–23618. https://doi.org/10.1021/acs.jpcc.0c05571.

(34) Kumbhar, V. S.; Lee, H.; Lee, J.; Lee, K. Recent Advances in Water-Splitting Electrocatalysts Based on Manganese Oxide. *Carbon Resources Conversion* **2019**, *2* (3), 242–255. https://doi.org/10.1016/j.crcon.2019.11.003.

(35) Luke, S.; Chatti, M.; Yadav, A.; Kerr, B. V.; Kangsabanik, J.; Williams, T.; Cherepanov, P. V.; Johannessen, B.; Tanksale, A.; MacFarlane, D. R.; Hocking, R. K.; Alam, A.; Yella, A.; Simonov, A. N. Mixed Metal–Antimony Oxide

Nanocomposites: Low pH Water Oxidation Electrocatalysts with Outstanding Durability at Ambient and Elevated Temperatures. *J. Mater. Chem. A* **2021**, *9* (48), 27468–27484. https://doi.org/10.1039/D1TA07293E.

(36) Luke, S.; Chatti, M.; Yadav, A.; Kerr, B. V.; Kangsabanik, J.; Williams, T.; Cherepanov, P. V.; Johannessen, B.; Tanksale, A.; MacFarlane, D. R.; Hocking, R. K.; Alam, A.; Yella, A.; Simonov, A. N. Mixed Metal–Antimony Oxide Nanocomposites: Low pH Water Oxidation Electrocatalysts with Outstanding Durability at Ambient and Elevated Temperatures. *J. Mater. Chem. A* **2021**, *9* (48), 27468–27484. https://doi.org/10.1039/D1TA07293E.

(37) Gao, X.; Zhou, H.; Wang, Z.; Zhou, G.; Wang, J.; Wu, Y. Acid-Stable Antimonate Based Catalysts for the Electrocatalytic Oxygen Evolution Reaction. *Nano Res.* **2022**. https://doi.org/10.1007/s12274-022-5132-6.

(38) Yang, R. B.; Bachmann, J.; Reiche, M.; Gerlach, J. W.; Gösele, U.; Nielsch, K. Atomic Layer Deposition of Antimony Oxide and Antimony Sulfide. *Chem. Mater.* **2009**, *21* (13), 2586–2588. https://doi.org/10.1021/cm900623v.

(39) Takashima, T.; Hashimoto, K.; Nakamura, R. Mechanisms of pH-Dependent Activity for Water Oxidation to Molecular Oxygen by MnO2 Electrocatalysts. *J. Am. Chem. Soc.* **2012**, *134* (3), 1519–1527. https://doi.org/10.1021/ja206511w.

(40) Walter, M. G.; Warren, E. L.; McKone, J. R.; Boettcher, S. W.; Mi, Q.; Santori, E. A.; Lewis, N. S. Solar Water Splitting Cells. *Chem. Rev.* **2010**, *110* (11), 6446–6473. https://doi.org/10.1021/cr1002326.

(41) Minke, C.; Suermann, M.; Bensmann, B.; Hanke-Rauschenbach, R. Is Iridium Demand a Potential Bottleneck in the Realization of Large-Scale PEM Water Electrolysis? *International Journal of Hydrogen Energy* **2021**, *46* (46), 23581–23590. https://doi.org/10.1016/j.ijhydene.2021.04.174.

(42) Jang, H.; Hieu, T. T.; Kim, S. H.; Lee, J. Reduction of Iridium Loading to the Minimum Level Required for Water Oxidation Electrocatalysis without Sacrificing the Electrochemical Stability. *J. Phys. Chem. C* **2019**, acs.jpcc.9b02819. https://doi.org/10.1021/acs.jpcc.9b02819.

(43) Vesborg, P. C. K.; Jaramillo, T. F. Addressing the Terawatt Challenge: Scalability in the Supply of Chemical Elements for Renewable Energy. *RSC Adv.* **2012**, *2* (21), 7933. https://doi.org/10.1039/c2ra20839c.

(44) Siddiqi, G.; Luo, Z.; Xie, Y.; Pan, Z.; Zhu, Q.; Röhr, J. A.; Cha, J. J.; Hu, S. Stable Water Oxidation in Acid Using Manganese-Modified TiO_2 Protective Coatings. *ACS Appl. Mater. Interfaces* **2018**, *10* (22), 18805–18815. https://doi.org/10.1021/acsami.8b05323.

(45) Heese-Gärtlein, J.; Rabe, A.; Behrens, M. Challenges in the Application of Manganese Oxide Powders as OER Electrocatalysts: Synthesis, Characterization,

Activity and Stability of Nine Different Mn $_x$ O $_y$ Compounds. *Zeitschrift anorg allge chemie* **2021**, *647* (13), 1363–1372. https://doi.org/10.1002/zaac.202000180.

(46) Siddiqi, G.; Luo, Z.; Xie, Y.; Pan, Z.; Zhu, Q.; Röhr, J. A.; Cha, J. J.; Hu, S. Stable Water Oxidation in Acid Using Manganese-Modified TiO_2 Protective Coatings. *ACS Appl. Mater. Interfaces* **2018**, *10* (22), 18805–18815. https://doi.org/10.1021/acsami.8b05323.

(47) Sun, W.; Kitchaev, D. A.; Kramer, D.; Ceder, G. Non-Equilibrium Crystallization Pathways of Manganese Oxides in Aqueous Solution. *Nat Commun* **2019**, *10* (1), 573. https://doi.org/10.1038/s41467-019-08494-6.

(48) Gunasooriya, G. T. K. K.; Nørskov, J. K. Analysis of Acid-Stable and Active Oxides for the Oxygen Evolution Reaction. *ACS Energy Lett.* **2020**, *5* (12), 3778–3787. https://doi.org/10.1021/acsenergylett.0c02030.

(49) Shinde, A.; Jones, R. J. R.; Guevarra, D.; Mitrovic, S.; Becerra-Stasiewicz, N.; Haber, J. A.; Jin, J.; Gregoire, J. M. High-Throughput Screening for Acid-Stable Oxygen Evolution Electrocatalysts in the (Mn–Co–Ta–Sb)O x Composition Space. *Electrocatalysis* **2015**, *6* (2), 229–236. https://doi.org/10.1007/s12678-014-0237-7.

(50) Crumlin, E. J.; Liu, Z.; Bluhm, H.; Yang, W.; Guo, J.; Hussain, Z. X-Ray Spectroscopy of Energy Materials under in Situ/Operando Conditions. *Journal of*

Electron Spectroscopy and Related Phenomena **2015**, *200*, 264–273. https://doi.org/10.1016/j.elspec.2015.06.008.

(51) Axnanda, S.; Crumlin, E. J.; Mao, B.; Rani, S.; Chang, R.; Karlsson, P. G.; Edwards, M. O. M.; Lundqvist, M.; Moberg, R.; Ross, P.; Hussain, Z.; Liu, Z. Using "Tender" X-Ray Ambient Pressure X-Ray Photoelectron Spectroscopy as A Direct Probe of Solid-Liquid Interface. *Sci Rep* **2015**, *5* (1), 9788. https://doi.org/10.1038/srep09788.

(52) Favaro, M.; Valero-Vidal, C.; Eichhorn, J.; Toma, F. M.; Ross, P. N.; Yano, J.; Liu, Z.; Crumlin, E. J. Elucidating the Alkaline Oxygen Evolution Reaction Mechanism on Platinum. *J. Mater. Chem. A* **2017**, *5* (23), 11634–11643. https://doi.org/10.1039/C7TA00409E.

(53) Favaro, M.; Jeong, B.; Ross, P. N.; Yano, J.; Hussain, Z.; Liu, Z.; Crumlin, E. J. Unravelling the Electrochemical Double Layer by Direct Probing of the Solid/Liquid Interface. *Nat Commun* **2016**, *7* (1), 12695. https://doi.org/10.1038/ncomms12695.

(54) Lichterman, M. F.; Richter, M. H.; Hu, S.; Crumlin, E. J.; Axnanda, S.; Favaro, M.; Drisdell, W.; Hussain, Z.; Brunschwig, B. S.; Lewis, N. S.; Liu, Z.; Lewerenz, H.-J. An Electrochemical, Microtopographical and Ambient Pressure X-Ray Photoelectron Spectroscopic Investigation of Si/TiO_2/Ni/Electrolyte Interfaces. *J. Electrochem. Soc.* **2016**, *163* (2), H139–H146. https://doi.org/10.1149/2.0861602jes.

(55) Gorlin, Y.; Lassalle-Kaiser, B.; Benck, J. D.; Gul, S.; Webb, S. M.; Yachandra, V. K.; Yano, J.; Jaramillo, T. F. In Situ X-Ray Absorption Spectroscopy Investigation of a Bifunctional Manganese Oxide Catalyst with High Activity for Electrochemical Water Oxidation and Oxygen Reduction. *J. Am. Chem. Soc.* **2013**, *135* (23), 8525–8534. https://doi.org/10.1021/ja3104632.

(56) Wang, P.; Zhang, S.; Wang, Z.; Mo, Y.; Luo, X.; Yang, F.; Lv, M.; Li, Z.; Liu, X. Manganese-Based Oxide Electrocatalysts for the Oxygen Evolution Reaction: A Review. *J. Mater. Chem. A* **2023**, *11* (11), 5476–5494. https://doi.org/10.1039/D2TA09039B.

Chapter 4

Localized Corrosion of Photoelectrode Protection Layers

4.1—Introduction and Background

Photoelectrochemical devices convert incident solar electromagnetic energy into chemical energy, allowing for energy storage in chemical bonds.[1–5] This technology has therefore been studied extensively to create practical, safe, and efficient systems for energy storage.[1–5] Hydrogen is a key fuel for a future energy system, owing to its wide range of applications, relative ease of production, and high gravimetric energy density.[3,6–9] Hydrogen is readily produced via water electrolysis as shown in the reaction in Scheme 4.1.1.[1,10]

Scheme 4.1.1

$$2H_2O\ (l) \rightarrow 2H_2(g) + O_2\ (g)$$

However, the overall reaction in Scheme X, when performed electrochemically, is separated into two half reactions.[1,10] The half reactions are denoted HER for hydrogen evolution or OER for oxygen evolution. The reactions vary in mechanism based on pH and are summarized in Schemes 4.1.2–4.1.3.[1,10,11]

Scheme 4.1.2

HER (acidic) $2H^+\ (aq) \xrightarrow{+2e^-} H_2\ (g)$ | OER (acidic) $2H_2O\ (l) \xrightarrow{-4e^-} 4H^+\ (aq) + O_2\ (g)$

Scheme 4.1.2

HER (alkaline) $2H_2O\ (l) \rightarrow H_2\ (g) + 2OH^-\ (aq)$ | OER (alkaline) $2OH^-\ (aq) \rightarrow H_2O(l) + O_2\ (g)$

Water electrolysis will, therefore, produce either protons or hydroxide ions at one electrode depending on the pH, and consume those species at the opposite electrode. Additionally, production of H_2 (g) and O_2 (g) in the same chamber presents an explosion hazard and is generally unsafe to do in practice.[1,12,13] To address this safety issue, cells are divided by an ion-selective membrane to prevent gaseous product mixing.[13] The membrane, however, necessitates the use of highly alkaline or highly acidic solutions to mitigate ohmic losses from pH gradients at the electrodes and allow continuous operation of the device as charge-compensating ion movement must be one of the species generated and consumed in the reaction or else the reaction will cease when a sufficient ion gradient is reached.[13,14]

The necessity of acidic or alkaline conditions presents a major chemical challenge to the development of practical photoelectrochemical devices due to stability issues. In a photoelectrochemical system, electrodes must conduct charge and absorb light, requiring the use of semiconductor electrodes.[2] Silicon is a common choice for semiconducting material and has been extensively studied for photoelectrochemical cells.[1,2,4,5,14–18] Analysis of the Si Pourbaix diagram, which denotes thermodynamically stable species as a function of pH and electric potential, shows that Si is thermodynamically stable in acidic, reducing conditions required for acidic HER.[19] However, Si passivates or corrodes by dissolution in alkaline, oxidizing environments.[19] Further, a photoelectrochemical cell based only on Si would fail to efficiently absorb solar radiation, requiring Si to instead be paired with a

semiconductor with a larger band gap, ideally ~1.6 eV.[20] III–V semiconductors such as GaAs and InP are thus of interest due to larger band gaps as compared to Si (E_g ~ 1.4 eV for GaAs and InP vs. 1.1 eV for Si) and ability to tune such materials into the ideal 1.6 eV range.[20] However, both of these materials are unstable in the oxidative conditions required for OER in both acidic and alkaline conditions.[19,21]

To address stability challenges, protective overlayers have been developed for semiconductor photoelectrodes that isolate the material chemically from solution to prevent corrosion but retain electrical conductivity and optical transparency required for a functional PEC.[14,22–30] Protection layers based on TiO_2 have shown immense promise for protecting a variety of semiconductors in both acidic and alkaline conditions.[14,23] However, defects in the protection layer lead to device failure and are a major obstacle for development of practical PECs.[4,31,32] In this work, research has focused on GaAs with a TiO_2 protection layer in alkaline OER-like conditions due to extreme stability issues in that system and ability to pair with relatively stable, self-passivating Si photocathodes.

4.2—Corrosion electrochemistry of GaAs/TiO_2 electrodes

Understanding GaAs corrosion is key for comparing the corrosion properties of protected and unprotected electrodes. Cyclic voltammetry of bare GaAs in 1.0 M KOH exhibits two features corresponding to corrosion, an irreversible reaction at approximately 0.8 V vs. RHE and a reversible reaction at approximately 1.0 V vs. RHE (Figure 4.2.1). GaAs corrodes in alkaline conditions according to the reactions in Schemes 4.2.1–4.2.2:[33,34]

Scheme 4.2.1

$$GaAs(s) + 6OH^-(aq) \rightarrow GaO_3^{3-}(aq) + As^0(s) + 3H_2O(l) + 3e^-$$

Scheme 4.2.2

$$As^0(s) + 4OH^-(aq) \leftrightarrow AsO_2^-(aq) + 2H_2O\ (l) + 3e^-$$

Where the reaction in Scheme 4.2.1 is irreversible and Scheme 4.2.2 is quasi-reversible in 1.0 M KOH. Both of these reactions occur below the thermodynamic potential required for OER and therefore in OER conditions, a GaAs electrode will corrode via Ga and As dissolution.[33,34] In Figure 4.2.1, potential is kept below OER initiation on GaAs, so all current is due to corrosion reactions. The current for an unprotected GaAs sample is above 40 mA cm^{-2} leading to rapid dissolution and device failure. When a protection layer of 100 nm amorphous TiO_2 (a-TiO_2) is deposited via ALD, the corrosion current decreases by two orders of magnitude (Figure 4.2.1). However, GaAs corrosion is still observed from a protected sample, as evidenced by similar features in the CV at nearly identical potentials and etch pit appearance.

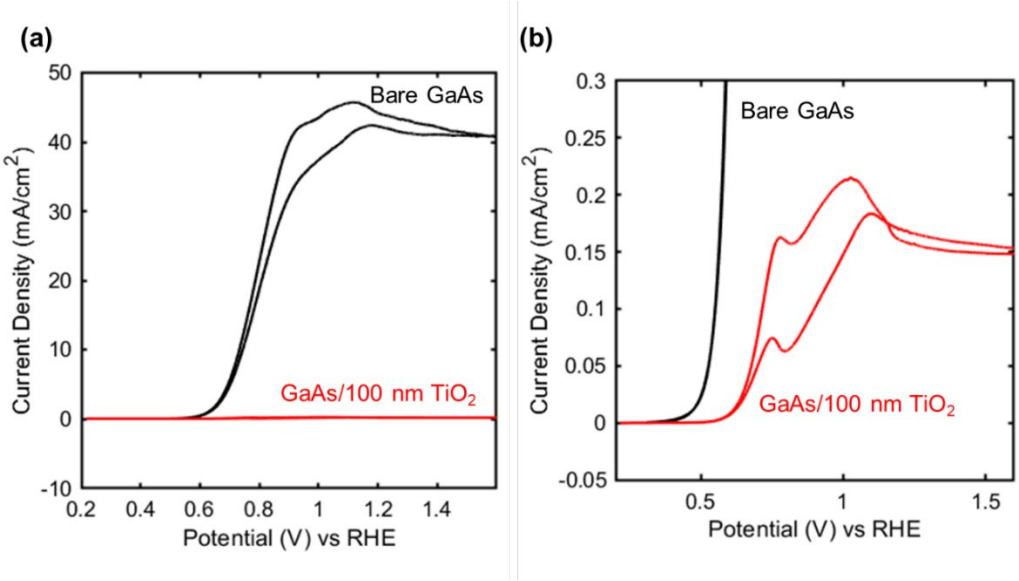

Figure 4.2.1. Cyclic voltammograms of p^+-GaAs and p^+-GaAs/*a*-TiO_2 electrodes in aqueous 1.0 M KOH solution scaled to (a) the p^+-GaAs current and (b) p^+-GaAs/*a*-TiO_2 current to visualize current response in both cases.

To characterize the corrosion reactions and compare between protected and unprotected electrodes, a variety of electrochemical tests have been performed. Of interest is the fundamental thermodynamics and kinetics of the corrosion reactions occurring at each electrode. In corrosion science, this is characterized by mild polarization of the electrode and determination of the corrosion potential E_{corr} and corrosion current i_{corr} from a log(|i|) vs. V plot, identical to Tafel analysis in traditional electrochemical analysis.[11,35] E_{corr} is the potential at which no net reaction occurs, where any potential above E_{corr} will exhibit net oxidative corrosion.[35] It is analogous to open-circuit potential and is controlled by the potential of the reactions occurring at the surface.[11] Thus, E_{corr} is a measurement of corrosion thermodynamics, where a more negative value indicates a more favorable oxidation.[35] Comparing E_{corr} between protected and unprotected reactions, the potentials

are within one standard deviation of one another. The corrosion current density, j_{corr} is a measurement of how rapidly the corrosion reaction takes place near open circuit. This is identical to the exchange current density calculated via Tafel analysis, thus, is directly related to the fundamental rate constant of the reaction. An order of magnitude decrease in j_{corr} is observed for GaAs/*a*-TiO_2 when compared to unprotected GaAs (Figure 4.2.2). Combined with $E_{corr,}$ this analysis indicates that the *a*-TiO_2 protection layer does not substantially protect GaAs thermodynamically, in fact it may cause corrosion to be more favorable. Instead, *a*-TiO_2 slows the kinetics of the reaction, leading to the observed decrease in corrosion current but similar reactivity.

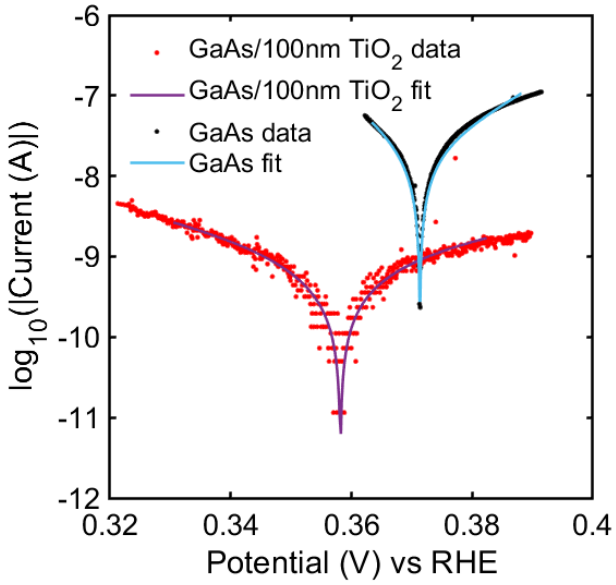

Figure 4.2.2. Tafel plots of p^+-GaAs and p^+-GaAs/*a*-TiO_2 electrodes in aqueous 1.0 M KOH solution with example fits of linear regions of both voltammograms.

Further information on the corrosion characteristics of GaAs/*a*-TiO_2 can be gained by measuring the polarization resistance of the electrodes. Polarization resistance is a measurement of the corrosion rate near the open-circuit potential in the regime where the forward and reverse reactions are occurring at similar rates. This is in the Butler-Volmer regime in traditional electrochemistry terminology. The response of the electrode at potentials very near open circuit is given by Eq. 4.2.1.

Equation 4.2.1

$$i = i_{corr}(\exp\left[\frac{2.303\eta}{\beta_a}\right] - \exp\left[\frac{2.303\eta}{\beta_c}\right])$$

The potential of the electrode is swept very slowly (0.1 mV/s) to ensure steady-state conditions and the slope of the linear regime in I-V response is recorded and the slope of the response in the linear regime is R_p which can be decomposed as Eq. 4.2.2.

Equation 4.2.2

$$R_p = \frac{1}{2.303} * \frac{\beta_a\beta_c}{\beta_a + \beta_c} * \frac{1}{i_{corr}}$$

Thus, the polarization resistance can be directly related to the corrosion current if the anodic and cathodic Tafel slopes are known. This measurement can be compared to that made using the Evans diagram to corroborate the change in kinetics. From these data it can be shown that the E_{corr} is again similar between protected and unprotected samples but that the calculated j_{corr} for protected samples is generally an order of magnitude lower than that of an unprotected sample (Figure 4.2.3). These findings corroborate the Tafel measurements and together lead to the conclusion that addition of a TiO_2 film to a GaAs

sample stabilizes the surface kinetically but has no statistically significant impact on the thermodynamics of the corrosion reactions occurring, thus only GaAs corrosion is ever observed and TiO_2 is electrochemically inactive in the conditions studied.

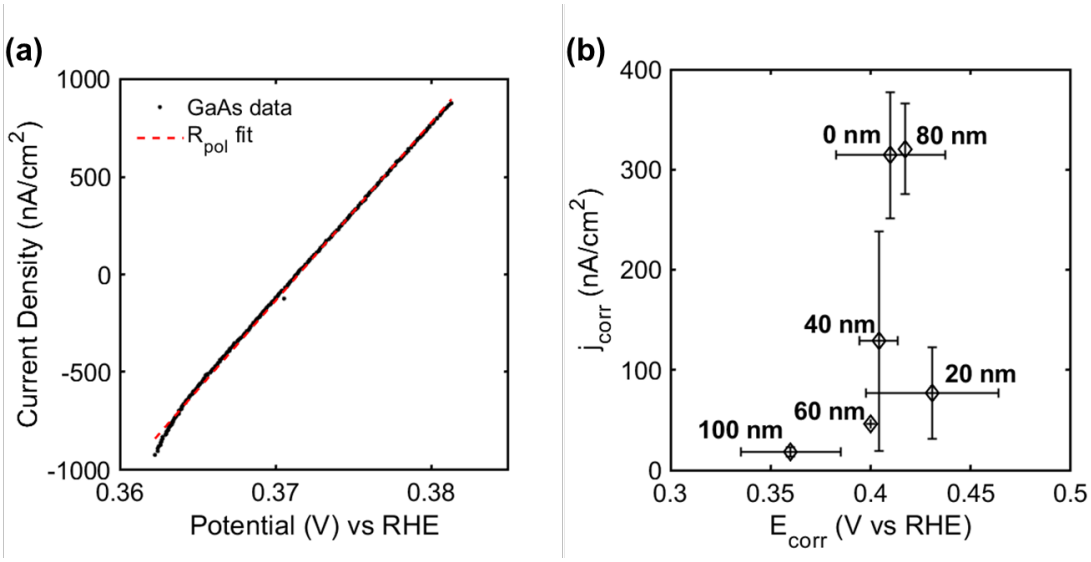

Figure 4.2.3. (a) Representative polarization resistance plot for p^+-GaAs electrodes including raw data (black dots) and linear fit (red dashed line) used to extract R_{pol}. (b) Comparison of j_{corr} and E_{corr} calculated via polarization resistance for p^+-GaAs and p^+-GaAs/*a*-TiO_2 electrodes. Error bars represent one standard deviation in data.

Cyclic polarization can also provide information on how corrosion behavior compares between GaAs/*a*-TiO_2 electrodes and unprotected GaAs. In this technique, the electrode is polarized in a cyclic manner as in a CV, but slow (0.5 mV/s) scan rates are used to ensure steady-state conditions and plotted as log(|i|) vs. V. The features of the graph in a cyclic polarization experiment differ from a traditional CV and it is frequently used to distinguish between pitting corrosion, passivation, and uniform corrosion in materials. Potential is swept anodically until a large takeoff is observed, known as the pitting potential

E_{pit}. The potential is then swept cathodically to return to the initial potential.

Two key observations are the presence of small current transients before E_{pit} which are indicative of metastable pitting corrosion, and the potential at which the current in the cathodic sweep crosses the current in the anodic sweep, known as the repassivation potential E_{rp}. Based on the relative potentials of E_{pit}, E_{corr}, and E_{rp}, the type of corrosion can be identified (Figure 4.2.4).

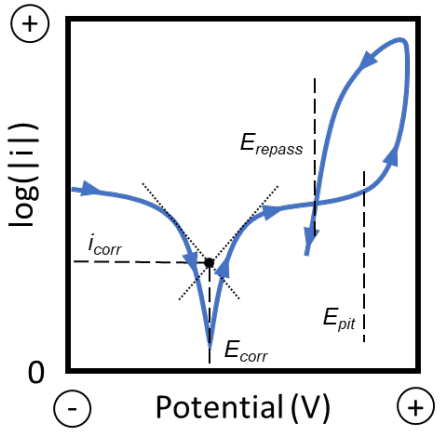

Figure 4.2.4. Sketched example of cyclic polarization data denoting how quantities such as i_{corr}, E_{pit}, E_{repass}, and E_{corr} are identified in a resulting voltammogram.

In the case of p^+-GaAs/*a*-TiO_2, E_{rp} is negative of E_{corr} and no current takeoff corresponding to E_{pit} is observed (Figure 4.2.5). This observation indicates that anodic polarization of p^+-GaAs/*a*-TiO_2 in 1.0 M KOH always results in transpassive behavior, i.e., the corrosion occurring is not due to breakdown of a passive film, but rather general uniform corrosion. If pitting corrosion were occurring, a passive region would be observed followed by a current spike as stable pits in the passive film form and E_{rp} would lie between E_{corr} and E_{pit}.

As E_{rp} is negative of E_{corr}, this means that passivation does not occur until applying a cathodic bias, so corrosion proceeds steadily at open-circuit and anodic polarization.

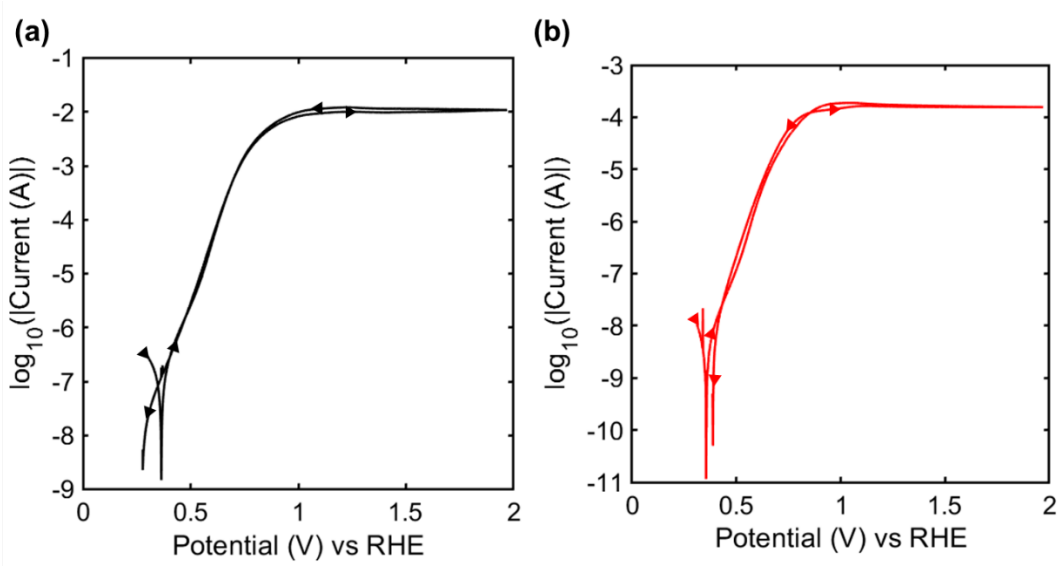

Figure 4.2.5. Cyclic polarization voltammograms for (a) p^+-GaAs and (b) p^+-GaAs/*a*-TiO_2 electrodes in aqueous 1.0 M KOH solutions. In both cases, the return scan results in a measured E_{corr} that is more negative than the initial forward scan.

This behavior is typical of metals with barrier layer films, wherein the metal undergoes general corrosion locally through pores in the barrier film and the barrier layer does not appreciably corrode. This is supported by the fact that only GaAs corrosion behavior is observed electrochemically and that cyclic polarization indicates general uniform corrosion. With this model, it is possible to further characterize the corrosion of the p^+-GaAs/*a*-TiO_2 system. The porosity of the film can be estimated by comparing the R_p of protected films to unprotected films using Equation 4.2.3:

Equation 4.2.3

$$P = \frac{R_{p,0}}{R_{p,film}}$$

Where P is the porosity, expressed as a percentage, $R_{p,0}$ is the polarization resistance of the unprotected surface, and $R_{p,film}$ is the polarization resistance of a sample with a barrier film. Porosity was calculated for a series of TiO_2 thicknesses (Figure 4.2.6). From this analysis, porosity is observed to increase with layer thickness, and porosity is generally on the order of 1% for thinner films and up to 5% for thicker films. These are high porosity values for these thicknesses of barrier layer and indicates that porosity is a major issue for this film deposition process.

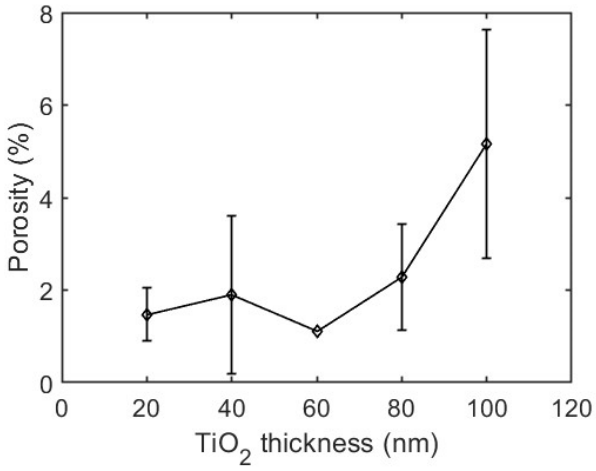

Figure 4.2.6. Porosity calculated via Equation 4.2.3 for p^+-GaAs/*a*-TiO_2 electrodes of varying thickness. Error bars indicate one standard deviation of the data.

From these analyses it can be concluded that GaAs/*a*-TiO_2 electrodes exhibit active corrosion and that the apparent pitting behavior is not due to the formation of metastable pits, but rather to the presence of small holes in the passive TiO_2 film that allow corrosion to proceed. This is supported by previously published results that identify atmospheric

particulates occluding some of the surface from the ALD treatment as the primary cause of failure in GaAs/*a*-TiO_2 films. This conclusion can be further supported by direct observation of μm-scale holes in TiO_2 films on Au after 48 h of corrosion in 1.0 M KOH. Holes in the TiO_2 film are observed which are ~18 nm in depth, corresponding to the expected thickness of the *a*-TiO_2 film. Coupled with conductive atomic force microscopy (AFM) measurements, these holes exhibit much higher conductivity than the surrounding TiO_2 due to the exposed Au surface.

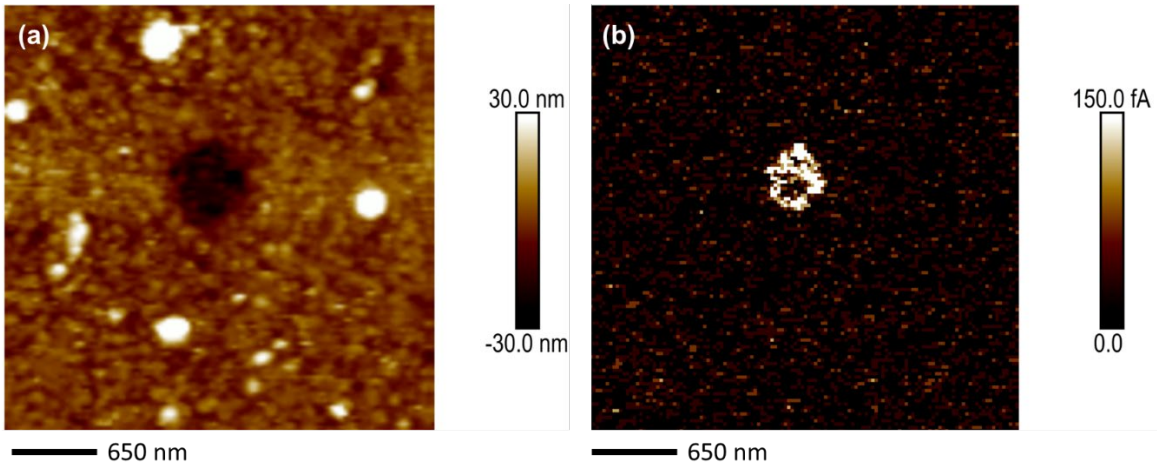

Figure 4.2.7. (a) AFM and (b) conductive AFM micrographs of pinhole pore in Si/TiAu/*a*-TiO_2 electrodes after potential hold at 1.0 V vs. RHE in aqueous 1.0 M KOH solution.

4.3—Mechanisms of short and long-term corrosion in GaAs/TiO_2 electrodes

While the primary corrosion mechanism of GaAs/*a*-TiO_2 electrodes has been characterized, prior work has suggested that a secondary corrosion mechanism may exist. When microislands of p^+-GaAs/*a*-TiO_2 are fabricated and exposed to 1.0 M KOH at 1.0 V vs. RHE, approximately 3% of the islands corrode immediately, consistent with the

hypothesis that pinholes are present in the TiO_2 film and cause immediate, rapid corrosion. However, between 2 and 20 hours, another 3% of islands fail. This observation has been hypothesized to be due to a second type of defect which is intrinsic to the TiO_2 film, which slowly reacts to eventually expose more GaAs surface to the corrosive 1.0 M KOH solution (Figure 4.3.1).

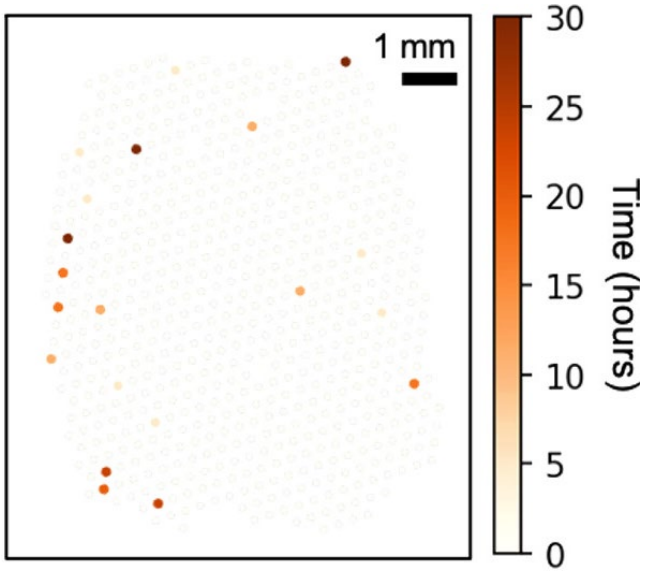

Figure 4.3.1. Graphical map of GaAs microisland electrode with failure time indicated by color.[32] Most islands do not fail at all but several islands fail nearly immediately and some fail after 20 h or more of operation at 1.0 V vs. RHE in 1.0 M KOH.

Based on literature studies of TiO_2 corrosion, three different mechanisms have been hypothesized to contribute to the corrosion behavior. The first hypothesis, known as the point defect model (PDM), involves the migration of vacancies and ions through the oxide film, resulting in voids between the GaAs substrate and TiO_2 overlayer that cause mechanical strain and eventually rupture to expose a new pinhole site. The second hypothesis invokes the presence of impurity inclusions in the films which dissolve over

time to form a new pinhole. The third hypothesis is more akin to pitting corrosion, wherein corrosive ions stochastically concentrate at a surface sites, resulting, in this case, in locally high pH that can corrode the TiO_2 and causing a cascading reaction that etches through to the substrate.

To verify the existence of long-term corrosion, chronoamperometry experiments were carried out over 5 hours with p^+-GaAs/*a*-TiO_2 electrodes in 1.0 M KOH solution at a potential of 1.0 V vs. RHE while monitoring the surface with optical microscopy. These experiments indicated that > 90% of etch pits observed initiated immediately upon application of anodic bias and grew steadily with time, though not all etch sites were the same size. Thus, the major point of failure remains the general corrosion enabled by porous barrier layer films. However, not all etch pits are of the same size, which is hypothesized to be due to differences in the size of initial pores. Over time, new, small pits are occasionally observed, indicated in Figure 4.3.2 by red arrows. This observation is consistent with the hypothesis that new pits form over time as the TiO_2 etches, however, the observation that pit size and growth rate is non-uniform leads to a competing hypothesis that these new pits are in fact pores present initially, but with pore diameters much smaller than other observed etch sites.

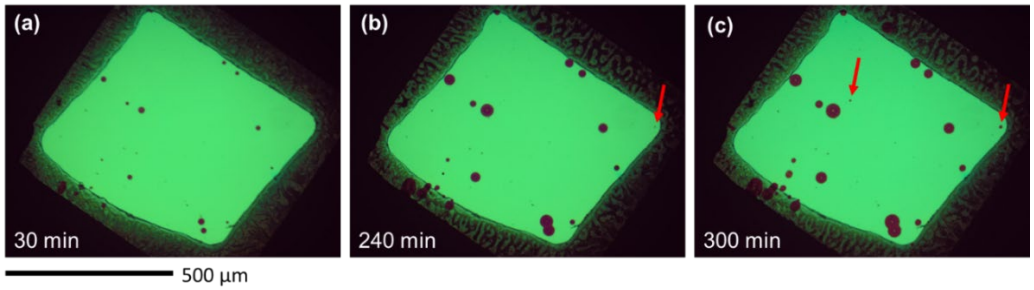

Figure 4.3.2. Time series of optical micrographs of p^+-GaAs/*a*-TiO_2 electrode under a bias of 1.0 V vs. RHE in 1.0 M KOH. As corrosion continues, new defects are exposed, indicated by red arrows.

To compare these hypotheses, *a*-TiO_2 was deposited on Au substrates and exposed to 1.0 M KOH and 1.0 V vs. RHE for 48 hours. Optical microscopy revealed what appeared to be many etched sites due to differences in color as well as a large site that may point to undercutting of the *a*-TiO_2 as a complicating factor. SEM of the discolored sites does not appear to show any etching at all, and EDX measurements point to K and C contamination but no loss in Ti signal in affected areas. Conductive AFM of the surface after experiment revealed etch pits ~1 µm in diameter, providing an upper bound for the possible size of pores leading to corrosion (Figure 4.3.3). Together, these results indicate that the TiO_2 layer may corrode over time, C and K contamination are present after etching in 1.0 M KOH and that most pores which cause corrosion are likely on the order of 1 µm in diameter.

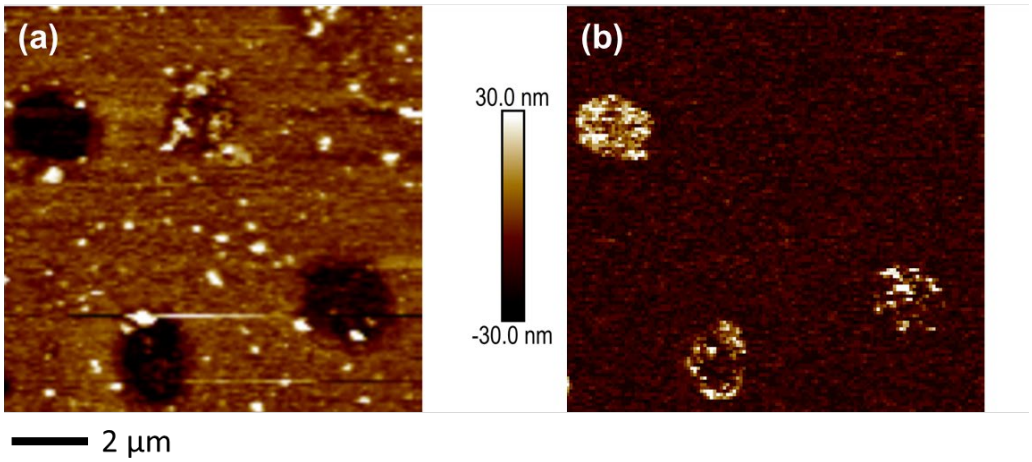

Figure 4.3.3. (a) AFM and (b) conductive AFM micrographs of Si/Ti/Au/*a*-TiO_2 electrode displaying conductivity at pinhole sites.

To identify whether impurities are present in *a*-TiO_2 films which may cause new corrosion sites, conductive AFM was performed on newly synthesized p^+-GaAs/*a*-TiO_2 electrodes. This analysis reproducibly reveals the presence of heterogeneous conductivity at the surface, nearly always linked to raised topological features (Figure 4.3.4). While many such features are present on the surface, relatively few are observed to be conductive. This observation is consistent with the hypothesis that impurity inclusions exist in the film which dissolve over time. To identify whether corrosion sites correlate with such impurities, a p^+-GaAs/*a*-TiO_2 electrode was corroded at 1.0 V vs. RHE in 1.0 M KOH for just 10 s to initiate corrosion without completely destroying sites that may dissolve over time. EDX analysis indicated the presence of Zr at some etched sites, likely from ZrO_2 used for wafer polishing. Thus, there is evidence to support the hypothesis that impurities are

present in the *a*-TiO_2 films as synthesized which may act as corrosion initiation sites and lead to additional failure points over hours of device operation.

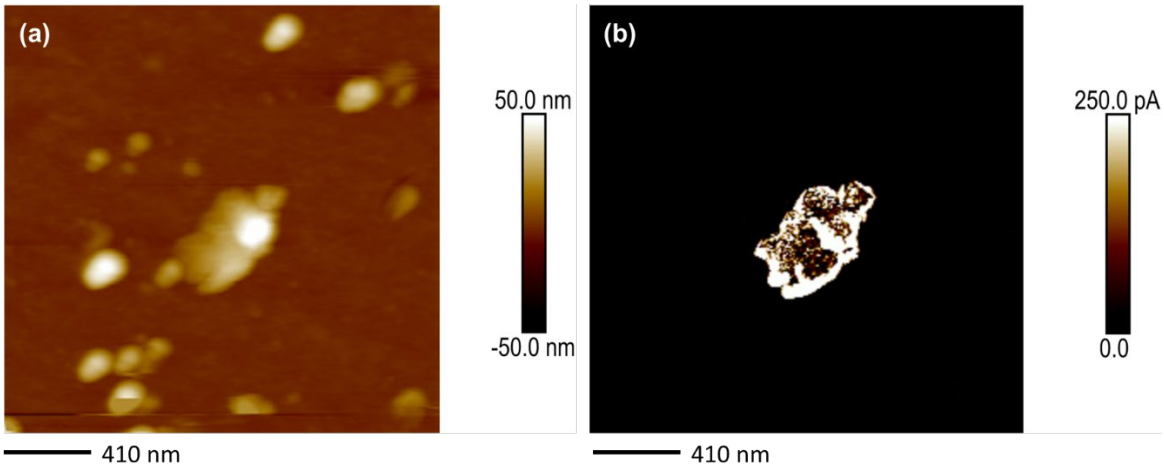

Figure 4.3.4. (a) AFM and (b) conductive AFM micrographs of a p^+-GaAs/*a*-TiO_2 electrode displaying anomalously high conductivity at a topological defect. While several defects are present in the scan, only one exhibits the conductivity which may contribute to long-term corrosion mechanisms.

If the majority of defects which cause device failure are present at the time of film synthesis, then a method which allows for the "repair" of defective surfaces is of considerable interest due to the possibility of greatly extending device lifetime and for more direct characterization of secondary defect sites. One such method for repair may be successive ALD-etch cycles. In this approach, an initial, defective layer of TiO_2 is deposited via ALD, and then an etch process is applied to remove any defect sites, then a second layer of TiO_2 is applied. It is hypothesized that, if the failure in the TiO_2 film is primarily due to randomized defects, then the likelihood of defects occurring at the same

site is very low and successive cycles of ALD and etch processes will produce films with more protective character than just additional ALD cycles alone.

To determine whether defects in successive layers of ALD are correlated with each other, GaAs was coated with 100 nm of TiO_2 and etched in 1.0 M KOH at 1.0 V vs. RHE for 1 hour, then sonicated in H_2O for 30 s and dried before coating with a second layer of 100 nm TiO_2 and etching again. Optical microscopy of the sample after this process indicates a high degree of correlation between etch sites in successive layers of TiO_2 . (Figure 4.3.5). However, some sites which were initially reactive were found to be stabilized by the second layer of TiO_2, indicating that this method may be promising if the correlation of defect sites between treatment cycles can be avoided.

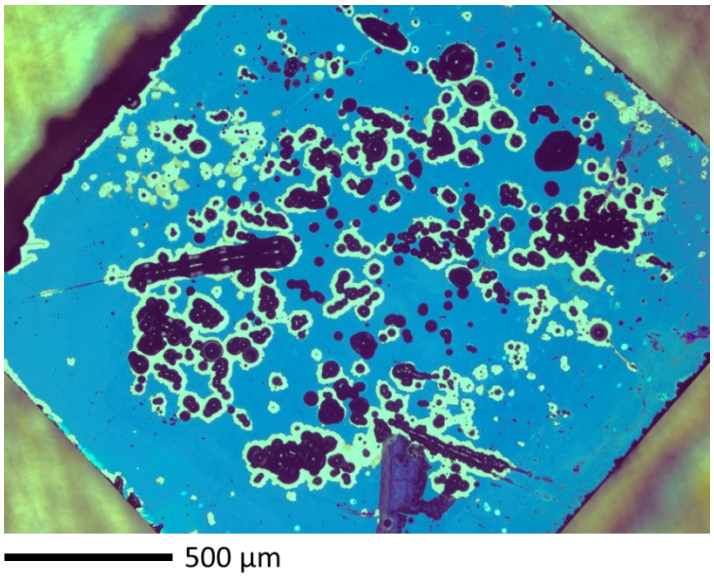

Figure 4.3.5. True-color optical microscopy image of GaAs/TiO_2 electrode which had 100 nm ALD-deposited TiO_2, then was etched for 1 h in 1.0 M KOH at 1.0 V vs. RHE, and then a second layer of 100 nm TiO_2 was deposited. This was then etched in KOH again to demonstrate how defects correlate with one another through successive depositions of TiO_2. Blue regions indicate pristine TiO_2, purple is area that was exposed by the first KOH

etch but covered by second ALD treatment, and silver regions are exposed GaAs from the second KOH etch.

Corrosion after the second ALD step was found to be most prevalent at the edges of etch pits produced in the first etch step, possibly indicating a geometric effect wherein the ALD process does not react quickly enough to form a conformal film at edge sites. To test this, the ALD process was given more time to react using the "exposure" mode wherein the vacuum line pulling precursor out of the reaction chamber is closed temporarily, giving molecules more time to diffuse and react with the surface. This experiment showed that exposure mode still results in a defective surface, and current is readily passed (Figure 4.3.6).

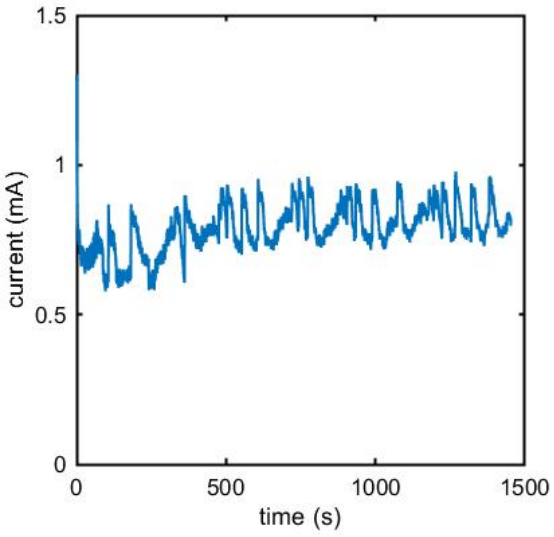

Figure 4.3.6. Chronoamperometry of GaAs/TiO_2 electrode which had 50 nm TiO_2 deposited, then etched in a modified RCA 1 solution (1:1:50 30% H_2O_2:35% NH_3:H_2O), rinsed, then etched in 1.0 M KOH at 1.0 V vs. RHE.

Additionally, to test whether edges posed a challenge to the standard ALD recipe, ALD was conducted on the roughened side of a GaAs wafer (Figure 4.3.7). It was found that the roughened surface could be readily passivated and only a few sites resulted in corrosion, similar to the polished case. It was noted, however, that successive cycles of ALD again failed to passivate. Optical microscopy of these sites revealed that etch pits had failure points inside them, in addition to the edge sites previously noted. Inspection of these sites appeared to show residue that prevented the second ALD cycle from effectively depositing.

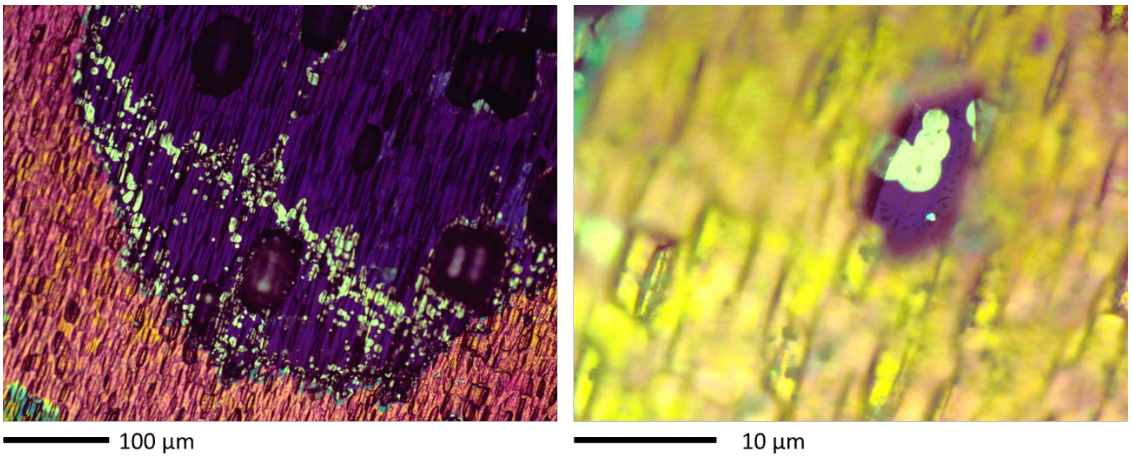

Figure 4.3.7. True-color optical microscopy image of p^+-GaAs/*a*-TiO_2 electrode which had 50 nm ALD-deposited TiO_2 on the rough side of the wafer, then was etched for 1 h in 1.0 M KOH at 1.0 V vs. RHE, and then a second layer of 50 nm TiO_2 was deposited. This was then etched in KOH again to demonstrate how defects correlate with one another through successive depositions of TiO_2.

Thus, geometric effects are unlikely to be the cause of the ALD-etch process failing to repair defective surfaces. Rather, chemical residues present on the surface, hypothesized to be from the etch process, prevent effective ALD deposition and leave the substrate

exposed. If this is the case, then a different etch process may reduce the amount or nature of chemical residues present and therefore allow for more reliable film repair.

4.4—Conclusions

In summary, the corrosion behavior of GaAs protected with TiO_2 ALD coatings has been investigated and possible mechanisms explored. Electrochemical measurements of such electrodes indicates the major source of corrosion is general GaAs corrosion through defects in the TiO_2 film. No passivity is observed and no electrochemical behavior linked to breakdown of TiO_2 is observed. Stability is only imparted by a decrease in kinetics caused by a decrease in the electrochemically active area, or porosity. The porosity of GaAs coated films is somewhat high and cannot be explained by the concentration of exposed GaAs sites previously reported. Instead, conductive defects linked to impurities have been observed which do occur in sufficient concentrations to explain the observed pitting and porosity. Attempts have been made to repair TiO_2 coatings, and it can be determined that the limiting factor in such repair attempts is the presence of chemical residues on the surface which are not removed in a water washing step. Defects are highly correlated between ALD deposition cycles, indicating that underlying chemistry is the culprit and that stochastic corrosion mechanisms such as the PDM and anion adsorption hypothesis are unlikely to contribute to overall corrosion behavior in the GaAs/TiO_2 system.

4.E—Experimental methods

Electrode preparation

GaAs wafers (p^+, Zn-doped, 0.5–5×10^{19} carriers cm^{-3}, AXT) were cleaned in a 0.04% Br/methanol solution and 1.0 M aqueous KOH solution. Bromine (reagent grade) was purchased from Sigma-Aldrich and methanol (anhydrous 99.8%) was purchased from Sigma-Aldrich. Potassium hydroxide (ACS grade) was purchased from Macron. 8 µL Br was diluted in 20 mL methanol to produce the Br/methanol solution. GaAs wafers were immersed first in Br/methanol solution and lightly agitated for 30 s, then rinsed with methanol and immersed in 1.0 M KOH for 15 s and rinsed with water and methanol. This process was repeated once (performed two times total) to produce clean, stoichiometric GaAs.

Wafers were then placed in a Savannah S200 ALD system for TiO_2 deposition. The Ti precursor was tetrakis(dimethylamido)titanium (TDMAT, 99% purity, Strem) and ultrapure water (≥18.2 MΩ, generated via Nanopure filtration system) was used as the oxidizing agent. The TDMAT precursor was held at 75 °C, the manifold and reactor were held at 150 °C, and the H_2O was at room temperature. Samples were held under vacuum with heating for 10 minutes to ensure consistent heating and sample interfaces between preps. To produce *a*-TiO_2, a 0.1 s pulse of TDMAT and 0.015 s pulse of H_2O was used, with a 15 s wait time between pulses. This process yielded a growth rate of 0.5 Å/cycle.

Ohmic back contacts were then added to the TiO_2-coated wafers. Ni back contacts were deposited on GaAs wafers via metal evaporation in a Denton Explorer 14 electron beam metal evaporation system with a base pressure < 1e-6 Torr. Ni pellets (99.995%, Kurt J. Lesker) were evaporated using an accelerating voltage of 10 kV and deposition current of

120 mA. Wafers were then manually cleaved into small (~0.04 cm^2) chips for electrode construction.

Electrodes were constructed by adhering completed GaAs chips to coiled solid-core wire encased in a borosilicate glass tube with conductive Ag paste, then, after the paste dried, covering all exposed wire and Ag paste with Loctite EA 9460 epoxy and left to cure for 24 h. The glass tube was used for structural support and the epoxy was used to insulate all electrical connections except the GaAs/TiO_2/solution interface. Before use in electrochemical experiments, completed electrodes were run through the Br/methanol and KOH GaAs cleaning process to dissolve any surface oxides that may complicate data interpretation.

Electrochemistry

Experiments were conducted in aqueous 1.0 M KOH solution unless otherwise specified. Pt mesh was used as a counter electrode and a Teflon-encased Hg/HgO reference electrode (CHI) was used for accuracy and stability in alkaline solution. Electrochemical experiments were carried out using a Solartron SI 1287 potentiostat equipped with a SI 1260 frequency response analyzer. Parameters for experiments varied and are specified in the text and figure captions of this chapter. Data analysis was accomplished using CorrWare software.

Additional characterization

Optical microscopy was performed with an Olympus BX51 microscope and images were analyzed with custom MATLAB image processing programs. Atomic force

microscopy was performed with a Bruker Dimension Icon AFM. Conductive AFM was performed using the same instrument with a PF-TUNA module and SCM-PIT conductive AFM tips. SEM and EDX were performed using an FEI Nova 450 SEM with an accelerating voltage of 10 kV and working distance of 5 mm using an in-lens secondary electron detector and integrated EDX detector.

References

(1) Bard, A. J.; Fox, M. A. Artificial Photosynthesis: Solar Splitting of Water to Hydrogen and Oxygen. *Acc. Chem. Res.* **1995**, *28* (3), 141–145. https://doi.org/10.1021/ar00051a007.

(2) Walter, M. G.; Warren, E. L.; McKone, J. R.; Boettcher, S. W.; Mi, Q.; Santori, E. A.; Lewis, N. S. Solar Water Splitting Cells. *Chem. Rev.* **2010**, *110* (11), 6446–6473. https://doi.org/10.1021/cr1002326.

(3) Davis, S. J.; Lewis, N. S.; Shaner, M.; Aggarwal, S.; Arent, D.; Azevedo, I. L.; Benson, S. M.; Bradley, T.; Brouwer, J.; Chiang, Y.-M.; Clack, C. T. M.; Cohen, A.; Doig, S.; Edmonds, J.; Fennell, P.; Field, C. B.; Hannegan, B.; Hodge, B.-M.; Hoffert, M. I.; Ingersoll, E.; Jaramillo, P.; Lackner, K. S.; Mach, K. J.; Mastrandrea, M.; Ogden, J.; Peterson, P. F.; Sanchez, D. L.; Sperling, D.; Stagner, J.; Trancik, J. E.; Yang, C.-J.; Caldeira, K. Net-Zero Emissions Energy Systems. *Science* **2018**, *360* (6396), eaas9793. https://doi.org/10.1126/science.aas9793.

(4) Spitler, M. T.; Modestino, M. A.; Deutsch, T. G.; Xiang, C. X.; Durrant, J. R.; Esposito, D. V.; Haussener, S.; Maldonado, S.; Sharp, I. D.; Parkinson, B. A.;

Ginley, D. S.; Houle, F. A.; Hannappel, T.; Neale, N. R.; Nocera, D. G.; McIntyre, P. C. Practical Challenges in the Development of Photoelectrochemical Solar Fuels Production. *Sustainable Energy Fuels* **2020**, *4* (3), 985–995. https://doi.org/10.1039/C9SE00869A.

(5) Tan, M. X.; Laibinis, P. E.; Nguyen, S. T.; Kesselman, J. M.; Stanton, C. E.; Lewis, N. S. Principles and Applications of Semiconductor Photoelectrochemistry. In *Progress in Inorganic Chemistry*; Karlin, K. D., Ed.; John Wiley & Sons, Inc.: Hoboken, NJ, USA, 2007; pp. 21–144. https://doi.org/10.1002/9780470166420.ch2.

(6) Ahluwalia, R. K.; Papadias, D. D.; Peng, J.-K.; Roh, H. S. System Level Analysis of Hydrogen Storage Options, 2019.

(7) Goldmeer, D. J. *Power to Gas: Hydrogen for Power Generation. Fuel Flexible Gas Turbines as Enablers for a Low or Reduced Carbon Energy Ecosystem*; General Electric Power, 2019.

(8) Carden, P.; Paterson, L. Physical, Chemical and Energy Aspects of Underground Hydrogen Storage. *International Journal of Hydrogen Energy* **1979**, *4* (6), 559–569.

(9) Chen, T.-P. *Hydrogen Delivey [sic] Infrastructure Option Analysis*; Nexant, Inc., 101 2nd St., San Francisco, CA 94105, 2010.

(10) Benson, E. E.; Zhang, H.; Schuman, S. A.; Nanayakkara, S. U.; Bronstein, N. D.; Ferrere, S.; Blackburn, J. L.; Miller, E. M. Balancing the Hydrogen Evolution

Reaction, Surface Energetics, and Stability of Metallic MoS_2 Nanosheets via Covalent Functionalization. *J. Am. Chem. Soc.* **2018**, *140* (1), 441–450. https://doi.org/10.1021/jacs.7b11242.

(11) Bard, A. J.; Faulkner, L. R. *Electrochemical Methods: Fundamentals and Applications*, 2nd ed.; Wiley: New York, 2001.

(12) Zeng, K.; Zhang, D. Recent Progress in Alkaline Water Electrolysis for Hydrogen Production and Applications. *Progress in Energy and Combustion Science* **2010**, *36* (3), 307–326. https://doi.org/10.1016/j.pecs.2009.11.002.

(13) Anantharaj, S.; Ede, S. R.; Sakthikumar, K.; Karthick, K.; Mishra, S.; Kundu, S. Recent Trends and Perspectives in Electrochemical Water Splitting with an Emphasis on Sulfide, Selenide, and Phosphide Catalysts of Fe, Co, and Ni: A Review. *ACS Catal.* **2016**, *6* (12), 8069–8097. https://doi.org/10.1021/acscatal.6b02479.

(14) Verlage, E.; Hu, S.; Liu, R.; Jones, R. J. R.; Sun, K.; Xiang, C.; Lewis, N. S.; Atwater, H. A. A Monolithically Integrated, Intrinsically Safe, 10% Efficient, Solar-Driven Water-Splitting System Based on Active, Stable Earth-Abundant Electrocatalysts in Conjunction with Tandem III–V Light Absorbers Protected by Amorphous TiO_2 Films. *Energy Environ. Sci.* **2015**, *8* (11), 3166–3172. https://doi.org/10.1039/C5EE01786F.

(15) Laskowski, F. A. L.; Oener, S. Z.; Nellist, M. R.; Gordon, A. M.; Bain, D. C.; Fehrs, J. L.; Boettcher, S. W. Nanoscale Semiconductor/Catalyst Interfaces in

Photoelectrochemistry. *Nat. Mater.* **2020**, *19* (1), 69–76. https://doi.org/10.1038/s41563-019-0488-z.

(16) Fu, H. J.; Moreno-Hernandez, I. A.; Buabthong, P.; Papadantonakis, K. M.; Brunschwig, B. S.; Lewis, N. S. Enhanced Stability of Silicon for Photoelectrochemical Water Oxidation through Self-Healing Enabled by an Alkaline Protective Electrolyte. *Energy Environ. Sci.* **2020**, *13* (11), 4132–4141. https://doi.org/10.1039/D0EE02250K.

(17) Vijselaar, W.; Tiggelaar, R. M.; Gardeniers, H.; Huskens, J. Efficient and Stable Silicon Microwire Photocathodes with a Nickel Silicide Interlayer for Operation in Strongly Alkaline Solutions. *ACS Energy Lett.* **2018**, *3* (5), 1086–1092. https://doi.org/10.1021/acsenergylett.8b00267.

(18) Warren, E. L.; Atwater, H. A.; Lewis, N. S. Silicon Microwire Arrays for Solar Energy-Conversion Applications. *J. Phys. Chem. C* **2014**, *118* (2), 747–759. https://doi.org/10.1021/jp406280x.

(19) Pourbaix, M. *Atlas of Electrochemical Equilibria in Aqueous Solutions.*; NACE International: Houston, 1974.

(20) Hu, S.; Xiang, C.; Haussener, S.; Berger, A. D.; Lewis, N. S. An Analysis of the Optimal Band Gaps of Light Absorbers in Integrated Tandem Photoelectrochemical Water-Splitting Systems. *Energy Environ. Sci.* **2013**, *6* (10), 2984. https://doi.org/10.1039/c3ee40453f.

(21) Jain, A.; Ong, S. P.; Hautier, G.; Chen, W.; Richards, W. D.; Dacek, S.; Cholia, S.; Gunter, D.; Skinner, D.; Ceder, G.; Persson, K. A. Commentary: The Materials Project: A Materials Genome Approach to Accelerating Materials Innovation. *APL Materials* **2013**, *1* (1), 011002. https://doi.org/10.1063/1.4812323.

(22) Bae, D.; Shayestehaminzadeh, S.; Thorsteinsson, E. B.; Pedersen, T.; Hansen, O.; Seger, B.; Vesborg, P. C. K.; Ólafsson, S.; Chorkendorff, I. Protection of Si Photocathode Using TiO2 Deposited by High Power Impulse Magnetron Sputtering for H2 Evolution in Alkaline Media. *Solar Energy Materials and Solar Cells* **2016**, *144*, 758–765. https://doi.org/10.1016/j.solmat.2015.10.020.

(23) Bae, D.; Seger, B.; Vesborg, P. C. K.; Hansen, O.; Chorkendorff, I. Strategies for Stable Water Splitting via Protected Photoelectrodes. *Chem. Soc. Rev.* **2017**, *46* (7), 1933–1954. https://doi.org/10.1039/C6CS00918B.

(24) Shen, X.; Yao, M.; Sun, K.; Zhao, T.; He, Y.; Chi, C.-Y.; Zhou, C.; Dapkus, P. D.; Lewis, N. S.; Hu, S. Defect-Tolerant TiO_2 -Coated and Discretized Photoanodes for >600 h of Stable Photoelectrochemical Water Oxidation. *ACS Energy Lett.* **2021**, *6* (1), 193–200. https://doi.org/10.1021/acsenergylett.0c02521.

(25) Benck, J. D.; Lee, S. C.; Fong, K. D.; Kibsgaard, J.; Sinclair, R.; Jaramillo, T. F. Designing Active and Stable Silicon Photocathodes for Solar Hydrogen Production Using Molybdenum Sulfide Nanomaterials. *Advanced Energy Materials* **2014**, *4* (18), 1400739. https://doi.org/10.1002/aenm.201400739.

(26) Seger, B.; Tilley, D. S.; Pedersen, T.; Vesborg, P. C. K.; Hansen, O.; Grätzel, M.; Chorkendorff, I. Silicon Protected with Atomic Layer Deposited TiO2: Durability Studies of Photocathodic H2 Evolution. *RSC Adv.* **2013**, *3* (48), 25902–25907. https://doi.org/10.1039/C3RA45966G.

(27) Richter, M. H.; Cheng, W.-H.; Crumlin, E. J.; Drisdell, W. S.; Atwater, H. A.; Schmeißer, D.; Lewis, N. S.; Brunschwig, B. S. X-Ray Photoelectron Spectroscopy and Resonant X-Ray Spectroscopy Investigations of Interactions between Thin Metal Catalyst Films and Amorphous Titanium Dioxide Photoelectrode Protection Layers. *Chem. Mater.* **2021**, *33* (4), 1265–1275. https://doi.org/10.1021/acs.chemmater.0c04043.

(28) Hu, S.; Richter, M. H.; Lichterman, M. F.; Beardslee, J.; Mayer, T.; Brunschwig, B. S.; Lewis, N. S. Electrical, Photoelectrochemical, and Photoelectron Spectroscopic Investigation of the Interfacial Transport and Energetics of Amorphous TiO_2 /Si Heterojunctions. *J. Phys. Chem. C* **2016**, *120* (6), 3117–3129. https://doi.org/10.1021/acs.jpcc.5b09121.

(29) Lichterman, M. F.; Richter, M. H.; Hu, S.; Crumlin, E. J.; Axnanda, S.; Favaro, M.; Drisdell, W.; Hussain, Z.; Brunschwig, B. S.; Lewis, N. S.; Liu, Z.; Lewerenz, H.-J. An Electrochemical, Microtopographical and Ambient Pressure X-Ray Photoelectron Spectroscopic Investigation of Si/TiO_2 /Ni/Electrolyte Interfaces. *J. Electrochem. Soc.* **2016**, *163* (2), H139–H146. https://doi.org/10.1149/2.0861602jes.

(30) Nunez, P.; Richter, M. H.; Piercy, B. D.; Roske, C. W.; Cabán-Acevedo, M.; Losego, M. D.; Konezny, S. J.; Fermin, D. J.; Hu, S.; Brunschwig, B. S.; Lewis, N. S. Characterization of Electronic Transport through Amorphous TiO_2 Produced by Atomic Layer Deposition. *J. Phys. Chem. C* **2019**, *123* (33), 20116–20129. https://doi.org/10.1021/acs.jpcc.9b04434.

(31) Buabthong, P.; Ifkovits, Z. P.; Kempler, P. A.; Chen, Y.; Nunez, P. D.; Brunschwig, B. S.; Papadantonakis, K. M.; Lewis, N. S. Failure Modes of Protection Layers Produced by Atomic Layer Deposition of Amorphous TiO_2 on GaAs Anodes. *Energy Environ. Sci.* **2020**, *13* (11), 4269–4279. https://doi.org/10.1039/D0EE02032J.

(32) Buabthong, P.; Evans, J. M.; Rinaldi, K. Z.; Kennedy, K. M.; Fu, H. J.; Ifkovits, Z. P.; Kuo, T.-J.; Brunschwig, B. S.; Lewis, N. S. GaAs Microisland Anodes Protected by Amorphous TiO_2 Films Mitigate Corrosion Spreading During Water Oxidation in Alkaline Electrolytes. *ACS Energy Lett.* **2021**, *6* (10), 3709–3714. https://doi.org/10.1021/acsenergylett.1c01174.

(33) Yu, W.; Richter, M. H.; Simonoff, E.; Brunschwig, B. S.; Lewis, N. S. Investigations of the Stability of GaAs for Photoelectrochemical H_2 Evolution in Acidic or Alkaline Aqueous Electrolytes. *J. Mater. Chem. A* **2021**, *9* (40), 22958–22972. https://doi.org/10.1039/D1TA04145B.

(34) Allongue, P.; Blonkowski, S. Corrosion of III–V Compounds; a Comparative Study of GaAs and InP. *Journal of Electroanalytical Chemistry and*

Interfacial Electrochemistry **1991**, *316* (1–2), 57–77. https://doi.org/10.1016/0022-0728(91)87036-4.

(35) Kelly, R.; Scully, J.; Shoesmith, D.; Buchheit, R. Electrochemical Techniques in Corrosion Science and Engineering. **2003**. https://doi.org/10.1201/9780203909133.

(36) Yu, Y.; Sun, C.; Yin, X.; Li, J.; Cao, S.; Zhang, C.; Voyles, P. M.; Wang, X. Metastable Intermediates in Amorphous Titanium Oxide: A Hidden Role Leading to Ultra-Stable Photoanode Protection. *Nano Lett.* **2018**, *18* (8), 5335–5342. https://doi.org/10.1021/acs.nanolett.8b02559.

Chapter 5

Selective Deposition via Anodic Electropolymerization at Electrochemically Active Defects in TiO_2 Protection Layers on GaAs

5.1—Introduction and background

Amorphous TiO_2 (*a*-TiO_2) deposited via atomic-layer deposition (ALD) has been developed as a protection layer for semiconductor photoanodes utilized in solar-driven water-splitting cells, as well as in CO_2 reduction cells that utilize strongly alkaline aqueous electrolytes.[1–7] *a*-TiO_2 coatings prolong the device lifetime due to the corrosion resistance of TiO_2, with some devices maintaining photoelectrochemical activity for > 600 h.[6,8] However, ALD *a*-TiO_2 coatings exhibit both extrinsic and intrinsic defects.[6,8–12] Extrinsic defects, caused by factors external to the protective film such as atmospheric particulates, lead to pinholes in the protection layer, and expose the underlying semiconductor to solution thereby facilitating corrosion.[8–10,13,14] Intrinsic defects are inhomogeneities within the film, such as crystalline regimes and grain boundaries.[11,12] These intrinsic defects can be electrically conductive and consequently can facilitate corrosion without direct exposure of the semiconductor substrate to the solution.[12] Moreover, corrosion through intrinsic defects may also contribute to the formation of new exposed sites.[9–12] Extrinsic and intrinsic defects can collectively limit lifetimes of planar devices to < 10 h.[6,8–10] Corrosion-tolerant device architectures can mitigate corrosion propagation from defective film

sites.[6,8–10,15] However, these architectures can require significant additional processing and still experience losses in device performance due to continuous, albeit slow, corrosion.

Identification and quantification of defect sites could provide information that can be applied toward improved device design and defect mitigation. Electroless Au deposition ("Au staining") allows for detection of defects in *a*-TiO_2 films, with reduction of Au^{3+} ions in solution to Au metal coupled to GaAs corrosion.[9] The deposition of Au is selective for extrinsic defects such as pinholes, but the technique is destructive and does not identify intrinsic defects.[9,11] Additionally, new pinholes attributed to intrinsic defects have been shown to form in protected electrodes over time.[9,10] The destructive property of this technique is due to GaAs corrosion being the counter reaction for Au deposition. Electrochemistry allows half reactions for material deposition and counter reactions to take place on separate electrodes, with the possibility of eliminating concurrent working electrode corrosion from the overall reaction.

The interfacial energetics of the GaAs/*a*-TiO_2/solution junction may be leveraged to facilitate identification of both extrinsic and intrinsic defects. When a material such as a metal catalyst having a work function (φ) < 5 eV is added to the interface, a defect band originating from Ti^{3+} species in the bulk allows for conductivity through the protection layer.[11,16–20] Without such a contact, the *a*-TiO_2/solution interface is rectifying.[16,19] This rectification allows for isolation of sites, such as pinholes or conductive intrinsic defects, at which anodic current can flow.

However, to prevent destruction of the substrate, the reaction conditions must be designed such that the corrosion half reaction does not occur. Aqueous deposition is unsuitable for this application as water assists in the initiation of GaAs corrosion.[21] Electropolymerization is a technique which has been widely used for material protection and can be performed in nonaqueous conditions.[22–24] Thus, it is hypothesized that nonaqueous anodic electropolymerization can be used to selectively react with electrochemically active defect sites in an *a*-TiO_2 protection layer without corroding the substrate. In this approach, monomer species at the interface are oxidized electrochemically and react with species in solution to form polymers. To properly identify defects, the polymers must not form without the initial oxidation event that occurs exclusively at sites on the surface where anodic current can flow.

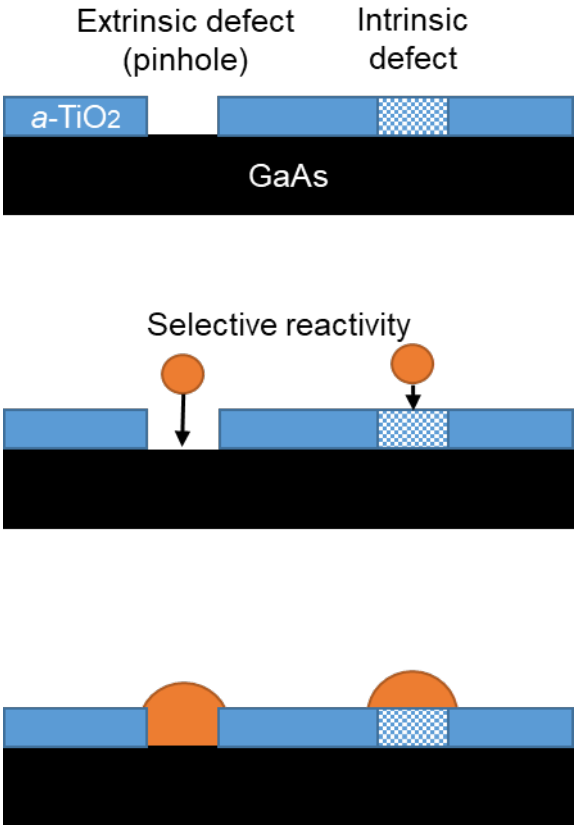

Figure 5.1.1. Schematic of an *a*-TiO_2 interface with a both extrinsic and intrinsic defects, demonstrating the proposed scheme by which electropolymerization can identify such defects.

5.2—Selective Electropolymerization and Defect Quantification

Electropolymerization allows for selective anodic deposition in conductive sites in the rectifying ALD *a*-TiO_2.[22–26] Electropolymerization, moreover, can be performed in non-aqueous solvents, minimizing effects associated with water as the primary cause of corrosion in semiconductors such as GaAs.[21,27] In aqueous environments or in the presence of H_2O, corrosion of the substrate occurs, eliminating the advantage of the system (Figure 5.2.1). For successful marking of defects, a monomer is required which is soluble in

nonaqueous solvent, can perform electrochemically initiated polymerization, and contains a moiety which acts as a tag for spectroscopic identification. 4-fluoro-ortho-phenylenediamine (F-oPD) was selected as it fulfills all requirements. The fluorine-free monomer has previously seen use in protection systems and defect passivation and the fluorine moiety will act as a unique identifier.[24,25]

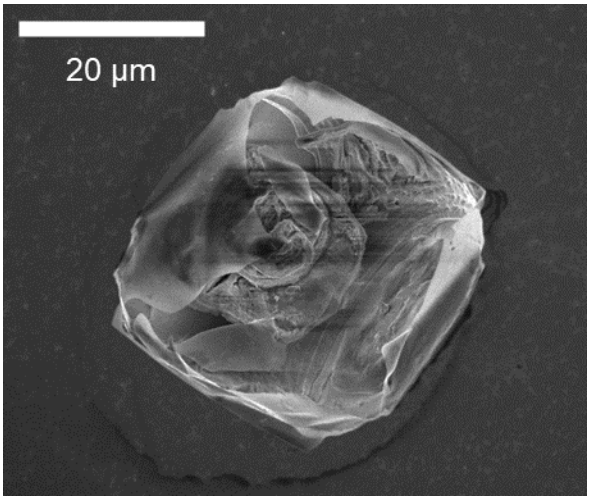

Figure 5.2.1. SEM of poly(F-oPD) deposited on *a*-TiO_2-protected p^+-GaAs in aqueous solution with concurrent pitting corrosion.

F-oPD electropolymerization was attempted using a series of cyclic voltammetric sweeps to create poly-F-oPD on the surface of *a*-TiO_2 protected p-GaAs. Deposits with a diameter of 320 ± 230 nm were observed on the surface by SEM. (Figure 5.2.1).[9] The diameter of the deposits varied with the number of voltammetric sweeps, although after 50 cycles, the deposit diameter only increased to 480 ± 140 nm (Figure 5.2.2). The concentration of defects identified by electropolymerization was $32 \pm 21 \times 10^4$ defects cm^{-2}, which is larger than the $4 \pm 3 \times 10^4$ defects cm^{-2} concentration of extrinsic defects indicated by Au staining

on nominally identically prepared samples (Figure 5.2.3d). At higher magnification, the deposits were found to be roughly uniform in diameter and no etch pits were visible underneath the deposits (Figure 5.2.3b). To confirm that etch pits were not formed during reaction, cross-sectional SEM was performed on deposit sites (Figure 5.2.3d). At the site of deposition, the underlying semiconductor did not exhibit substantial etching, and the imaged deposits were 220 ± 40 nm in height.

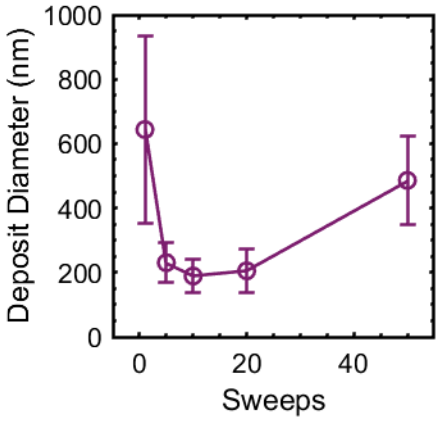

Figure 5.2.2. Distribution of deposit diameters as a function of the number of cyclic voltammetry sweeps performed.

Polymer deposits hypothesized to be due to reaction with defect sites were not observed to appear as clusters. This is consistent with prior work which has found a random distribution of extrinsic defects and accounts for the variability in defect concentration (Figure 5.2.3d).[8,9] The larger concentration of deposits observed using the electropolymerization method relative to using Au staining ($32 \pm 21 \times 10^4$ defects cm$^-$2 vs. $4 \pm 3 \times 10^4$ defects cm^{-2}, respectively) indicates that the electrochemical method, if successful, is not selective for extrinsic defects such as pinholes in the protective film. Instead, the electropolymerization

method can react with extrinsic defects, which are known to be conductive, as well as electrochemically active intrinsic defects that may also contribute to device failure.[9,11,12] This method, then, may be a straightforward approach for identifying any electrochemically active defects in *a*-TiO_2 without damaging the substrate. The order of magnitude increase in identified defects is consistent with prior observations that the initially present pinhole defects are not the sole cause of device failure and that more corrosion pits form over time.[8–10,12] Thus, nonaqueous electropolymerization may assist in identifying defect sites which are susceptible to pitting corrosion during device operation.

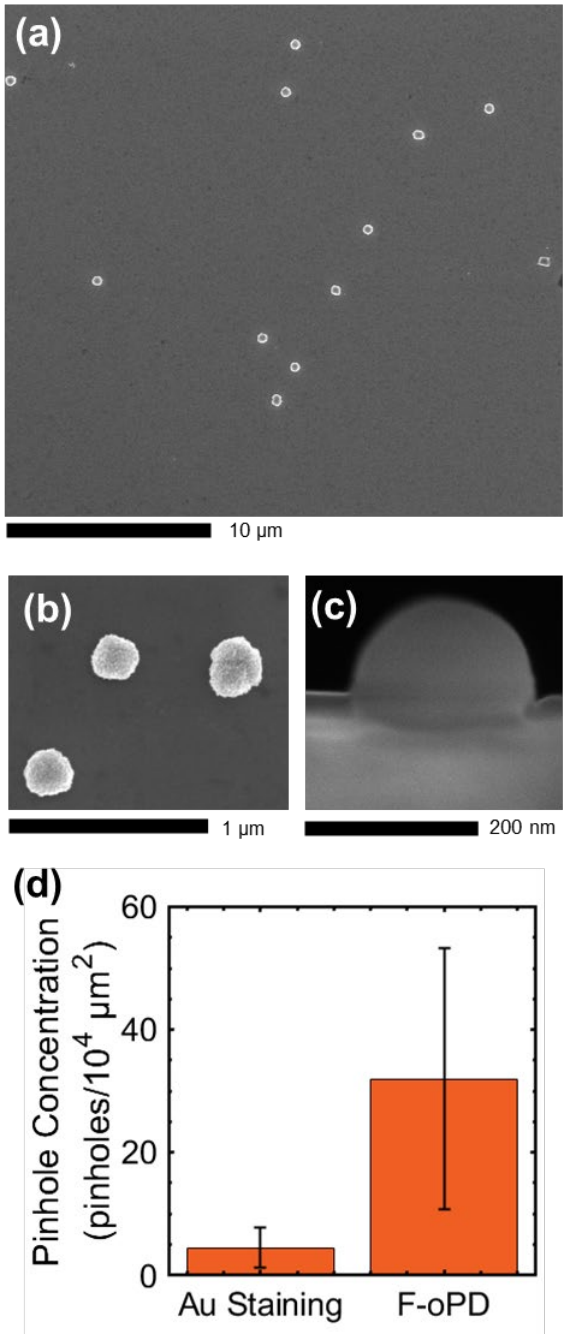

Figure 5.2.3. (a) Large-scale and (b) zoomed in scanning electron micrograph of F-oPD deposits on *a*-TiO_2 protected p-GaAs. Brighter spots are hypothesized to be polymer deposits. (c) Cross-sectional scanning electron micrograph of a polymer deposit. (d) Measurement and statistical analysis of defect concentration using Au staining and polymer deposition methods.

5.3—Characterization of Deposits

To confirm the presence of polymer on the surface, XPS was performed on polymer-treated GaAs/*a*-TiO_2 electrodes. The XP survey spectrum (Figure 5.3.1a) indicated the presence of F, Ti, O, and C. No signal was observed for Ga or As, though this is consistent with a TiO_2 film of ~20 nm preventing detection. Interpretation of the C 1s spectrum was complicated by adventitious C (AdC), which is a contaminant on nearly all surfaces. However, the F moiety in the F-oPD monomer and polymer provided a signal that was clearly differentiated from spectator species in the solution. The C 1s region contained a contribution from electron-poor C at a BE of 288.6 eV (Figure 5.3.1b). This signal may be attributable to F bound to an aromatic C group, such as F bound to aromatic C, though other species such as C=O bonds may be responsible for, or interfere with, emissions at this energy.[28–30] To confirm the presence of F-containing organic species, the F 1s region was examined. A peak at a BE of 688.0 eV was observed, consistent with an organic F species (Figure 5.3.1c).[29–31]

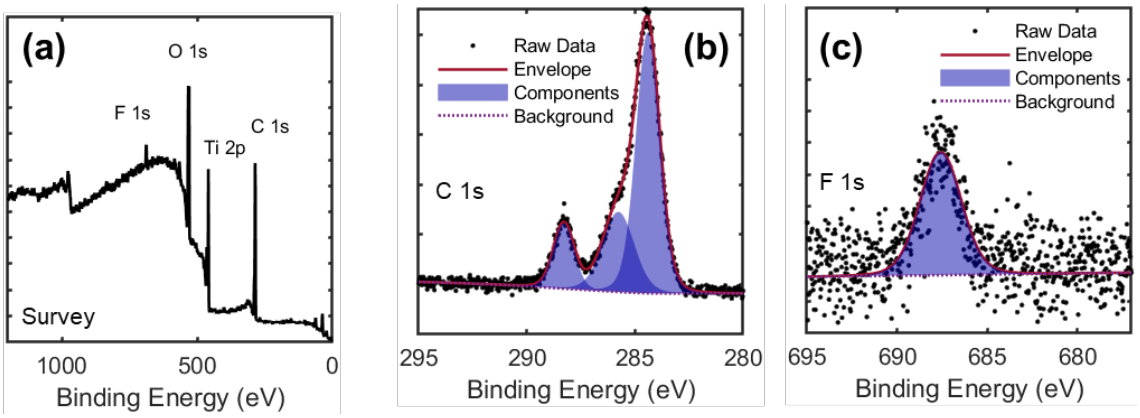

Figure 5.3.1. XPS of F-oPD treated electrodes after sequential rinsing with water, isopropyl alcohol, and acetone. (a) The survey scan showed emissions from C, Ti, O, and F. High-resolution XPS scans of the (b) C 1s and (c) F 1s regions.

AFM was performed on polymer-treated GaAs/*a*-TiO_2 electrodes to reveal the 3-D morphology of the deposits and to spatially resolve any differences in conductivity. The deposits analyzed were larger than those imaged with SEM, with a measured diameter of 780 ± 90 nm and height of 310 ± 20 nm (Figure 5.3.2a, c). To determine whether the deposited polymer was insulating, conductive AFM using PF-TUNA was performed on single deposits as well as on a group of deposits. The current at the center of the deposits was similar to that of the surrounding *a*-TiO_2, consistent with an insulating deposit.

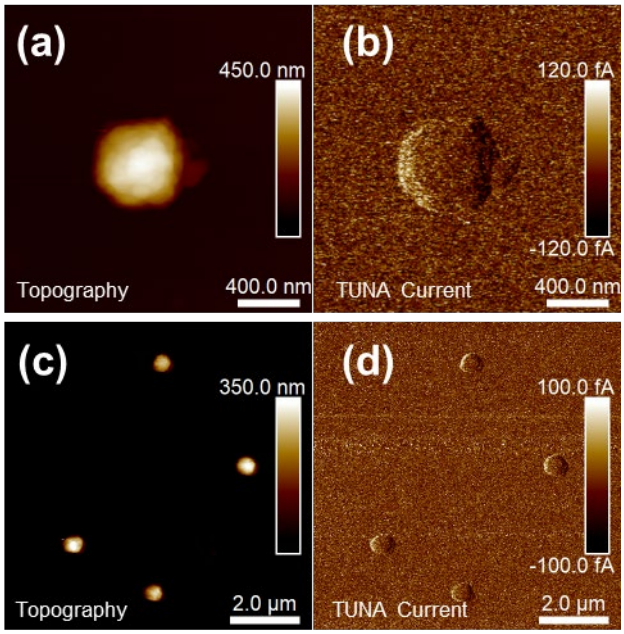

Figure 5.3.2. Topographic (a,c) and conductivity (b,d) measurements of poly-F-oPD deposits via AFM. Height scale in topographic measurements referenced to minimum height in scan.

The insulating character indicates that the deposits may have a critical size above which no current was able to flow from the electrode into solution. However, the current observed during deposition may increase (Figure 5.3.3). Electrochemically deposited polymers often display ionic conductivity that can be observed as capacitive current increases in cyclic voltammograms, consistent with the observed behavior.[23] These observations, combined with the deposit size distribution as a function of cycle number (Figure 5.2.2), lead to the hypothesis that deposits of F-oPD were limited in size by poor conductivity but that ionic conduction through these sites remains possible and therefore this technique does not prevent corrosion through marked sites.

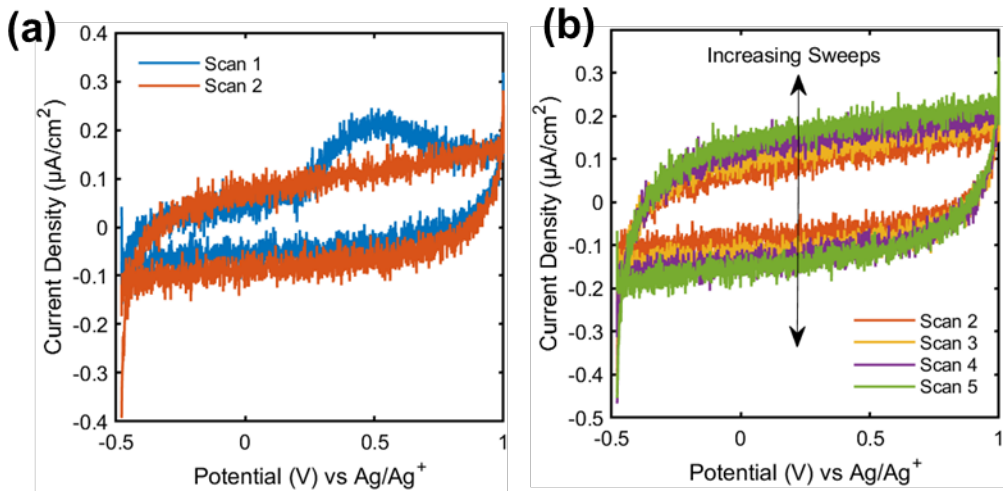

Figure 5.3.3. Cyclic voltammogram of F-oPD oxidation on p^+-GaAs/a-TiO_2 working electrode (a) on initial sweep, an irreversible oxidation is observed at ~0.5 V vs. Ag/Ag^+ which is assigned to F-oPD oxidation. On subsequent scans (b) no oxidation event is observed but capacitance increases with increasing scan number.

5.4—Contamination of surface and refutation of deposition hypothesis

Localized elemental analysis was performed to verify the identity of the deposits and whether polymer was in fact the most likely source of the depositions. EDX analysis indicated that deposits contained significant quantities of Al and Ag, with no detectable F. This observation calls into question the prior work, as metal oxide impurities present at the surface would also be observed to be insulating, and the size of the deposits is identical to previous analyses.

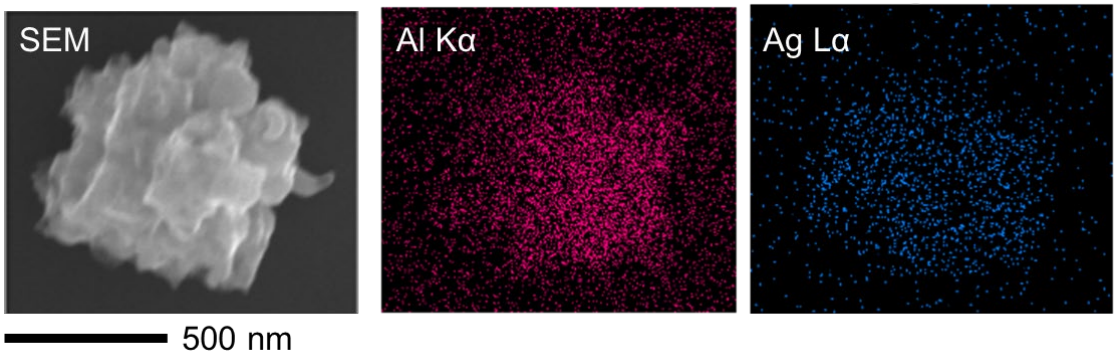

Figure 5.4.1. (a) SEM of deposit observed on p^+-GaAs/*a*-TiO_2 electrode. (b) Al Kα and (c) Ag Lα EDX maps collocated on the deposit in (a). The deposit is found to be composed primarily of Ag and Al, not C as hypothesized.

As the prior results were called into question, a control experiment was conducted to identify whether electropolymerized material would be selective for conductive sites. In this experiment, Au staining is done to deposit Au selectively at exposed GaAs sites at the surface. The resulting Au deposits are recognizable under SEM and must correspond to conductive defect sites. Polypyrrole was used as it readily polymerizes into a conductive polymer in the studied conditions and therefore can grow to a thickness that is readily visible via SEM. If the polymer is selectively depositing at conductive sites, then all Au

deposits should be covered in polymer. However, the results of these experiments showed that only some Au sites were covered by polypyrrole when anodically scanning (Figure 5.4.2). The results of this experiment further invalidate prior observations of selective electropolymerization at the surface, as there is no conclusive evidence that electropolymerization will selectively occur at known conductive sites. Future work should investigate the polymer deposition method from first principles, focusing on deposition of an insulating, stable polymer and controlling deposition such that electropolymerization is confirmed to occur only at conductive sites.

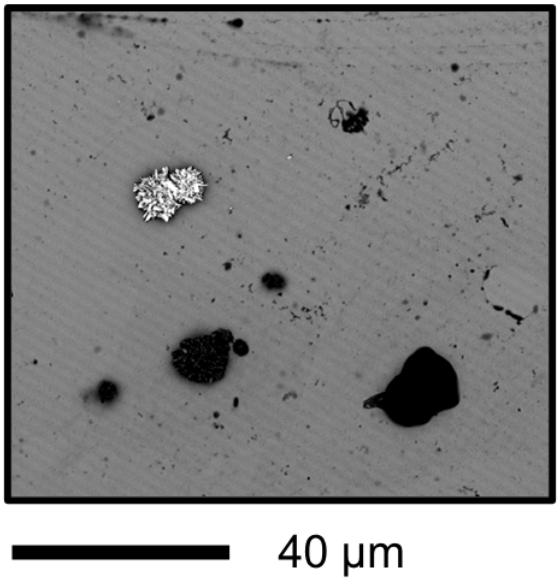

Figure 5.4.2. SEM of p^+-GaAs/*a*-TiO_2 electrode which has undergone Au staining in 5 mM $HAuCl_4$ for 10 minutes, then electropolymerization of pyrrole via cyclic voltammetry in acetonitrile. Bright feature is a Au deposit which has not had polypyrrole deposited on it while dark, black features are polypyrrole deposits.

5.5—Conclusions

Thus, while electropolymerization may yet be a method for selectively reacting with defects in a *a*-TiO_2 film, F-oPD has not conclusively been observed to selectively deposit at defect sites. Instead, impurities such as Al and Ag were observed at deposit sites which may explain nearly all of the observations attributed to F-oPD. Future work should focus on developing polymer deposition on conductive, stable substrates such as Au to characterize how polymers deposit and then use artificial pores to identify how such polymers can be distinguished and confirm deposition at all conductive sites. Additionally, development of an electropolymerization technique which is selective and results in a passive deposit that is stable in alkaline conditions would enable "repair" of defective surfaces in a scalable, efficient manner.

5.E—Experimental methods

Materials and Chemicals

4-fluoro-1,2-phenylenediamine (97 %, Millipore Sigma), acetonitrile (HPLC grade, VWR), tetrabutylammonium perchlorate ($TBAClO_4$, 98 %, Fisher Scientific), ethanol (200 proof, Koptec), acetone (ACS grade >99.5%, Millipore Sigma), and HCl (ACS grade 36.5–38%, Millipore Sigma), were used as received. Deionized water (> 18 MΩ resistivity) was obtained using a Barnstead Nanopure system. p^+-GaAs(100) (Zn doped at 0.5–5.0 · 10^{19}, AXT incorporated) was used as the semiconducting substrate. Photoelectrode assemblies were generated using conductive Ag paint (SPI Supplies) and EA 9460 epoxy (Loctite).

Electrode Fabrication

Protection layers were synthesized via ALD with 400 cycles of tetrakis(dimethylamido)titanium (TDMAT) with water as the counter reactant at 150 °C. To remove the native oxide prior to ALD treatment, p^+-GaAs(100) wafer sections were etched for 30 min in 10% HCl(aq). Back contacts were formed by sputtering Ni and Cu. The ALD-treated GaAs samples were attached to a Cu wire with Ag paint. The samples were then encased in a glass tube for structural support, and were protected with epoxy to seal all but the polished electrode surface.

Electrochemistry

Electrochemical experiments were performed using a BioLogic SP-200 potentiostat with a Pt mesh counter electrode in a glass cell. Electropolymerization was performed using cyclic voltammetry with a 0.1 M $TBAClO_4$ solution in CH_3CN that contained 0.01 M of monomer. The working electrode was GaAs/TiO_2 and the quasi-reference electrode was Ag^+/Ag. The potential was scanned at a rate of 50 mV s^{-1} from 0.00 V to 1.00 V vs. Ag^+/Ag and the scans were repeated five times in a deposition.

Prior to analysis, the surfaces of polymer-treated samples were rinsed sequentially with water, ethanol, acetonitrile, and acetone to remove any solution residue or poorly adhered polymer.

To minimize interference from side reactions and additionally to minimize the impact of electronic conduction through bulk *a*-TiO_2, the redox reaction of interest must be oxidative. The redox system must also be nonaqueous to inhibit GaAs corrosion, and should occur at a potential more negative than that required to effect oxidation and corrosion of GaAs.

Decamethylferrocene fulfilled these requirements (Figure S2). The diffusion coefficient was calculated for the redox species in solution (here, 5 mM decamethylferrocene in MeCN with 0.10 M $TBAClO_4$ supporting electrolyte) via chronocoulometry with a Pt disk working electrode of known area in the same solution as was used for the p^+-GaAs/*a*-TiO_2 electrodes. For chronocoulometry, a potential of -0.25 V vs. Ag/Ag^+ was applied for 5 s, then the system was returned to open circuit for 10 s and the cycle was repeated for three oxidation cycles. These data were fit to the Anson equation to calculate D_0.

X-Ray Photoelectron Spectroscopy

X-ray photoelectron spectroscopy (XPS) was performed using a Kratos Axis Ultra system with a base pressure of $< 10^{-9}$ Torr in the analysis chamber. A monochromatic Al Kα source was used to irradiate the sample with X-rays (1486.7 eV) at 150 W. The data were analyzed using CasaXPS computer software. High-resolution scans were fit using a U 2 Tougaard background.

Scanning Electron Microscopy

SEM was performed with an FEI Nova NanoSEM 450 at an accelerating voltage of 5.00 kV with a working distance of 5 mm and an in-lens secondary electron detector.

Atomic Force Microscopy

Atomic force microscopy (AFM) was performed with a Bruker Dimension Icon atomic force microscope. Conductive AFM was performed on the same instrument through use of PeakForce Tunneling AFM (PF-TUNA).

References

(1) Chen, Y. W.; Prange, J. D.; Dühnen, S.; Park, Y.; Gunji, M.; Chidsey, C. E. D.; McIntyre, P. C. Atomic Layer-Deposited Tunnel Oxide Stabilizes Silicon Photoanodes for Water Oxidation. *Nature Mater* **2011**, *10* (7), 539–544. https://doi.org/10.1038/nmat3047.

(2) Hu, S.; Shaner, M. R.; Beardslee, J. A.; Lichterman, M.; Brunschwig, B. S.; Lewis, N. S. Amorphous TiO2 Coatings Stabilize Si, GaAs, and GaP Photoanodes for Efficient Water Oxidation. *Science* **2014**, *344* (6187), 1005–1009. https://doi.org/10.1126/science.1251428.

(3) Verlage, E.; Hu, S.; Liu, R.; Jones, R. J. R.; Sun, K.; Xiang, C.; Lewis, N. S.; Atwater, H. A. A Monolithically Integrated, Intrinsically Safe, 10% Efficient, Solar-Driven Water-Splitting System Based on Active, Stable Earth-Abundant Electrocatalysts in Conjunction with Tandem III–V Light Absorbers Protected by Amorphous TiO $_2$ Films. *Energy Environ. Sci.* **2015**, *8* (11), 3166–3172. https://doi.org/10.1039/C5EE01786F.

(4) Sun, K.; Liu, R.; Chen, Y.; Verlage, E.; Lewis, N. S.; Xiang, C. A Stabilized, Intrinsically Safe, 10% Efficient, Solar-Driven Water-Splitting Cell Incorporating Earth-Abundant Electrocatalysts with Steady-State pH Gradients and Product Separation Enabled by a Bipolar Membrane. *Adv. Energy Mater.* **2016**, *6* (13), 1600379. https://doi.org/10.1002/aenm.201600379.

(5) Zhou, X.; Liu, R.; Sun, K.; Chen, Y.; Verlage, E.; Francis, S. A.; Lewis, N. S.; Xiang, C. Solar-Driven Reduction of 1 Atm of CO_2 to Formate at 10% Energy-Conversion Efficiency by Use of a TiO_2 -Protected III–V Tandem Photoanode in Conjunction with a Bipolar Membrane and a Pd/C Cathode. *ACS Energy Lett.* **2016**, *1* (4), 764–770. https://doi.org/10.1021/acsenergylett.6b00317.

(6) Shen, X.; Yao, M.; Sun, K.; Zhao, T.; He, Y.; Chi, C.-Y.; Zhou, C.; Dapkus, P. D.; Lewis, N. S.; Hu, S. Defect-Tolerant TiO_2 -Coated and Discretized Photoanodes for >600 h of Stable Photoelectrochemical Water Oxidation. *ACS Energy Lett.* **2021**, *6* (1), 193–200. https://doi.org/10.1021/acsenergylett.0c02521.

(7) Saari, J.; Ali-Löytty, H.; Kauppinen, M. M.; Hannula, M.; Khan, R.; Lahtonen, K.; Palmolahti, L.; Tukiainen, A.; Grönbeck, H.; Tkachenko, N. V.; Valden, M. Tunable Ti^{3+} -Mediated Charge Carrier Dynamics of Atomic Layer Deposition-Grown Amorphous TiO_2. *J. Phys. Chem. C* **2022**, acs.jpcc.1c10919. https://doi.org/10.1021/acs.jpcc.1c10919.

(8) Kennedy, K. M.; Kempler, P. A.; Cabán-Acevedo, M.; Papadantonakis, K. M.; Lewis, N. S. Primary Corrosion Processes for Polymer-Embedded Free-Standing or Substrate-Supported Silicon Microwire Arrays in Aqueous Alkaline Electrolytes. *Nano Lett.* **2021**, *21* (2), 1056–1061. https://doi.org/10.1021/acs.nanolett.0c04298.

(9) Buabthong, P.; Ifkovits, Z. P.; Kempler, P. A.; Chen, Y.; Nunez, P. D.; Brunschwig, B. S.; Papadantonakis, K. M.; Lewis, N. S. Failure Modes of

Protection Layers Produced by Atomic Layer Deposition of Amorphous TiO2 on GaAs Anodes. *Energy Environ. Sci.* **2020**. https://doi.org/10.1039/D0EE02032J.

(10) Buabthong, P.; Evans, J. M.; Rinaldi, K. Z.; Kennedy, K. M.; Fu, H. J.; Ifkovits, Z. P.; Kuo, T.-J.; Brunschwig, B. S.; Lewis, N. S. GaAs Microisland Anodes Protected by Amorphous TiO_2 Films Mitigate Corrosion Spreading During Water Oxidation in Alkaline Electrolytes. *ACS Energy Lett.* **2021**, *6* (10), 3709–3714. https://doi.org/10.1021/acsenergylett.1c01174.

(11) Ros, C.; Carretero, N. M.; David, J.; Arbiol, J.; Andreu, T.; Morante, J. R. Insight into the Degradation Mechanisms of Atomic Layer Deposited TiO_2 as Photoanode Protective Layer. *ACS Appl. Mater. Interfaces* **2019**, *11* (33), 29725–29735. https://doi.org/10.1021/acsami.9b05724.

(12) Yu, Y.; Sun, C.; Yin, X.; Li, J.; Cao, S.; Zhang, C.; Voyles, P. M.; Wang, X. Metastable Intermediates in Amorphous Titanium Oxide: A Hidden Role Leading to Ultra-Stable Photoanode Protection. *Nano Lett.* **2018**, *18* (8), 5335–5342. https://doi.org/10.1021/acs.nanolett.8b02559.

(13) Bae, D.; Seger, B.; Vesborg, P. C. K.; Hansen, O.; Chorkendorff, I. Strategies for Stable Water Splitting via Protected Photoelectrodes. *Chem. Soc. Rev.* **2017**, *46* (7), 1933–1954. https://doi.org/10.1039/C6CS00918B.

(14) Bae, D.; Shayestehaminzadeh, S.; Thorsteinsson, E. B.; Pedersen, T.; Hansen, O.; Seger, B.; Vesborg, P. C. K.; Ólafsson, S.; Chorkendorff, I. Protection

of Si Photocathode Using TiO2 Deposited by High Power Impulse Magnetron Sputtering for H2 Evolution in Alkaline Media. *Solar Energy Materials and Solar Cells* **2016**, *144*, 758–765. https://doi.org/10.1016/j.solmat.2015.10.020.

(15) Clark, W. E.; Whitby, K. T. Concentration and Size Distribution Measurements of Atmospheric Aerosols and a Test of the Theory of Self-Preserving Size Distributions. *J. Atmos. Sci.* **1967**, *24* (6), 677–687. https://doi.org/10.1175/1520-0469(1967)024%3C0677:CASDMO%3E2.0.CO;2.

(16) Richter, M. H.; Cheng, W.-H.; Crumlin, E. J.; Drisdell, W. S.; Atwater, H. A.; Schmeißer, D.; Lewis, N. S.; Brunschwig, B. S. X-Ray Photoelectron Spectroscopy and Resonant X-Ray Spectroscopy Investigations of Interactions between Thin Metal Catalyst Films and Amorphous Titanium Dioxide Photoelectrode Protection Layers. *Chem. Mater.* **2021**, *33* (4), 1265–1275. https://doi.org/10.1021/acs.chemmater.0c04043.

(17) Hu, S.; Richter, M. H.; Lichterman, M. F.; Beardslee, J.; Mayer, T.; Brunschwig, B. S.; Lewis, N. S. Electrical, Photoelectrochemical, and Photoelectron Spectroscopic Investigation of the Interfacial Transport and Energetics of Amorphous TiO_2 /Si Heterojunctions. *J. Phys. Chem. C* **2016**, *120* (6), 3117–3129. https://doi.org/10.1021/acs.jpcc.5b09121.

(18) Lichterman, M. F.; Richter, M. H.; Hu, S.; Crumlin, E. J.; Axnanda, S.; Favaro, M.; Drisdell, W.; Hussain, Z.; Brunschwig, B. S.; Lewis, N. S.; Liu, Z.; Lewerenz, H.-J. An Electrochemical, Microtopographical and Ambient Pressure X-

Ray Photoelectron Spectroscopic Investigation of Si/TiO_2 /Ni/Electrolyte Interfaces. *J. Electrochem. Soc.* **2016**, *163* (2), H139–H146. https://doi.org/10.1149/2.0861602jes.

(19) Nunez, P.; Richter, M. H.; Piercy, B. D.; Roske, C. W.; Cabán-Acevedo, M.; Losego, M. D.; Konezny, S. J.; Fermin, D. J.; Hu, S.; Brunschwig, B. S.; Lewis, N. S. Characterization of Electronic Transport through Amorphous TiO_2 Produced by Atomic Layer Deposition. *J. Phys. Chem. C* **2019**, *123* (33), 20116–20129. https://doi.org/10.1021/acs.jpcc.9b04434.

(20) McDowell, M. T.; Lichterman, M. F.; Carim, A. I.; Liu, R.; Hu, S.; Brunschwig, B. S.; Lewis, N. S. The Influence of Structure and Processing on the Behavior of TiO_2 Protective Layers for Stabilization of n-Si/TiO_2 /Ni Photoanodes for Water Oxidation. *ACS Appl. Mater. Interfaces* **2015**, *7* (28), 15189–15199. https://doi.org/10.1021/acsami.5b00379.

(21) Allongue, P.; Blonkowski, S. Corrosion of III–V Compounds; a Comparative Study of GaAs and InP: II. Reaction Scheme and Influence of Surface Properties. *Journal of Electroanalytical Chemistry and Interfacial Electrochemistry* **1991**, *317* (1), 77–99. https://doi.org/10.1016/0022-0728(91)85004-9.

(22) Mengoli, G. An Overview of Phenol Electropolymerization for Metal Protection. *J. Electrochem. Soc.* **1987**, *134* (12), 643C. https://doi.org/10.1149/1.2100379.

(23) Heinze, J.; Frontana-Uribe, B. A.; Ludwigs, S. Electrochemistry of Conducting Polymers—Persistent Models and New Concepts †. *Chem. Rev.* **2010**, *110* (8), 4724–4771. https://doi.org/10.1021/cr900226k.

(24) D'Elia, L. F.; Ortíz, R. L.; Márquez, O. P.; Márquez, J.; Martínez, Y. Electrochemical Deposition of Poly(o-Phenylenediamine) Films on Type 304 Stainless Steel. *J. Electrochem. Soc.* **2001**, *148* (4), C297. https://doi.org/10.1149/1.1354619.

(25) Long, J. W.; Rhodes, C. P.; Young, A. L.; Rolison, D. R. Ultrathin, Protective Coatings of Poly(*o* -Phenylenediamine) as Electrochemical Proton Gates: Making Mesoporous MnO_2 Nanoarchitectures Stable in Acid Electrolytes. *Nano Lett.* **2003**, *3* (8), 1155–1161. https://doi.org/10.1021/nl0343598.

(26) Cabrera, C. R.; Abruna, H. D. Blocking of Recombination Sites and Photoassisted Hydrogen Evolution at Surface-Modified Polycrystalline Thin Films of p-Tungsten Diselenide. *J. Phys. Chem.* **1985**, *89* (7), 1279–1285. https://doi.org/10.1021/j100253a045.

(27) Allongue, P.; Blonkowski, S. Corrosion of III–V Compounds; a Comparative Study of GaAs and InP: Part I. Electrochemical Characterization Based on Tafel Plot Measurements. *Journal of Electroanalytical Chemistry and Interfacial Electrochemistry* **1991**, *316* (1), 57–77. https://doi.org/10.1016/0022-0728(91)87036-4.

(28) Gengenbach, T. R.; Major, G. H.; Linford, M. R.; Easton, C. D. Practical Guides for X-Ray Photoelectron Spectroscopy (XPS): Interpreting the Carbon 1s Spectrum. *Journal of Vacuum Science & Technology A* **2021**, *39* (1), 013204. https://doi.org/10.1116/6.0000682.

(29) Nansé, G.; Papirer, E.; Fioux, P.; Moguet, F.; Tressaud, A. Fluorination of Carbon Blacks: An X-Ray Photoelectron Spectroscopy Study: I. A Literature Review of XPS Studies of Fluorinated Carbons. XPS Investigation of Some Reference Compounds. *Carbon* **1997**, *35* (2), 175–194. https://doi.org/10.1016/S0008-6223(96)00095-4.

(30) Palchan, I.; Crespin, M.; Estrade-Szwarckopf, H.; Rousseau, B. Graphite Fluorides: An XPS Study of a New Type of C-F Bonding. *Chemical Physics Letters* **1989**, *157* (4), 321–327. https://doi.org/10.1016/0009-2614(89)87255-0.

(31) *Handbook of X-Ray Photoelectron Spectroscopy: A Reference Book of Standard Spectra for Identification and Interpretation of XPS Data*, Update.; Moulder, J. F., Chastain, J., Eds.; Perkin-Elmer Corporation: Eden Prairie, Minn, 1992.

Chapter 6

Empirical Verification of Fermi's Golden Rule Approach to Heterogeneous Electron Transfer

6.1—Introduction and background

Heterogeneous electron-transfer reactions are widely used in academic and industrial settings, with applications in photovoltaics, catalysis, batteries, and more.[1–7] Owing to this broad applicability, a complete theoretical framework for understanding such reactions is critical.[4] Electron-transfer theory (often called Marcus theory) has been highly successful at describing homogeneous and heterogeneous electron transfer, but modifications are necessary to describe non-metallic heterogeneous electrochemical reactions.[1,8,9] One such approach is the Fermi Golden Rule equation (Eq. 6.1.1).

Equation 6.1.1

$$k(E) = \frac{4\pi^2}{h}(4\pi kT\lambda)^{-\frac{1}{2}} H_{AB}\beta^{-1}\rho_{eff} I(\lambda, E)$$

Where $k(E)$ is the rate constant as a function of potential, H_{AB} is the integral coupling of all reactant and product energies, β is a coupling attenuation factor, ρ_{eff} is the effective density of states, $I(\lambda,E)$ is an integral weighting rate of reaction across all energies, k is Boltzmann's constant, and T is temperature.[8] Of note is the ρ_{eff} term, which can be decomposed as in Eq. 6.1.2:

Equation 6.1.1

$$\rho_{eff}=\rho\frac{l}{\delta}$$

Where ρ is the states per atom per eV, δ is the average diameter of an atom in the lattice, and l is an effective coupling length of the redox acceptor wave function into a solid electrode.[8] This equation enables calculation of the rate constant as a function of applied potential if some empirical parameters are known. However, the effective coupling length, l, has not been empirically measured. When originally reported, the coupling length l was estimated at 3 Å, meaning only the states present in the first 3 Å could be accessed by a redox couple and states from further inside the electrode were "bulk" states that have no impact on heterogeneous electron-transfer rate.[8] To accurately describe electrochemical systems, this quantity must be empirically measured and compared between multiple heterogeneous reactions. Accurate measurement of this quantity requires measurement of electron-transfer rate constants as a function of thickness with atomic-layer precision.

Two-dimensional (2D) materials such as graphene are layered materials which enable single-atomic-layer precision when constructing electrodes. However, defective sites on graphene flakes exhibit higher electron-transfer rates than basal-plane sites, causing macroscopic measurements of graphene electron-transfer rates to be dominated by defective character.[10] Thus, localized electrochemistry is necessary to ensure defects are not contributing to the signal measured at these electrodes. Scanning electrochemical cell microscopy (SECCM) has emerged as a technique for spatially resolved electrochemistry which can isolate small (< 100 nm) areas of an electrode.[11–16] This technique has previously

been used to quantify graphene electron-transfer rates, with one report concluding that bulk reactivity is achieved at approximately six layers of graphene (~3 nm, an order of magnitude thicker than previously estimated) and another report demonstrating that the change in density of states by twisting graphene bilayers has a significant impact on electron-transfer kinetics.[10,17] A similar technique utilizing microdroplets and various redox couples showed differing dependence of redox kinetics on electrode thickness, though the presence of defects impacted measurements.[18] SECCM has also been used to measure redox kinetics of MoS_2, a semiconducting 2D material, showing a decrease in electron-transfer rate as the thickness increased, attributed to changes in the band gap.

In this work, SECCM is applied to mechanically exfoliated, few-layer graphene to determine whether redox kinetics depend on electrode thickness. Graphene enables atomic-layer precision in electrode thickness while SECCM utilizes high spatial resolution to mitigate the impact of defects on observed rate constants. By combining these traits, an accurate measurement of heterogeneous electron-transfer rate constants as a function of electrode thickness can be achieved, enabling direct measurement of the effective coupling length in the Fermi's Golden Rule equation which will enable more accurate calculations of heterogenous electron-transfer rate constants.

6.2—Electrochemical theory for analysis of voltammograms collected via SECCM

Cyclic voltammetry was first performed with multiple redox couples on bulk highly ordered pyrolytic graphite (HOPG). Theory using the estimated value of l predicts rate constants for the 1-electron redox reaction of $Ru(NH_3)_6^{3+/2+}$ on monolayer graphene to be

3.8×10^{-5} cm/s.[9] Bulk measurements of rate constant on few-layer graphene electrodes are complicated reactive defects overwhelming the response of basal-plane graphene.[10,18–21] Thus, SECCM measurements were performed to eliminate the possibility of defects influencing the measurements.

To calculate the rate constant for the species studied, the voltammetric response must be analyzed. SECCM tips are similar in diffusion profile to hemispherical ultramicroelectrodes (UMEs), and thus equations relating to UMEs will be used here as Tafel analysis requires no mass transport limitation, which is nearly always the case for UMEs.[1] Additionally, scan rates used in this study were sufficiently slow (10 mV/s) to enable a steady-state approximation for the electrode. Utilizing these assumptions, the current density as a fraction of the limiting current density has the limiting form:

Equation 6.2.1

$$\frac{i}{i_{lim}} = \frac{\kappa}{1 + \kappa(1 + \xi^2\theta)}$$

Where i is the current and i_{lim} is the limiting current.[1] The κ term is decomposed as:

Equation 6.2.2

$$\kappa = \frac{r_0 k_f}{D_0}$$

Where r_0 is the radius of the electrode, k_f is the rate constant of the forward reaction, and D_0 is the diffusion coefficient of the redox species.[1] The θ term in Equation 6.2.1 evaluates to:

Equation 6.2.3

$$\theta = e^{\frac{F}{RT}\left(E - E^{0\prime}\right)}$$

Where R is the ideal gas constant, T is temperature in Kelvin, E is the potential, and $E^{0'}$ is the thermodynamic reduction potential of the redox species.[1] The ξ term in 6.2.1 is:

Equation 6.2.4

$$\xi^2 = \frac{D_O}{D_R}$$

Where D_O is the diffusion coefficient of the oxidized species and D_R is the diffusion coefficient of the reduced species.[1] Assuming Butler-Volmer kinetics, k_f in Equation 6.2.2 is a function of E as:

Equation 6.2.5

$$k_f = k^0 \exp\left[-\frac{\alpha F}{RT}\left(E - E^{0\prime}\right)\right]$$

Where k^0 is the fundamental rate constant, F is Faraday's constant, and α is the transfer coefficient.[1] Thus, if ξ is assumed to be unity, which is often the case for self-exchange reactions such as $Ru(NH_3)_6^{3+/2+}$, Equation 6.2.1 simplifies to:

Equation 6.2.6

$$\frac{i}{i_{lim}} = \frac{\kappa}{1 + \kappa(1 + \theta)}$$

Where both κ and θ are functions of E-$E^{0'}$ and thus functions of the applied potential.[1] If the current from the SECCM experiment is normalized to the limiting value, the resultant plot can be fit using Equation 6.2.6. The response is a function of several variables, but assuming that r^0, D_0, and $E^{0'}$ are known, the function simply becomes dependent on the

applied potential, E, and the fundamental rate constant k^0 and transfer coefficient α can be fit.

Key to evaluating these expressions is the value of r_0, which in the UME context is the radius of the hemispherical electrode. In UMEs, the limiting current directly scales with r_0, but for SECCM, the relationship is more complex.[22] The steady-state limiting current in SECCM is given by:

Equation 6.2.7

$$i_{lim} = i_{lim}^{hemi}(1 - \cos(\gamma))$$

Where γ is the half-angle of the pipette, here assumed to be approximately 7.5°.[22] The term i_{lim}^{hemi} is the current at a hemispherical UME and is expressed:

Equation 6.2.8

$$i_{lim}^{hemi} = 2\pi R_{eff} n F D_O c_{b,O}$$

Where n is the number of electrons transferred, and c_b is the bulk concentration of the redox species in mol cm^{-3}, and R_{eff} is the equivalent radius of a hemispherical UME that describes the behavior of the SECCM probe.[1,22] A reasonable algebraic expression approximating R_{eff} is given by:

Equation 6.2.9

$$R_{eff} = \frac{r_p}{\tan(\gamma)}$$

Where r_p is the radius of the pipette and h is the height of the microdroplet.[22] Thus, the radius of the nanopipette opening can be estimated electrochemically using just the limiting current - i_{lim} - and known constants.

6.3—SECCM of $Ru(NH_3)_6^{3+/2+}$ on multi-layered graphene sample

Samples were prepared by stamping of mechanically exfoliated graphene flakes onto hexagonal boron nitride (HBN) flakes of similar size. The combined flake was then stamped onto a mica substrate with Au contacts deposited on the surface by metal evaporation. A HOPG contact was then added to connect the graphene sample and Au contact. Samples were analyzed via AFM and Raman spectroscopy to confirm layer thickness. The sample utilized in this chapter is displayed in Figure 6.3.2.

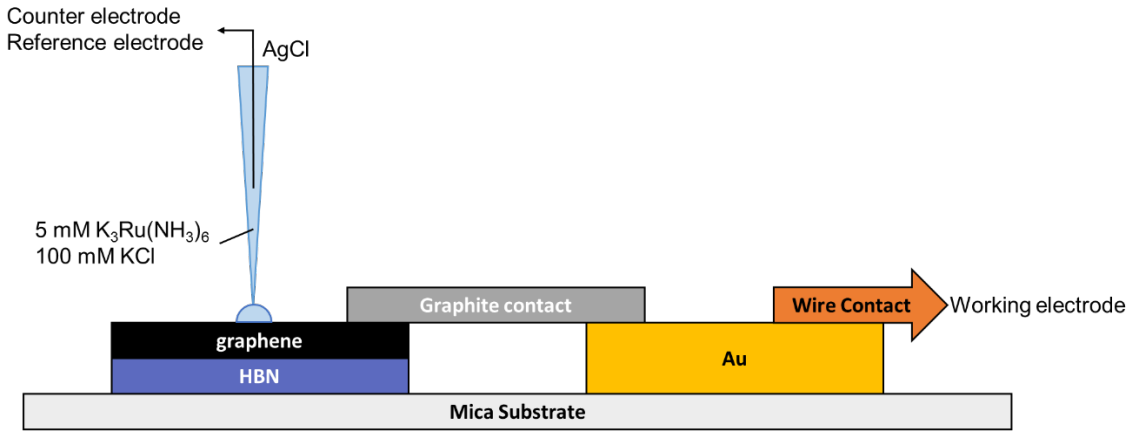

Figure 6.3.1. Schematic of experimental setup for SECCM measurement of $Ru(NH_3)_6^{3+/2+}$ rate constant on graphene electrodes

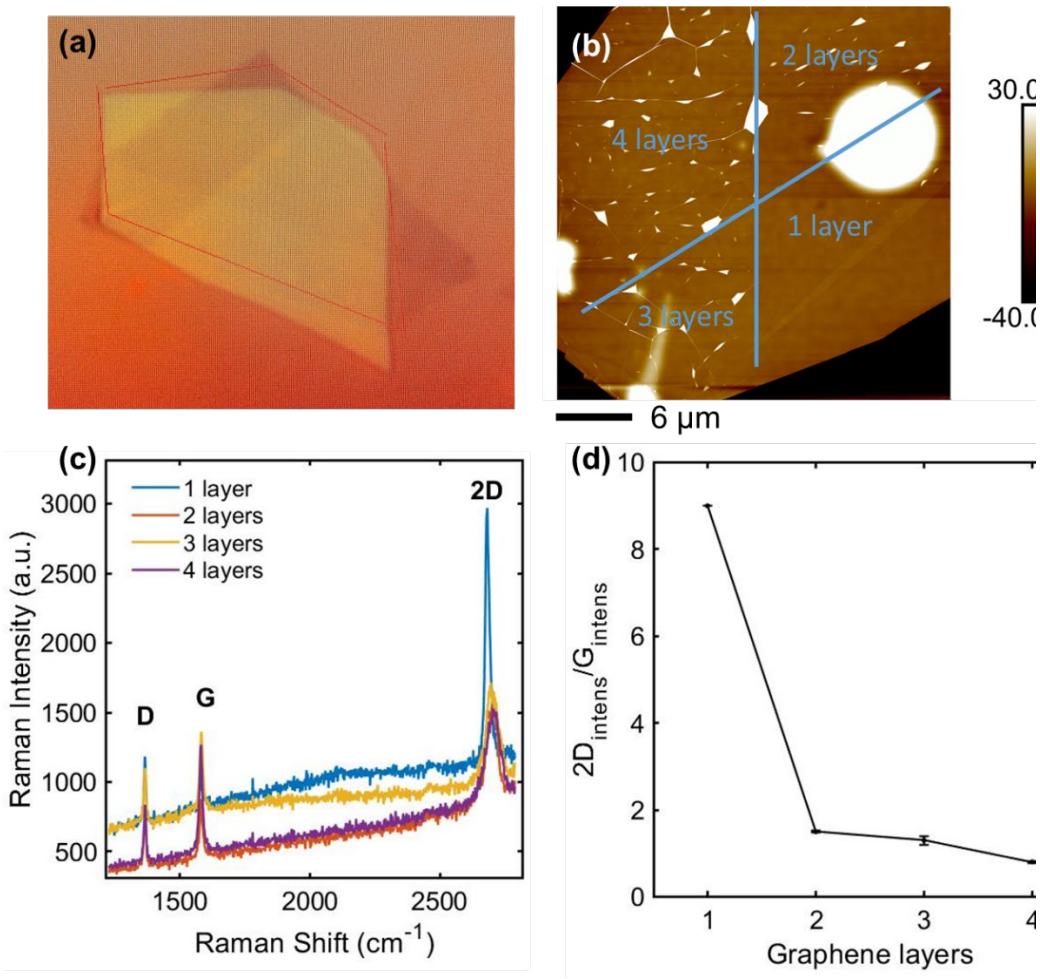

Figure 6.3.2. (a) Optical image and (b) AFM micrograph of graphene electrode assembly used in this work with regions of varying thickness denoted. (c) Raman spectra of graphene with D, G and 2D modes labeled and (d) ratio of 2D/G Raman mode intensity used to identify thickness of graphene layers

Once the sample was prepared, nanopipettes were prepared using the procedure outlined in Section 6.E and filled with solution. Contact was made within each of the regions noted above and CVs were collected at each point. Resulting voltammograms are plotted below in Figure 6.3.3. Maximum current values were small, less than 1 pA, indicating small tip radius.

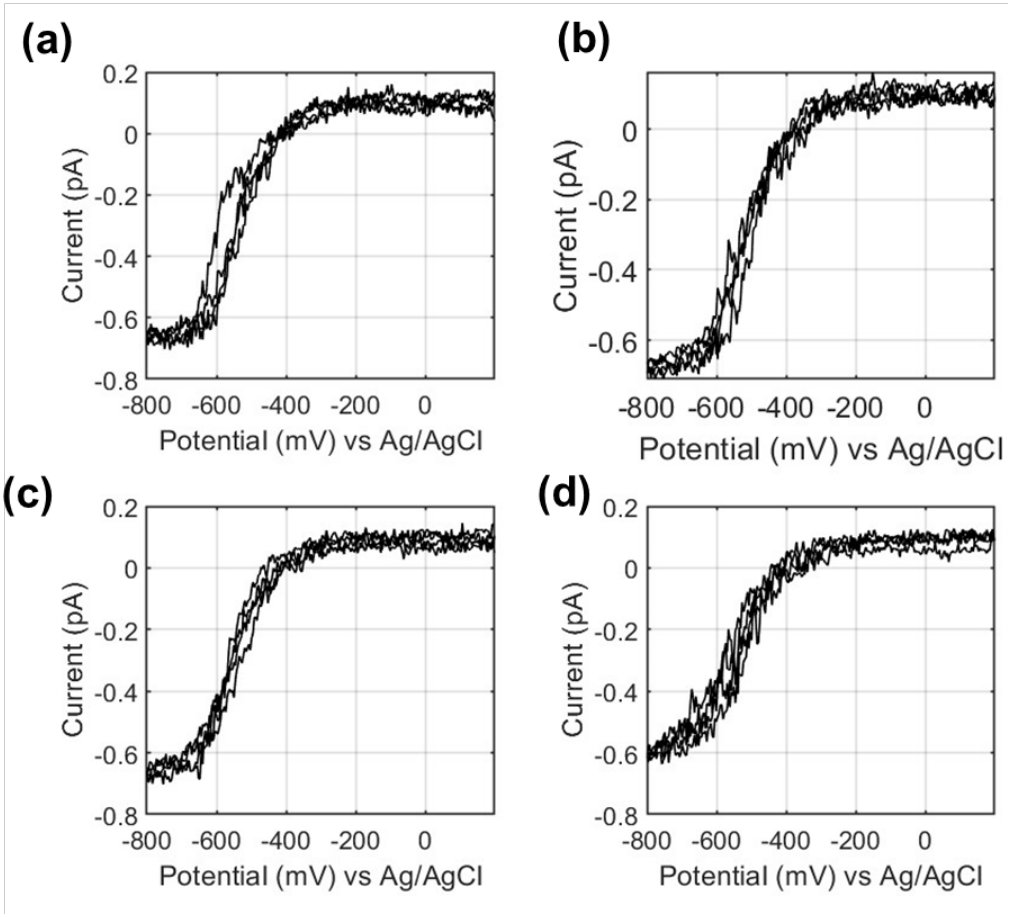

Figure 6.3.3. Cyclic voltammograms collected via SECCM at 10 mV/s in 5 mM $K_3Ru(NH_3)_6$, 100 mM KCl solution on (a) monolayer, (b) bilayer, (c) trilayer, and (d) four-layer graphene working electrodes.

The effective radius, R_{eff}, and pipette radius, r_p, were calculated using Equations 6.2.7–6.2.9. Resultant tip radii are tabulated in Table 6.3.1. Effective radii measurements are consistent, at approximately 30 nm, with a much larger r_p of approximately 250 nm. These values are consistent with expectations for nanopipette radii, giving confidence to further calculated results. These radii are also sufficiently small that defects in the graphene flake can be avoided.

Table 6.3.1. Effective UME radius and pipette tip radius measured electrochemically

Graphene layers	R_{eff} *(nm)*	r_p *(nm)*
1	32.8	248.8
2	33.8	256.6
3	33.3	253.0
4	29.8	226.3

To verify the predictions made using Equation 6.1.1, the fundamental rate constant, k^0, must be calculated for each voltammogram collected. This was accomplished by fitting the collected data to Equation 6.2.6, where k^0 and α were allowed to vary to achieve a good fit, and the other parameters were fixed as tabulated in Table 6.3.2. Resulting fits with raw data are displayed in Figure 6.3.4.

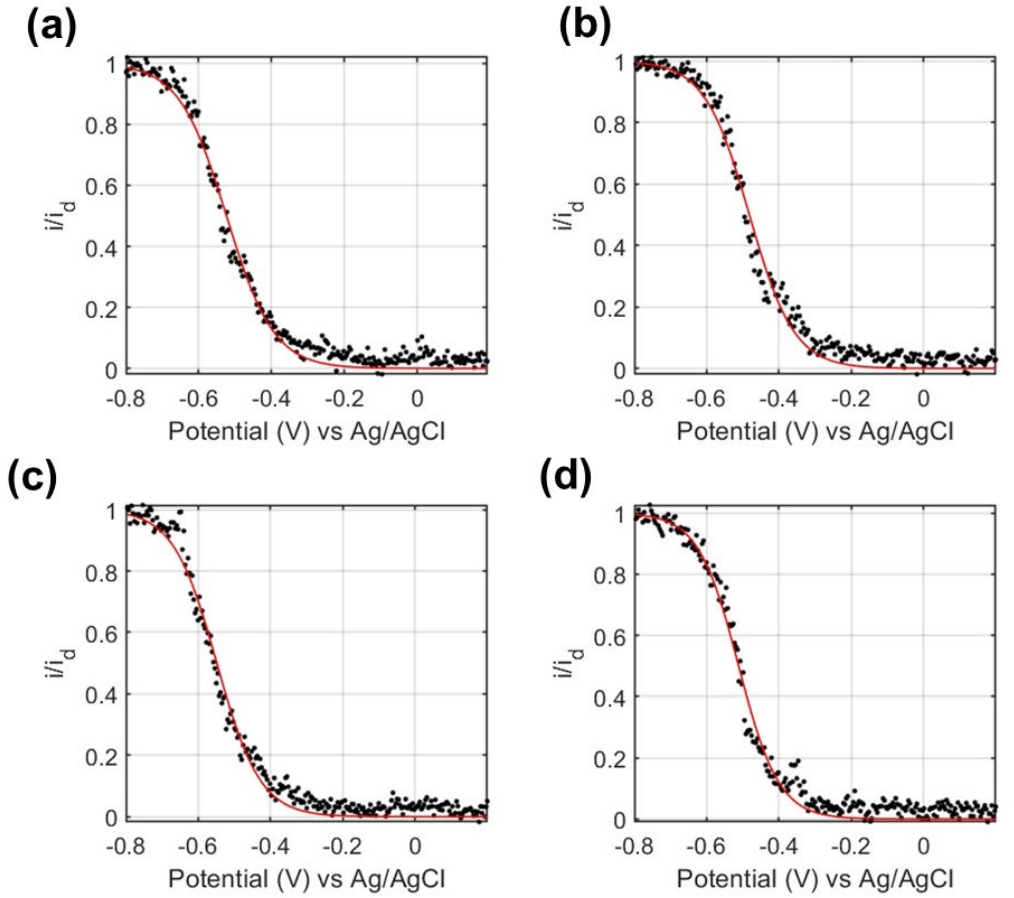

Figure 6.3.4. Raw data from cyclic voltammograms collected via SECCM at 10 mV/s in 5 mM $K_3Ru(NH_3)_6$, 100 mM KCl solution (black dots) with resulting fits to Equation 6.2.6 (red line) on (a) monolayer, (b) bilayer, (c) trilayer, and (d) four-layer graphene working electrodes.

From these fits, k^0 was and α were calculated and plotted as a function of graphene layer thickness (Figure 6.3.5). The values of k^0 show a negative dependence on the number of graphene layers, and are approximately two orders of magnitude larger than expected based on calculations of $Ru(NH_3)_6^{2+/3+}$ on HOPG using Equation 6.1.1.[9] Values of α, however, do show a dependence on thickness, where α increases with increasing graphene thickness. The values of α are between 0.4 and 0.5, which is reasonable for $Ru(NH_3)_6^{3+/2+}$

as it is a self-exchange reaction which is expected to have a nearly symmetrical reaction coordinate diagram and therefore should have an α close to 0.5.[1] A value of 0.5 indicates a perfectly symmetrical reaction, and as the values measured are approaching this value, it is hypothesized that the increase in thickness enables the reaction to become more symmetric, and that this effect is greater than any impact the electrode thickness has on fundamental rate constant.

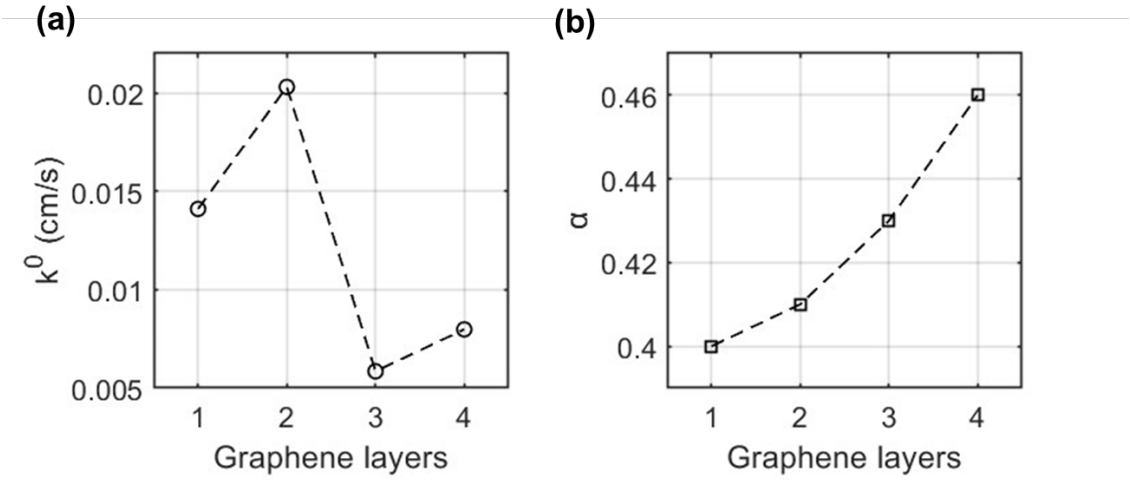

Figure 6.3.5. (a) Fundamental rate constant and (b) transfer coefficient calculated via the fits in Figure 6.3.4 as a function of graphene electrode thickness.

To test whether the variance observed in α is masking a change in the rate constant, α was fixed at 0.5 and the voltammograms were re-fit, allowing only k^0 to change. The fits were qualitatively similar to those in Figure 6.3.3, and the extracted k^0 values were plotted as a function of graphene thickness (Figure 6.3.5). No substantial difference is found in the trend of k^0 vs. electrode thickness.

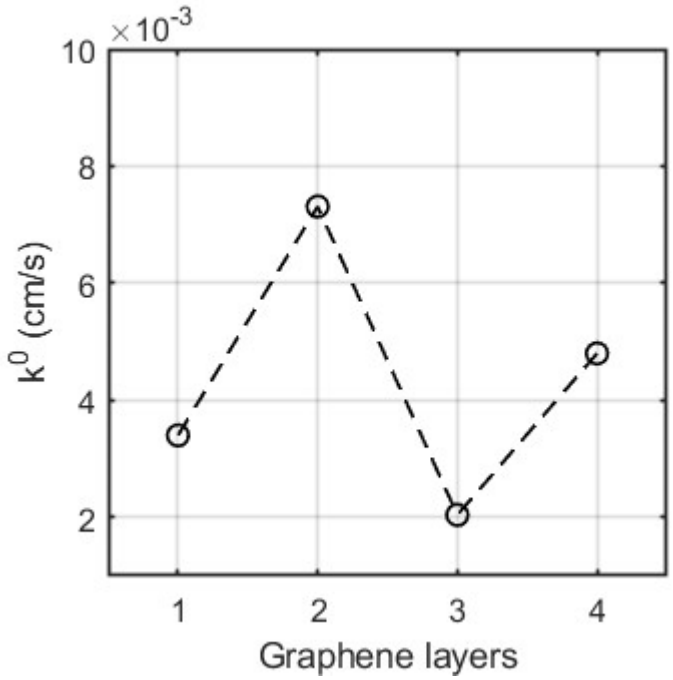

Figure 6.3.6. Fundamental rate constant as a function of graphene electrode thickness by fitting the raw data in Figure 6.3.4 to Equation 6.2.6 while holding α constant at 0.5.

Table 6.3.2. Fundamental rate constant and transfer coefficient calculated as a function of graphene electrode thickness

Graphene layers	k^0	α
1	1.41×10^{-2}	0.4
2	2.03×10^{-2}	0.41
3	5.85×10^{-3}	0.43
4	7.98×10^{-3}	0.46

Measurements of k^0 on few-layer graphene electrodes indicate little to no dependence on electrode thickness, but these values need to be compared to measurements on bulk HOPG to determine whether bulk reactivity is achieved at a single layer of graphene, and thus l in

Equation 6.1.2 would, in this analysis, be assumed to be less than or equal to the thickness of a single graphene layer. However, due to the impact of defects already described, bulk measurements of HOPG are expected to be dominated by the reactivity of defective sites. To minimize this effect, SECCM mapping was utilized on HOPG electrodes, enabling spatially resolved measurements of electrochemical activity and identification of anomalously reactive sites. Cyclic voltammograms collected in a 5 μm x 5 μm square on an HOPG electrode were fit to Equation 6.2.6 and are displayed in Figure 6.2.7.

Examining Figure 6.2.7a, transfer coefficients near and above 1.0 are observed, which is non-physical as the definition of α mathematically prevents such values. This indicates that the assumption of irreversibility or quasi-reversibility in Equation 6.2.6 is invalid in these cases and that reversible kinetics are observed. Fully reversible steady-state UME voltammograms cannot be straightforwardly decomposed to yield kinetic parameters and therefore the corresponding k^0 values are invalid (Figure 6.2.7b). These reversible measurements are hypothesized to have been collected on defective HOPG where facile reactivity is observed. However, some HOPG sites had fit α values below 0.8, which is within the feasible α range.[1] These sites are hypothesized to be defect-free basal-plane HOPG and the physically allowable α values fit indicate that the k^0 values calculated may be meaningful. The average k^0 at these sites was 2.5×10^{-3} cm s^{-1} with a standard deviation of 2.3×10^{-3} cm s^{-1}. This value is statistically indistinguishable from the values of k^0

calculated for few-layer graphene. Thus, in this analysis, the value of *l* in Equation 6.1.2 would be evaluated as less than or equal to the thickness of a single graphene layer.

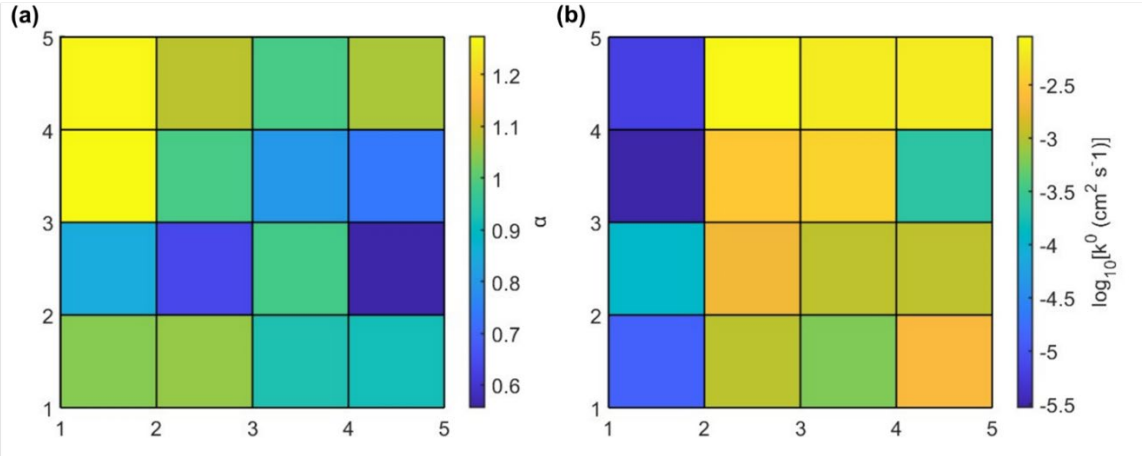

Figure 6.2.7. SECCM map of HOPG surface where (a) transfer coefficient and (b) fundamental rate constant are calculated via fitting of Equation 6.2.6 to spatially resolved cyclic voltammograms on the HOPG electrode.

The thickness of a single graphene layer is a more complex quantity to measure than might first be assumed. A single graphene layer is one atom thick, and the atomic radius of C is 0.9 Å, thus one can reasonably assume that one graphene layer is approximately 1 Å thick and this analysis would indicate that *l* has been overestimated by a factor of 3.[23] However, orbital hybridization of C in graphene induces a change in geometry, and experimental attempts to measure the thickness of monolayer graphene have generated debate.[24] Use of AFM to measure graphene thickness is particularly fraught, with thicknesses between 4 and 17 Å reported.[24,25] Transmission electron microscopy measurements, which can directly image the layers, commonly report graphene layer

thickness between 3 and 4 Å.[25] Comparing this value to the estimated value of *l*, the present analysis would indicate that 3 Å is in fact a reasonable, experimentally observed value.

Experimental difficulties in SECCM measurement should temper this conclusion. SECCM measurements on single points of a multilayer sample are vulnerable to defect sites, as described. While SECCM decreases the likelihood of measuring a defective site, the chance is non-zero, and it is difficult to ascertain whether a single measurement was or was not influenced by a defect. Additionally, SECCM measurements may induce defects in the film, as salt deposits on the sample, or warping is induced as the tip contacts the graphene. Ideally, high-resolution SECCM mapping can be conducted on a well-defined graphene sample with multiple confirmed layers so that any differences in kinetics caused by defect or thickness can be decoupled. However, even this analysis may prove insufficient to accurately evaluate the value of *l*, as the thickness of graphene layers prevents conclusive determination with precision of more than 3 to 4 Å. Thus, SECCM could in principle be used to prove whether *l* is less than or equal to a certain thickness with error of, at minimum, 3 Å but cannot determine whether *l* is less than 3 Å as estimated.

6.3—Conclusions

SECCM was employed to experimentally determine the effective coupling length of a redox couple into a heterogeneous electrode, empirically verifying an assumption made in the Fermi Golden Rule approach to evaluation of heterogeneous electron transfer at semi-metallic and semiconducting electrodes. The spatial resolution of SECCM enables

avoidance of defective sites that can induce artificially fast kinetics that are not descriptive of pristine basal-plane kinetics. SECCM measurements on spectroscopically confirmed mono- and multilayer graphene using the $Ru(NH_3)_6^{2+/3+}$ redox couple indicated little to no dependence of k^0 on thickness up to four layers, though α was observed to increase with thickness. SECCM on bulk HOPG demonstrated the impact of defects and the spatial variability of kinetics on such electrodes. Extracting k^0 from quasireversible regions on HOPG indicated no statistical difference between few-layer graphene and bulk HOPG kinetics. Thus, in this analysis, l can be reasonably estimated at no more than 3–4 Å, though experimental uncertainties and limitations in electrode thickness resolution due to graphene layer thickness prevent precise empirical verification. Improvements to this analysis could include high-resolution SECCM on few-layer graphene with a variety of redox couples, but any measurements would have inherent error of 3–4 Å.

Experimental Methods

Preparation of graphene electrodes

Graphene flakes were mechanically exfoliated from bulk HOPG (supplier) by repeatedly cleaving with standard adhesive tape and then adhered to polydimethylsiloxane (PDMS). Substrates were prepared by cleaving bulk mica (grade V-5, SPI supplies) to be flat on both sides, then 3 nm Ti was deposited as an adhesion layer using a Denton Explorer 14 electron beam metal evaporation system (base pressure < 1e-6 Torr, 40 mA deposition current, 10 kV accelerating voltage). 40 nm Au was then deposited to make the final contact (150 mA deposition current). A physical mask was used to make circular

contacts. A custom PDMS stamp was used to pick up flakes of HBN (Trivial Transfer HBN, 1 layer, ACS Materials) at 90 °C, then graphene at 60 °C. The stamp was then flipped upside down and the assembled HBN-graphene stack was then picked up with another stamp and placed on the mica/Au substrate near the Au contact.

A graphite contact was fabricated by mechanically exfoliating HOPG and selecting a thin (in width) sample. The thin graphite contact was then picked up using the custom stamp and aligned such that it can connect the Au contact and graphene stack, then dropped on to the stack at 60 °C to make the full electrode stack. Electrical contact was made by adhering Cu metal to the Au contact with conductive Ag paste (SPI supplies). The Cu metal was then connected to the working electrode contact of the AFM.

Preparation of nanopipettes

Nanopipettes were prepared using a Sutter P-2000 micropipette puller. Capillaries used to create nanopipettes were flame-polished borosilicate glass with a filament with nominal outer diameter of 1.2 mm, inner diameter 0.69 mm, and 10 cm in length (Sutter part number BF120-69-10). Pipettes were pulled using the settings in Table 6.E.1. Aqueous solutions of 5 mM hexaammineruthenium (III) chloride (98%, Sigma-Aldrich) and 100 mM potassium chloride (ACS grade, EMD) were prepared in a 25 mL volumetric flask. Solutions must be re-made each day due to decomposition of the ruthenium compound. Nanopipettes were filled with solution using a syringe with a filter and microfil flexible needle (WPI M28G-5). Mechanical and thermal agitation was required to completely fill nanopipettes. Thermal agitation was performed by filling the pipettes as above, then setting

them on a hot plate set to low heat with pulled tip hanging off of the edge as in literature.[26] Mechanical agitation was accomplished via rubbing of tweezer grips on nanopipettes at the non-pulled ends. This occasionally resulted in fractured tips due to high vibration so care must be taken in this approach. The presence of bubbles and quality of the pipette filling was checked with an optical microscope.

Table 6.E.1. Sutter P-2000 settings for micropipette pulling

HEAT	FIL	VEL	DEL	PUL
350	4	50	225	150

SECCM Procedure

SECCM measurements were performed with a Park NX12 AFM equipped with SICM head. Filled pipettes were attached to the SICM head, and then a AgCl wire was inserted into the pipetted to form the counter/reference electrode. The camera and focus were adjusted to focus on the pipette tip, then the focal plane was lowered slightly below the visible tip. The head was lowered until the sample was in focus, then contact was achieved electrochemically using the "form cell" procedure using the settings in Table 6.E.2. The "threshold" value can be adjusted depending on expected pipette diameter, where smaller pipette diameters generate less current (see Equations 6.2.7–6.2.9). Once contact was achieved, desired mapping parameters were input, if desired, and cyclic voltammetry was performed from +0.2 V vs. reference to -0.8 V vs. reference at 10 mV/s to achieve approximately steady-state conditions.

Table 6.E.2. Form cell settings for SECCM contact in Park NX12

THRESHOLD	SPEED	FORM CELL BIAS	END BIAS
1.5 pA	0.5 μm s^{-1}	-1.0 V	0.0 V

References

(1) Bard, A. J.; Faulkner, L. R. *Electrochemical Methods: Fundamentals and Applications*, 2nd ed.; Wiley: New York, 2001.

(2) Dunn, B.; Kamath, H.; Tarascon, J.-M. Electrical Energy Storage for the Grid: A Battery of Choices. *Science* **2011**, *334* (6058), 928–935.

(3) McCrory, C. C. L.; Jung, S.; Peters, J. C.; Jaramillo, T. F. Benchmarking Heterogeneous Electrocatalysts for the Oxygen Evolution Reaction. *J. Am. Chem. Soc.* **2013**, *135* (45), 16977–16987. https://doi.org/10.1021/ja407115p.

(4) Bard, A. J.; Fox, M. A. Artificial Photosynthesis: Solar Splitting of Water to Hydrogen and Oxygen. *Acc. Chem. Res.* **1995**, *28* (3), 141–145. https://doi.org/10.1021/ar00051a007.

(5) Walter, M. G.; Warren, E. L.; McKone, J. R.; Boettcher, S. W.; Mi, Q.; Santori, E. A.; Lewis, N. S. Solar Water Splitting Cells. *Chem. Rev.* **2010**, *110* (11), 6446–6473. https://doi.org/10.1021/cr1002326.

(6) Tan, M. X.; Laibinis, P. E.; Nguyen, S. T.; Kesselman, J. M.; Stanton, C. E.; Lewis, N. S. Principles and Applications of Semiconductor

Photoelectrochemistry. In *Progress in Inorganic Chemistry*; Karlin, K. D., Ed.; John Wiley & Sons, Inc.: Hoboken, NJ, USA, 2007; pp. 21–144. https://doi.org/10.1002/9780470166420.ch2.

(7) Kelly, R.; Scully, J.; Shoesmith, D.; Buchheit, R. Electrochemical Techniques in Corrosion Science and Engineering. **2003**. https://doi.org/10.1201/9780203909133.

(8) Royea, W. J.; Fajardo, A. M.; Lewis, N. S. Fermi Golden Rule Approach to Evaluating Outer-Sphere Electron-Transfer Rate Constants at Semiconductor/Liquid Interfaces. *J. Phys. Chem. B* **1997**, *101* (51), 11152–11159. https://doi.org/10.1021/jp972222y.

(9) Royea, W. J.; Hamann, T. W.; Brunschwig, B. S.; Lewis, N. S. A Comparison between Interfacial Electron-Transfer Rate Constants at Metallic and Graphite Electrodes. *J. Phys. Chem. B* **2006**, *110* (39), 19433–19442. https://doi.org/10.1021/jp062141e.

(10) Güell, A. G.; Ebejer, N.; Snowden, M. E.; Macpherson, J. V.; Unwin, P. R. Structural Correlations in Heterogeneous Electron Transfer at Monolayer and Multilayer Graphene Electrodes. *J. Am. Chem. Soc.* **2012**, *134* (17), 7258–7261. https://doi.org/10.1021/ja3014902.

(11) Ebejer, N.; Güell, A. G.; Lai, S. C. S.; McKelvey, K.; Snowden, M. E.; Unwin, P. R. Scanning Electrochemical Cell Microscopy: A Versatile Technique for

Nanoscale Electrochemistry and Functional Imaging. *Annual Rev. Anal. Chem.* **2013**, *6* (1), 329–351. https://doi.org/10.1146/annurev-anchem-062012-092650.

(12) Bentley, C. L.; Edmondson, J.; Meloni, G. N.; Perry, D.; Shkirskiy, V.; Unwin, P. R. Nanoscale Electrochemical Mapping. *Anal. Chem.* **2019**, *91* (1), 84–108. https://doi.org/10.1021/acs.analchem.8b05235.

(13) Yule, L. C.; Bentley, C. L.; West, G.; Shollock, B. A.; Unwin, P. R. Scanning Electrochemical Cell Microscopy: A Versatile Method for Highly Localised Corrosion Related Measurements on Metal Surfaces. *Electrochimica Acta* **2019**, *298*, 80–88. https://doi.org/10.1016/j.electacta.2018.12.054.

(14) Bentley, C. L.; Kang, M.; Unwin, P. R. Scanning Electrochemical Cell Microscopy (SECCM) in Aprotic Solvents: Practical Considerations and Applications. *Anal. Chem.* **2020**, *92* (17), 11673–11680. https://doi.org/10.1021/acs.analchem.0c01540.

(15) Snowden, M. E.; Güell, A. G.; Lai, S. C. S.; McKelvey, K.; Ebejer, N.; O'Connell, M. A.; Colburn, A. W.; Unwin, P. R. Scanning Electrochemical Cell Microscopy: Theory and Experiment for Quantitative High Resolution Spatially-Resolved Voltammetry and Simultaneous Ion-Conductance Measurements. *Anal. Chem.* **2012**, *84* (5), 2483–2491. https://doi.org/10.1021/ac203195h.

(16) Wahab, O. J.; Kang, M.; Unwin, P. R. Scanning Electrochemical Cell Microscopy: A Natural Technique for Single Entity Electrochemistry. *Current*

Opinion in Electrochemistry **2020**, *22*, 120–128. https://doi.org/10.1016/j.coelec.2020.04.018.

(17) Yu, Y.; Zhang, K.; Parks, H.; Babar, M.; Carr, S.; Craig, I. M.; Van Winkle, M.; Lyssenko, A.; Taniguchi, T.; Watanabe, K.; Viswanathan, V.; Bediako, D. K. Tunable Angle-Dependent Electrochemistry at Twisted Bilayer Graphene with Moiré Flat Bands. *Nat. Chem.* **2022**, *14* (3), 267–273. https://doi.org/10.1038/s41557-021-00865-1.

(18) Velický, M.; Bradley, D. F.; Cooper, A. J.; Hill, E. W.; Kinloch, I. A.; Mishchenko, A.; Novoselov, K. S.; Patten, H. V.; Toth, P. S.; Valota, A. T.; Worrall, S. D.; Dryfe, R. A. W. Electron Transfer Kinetics on Mono- and Multilayer Graphene. *ACS Nano* **2014**, *8* (10), 10089–10100. https://doi.org/10.1021/nn504298r.

(19) Brownson, D. A. C.; Munro, L. J.; Kampouris, D. K.; Banks, C. E. Electrochemistry of Graphene: Not Such a Beneficial Electrode Material? *RSC Adv.* **2011**, *1* (6), 978. https://doi.org/10.1039/c1ra00393c.

(20) Brownson, D. A. C.; Kampouris, D. K.; Banks, C. E. Graphene Electrochemistry: Fundamental Concepts through to Prominent Applications. *Chem. Soc. Rev.* **2012**, *41* (21), 6944. https://doi.org/10.1039/c2cs35105f.

(21) Chen, R.; Nioradze, N.; Santhosh, P.; Li, Z.; Surwade, S. P.; Shenoy, G. J.; Parobek, D. G.; Kim, M. A.; Liu, H.; Amemiya, S. Ultrafast Electron Transfer

Kinetics of Graphene Grown by Chemical Vapor Deposition. *Angew. Chem. Int. Ed.* **2015**, *54* (50), 15134–15137. https://doi.org/10.1002/anie.201507005.

(22) Anderson, K. L.; Edwards, M. A. Evaluating Analytical Expressions for Scanning Electrochemical Cell Microscopy (SECCM). *Anal. Chem.* **2023**, *95* (21), 8258–8266. https://doi.org/10.1021/acs.analchem.3c00216.

(23) Wilson, A. J. C. Tables of Interatomic Distances and Configuration in Molecules and Ions. *Acta Cryst* **1959**, *12* (2), 174–174. https://doi.org/10.1107/S0365110X59003024.

(24) Shearer, C. J.; Slattery, A. D.; Stapleton, A. J.; Shapter, J. G.; Gibson, C. T. Accurate Thickness Measurement of Graphene. *Nanotechnology* **2016**, *27* (12), 125704. https://doi.org/10.1088/0957-4484/27/12/125704.

(25) Kumar, V.; Kumar, A.; Lee, D.-J.; Park, S.-S. Estimation of Number of Graphene Layers Using Different Methods: A Focused Review. *Materials* **2021**, *14* (16), 4590. https://doi.org/10.3390/ma14164590.

(26) Sun, L.; Shigyou, K.; Ando, T.; Watanabe, S. Thermally Driven Approach To Fill Sub-10-Nm Pipettes with Batch Production. *Anal. Chem.* **2019**, *91* (21), 14080–14084. https://doi.org/10.1021/acs.analchem.9b03848.